

Surfaces of Pd-based alloys as catalysts for CO₂ activation and hydrogenation to methanol

DOCTOR OF PHILOSOPHY

IGOR KOWALEC

DEPARTMENT OF CHEMISTRY

CARDIFF CATALYSIS INSTITUTE

CARDIFF UNIVERSITY

SUPERVISOR: PROFESSOR SIR C. R. A. CATLOW

CO-SUPERVISOR: DR A. J. LOGSDAIL

JUNE 2023

I. Abstract

This thesis investigates the active sites and reactions involved in CO₂ hydrogenation to methanol on the promising Pd-based catalysts. Using state-of-the-art simulation techniques, the study aims to identify catalyst features enhancing CO₂ activation via the formate mechanism and develop descriptors for high-throughput computational analysis of Pd-alloy surfaces.

The mechanism of CO₂ hydrogenation to methanol on low-index Pd facets is explored in detail using density functional theory calculations. The rate-determining step involves HCOOH to H₂COOH conversion; however, the Gibbs free energy analysis reveals that the reaction on Pd surfaces is limited at the initial hydrogenation of CO₂ to formate.

Further, hydrogen adsorption on Pd (111) and Pd (100) surfaces is analysed, considering an exhaustive number of configurations at coverages of up to 2 monolayers. We predict that subsurface hydrogen is present on Pd surfaces at hydrogen coverages expected at reaction conditions relevant for CO₂ hydrogenation.

Initial stages of CO₂ hydrogenation are modelled on low-index metallic Cu, Pd, Zn and alloy CuPd and PdZn surfaces. CuPd (110) surface shows a CO₂ hydrogenation barrier similar to that on Pd (100) but inhibits CO₂ dissociation linked to lower selectivity of CO₂ hydrogenation to methanol. Moreover, the CuPd (110) surface shows a significantly stronger hydrogen adsorption as compared to Cu surfaces. The PdZn surfaces show lower activation energy barriers for CO₂ hydrogenation than Pd facets, but CO₂ chemisorption constitutes most of the barrier, suggesting an Eley-Rideal mechanism of CO₂ hydrogenation on PdZn surfaces. The observed reaction energy barriers correlate with the characteristics of the monodentate formate intermediate.

Overall, this thesis aims to understand the behaviour of CO₂ and hydrogen on Pd-based catalysts, illustrating the power of simulation in explaining experimental observations and facilitating rational catalyst design to address climate change in the transportation sector.

II. Table of Contents

| | |
|---|----|
| I. Abstract..... | i |
| II. Table of Contents..... | ii |
| Numbered Item List – Figures | v |
| Numbered Item List – Tables | xi |
| III. Acknowledgements..... | xv |
| Chapter 1. Hydrogenation of carbon dioxide to methanol | 1 |
| 1.1. Green chemistry in the transportation industry | 1 |
| 1.2. Heterogeneous Catalysis..... | 2 |
| 1.3. Transition metal nanoparticle catalysts | 2 |
| 1.4. Cu, Pd and ZnO in TMNP catalysts | 3 |
| 1.5. TMNP alloys and intermetallic compounds | 5 |
| 1.6. CO ₂ hydrogenation to methanol | 6 |
| 1.7. What makes a good CO ₂ hydrogenation catalyst?..... | 9 |
| 1.8. Research Outline | 10 |
| Chapter 2. Computational theory..... | 12 |
| 2.1. Quantum chemistry concepts | 12 |
| 2.1.1. Schrödinger Equation and the self-consistent field..... | 12 |
| 2.1.2. Density functional theory | 14 |
| 2.1.3. Approximation levels of the density functional..... | 16 |
| 2.1.4. Computational modelling of periodic materials | 18 |
| 2.1.5. Basis sets | 19 |
| 2.2. Potential energy surface | 20 |
| 2.2.1. Geometry optimisation..... | 22 |
| 2.2.2. Vibrations and Thermodynamics | 23 |

| | | |
|------------|--|----|
| 2.2.3. | Transition state calculations | 25 |
| 2.3. | Software details..... | 26 |
| Chapter 3. | A computational study of direct CO ₂ hydrogenation to methanol on Pd surfaces | 27 |
| 3.1. | Introduction..... | 27 |
| 3.2. | Methodology | 31 |
| 3.2.1. | Bulk models..... | 32 |
| 3.2.2. | Surface models..... | 35 |
| 3.2.3. | Surface adsorption..... | 37 |
| 3.2.4. | Transition state structures | 38 |
| 3.2.5. | Vibrations and Thermodynamics | 40 |
| 3.3. | Results and discussions | 40 |
| 3.3.1. | Hydrogen adsorption | 40 |
| 3.3.2. | CO ₂ adsorption..... | 43 |
| 3.3.3. | Interactions of intermediates with Pd surfaces..... | 48 |
| 3.3.4. | Transition states and reaction profile..... | 50 |
| 3.3.5. | Gibbs free energy analysis | 55 |
| 3.4. | Summary and conclusions..... | 60 |
| Chapter 4. | Hydrogen coverage on low-index Pd surfaces..... | 62 |
| 4.1. | Introduction..... | 62 |
| 4.1.1. | Simulation of surface compositions of transition metal hydrides and oxides .. | 64 |
| 4.1.2. | Hydrogen on late transition metals | 65 |
| 4.2. | Computational Methods | 67 |
| 4.2.1. | Density functional theory (DFT) calculations..... | 67 |
| 4.2.2. | Adsorption enthalpy | 67 |
| 4.2.3. | Enumeration of unique surface hydrogen arrangements | 72 |

| | | |
|------------|---|-----|
| 4.2.4. | Adsorption on Pd (111)..... | 75 |
| 4.2.5. | Adsorption on Pd (100)..... | 78 |
| 4.2.6. | Vibrations and Thermodynamics..... | 79 |
| 4.3. | Results and discussion..... | 82 |
| 4.3.1. | Adsorption on Pd (111)..... | 82 |
| 4.3.2. | Adsorption on Pd (100)..... | 88 |
| 4.3.3. | Pd (111) – Gibbs free energy | 91 |
| 4.4. | Conclusions..... | 92 |
| Chapter 5. | CO ₂ hydrogenation to formate on Cu, Pd, Zn and PdZn and CuPd alloy surfaces | 94 |
| 5.1. | Introduction..... | 94 |
| 5.2. | Computational methods | 96 |
| 5.3. | Results and discussion..... | 98 |
| 5.3.1. | Hydrogen adsorption on Cu, Pd and Zn, CuPd and PdZn surfaces | 98 |
| 5.3.2. | CO adsorption | 104 |
| 5.3.3. | CO ₂ adsorption..... | 106 |
| 5.3.4. | CO ₂ dissociation | 110 |
| 5.3.5. | HCOO..... | 113 |
| 5.3.6. | Mulliken charge analysis of Cu, Pd and CuPd (110) surfaces | 116 |
| 5.3.7. | Transition states..... | 119 |
| 5.3.8. | Reaction energetics..... | 120 |
| 5.4. | Conclusions and future work | 128 |
| Chapter 6. | Summary, Conclusions and Future Prospects | 130 |
| References | | 134 |
| Appendix | | 146 |
| | Tabulated adsorption enthalpy and energy | 146 |

| | |
|---|-----|
| Tabulated energy of individual reaction steps | 146 |
| Visualised adsorbates and transition states | 149 |
| CO ₂ dissociation and hydrogenation to formate | 158 |

Numbered Item List – Figures

| | |
|---|----|
| Figure 1. Sabatier principle - effect of the surface-intermediate bond strength on the rate of the reaction. ²³ | 3 |
| Figure 2. Diagram of possible reaction intermediates in CO ₂ hydrogenation to methanol on Cu- TMNP catalysts; the formation of water, carbonates and carbon-carbon bonds is not considered; the desorption of formaldehyde and formic acid is not considered as not observed in the CZA or Pd-based catalysts ^{21,91} ; * denotes a stabilised surface-bound intermediate. | 8 |
| Figure 3. Origin of basis set superposition error and its quantification; A and B are atom centres in a 2-atom system, blue and green regions depict basis orbitals for description of electrons around A and B, respectively. I.) The regions A and B are far apart and non-interacting. II.) The regions A and B are overlapping, and system is artificially stabilised where orbitals of B are accessible to electrons of A and vice versa. III.) Atom B is a “ghost” and has no electrons or a nucleus, just a basis set centred around B origin. Basis orbitals of B are available to A in the overlapping region, artificially stabilising the system. | 20 |
| Figure 4. A visual representation of an example potential energy surface; labelled are the transition state at the saddle point, and the local minimum at the potential energy well; units on all axes are arbitrary. | 21 |
| Figure 5. Formate pathway of direct CO ₂ hydrogenation to methanol on metallic surfaces, as proposed by Grabow <i>et al.</i> (via HCOOH*, blue) and Huš <i>et al.</i> (via H ₂ COO*, orange). * indicates a surface-bound species and δ- indicates that CO ₂ is partially charged (<i>i.e.</i> , activated). ^{91,162} ... | 30 |
| Figure 6. Convergence of energy with respect to k-grid and basis set choice, sampled on a Pd primitive cell with a unit cell vector of 2.69 Å, where <i>n</i> corresponds to the k-grid sampling. The energy difference (Δ <i>E</i>) is presented relative to that calculated with a “tight” basis set and a (9 x 9 x 9) k-grid..... | 33 |

Figure 7. E_{cleave} calculated for Pd FCC (111), (110) and (100) surfaces as a function of increasing model thickness, n . A key is provided to identify the symbols and linear fits; the average cleave energy (solid horizontal line) was taken from $n \geq 5$, to avoid bias from inaccurate thin slabs (dashed lines). The oscillations between the odd and even n can be attributed to the quantum size effect.¹⁷¹36

Figure 8. Energy profile of the initial CO₂ hydrogenation step towards HCOO on the Pd (111) surface, as calculated using the MLNEB approach. Top: Results with $f_{\text{max}} = 0.05 \text{ eV \AA}^{-1}$, fit uncertainty = 0.03 eV; Bottom: $f_{\text{max}} = 0.01 \text{ eV \AA}^{-1}$ and fit uncertainty = 0.03 eV. Activation energy forward along the reaction coordinate and the activation energy in the reverse direction are denoted as E_f and E_r , respectively, and ΔE is the overall reaction energy.39

Figure 9. (i) Adsorption energy (E_{ads}) of a hydrogen atom on Pd (111) surface, calculated as a function of x - and y -coordinate; the H atom remained constrained in the xy -plane during each geometry optimisation. A key is provided for the adsorption energies, in units of eV. (ii) Top-down view of the FCC Pd (111) surface with a 3 x 3 x 5 atoms simulation cell. Blue spheres represent Pd atoms and yellow circles represent unique adsorption sites: a) hollow-FCC, b) hollow-HCP, c) bridge, d) atop. Black lines represent the x - and y -direction cell boundaries.42

Figure 10. (i) Adsorption energy (E_{ads}) of hydrogen atom on Pd (100) surface calculated as a function of x - and y -coordinate; the H atom remained constrained in the xy -plane during each geometry optimisation. A key is provided for the adsorption energies, in units of eV. (ii) Top-down view of the FCC Pd (100) surface with a 3 x 3 x 5 atoms simulation cell. Blue spheres represent Pd atoms and yellow circles represent unique adsorption sites: a) atop, b) bridge c) hollow. Black lines represent the x - and y -direction cell boundaries.....42

Figure 11. (i) Adsorption energy (E_{ads}) of hydrogen atom on Pd (110) surface calculated as a function of x - and y -coordinate; the H atom remained constrained in the xy -plane during each geometry optimisation. A key is provided for the adsorption energies, in units of eV. (ii) Top-down view of the FCC Pd (110) surface with a 3 x 3 x 5 atoms simulation cell. Blue spheres represent Pd atoms and yellow circles represent unique adsorption sites: a) short bridge, b) "FCC" c) atop, d) long bridge, e) hollow. Black lines represent the x - and y -direction cell boundaries.43

Figure 12. Side- and top-view of CO₂ chemisorbed on the FCC Pd (100) surface, illustrating notations used for Mulliken analysis. Blue, red, and grey spheres represent Pd, O, and C atoms, respectively. Black crosses mark constrained bulk Pd layers.....46

Figure 13. A red-white-blue (negative-neutral-positive charges) color-coded visualisation of the net Mulliken charge on atoms for (a) CO₂ physisorbed and (b) CO₂^{δ-} chemisorbed on the Pd (111) surface.47

Figure 14. H_{ads} of the intermediates in the direct CO₂ hydrogenation to methanol, as studied on the low-index Pd surfaces, presented in order of increasing E_{surf} : (111), (100) and (110),⁹¹ in blue, orange and grey, respectively. Error bars of ± 0.05 eV are provided to account for the spin-paired approximation applied to the adsorbed species, as described in Section 3.2.3. .48

Figure 15. E_{surf} of the Pd (111), (100) and (110) surfaces plotted against H_{ads} of intermediates in the mechanism of CO₂ hydrogenation to methanol. The red dashed line is the linear fit of the data points, and R^2 is the linear coefficient of determination showing the quality of the fit.50

Figure 16. The ZPE-corrected activation energies (H_{act} , eV) of reaction steps in the pathway for CO₂ hydrogenation to methanol, presented for Pd surfaces in order of increasing E_{surf} , *i.e.*, (111), (100), and (110), given in blue, orange, and grey, respectively. In each case, the label refers to the initial reaction species, and the activation energies are also tabulated.....51

Figure 17. The ZPE-corrected energy profile of CO₂ hydrogenation to methanol, via the formate pathway, on Pd (111), (100), and (110) surfaces, plotted in blue, orange, and grey, respectively, relative to the energy of pristine surface and gas phase reactants.⁹¹ Energies of intermediate structures and transition state geometries have been stoichiometrically balanced with energies of gas phase reactants; * indicates surface bound species.54

Figure 18. The Gibbs free energy changes between reaction steps in CO₂ hydrogenation reaction via formate on Pd (111) at p of 1 atm and T of 0K, 300K and 500K; reaction steps a-v are explained in Table 7.57

Figure 19. The Gibbs free energy changes between reaction steps in CO₂ hydrogenation reaction via formate on Pd (100) at p of 1 atm and T of 0K, 300K and 500K; reaction steps a-v are explained in Table 7.58

Figure 20. The Gibbs free energy changes between reaction steps in CO₂ hydrogenation reaction via formate on Pd (110) at p of 1 atm and T of 0K, 300K and 500K; reaction steps a-v are explained in Table 7.58

Figure 21. The Gibbs free energy changes between reaction steps in CO₂ hydrogenation reaction via formate on Pd (111), (100) and (110) at *p* of 1 atm and *T* of 500K; reaction steps a-v are explained in Table 7.59

Figure 22. Top view of FCC a) (111) and b) (100) surfaces, with blue, purple and yellow spheres indicating the 1st, 2nd and 3rd atomic layers of the surface, respectively. Black lines are unit cell boundaries as viewed along the z-axis; red spheres mark the positions of the adsorption sites: the (111) surface: A) HCP, B) FCC, C) atop, D) bridge; and Pd (100) surface: E) hollow, F) bridge and G) atop.73

Figure 23. Effect of supercell symmetry on the placement of two H atoms on a Pd (111) *p*(3×3) slab surface in a) FCC sites and b) FCC site followed by a HCP site. The first H atom placed is coloured white with equivalent 1st, 2nd and 3rd neighbour placements shown in green, red and purple, respectively; Pd atoms are coloured blue; black lines represent the unit cell boundaries; atoms in neighbouring cells are included to aid visualisation of equivalent positions.....76

Figure 24. E_{ads} per H₂ for structures enumerated in the $\frac{8}{9}$ ML coverage on Pd (111) surface; the coloured lines represent sets of structures which relaxed to a common structure; blue and white circles correspond to Pd and H atoms of the $\frac{8}{9}$ ML hydrogen covered *p*(3×3) Pd (111) surface; representative examples of structures with common features are also provided for relevant coloured lines.83

Figure 25. Second most favourable configuration of H atoms (white circles) on the Pd (111) surface (blue circles) at $\frac{8}{9}$ ML coverage of hydrogen, with 7 atoms in the FCC site and one atom in the HCP site; the view is in the xy-plane and dotted lines represent the unit cell boundaries.84

Figure 26. The average adsorption energy ($\langle E_{\text{ads}} \rangle$) per H₂ molecule on the Pd (111) surface at 293 K (triangles) and at 523 K (crosses). $\langle E_{\text{ads}} \rangle$ for configurations with a single sub-surface H atom included at 293 K and 523 K is shown by open and green circles, respectively. Dotted lines show the position of 1 ML and 2 ML coverage levels for this *p*(3×3) supercell.....85

Figure 27. The average adsorption enthalpy ($\langle H_{\text{ads}} \rangle$) per H₂ molecule on the Pd (111) surface at 293 K (triangles) and at 523 K (crosses). $\langle H_{\text{ads}} \rangle$ for configurations with a single sub-surface H atom included at 293 K and 523 K is shown by open and green circles, respectively. Dotted lines show the position of 1 ML and 2 ML coverage levels for the *p*(3×3) used.87

Figure 28. The average adsorption enthalpy ($\langle H_{\text{ads}} \rangle$) per H_2 molecule on the Pd (100) surface calculated using equation (3) at 293 K (grey triangles) and at 523 K (yellow circles). The ΔH_{ads} without vibrational energy contributions (*i.e.*, $\Delta E_{\text{ads}} + \Delta \text{ZPE}$) for configurations with a single sub-surface H atom is shown by blue squares, and ΔH_{ads} of the most stable configuration of surface hydrogen atoms at coverages between $\frac{1}{9}$ and $\frac{10}{9}$ are shown using green circles.89

Figure 29. Most favourable configuration of H atoms (white circles) on the Pd (100) surface (blue circles) at $\frac{4}{9}$ and $\frac{5}{9}$ ML (left and right, respectively) coverage of hydrogen; the view is in the xy -plane and dotted lines are representing the unit cell boundaries.90

Figure 30. Enthalpy and free energy of adsorption for $\text{H}_2(\text{g}) \rightarrow 2\text{H}(\text{ads})$ on Pd (111) as a function of number of adsorbates on the $p(3 \times 3)$ supercell, $n_{\text{H}} = 9$ corresponds to 1 ML coverage. At *a*) $T = 293$ K and *b*) $T = 523$ K. In both cases, $\Delta H_{\text{ads}} = \Delta E_{\text{DFT}} + \Delta \text{ZPE}$: open triangles and orange line, $\Delta H_{\text{ads}} = \Delta E_{\text{DFT}} + \Delta \text{ZPE} + U_{\text{vib}}$: closed triangles and blue line, $\Delta G_{\text{ads}} = \Delta E_{\text{DFT}} + \Delta \text{ZPE} + U_{\text{vib}} - T\Delta S_{\text{HO}}$: Open circles and dotted line, $\Delta G_{\text{ads}} = \Delta E_{\text{DFT}} + \Delta \text{ZPE} + U_{\text{vib}} - T(\Delta S_{\text{hindxy}} + \Delta S_{\text{HOz}})$: Closed circles and solid line.91

Figure 31. Adapted from Nowicka *et al.*²³¹: high angle annular dark field scanning transmission electron microscopy (STEM-HAADF) imaging of the C_{Imp} 3% PdZn/ZnO catalyst. (e) A higher magnification STEM-HAADF image of a PdZn particle, showing the tetragonal PdZn phase. (f) A higher magnification HAADF image of a [001] projection of a PdZn, with Pd and Zn atoms highlighted in red and yellow, respectively.95

Figure 32. Top-down view of unique adsorption sites (white circles) on the FCC (110) surface of Pd (blue circles): (A) atop, (B) short-bridge, (C) 'FCC', (D) hollow, (E) long-bridge. The black lines represent boundaries of the model simulation cell.99

Figure 33. Top-down view of unique adsorption sites (white circles) on BCC (110) surface of CuPd alloy (Pd: blue circles; Cu: yellow circles): (A) Pd atop, (B) Cu atop, (C) Pd-Cu bridge, (D) Pd-Pd bridge, (E) Cu-Cu bridge, (F) Cu hollow and (G) Pd hollow. The black lines represent boundaries of the simulation cell.100

Figure 34. E_{ads} of CO_2 , $\text{CO}_2^{\delta-}$ in units of eV, with and without co-adsorbed hydrogen atom in the most favourable adsorption position, across Pd (111), (100), (110), Zn (0001), Cu (111), (100), (110), CuPd (110) and PdZn (101) and (110) surfaces. No metastable structures of $\text{CO}_2^{\delta-}$ were found on Cu (111) and Zn (0001) surfaces.107

Figure 35. CO₂ dissociation reaction energetics across Pd (111), (100), (110), Cu (100), (110), CuPd (110) and PdZn (101) and (110) surfaces; $E_a(\text{CO}_2^{\delta-})$ is the activation barrier for C-O bond dissociation of chemisorbed CO₂^{δ-}; $E_a(\text{CO}_2)$ constitutes of $E_a(\text{CO}_2^{\delta-})$ with included the difference between E_{ads} of CO₂ and CO₂^{δ-}; $E_a(\text{CO} + \text{O})$ is the activation energy towards the formation of CO₂^{δ-} from co-adsorbed CO and O species.....111

Figure 36. Intermediates considered in CO₂ hydrogenation to formate shown on the Cu (110) surface: A) co-adsorbed CO₂* and H*, B) co-adsorbed CO₂^{δ-*} and H*, C) HCOO^{m*}, D) HCOO^{b*}; brown, red, grey and white spheres represent Cu, O, C and H atoms, respectively.113

Figure 37. E_{ads} of surface-bound (*) monodentate (m) and bidentate (b) formate (HCOO) intermediates on FCC Pd (111), (100), (110), Cu (111), (100), (110), HCP Zn (0001), BCC CuPd (110) and PdZn (101) and (110) surfaces. HCOO^{b*} is in the most stable conformation with both oxygen atoms bound to metal atoms, while the HCOO^{m*} is bound to the surface via a single oxygen atom and a short hydrogen-metal bond allowing a significant electronic interaction. No metastable HCOO^{m*} structure has been identified on Cu (111) and Zn (0001) surfaces.115

Figure 38. Activation energy of CO₂ and CO₂^{δ-} hydrogenation to HCOO and the reverse reaction on FCC Pd (111), (100), (110), FCC Cu (111), (100), (110), HCP Zn (0001), BCT PdZn (101), (110) and BCC CuPd (110) surfaces. Values missing for $E_a(\text{CO}_2^{\delta-} + \text{H})$ are due to lack of a metastable CO₂^{δ-} species on the Cu (111) and Zn (0001) surfaces.....120

Figure 39. Reaction energy profiles of initial hydrogenation of CO₂ to HCOO on FCC Cu, Pd, HCP Zn, BCT PdZn and BCC CuPd surfaces in units of eV. The preferred adsorbed CO₂ geometry for the transition state calculation was the bent chemisorbed CO₂^{σ-} (solid line). Metastable CO₂^{σ-} geometry was not found on FCC Cu (111) and HCP Zn (0001), thus the physisorbed CO₂ was used instead (dotted lines); * denotes a surface and surface-bound intermediates....122

Figure 40. Pearson correlation of $E_a(\text{CO}_2 + \text{H})$ and E_{ads} of HCOO^m across Pd (111), (100), (110), Cu (100), (110), CuPd (110), PdZn (101) and (110) surfaces. A positive Pearson correlation of 0.94 was found, the linear coefficient of determination, R², is 0.88.124

Figure 41. Pearson correlation of $E_a(\text{CO}_2^{\delta-} + \text{H})$ and HCOO^m O-C-O angle across Pd (111), (100), (110), Cu (100), (110), CuPd (110), PdZn (101) and (110) surfaces. A positive Pearson correlation of 0.94 was found, the linear coefficient of determination, R², is 0.92.125

Figure 42. Pearson correlation of E_f/E_r , *i.e.*, the ratio of the activation energy of the forward and reverse reaction of CO₂ hydrogenation to formate ($E_a(\text{CO}_2 + \text{H})$ divided by $E_a(\text{HCOOb})$),

and HCOO^m O-C-O bond angle across Pd (111), (100), (110), Cu (100), (110), CuPd (110), PdZn (101) and (110) surfaces. A positive Pearson correlation of 0.95 was found, the linear coefficient of determination, R², is 0.90.126

Figure 43. Pearson correlation of $E_a(\text{CO}_2^{\delta^-} + \text{H})$ and hydrogen-carbon bond distance in HCOO^{m*}, dHCOO(H-C), across Pd (111), (100), (110), Cu (100), (110), CuPd (110), PdZn (101) and (110) surfaces. A positive Pearson correlation of 0.94 was found, the linear coefficient of determination, R², is 0.88.....127

Figure 44. The energy profile of CO₂ hydrogenation to methanol, via the formate pathway, on Pd (111), (100), and (110) surfaces with and without ZPE-correction included, plotted in blue, orange, and grey, respectively, relative to the energy of pristine surface and gas phase reactants.⁹¹ Energies of intermediate structures and transition state geometries have been stoichiometrically balanced with energies of gas phase reactants; * indicates surface bound species.....148

Numbered Item List – Tables

Table 1. Comparison of activation energy (E_{act}) when using spin-paired or spin-collinear approximations, with impact considered across all intermediate steps in the CO₂ hydrogenation reaction over the FCC Pd (111), (110) and (100) surfaces. Species given in the Table are those at the start of the reaction step. All energies are in eV.....32

Table 2. Screening of exchange correlation functionals with respect to accuracy for a_0 (Å), B_0 (GPa) and E_{coh} (eV), as acquired using a Birch-Murnaghan Equation of State, and the difference in each property with respect to experiment (Δ , given in %). PBE+MBD includes the many-body dispersion (MBD) correction of Tkatchenko *et al.*^{168,169}34

Table 3. Pd FCC (111), (100) and (110) surface energies calculated using the outlined settings. Literature and experiment are provided for comparison.37

Table 4. Geometric and energetic observations for CO₂ and CO₂^{δ-} physisorbed and chemisorbed species on low-index Pd surfaces, respectively; CO₂^{TS} is the transition state geometry between these stable local minima. H_{ads} is the ZPE-corrected species adsorption

energy, given in eV; d_{C-Pd_1} is the distance between the carbon and the nearest neighbouring Pd given in Å, and \angle_{O-C-O} is the angle between the oxygen, carbon and oxygen, given in °. ...44

Table 5. Net Mulliken charges, in units of e, on relevant atoms for CO₂ physisorption and chemisorption on the Pd (111), (110) and (100) surfaces; the charges (q) over Pd atoms have been averaged in the first surface layer surface (Pd_{surf}) and sublayer (Pd_{sublayer}), and summated over the whole slab (Pd_{slab}).46

Table 6. Detailed reaction steps towards which the $H_{act}(\text{species})$ abbreviations refer to in Figure 16.52

Table 7. Calculated reaction steps in CO₂ hydrogenation reaction via formate on Pd.56

Table 8. Average adsorption energy with and without Hartree potential correction at different H coverages and 293 K. The addition of the Hartree potential force correction (column 3) provides a reliable way to save computational resources save computational resources without affecting the rationalization of the results. All the energies are reported in kJ mol⁻¹.68

Table 9. Pd FCC (111) and (100) hydrogen adsorption energies calculated using the outlined settings; literature and experiment are provided for comparison, with energies normalised to H_{ads} in units of kJ mol⁻¹, and the adsorption site description follows the naming convention summarised in Figure 22. Abbreviations of experimental methods are: TPD – temperature programmed desorption, LEED – low energy electron diffraction, MB – molecular beam. ... 73

Table 10. Enumeration of possible adsorption patterns on a $p(3 \times 3)$ Pd (111) surface with and without symmetry consideration, and the number of unique metastable configurations found after relaxation for each calculated hydrogen coverage..... 77

Table 11. Enumeration of possible configurations of H atoms on a $p(3 \times 3)$ Pd (100) supercell surface with and without symmetry considerations at coverages between $\frac{1}{9}$ and $\frac{7}{9}$ ML..... 79

Table 12. Comparison of $\langle E_{ads} \rangle$ and $\langle H_{ads} \rangle$ at temperature of 293 K and 523 K for 1 ML of hydrogen, with 8 atoms on the surface and 9th atom in a subsurface site: full enumeration and results for the lowest structure from the $\frac{8}{9}$ ML dataset used as starting point.86

Table 13. $E_{ads}(H)$ on FCC Cu and Pd (110) surfaces, relative to the energy of $\frac{1}{2}H_2(g)$. Unstable adsorption sites are marked as hyphens only.99

Table 14. $E_{ads}(H)$ on BCC CuPd (110) surface, relative to the energy of $\frac{1}{2}H_2(g)$. Unstable adsorption sites are marked as hyphens only.101

| | |
|---|-----|
| Table 15. E_{ads} of a hydrogen atom on PdZn (101) and (110) surfaces; blue, grey and white spheres represent Pd, Zn and H atoms, respectively; the black lines represent the simulation cell boundaries as viewed in the xy-plane. | 102 |
| Table 16. E_{ads} of CO on FCC Pd (111), (100) and (110), and BCT PdZn (101) and (110) across the unique metastable adsorption sites; energy units are provided in eV. | 104 |
| Table 17. E_{ads} of CO ₂ and CO ₂ ^{δ-} with and without co-adsorbed H atom on FCC Cu and Pd (110) surfaces; the energies are relative to the gas-phase ½H ₂ and CO ₂ . Unstable adsorption sites are marked as hyphens only. | 107 |
| Table 18. E_{ads} (HCOO) on FCC Cu and Pd (110) surfaces, relative to gas-phase ½H ₂ and CO ₂ ; ^{m*} represents monodentate geometry and ^{b*} corresponds to the bidentate geometry. Unstable adsorption sites are marked as hyphens only. | 114 |
| Table 19. E_{ads} of HCOO on BCC CuPd (110) surface, relative to gas-phase ½H ₂ and CO ₂ ; ^{m*} represents monodentate geometry and ^{b*} corresponds to the bidentate geometry. | 114 |
| Table 20. Net change in Mulliken charges, in units of e, on relevant surface atoms of CO ₂ , CO ₂ ^{δ-} , HCOO ^b and HCOO ^m adsorbed on Cu (110), Pd (110) and CuPd (110) surfaces relative to the atomic charges on the pristine surface; the charge differences (Δq) have been averaged over the first surface layer (Δq_{surf}), summated over the whole slab (Δq_{slab}); the maximum change in the atomic surface atomic layer charge ($\Delta q_{\text{surf_max}}$) and the OCO angle ($\angle\text{OCO}$) in degrees are also shown. | 117 |
| Table 21. Comparison of the effect of starting geometries in CO ₂ hydrogenation to formate on the resulting transition state (TS) energy and geometry, and the length of the minimum energy path (MEP); - denotes lack of data for a calculation which failed to converge. | 119 |
| Table 22. The adsorption energy, E_{ads} , and the adsorption enthalpy, H_{ads} , across all intermediates in the CO ₂ hydrogenation reaction over the FCC Pd (111), (110) and (100) surfaces. All numerical values are in eV. | 146 |
| Table 23. The reaction energy (eV) of intermediate steps in CO ₂ hydrogenation on the Pd (111), (110), and (100) surfaces. Each calculation is balanced stoichiometrically with energies of gas-phase molecules. * represents the catalyst surface. | 146 |
| Table 24. Graphical representation of initial, transition state and final geometries in E_{act} calculations on Pd (111) surface. The blue, red, grey and white spheres represent Pd, O, C and H atoms; the black lines indicate the edges of the simulation cell. The full size of the simulation | |

| | |
|---|-----|
| cell, including all unit cell borders, is depicted for the initial reaction step to illustrate the vacuum region size. | 149 |
| Table 25. Graphical representation of initial, transition state and final geometries in E_{act} calculations on Pd (100) surface. The blue, red, grey and white spheres represent Pd, O, C and H atoms; the black lines indicate the edges of the simulation cell. The full size of the simulation cell, including all unit cell borders, is depicted for the initial reaction step to illustrate the vacuum region size. | 152 |
| Table 26. Graphical representation of initial, transition state and final geometries in E_{act} calculations on Pd (110) surface. The blue, red, grey and white spheres represent Pd, O, C and H atoms; the black lines indicate the edges of the simulation cell. The full size of the simulation cell, including all unit cell borders, is depicted for the initial reaction step to illustrate the vacuum region size. | 155 |
| Table 27. Numerical data for CO ₂ dissociation and CO ₂ hydrogenation to formate on FCC Pd (111), (100), (110), FCC Cu (111), (100), (110), HCP Zn (0001), CuPd (110) and PdZn (101) and (110) surfaces; physisorbed and chemisorbed carbon dioxide species are denoted as CO ₂ and CO ₂ ^{δ-} , respectively; monodentate and bidentate forms of formate intermediate are represented as HCOO ^m and HCOO ^b , respectively; + denotes co-adsorption of species; E_{ads} is measured with respect to gas phase substrates (CO ₂ and/or ½H ₂) and pristine surfaces in units of eV; atomic bond lengths, d(atom–atom) are measured in Å, where M represents the metal atom closest to the second atom; ∠species(O–C–O) is the oxygen-carbon-oxygen bond angle in units of °; E_{ads} of H is reported from structures with co-adsorbed physisorbed CO ₂ and chemisorbed H atom; E_a (species) is the activation energy required for the formation of a transition state in reactions described in Chapter 5.3.4 and 5.3.8, starting from the species in brackets.; E_i/E_r , is the ratio of the activation energy of the forward and reverse reaction of CO ₂ hydrogenation to formate (E_a (CO ₂ + H) divided by E_a (HCOO ^b)). | 158 |

III. Acknowledgements

Completion of this thesis has been one of the most demanding projects in my life. It would not be an exaggeration to say that I would not be here writing these words if not for some brilliant and truly inspiring people along the way. But first a quick word on the institutions which contributed to the work herein.

I would like to acknowledge Cardiff University for the academic support and a fully funded PhD scholarship. The research within this thesis has been funded by the EPSRC Centre-to-Centre Project (Grant reference: EP/S030468/1). I want to acknowledge computational resources and support from: the Supercomputing Wales project, which is part-funded by the European Regional Development Fund (ERDF) via the Welsh Government; the UK National Supercomputing Services ARCHER and ARCHER2, accessed via membership of the Materials Chemistry Consortium, which is funded by Engineering and Physical Sciences Research Council (EP/L000202/1, EP/R029431/1, EP/T022213/1), the Isambard UK National Tier-2 HPC Service operated by GW4 and the UK Met Office, and funded by EPSRC (EP/P020224/1), the local supercomputing facilities of the Advanced Research Computing at Cardiff; and the Royal Society of Chemistry for the Grants for Carers and Researcher Development and Travel Grant.

If you made it this far reading, know this: the list of people I am grateful to is enormous, but I will limit it here to those who hold a special place in my heart. First and foremost, I would like to thank my extraordinary wife, Gabrysia, my best friend and partner in life, who has always been my wonderwall even in my darkest moments. Secondly, I want to thank my wonderful daughters, Maya and Olivia, for bringing so much joy into my life and making the journey so rewarding, even if a little more challenging. I deeply love the three of you and dedicate this work to you, as I embarked on the scientific journey hoping to make the world a better place to live in.

I want to thank my parents, Małgosia and Robert, for the hard work they have put into my upbringing, for their love and encouragement in seeking to broaden my horizons, and for their support in my life decisions, even if they meant we had to part ways. I also want to thank my brother, Maciej, who instilled in me the curiosity that with time turned into the love for science. Great thanks to all of my family members in Poland, who have always been

supportive and made me feel at home whenever I visit. Of course, I also want to thank my parents-in-law, Agnieszka and Arek, and my sister-in-law, Zuzanna, for treating me like family when all my relatives were across the sea. It really means the world to me.

Massive thanks to my closest friends, Bartosz, Daniel, Michał, Piotr, and Stiliyan, thank you for being there for me, for making me laugh, and for listening when needed, even when we mostly meet online these days! With you, I can always be my geeky self, and even after months have passed, we still chat like we've seen each other the day before. Special thanks to my colleague, Lara for being a great friend to me, I truly enjoyed the three years we worked together. Thank you for the hours spent chatting, be it about science or parenthood.

I would also like to acknowledge my teachers, especially the amazing Mrs Sznajder, who genuinely cared about my growth and prepared me for studying abroad. I want to thank Dr Rob Armstrong for being a great mentor and sparking in me the idea of pursuing further academic achievements.

Finally, I want to thank my supervisors, Richard and Andy, who are not only great leaders and mentors but genuinely wonderful people who encouraged me to seize opportunities and were always understanding when life was difficult. They never hesitated for a moment in reassuring me that family is the number one priority, and I knew I could always count on them. I am truly honoured that I could learn from you, and without a doubt, working with you for the past few years has been an absolute pleasure, and I know I have become a better person just by being around you.

To everyone mentioned and not mentioned, from the bottom of my heart, thank you.

“It is not our part to master all the tides of the world, but to do what is in us for the succour of those years wherein we are set, uprooting the evil in the fields that we know, so that those who live after may have clean earth to till. What weather they shall have is not ours to rule.”

— J.R.R. Tolkien, *The Return of the King*

Chapter 1. Hydrogenation of carbon dioxide to methanol

1.1. Green chemistry in the transportation industry

The transportation industry heavily relies on liquid fossil-derived fuel and it is estimated that around 60% of global oil demand is due to the transport sector.¹ Green chemistry plays a crucial role in advancing the development of more efficient and sustainable fuels, thus contributing to the mitigation of environmental consequences linked to transportation. Anastas *et al.* introduced the concept of green chemistry, focusing on minimising the environmental impact during the design of chemical processes.²⁻⁴ The green chemistry principles proposed by Anastas *et al.* encompass various aspects, including the utilisation of renewable materials, the pursuit of energy efficiency, waste prevention and less hazardous synthesis methodologies among others. Embracing these principles enables chemists to strive toward sustainable practices and environmentally friendly solutions within the chemical industry.

The concept of a circular fuel economy, stemming from ongoing discussions on sustainability and resource management, revolves around utilising waste from one process as a fuel source for another to maximise resource utilisation. A significant application of the circular fuel economy pertains to reducing the carbon intensity of the transportation sector, which heavily relies on fossil fuels.^{4,5} The route towards achieving a circular economy based on sustainable liquid fuels includes advancements in materials science, catalysis, and process optimization, all aimed at minimising the environmental impact of not only transportation but also other industrial sectors. Catalysis in particular plays here an enormous role as an enabler of technologies by pushing “green” and sustainable chemistry processes over the profitability threshold due to cost reductions, which makes the adoption of such technologies attractive to the government and private companies alike.

1.2. Heterogeneous Catalysis

Catalysis is vital to modern society, with about 90 % of industrially produced chemicals estimated as dependent on the use of catalysts in their manufacturing process.⁵ Catalysts are substances enhancing the rate of a reaction by offering an alternative pathway for product formation and decrease the activation energy required for the formation of chemical intermediates.⁶ Catalysts enable the synthesis of compounds that may not be economically feasible using conventional methods, such as direct thermal synthesis from gas substrates, due to energy consumption or insufficient conversion and selectivity for industrial-scale production. Inorganic catalysts can be categorised into two primary groups: homogeneous, *i.e.*, in the same phase as the substrates and heterogeneous, which remain in a phase distinctive from that of the reactants.

Of particular importance are heterogeneous hydrogenation catalysts, due to their useful applications in the food, pharmaceutical and the petrochemical industries.^{7–9} Green routes to synthesis of value added products are in demand to support a transition to Net Zero¹⁰, with promising routes including hydrogenation of chemical waste or renewable feedstocks using metal nanoparticle catalysts, *e.g.*, glycerol waste from biodiesel production or carbon dioxide (CO₂) as feedstocks for liquid fuel synthesis.^{7,11} The efficient utilisation of CO₂, a major greenhouse gas that contributes to climate change, to produce valuable substances is a significant objective within the realm of green chemistry.⁴ The use of stoichiometric reagents in CO₂ hydrogenation presents several drawbacks when compared to catalytic processes, including inherent safety hazards and dramatically low conversion and selectivity, well below the profitability threshold.¹²

1.3. Transition metal nanoparticle catalysts

Transition metal nanoparticle-based (TMNP) catalysts, where the highly active transition metal material is finely dispersed onto a supporting material such as metal oxides, zeolites, and modified carbon, are a particularly important class of heterogeneous catalysts.^{11,13–22} By

maximising the surface area of the active catalyst, supported transition metal nanoparticle-based catalysts can be used very efficiently and in very small non-stoichiometric ratios. The catalysts can be designed and tailored to the specific needs of a particular reaction process; for example, a hydrogenation catalyst must be able to activate the hydrogen molecule and efficiently dissociate it on its surface for subsequent reactivity involving the transfer of adsorbed hydrogen onto reaction intermediates. According to the Sabatier principle (Figure 1)²³, a balance must be struck in target properties of a catalyst suitable for hydrogenation processes: if a catalyst binds the hydrogen atoms too strongly, then hydrogen will not actively partake in the reaction, while weakly bound hydrogen atoms can recombine to form diatomic hydrogen and leave the surface in preference over any other desired reactivity.

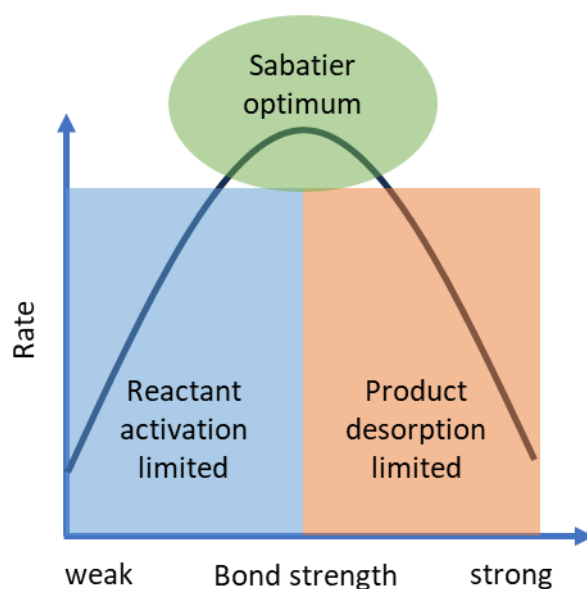


Figure 1. Sabatier principle - effect of the surface-intermediate bond strength on the rate of the reaction.²³

1.4. Cu, Pd and ZnO in TMNP catalysts

Pd and Cu metals are widely known to be good hydrogenation catalysts as they are capable of dissociative adsorption of hydrogen molecules even under mild reaction conditions, thus providing active surface-bound hydrogen atoms for hydrogenation reactions.^{14,15,19,21,24-34} Pd-based catalysts are used both for large scale production and for the synthesis of fine chemicals

due to their strict selectivity in hydrogenation, oxidative dehydrogenation, coupling, and cycloaddition reactions.^{30,35} Pd catalysts are capable of activating C=O double bonds, which is why they were explored in the 1980s in the context of hydrogenation of syngas, *i.e.*, a mixture of CO, CO₂ and H₂.^{13,36–38} The products observed in CO₂ hydrogenation on supported Pd catalysts are exclusively C₁ products, *i.e.*, CO, CH₄ and CH₃OH.^{39,40} Pd nanoparticles exhibit a face-centred cubic structure and are mostly covered with the (111) Miller index surface, showing no evidence of chemical activation of CO₂.³⁷ The chemisorption of CO₂, *i.e.*, binding to the surface involving a chemical bond rather than long range atomic forces as in physisorption, was only observed spectroscopically on the less stable and lower coverage (100) and (110) surfaces of Pd and was promoted by inclusion of either metal dopants or presence of water.^{38,41} Nevertheless, supported Pd catalysts can form methanol from CO₂, but selectivity and conversion are inferior to those of the industrial standard catalyst for hydrogenation of syngas, Cu/ZnO/Al₂O₃ (CZA), which has been commercialised in the 1950s.^{11,13,21,27,42,43} One advantage of CZA over Pd catalysts for the hydrogenation of syngas to methanol is the lack of methane in the product stream, allowing multiple recycling steps that overall lead to very high conversion rates and high selectivity to methanol.²¹

Catalysis is an intricate phenomenon and there are many factors that contribute to the activity of a catalytic material. For supported transition metal nanoparticle-based catalysts, reactivity can depend on a range of properties including nanoparticle size, surface structure, the bulk structure and electronic properties of the materials. The reaction can have multiple mechanistic steps, some of which could be happening on the supporting material itself. There can be a synergistic effect at the so-called metal-support interface; for example, in the context of CO₂ hydrogenation, ZnO has gained a lot of attention as a supporting material and is a constituent of the commercial (CZA) catalyst for hydrogenation of syngas.^{19,20,42–48,48–50} However, the ZnO support alone remains largely inactive at mild reaction conditions required for maximising efficiency.^{15,19,50,51} In fact, Bowker *et al.* found no synergy between the zinc oxide and copper components of the catalyst in terms of the energetics of the rate-determining step.²¹ Formation of ZnO islands on Cu nanoparticles was observed on Cu/ZnO/ZrO₂ catalysts, similar to CZA, and ZnO was attributed the role of a hydrogen reservoir for the hydrogenation process.^{52,53}

Solid catalytic materials are dynamic at a nanoscale, as the reaction conditions can induce morphological changes in the structure of the material impacting the reactivity, such as formation of oxide layers on the Cu and Pd metal nanoparticles on exposure to air or due to a contact with water produced *in-situ*, thus the freshly prepared catalyst and the actual active material might not be identical.^{45,51,54} A so-called induction period after the initialization of the reaction might be required to reach optimum catalytic activity, which in a reducing environment of hydrogenation reactions on Cu or Pd might be, *e.g.*, the removal of the oxide layer on metal nanoparticles, allowing dissociation of hydrogen on exposed active metal surfaces.^{45,51} *In situ* spectroscopic techniques are constantly evolving, but capturing the nature of the catalytic species and their behaviour can be difficult at a nanoscale level. For instance, *in-situ* characterisation techniques often require mild reaction conditions strongly deviating from industrial operating conditions.⁴² Furthermore, the specific locations where reactants come into contact with the surface of a catalyst, and where the desired reactivity is promoted, *i.e.*, active sites, are challenging to accurately characterise. Computational modelling techniques, such as density functional theory (DFT), can aid experiments by providing fundamental insight into the electronic properties of materials and the nature of the active sites and their role in promoting catalytic activity, thereby enabling rational design of catalysts.^{47,55–64}

1.5. TMNP alloys and intermetallic compounds

When more than one transition metal is present in a solid catalyst precursor during catalyst treatments such as calcination or reduction (thermal treatment under oxidative or reductive conditions), the metals can mix, forming either irregular alloys or highly ordered (or from an entropic point of view, perfectly disordered) structures with repeated patterns and intimately mixed metals at a nanoscale level.^{15,20,51,65–71} Such nanoalloy materials then show sets of properties distinct from those of their monometallic counterparts but partially share some of their characteristics.^{15,51,65,67,68,72} For example, Pd, a good hydrogenation catalyst, when alloyed with other transition metals, enhances the interaction of the secondary metal with hydrogen by inducing changes in electronic structure around the Fermi level via charge transfer between the metallic species, thereby enabling new desired reactivity.^{15,22,51,65,68,73,74}

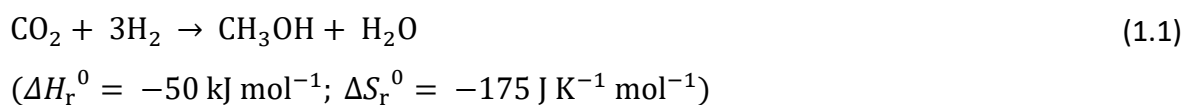
Catalysts containing two active metals are referred to as bimetallic catalysts, while a mixture of three transition metals would be referred to as a ternary catalyst, or a trimetallic nanoparticle catalyst if there is evidence of intimately mixed intermetallic structure.^{22,65} Similarly to the MSI concept mentioned earlier, the surface of a bimetallic nanoparticle catalyst may be capable of performing tandem reactivity where active sites can consist of two distinct transition metal atoms, with each playing a different role in the localised surface reactivity, offering strategies for tuning catalytic activity with modified alloy surface structures.^{66,72,75,76}

The field of nanoalloys is very complex and, while bimetallic systems are slowly becoming better understood, there are simply too many possible material structures to investigate experimentally.^{77,78} A nanoparticle is affected by the reaction environment; its structure will be affected both on the surface and inside the bulk of the material, and the process in which the nanoparticles were created also dictates the final structure of the particle.^{22,65,77} Given the large number of variables and potential candidates for the active metal components, the search space expands enormously due to a combinatorial explosion of possibilities. Such materials cannot be efficiently sampled by trial and error, which is where recent advances in computational methods for modelling nanoalloy materials are emerging as useful tools for design of such materials.^{22,78–80} Furthermore, there is an increasingly large gap between the availability of the experimental reference data for characterisation of the nanoalloy catalysts, and benchmarks of their activity.²² Due to the paradigm shift in computational chemistry, where simulations can now effectively guide experiments, there is a growing need for new data-driven approaches.^{22,78,80–82}

1.6. CO₂ hydrogenation to methanol

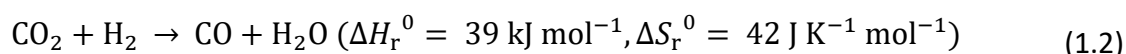
The process of direct CO₂ hydrogenation to methanol is actively explored as a sustainable route towards circular fuel economy.^{4,11,83–87} Methanol is currently predominantly produced from fossil-derived syngas^{11,42,43}, but suitable catalysts have the potential to shift the industry towards the more sustainable CO₂ feedstock. Methanol synthesis from CO₂ (Equation 1.1) is

has a standard enthalpy change of the reaction (ΔH_r^0) of -50 kJ mol^{-1} , indicating overall exothermicity of the reaction.⁸⁸



The standard entropy change of the reaction (ΔS_r^0) is strongly negative; therefore, due to the changes in system disorder, the reaction is more difficult to perform at high temperatures, hence the need for a catalyst capable of CO_2 activation at low temperatures.⁸⁸ Around 111 million metric tonnes of methanol are estimated to have been produced in year 2022 alone from all technological processes, which shows the industrial importance of this chemical as a fuel, solvent and a substrate, but 90% was derived from fossil-derived feedstock.⁸⁹ To minimise carbon emissions and halt global warming effects, “green” methanol must be produced from anthropogenically generated CO_2 and renewable sources of H_2 . Embracing new sustainable technologies of methanol synthesis and incorporation of “green” methanol as fuel into the transportation sector have the potential to strongly impact the climate.

A suitable catalyst for methanol synthesis from CO_2 must facilitate CO_2 activation, but strictly towards the hydrogenation reaction and not the competing process of reverse water-gas shift (RWGS) reaction in Equation 1.2.^{11,88}



The ΔH_r^0 of the RWGS reaction is positive, *i.e.*, the reaction is endothermic, however due to a positive ΔS_r^0 the RWGS is facilitated at elevated temperatures.⁸⁸ Thus, an efficient catalyst must be capable of activating and dissociating the molecular hydrogen, activating the CO_2 species for hydrogenation and facilitate further reaction via the formate intermediate and not formate decomposition, and ideally such reactivity should be enabled in a localised active site.^{21,27,44,55,90,91}

Using isotopically labelled syngas mixtures, CO_2 was identified as the main source of carbon in methanol produced on Cu catalysts in the work of Bussche *et al.*⁴⁴ Figure 2 shows possible reaction steps during CO_2 hydrogenation to methanol on TMNP catalysts, such as the commercial CZA catalyst, with formate (HCOO^*) pathway shown in blue and orange, and the

carboxyl (COOH*) pathway shown in brown. The black boxes indicate hydrocarbon intermediates leading to undesirable formation of methane. There are many proposed mechanisms of the heterogeneously catalysed CO₂ hydrogenation to methanol reaction.^{21,27,55,66,90–93} The proposed mechanism for direct CO₂ hydrogenation facilitating methanol formation involves a surface formate intermediate (HCOO*⁹⁴).

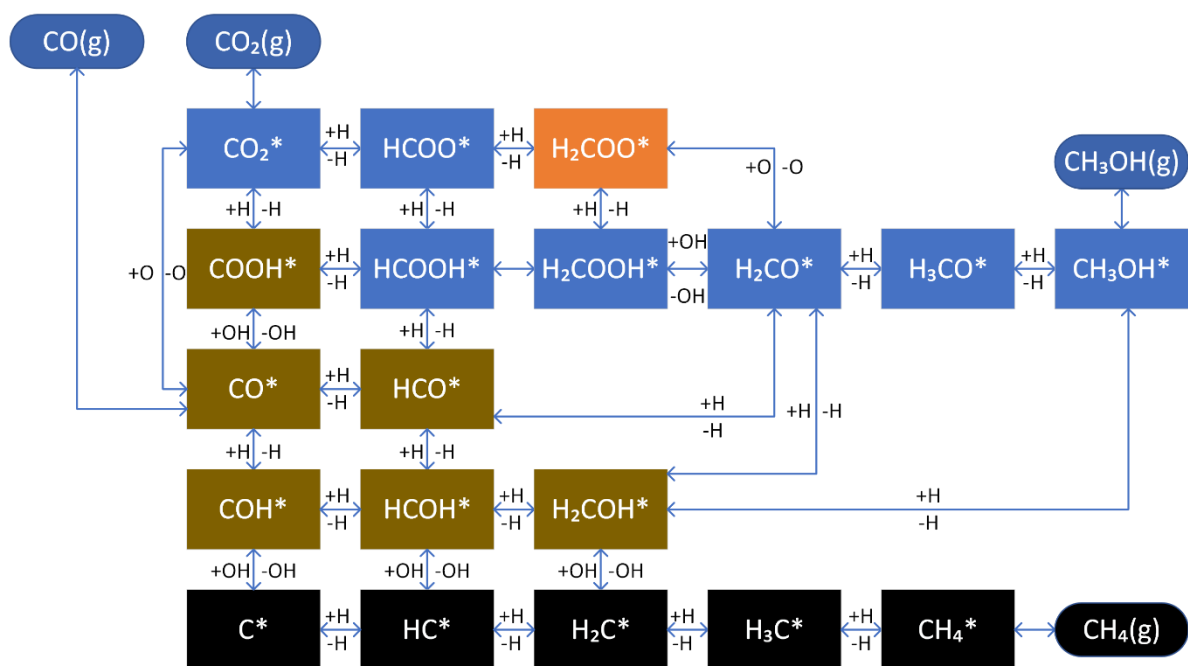


Figure 2. Diagram of possible reaction intermediates in CO₂ hydrogenation to methanol on Cu-based TMNP catalysts; the formation of water, carbonates and carbon-carbon bonds is not considered; the desorption of formaldehyde and formic acid is not considered as not observed in the CZA or Pd-based catalysts^{21,91}; * denotes a stabilised surface-bound intermediate.

Medford *et al.* demonstrated that HCOO* can act as a poison for other reaction pathways on ZnO due to its high thermodynamic stability on the catalyst's surface, hence the need for driving the reaction via HCOO* to prevent the formation of methane.⁹⁴ Alternative routes towards methanol involve intermediates resulting from hydrogenation of CO generated from direct dissociation of CO₂ or the COOH*. High partial pressures of hydrogen used in CO₂ hydrogenation reactions push the equilibria towards hydrogenated C₁ products shown in round boxes in Figure 2; formaldehyde and formic acid are not observed in the products of the CO₂ hydrogenation on Cu catalysts.^{21,91} By changing specific reaction barriers through

electronic interactions with the intermediates, TMNP hydrogenation catalysts can kinetically favour specific reaction pathways in Figure 2.

1.7. What makes a good CO₂ hydrogenation catalyst?

There are important factors to consider for CO₂ hydrogenation to methanol with supported transition metal catalysts. These include the behaviour of reaction intermediates, which do not actually leave the catalytic surface, but do play an important role in the overall activity of the catalyst. In liquid phase methanol synthesis, the HCOO can be solvated and dispersed into the solvent, and reaction efficiency is intricately linked to that intermediate.⁹⁵ However, in gas-phase CO₂ hydrogenation at the gas-solid interface, the electron-withdrawing formate intermediate binds to the electron donating transition metals via oxygen atoms to form particularly strong chemical bonds.^{21,55,90,91} The formate species can saturate the surface active sites of Cu, Pd or ZnO, at which point the activation of the metal-oxygen bond effectively becomes the rate determining step in the reaction, thus inhibiting the reaction.^{11,44,94}

In the formate pathway, once C-O bond scission occurs, molecules of formaldehyde and water are formed.^{90,91} The presence of water in the system reduces the lifetime of the conventional CZA catalyst in industrial scale reactions by causing the agglomeration of the Cu particles in the deactivation of γ -Al₂O₃, which poses a problem in the case of CO₂ hydrogenation to methanol and RWGS, which both inherently result in water generation.^{11,96,97} Moreover, only the first of the two C-O bonds must be activated to prevent subsequent hydrogenation of single-oxygen intermediates, which would otherwise result in the chemically less versatile methane.^{14,19} In the context of methanol production, a highly selective CO₂ hydrogenation catalyst must exhibit many perfect balances in its activity; therefore, the search for optimally designed materials is the subject of extensive research for nanoalloy TMNP catalysts.

As previously mentioned, catalytic properties of TMNP alloy catalysts often correspond to intermediary properties of the metallic components. Therefore, capability of Pd for hydrogen and CO₂ activation at mild conditions with desired selectivity in CO₂ hydrogenation on Cu and ZnO hints at the great catalytic potential of the TMNP CuPd and PdZn alloy catalysts.

Supported PdZn alloy TMNP catalysts have been explored for CO₂ hydrogenation to methanol and were vastly more selective towards the desired product than the monometallic Pd catalysts.^{14,20,51,71,72,97–99} Nanoparticles of PdZn in TMNP catalysts have a highly ordered structure with a 1:1 ratio of Pd and Zn, regardless of the relative amount of the metals during catalyst preparation, signifying a very strong intermetallic effect.²⁰ CuPd alloy TMNP catalysts were found to have varying degree of disorder in the structure, and only the catalysts containing the highly-ordered CuPd nanoparticles were particularly selective to C₁ products.^{101–106} Due to the recent advances, a fundamental understanding of the catalyst active sites and the surface structure over the course of the CO₂ hydrogenation to methanol is required to understand the activity shown by Pd and Pd-based alloy catalysts.

1.8. Research Outline

The global population is increasingly aware of the hazards of climate change due to excessive fossil fuel use. Exploring aspects of circular economy involving transformation of waste CO₂ into methanol fuels is actively pursued to reduce the environmental impact of transportation. Pd-based alloys have emerged as promising catalysts for CO₂ hydrogenation to methanol, exhibiting superior catalytic activity compared to Pd catalysts. However, the underlying reasons for their enhanced performance are not well understood. Theoretical simulations have proven effective in elucidating reactivity phenomena observed in transition metal nanoparticle catalysts.

In this thesis, state-of-the-art density functional theory (DFT) calculations are utilised to investigate the mechanism of CO₂ hydrogenation to methanol on Pd-based alloy surfaces. By accurately capturing the physical properties and reaction energetics, DFT simulations provide valuable insights into the observed catalytic reactivity. The primary focus of Chapter 3 is to deepen the understanding of CO₂ and hydrogen behaviour on Pd (111), (110), and (100) surfaces using DFT computational methods. The objective is to identify the characteristics that inhibit the effectiveness of Pd as a catalyst for methanol synthesis from CO₂. Further, to rationalise the surface morphology of Pd in a reducing environment, Chapter 4 provides a detailed examination of the thermodynamics of hydrogen adsorption on Pd (111) and (100)

surfaces, considering industrially relevant temperature and pressure. In Chapter 5, the performance of Cu, Pd, and Zn metal surfaces is compared with CuPd and PdZn alloy facets by simulating the initial stage of CO₂ hydrogenation to formate and the dissociation of CO₂. The study has a twofold objective: first, to gain a comprehensive understanding of the improvements in catalytic activity resulting from the alloying of Pd with Cu or Zn, and second, to identify reliable descriptors that allow high-throughput computational analysis of alloy surfaces. The findings of the thesis provide a solid foundation for the rational design of efficient catalysts for methanol synthesis from CO₂.

Chapter 2. Computational theory

The aim of this chapter is to introduce the fundamental concepts of the methodology employed consistently across the thesis. The explained quantum chemistry concepts provide a background for subsequent chapters that offer concise overviews of the technical aspects of the computational methods applied in each respective research area.

2.1. Quantum chemistry concepts

2.1.1. Schrödinger Equation and the self-consistent field

In classical mechanics, equations of motion depict the behaviour of a physical system over time, while in quantum mechanics, a fundamental Schrödinger equation can be used to describe the wavefunction (Ψ), *i.e.*, a mathematical function describing the quantum state of a physical system.¹⁰⁷ The Hamiltonian (\hat{H}) is an operator corresponding to the total energy of a particular system, bringing together both potential and the kinetic energy with a specific spectrum of energy eigenvalues, or possible values for a measurement of the total energy of the system. In principle, all electronic interactions of matter and the resulting energy (E) of the system can be described by the Hamiltonian. However, the time-independent Schrödinger in the form presented in Equation 2.1 can only be solved for hydrogenic systems.^{6,108}

$$\hat{H}\Psi = E\Psi \quad (2.1)$$

The challenge lies in the complexity of the many-body problems that involve electron-electron interactions, which themselves arise from quantum entanglement of the electrons to the nuclei, *i.e.*, the particles cannot be deconvoluted and accurately described independently of each other. The quantum entanglement yields wavefunctions containing vast amounts of information and, thus, it is difficult to accurately describe the electron-electron interactions within a stationary external potential.

The Hamiltonian of a many-body system can be represented as a sum of the following components:

$$\hat{H} = \hat{T}_e(r) + \hat{T}_n(R) + \hat{V}_{ne}(R, r) + \hat{V}_e(r) + \hat{V}_n(r) \quad (2.2)$$

where kinetic and potential terms (\hat{T} and \hat{V} , respectively) are functions of the nuclear and electronic coordinates (r and R , respectively) for the electronic and nuclear contributions (e and n subscripts, respectively).

The Born-Oppenheimer approximation circumvents the challenges of many-body perturbation systems by exploiting the ratio of the electronic to the nuclear mass and instantaneous treatment of electron dynamics relative to nuclear motion. In other words, the Born-Oppenheimer approximation allows the nuclei to be treated as stationary bodies with respect to the electrons, thus making the $\hat{T}_n(R)$ negligible and leading to electrons-only Schrödinger equation, thereby facilitating the determination of exact solutions for hydrogen atoms and diatomic molecules.^{6,109,110}

The Hartree method, building on the Born-Oppenheimer approximation, assumes that instead of the abundance of electron-electron interactions, motion of each electron can be treated independently as if taking place in an average field created by all the other electrons, and that each electron occupies an orbital described as a one-electron Hartree wavefunction. However, when dealing with electrons, their indistinguishability poses a challenge, contravening the Pauli exclusion principle that prohibits multiple electrons with identical spins from occupying the same quantum state.¹¹¹ To address this, Fock expanded upon Hartree's initial approach by introducing an asymmetric wavefunction, leading to the development of the Hartree-Fock (HF) wavefunction.^{6,112}

The HF method, apart from kinetic and potential energy contributions, considers an exchange correction that takes into account the collinear spin correlation effects, *i.e.*, intrinsic magnetic moment associated with the particle and its possible correlation with spin of other particles. Once all HF one-electron wavefunctions are numerically solved and the initial approximation of the electronic density and energy has been evaluated, progressively improved sets of calculations based on the previous guesses can be solved, guided by the minimisation of energy hinting the ground state solution. Once the new solutions result only in marginal improvements, then they are considered 'self-consistent' and are accepted as the solutions to the problem.⁶

A significant fault of the Hartree-Fock method is the neglect of electron correlation effects between the electron with antiparallel spin, resulting in underestimation of molecular bonding interactions.¹¹³ HF theory serves as a viable method for solving the time-independent Schrödinger equation in systems containing multiple electrons; however, despite its significance as a cornerstone in modern computational approaches, the computational demands and time required to investigate complex materials render HF theory approach intractable.

To model heavy elements, such as transition metals, additional approximations are necessary, as the core electrons require a special treatment due to relativistic effects. In heavy elements, the speed of core electrons approaches a significant portion of the speed of light due to the proximity to the larger nucleus, causing an increase of the effective electron mass, which causes changes in the energy levels in the atom. Moreover, a secondary spin-orbit coupling relativistic effect occurs during the motion of core electrons around the nucleus, which further affects the electronic structure of the heavy element. A common approach to inclusion of relativistic effects into quantum chemical calculations is the zero-order regular approximation (ZORA), which corrects for the increases in effective mass and increases the calculation accuracy without introducing significant computational overhead.¹¹⁴

There are several methods for improving upon the original Hartree-Fock (HF) theory, also known as post-HF methods. These include Configuration Interaction methods, involving a linear combination of Slater determinants; Coupled Cluster, based on a truncated exponential series expansion of the wavefunction; Many-Body Perturbation Theory, an expansion of the wavefunction in terms of the electron-electron interaction; and Random Phase Approximation (RPA), which considers dynamic electron correlation¹¹⁵. However, it is worth noting that these methods are not employed in this thesis and Density Functional Theory (DFT) is the chosen approach instead.

2.1.2. Density functional theory

Hohenberg and Kohn established the theoretical foundation for the use of density functional theory (DFT) in *ab initio* studies of the electronic structure of many-electron systems.¹¹⁶ In

their work, Hohenberg and Kohn proved that the external potential acting on the electron density is uniquely defined by the electron density; then postulated that there must exist a universal energy functional that is only dependent on the electron density, and they provided proof of the ground state electron density yielding the minimum energy.¹¹⁶ In an extension of the work, the Kohn-Sham theorem further addresses the issue of handling computationally challenging many-electron problems by considering noninteracting electrons that move within a self-consistent field, thus allowing a precise calculation of the kinetic energy.^{117,118} Solutions of exact self-consistent one-electron Schrödinger equations for Kohn-Sham orbitals, also known as Kohn-Sham eigenstates, with occupation numbers of one or zero yield the ground state density. In Kohn-Sham theory, the total ground-state electronic energy (E_{KS}) is the sum of the following four components: kinetic energy of the occupied orbitals (T_e), interaction of the density with the external potential (V_{en}), Hartree electrostatic energy of the density interacting with itself (J_{ee}) and exchange-correlation energy (E_{XC}), as summarised in Equation 2.3.¹¹⁷

$$E_{KS} = T_e + V_{en} + J_{ee} + E_{XC} \quad (2.3)$$

The E_{XC} is a small but significant contribution to the total energy of a system, which stems from the reduced randomness of electron motion through the density caused by minimisation of Coulomb electron-electron interactions.¹¹⁷ The E_{XC} is unknown, and since the exact form of the universal Hohenberg and Kohn functional is not yet discovered, it must be approximated in other ways for a physically accurate representation of the electron-electron interactions in a many-electron system.^{116–118}

There are three main components to the E_{XC} : the negative potential energy of exchange (as per the HF method), the negative potential energy of correlation (smaller Coulomb electron-electron repulsion expected) and a smaller positive kinetic energy component resulting from additional movement of negative interaction-avoiding electrons.¹¹⁷ In 1979, Levy demonstrated that searching over many-electron wavefunctions constrained to produce a specific density allows for the derivation of the exact density functional for describing the exchange-correlation energy.¹¹⁹ Then using such an ideal exchange-correlation functional, the self-consistent electronic structure of a many-electron system can be solved with the inclusion of all relevant correlations.

2.1.3. Approximation levels of the density functional

Kohn and his colleagues have shown that DFT can provide physically relevant information about the ground state density and the electronic structure, thus providing a tool for simulation and understanding of the interactions of matter on a quantum chemical level. However, an approximation of the density functional must be chosen based on research goals as, 70 years later, there still is no one-size-fits-all functional.

Since the work of Levy in 1979, the DFT research field dynamically progressed and over 7800 publications used the “density functional theory” phrase in year 2022 alone, *i.e.*, a year prior to the submission of this thesis.¹²⁰ In 2001, Perdew *et al.* introduced a concept of the Jacob’s ladder of density functional approximations for the exchange-correlation energy, where the authors suggested a ranking system for the density functional approximation based on the increasing complexity of calculation and conversely a better physical and chemical accuracy of the calculations.¹²¹

At the bottom rung of this imaginary ladder lies the local spin density approximation (LSDA), an improvement upon the simplest of approximations in DFT, the local density approximation (LDA). The LDA represents the system as a homogeneous electron gas with uniformly distributed charges. The LSDA also considers the spin polarization in the calculation of the exchange-correlation energy. The LSDA proved to be useful for solids and indeed was favoured by solid state physicists, but lacked the support among quantum chemistry community due to significant overestimation of atomization energies.¹²¹

The general gradient approximation (GGA) improves upon LDA and LSDA by considering the gradient of the electron density in addition to the electron density at a given position, thereby capturing electronic effects such as bond stretching and charge transfer more accurately, but also overcompensates in the correlation energies of atoms.^{117,121}

One of the most popular DFT methods among quantum chemists in the 1990s and still used today is the GGA-level Perdew-Burke-Ernzerhof (PBE) exchange-correlation functional, particularly useful in the studies of bulk properties of transition metals, a domain in which the functional actually outperforms more sophisticated approaches.^{122,123} However, where catalysis and reactivity of molecules on transition metal surfaces are considered, PBE is lacking

accurate representation of the long-range van der Waals dispersion interactions and self-interactions, which are crucial for good prediction of reaction energetics. Commonly used alongside the PBE exchange-correlation functional is the Tkatchenko-Scheffler method of van der Waals (vdW) correction proposed by Tkatchenko *et al.* in 2009, useful for accurate modelling of solids and reaction energetics.^{124–128} The Tkatchenko-Scheffler method remedies the missing vdW interaction in GGA functionals by addition of a pairwise interatomic E_{vdW} term to the DFT energy.¹²⁴ One advantage of the Tkatchenko-Scheffler scheme is that E_{vdW} method relies on the derivation of the correction term from the ground state electronic density, thus having a lower extent of parametrisation in comparison with, *e.g.*, methods proposed by Grimme *et al.*^{129,130}

Above the GGA approximation on the Jacob's ladder of density functionals lies the meta-GGA approximation, which in addition to the gradient of electron density also considers its second derivative (Laplacian), improving the electronic accuracy by cancellation of errors between exchange and correlation by including the kinetic energy density of the occupied Kohn-Sham eigenstates.¹¹⁷

The main difference between GGA and meta-GGA is that the former is a semi-local functional, as it relies on the density within an infinitesimally small area around a given point, \mathbf{r} , while the latter is a completely non-local functional with respect to the density, but only semi-local in terms of the orbitals.¹²¹ The enhancement results in better description of the long-range forces, which is sufficient for chemical accuracy without additional dispersion corrections, such as those often used with the GGA PBE functional.^{121,131}

The spin-unpolarised meta-GGA functional formalism can be summarised in the following equation:

$$E_{xc}[n] = \int d\mathbf{r} n \varepsilon_{xc}(n \nabla n \tau), \quad (2.4)$$

where n is the total density and τ is the functional of kinetic energy density for the occupied Kohn-Sham eigenstates, which is a non-local functionals of the density n .¹³¹

An example of a meta-GGA functional emerging in the field of transition metal-based materials design is the semi-local Bayesian error estimation density functional (mBEEF).¹³² The mBEEF functional is part of the wider family of density functionals called Bayesian error

estimate (BEE) density functionals. BEE density functionals (BEEF) utilise machine learning to select a group of functionals suitable for reproducing desired properties, such as material or reaction energetics. BEE approach generates a combined output based on a previously provided training data that is applicable to the training set and also for exploring technologically relevant novel materials or reactions beyond the fitting process.¹³² The mBEEF density functional employs the optimization strength of machine learning and the precision of meta-GGA functionals in its fitting process, which produces a versatile exchange-correlation functional that can serve as a tool for tracking reaction energetics on transition metal surfaces across a broad search space.¹³²

2.1.4. Computational modelling of periodic materials

In solid-state physics, the crystal lattice is often represented as a Fourier transform of the real-space lattice, or a reciprocal lattice, where the Brillouin zone is the smallest volume in that reciprocal lattice without duplicate points. In crystal lattices, there is typically a recurring pattern, and the smallest unit of this pattern is known as the unit cell. Bloch's theorem tells us that the wavefunction in a crystal can be written as a product of a plane wave and a function with the same periodicity as the crystal lattice. The Brillouin zone is comprised of all the unique Bloch vectors or **k**-points necessary for calculating meaningful information about the electron density.^{6,133}

Monkhorst and Pack introduced a method for sampling of the Brillouin zone and finding the "special points" in reciprocal space, which contain most of the information about the electronic structure and total potential energy.¹³³ The approach is more computationally tractable thanks to an averaged summation rather than an integration of the whole Brillouin zone.¹³³ The **k**-point sampling procedure is crucial for ensuring accurate results while maintaining the calculations of periodic materials feasible and the procedure for choosing the right sampling of the Monkhorst-Pack **k**-point grid is described in more detail in Chapter 3.2.

2.1.5. Basis sets

The quantum state of a system can be represented using a specific set of atomic orbitals, known as a basis set. The Fritz Haber *ab initio* materials simulations (FHI-aims) package was used throughout the entirety of this work. For all atomistic simulations, FHI-aims operates on a numeric all-electron atom-centred quantum mechanical approach, meaning that all the electrons within the system are taken into account and their complete potential is utilised without simplifying the form.¹³⁴ As a result, numeric atom-centred all-electron codes offer an accurate depiction of the electron density in proximity to the atomic nuclei.

The choice of basis set greatly impacts the chemical accuracy and efficiency of DFT calculations. To ensure that DFT results obtained within the FHI-aims framework are applicable in a wider range of scenarios, a meticulously curated collection of basis sets has been established, balancing the competing needs for precision and computational affordability.¹³⁴ The basis sets are preconstructed with well-defined meV accuracy thresholds for elements with atomic numbers up to 102 in terms of density of the integration grid, the Hartree potential, basis cut-off and others.¹³⁴

Inherently, no basis set is complete as it does not contain all possible functions that can be used to describe the electronic structure of a molecule. Basis set incompleteness can lead to errors in calculations, particularly when dealing with interactions between molecules. If the incomplete basis cannot accurately describe the interaction of two different molecules in a system, an overestimation of the interaction strength can occur. By increasing the size of the basis set, the basis set incompleteness error can be effectively mediated.

Localised nature of the basis set can also give rise to the basis set superposition error (BSSE) in surface-adsorbate interactions, where overlapping atom-centred basis from separate species can lead to artificial stabilisation as depicted in Figure 3.II. A Boys-Bernardi counterpoise correction can be used to account for BSSE.¹³⁵ In the context of molecular adsorptions on surfaces, the BSSE error correction involves calculating the interaction energy between the molecule and the surface using two different basis sets.

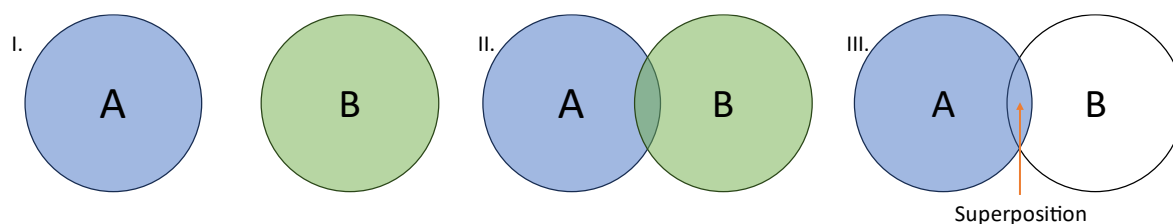


Figure 3. Origin of basis set superposition error and its quantification; A and B are atom centres in a 2-atom system, blue and green regions depict basis orbitals for description of electrons around A and B, respectively. I.) The regions A and B are far apart and non-interacting. II.) The regions A and B are overlapping, and the system is artificially stabilised where orbitals of B are accessible to electrons of A and vice versa. III.) Atom B is a “ghost” and has no electrons or a nucleus, just a basis set centred around B origin. Basis orbitals of B are available to A in the overlapping region, artificially stabilising the system.

Calculations are performed for the molecule and surface separately (as per Figure 3.I), and one for the molecule and the surface with the atoms of the other species being present in the form “ghosts”, i.e., atom-centred basis orbitals without electrons or a nucleus as per Figure 3.III. The difference between the energies can be used to effectively correct for BSSE.¹³⁶ For additional insight into the electronic density, Mulliken population analysis can be performed to determine the distribution of electrons throughout the system and monitor charge accumulation on atomic species.¹³⁷ The Mulliken electronic population analysis is prone to reduced charge distribution accuracy with larger and more diffuse basis sets, hence a particular attention must be paid to the basis set choice.¹³⁸

2.2. Potential energy surface

One of the main concepts in DFT research is exploration of the potential energy surface (PES) of the system, which is the representation of the total potential energy as a function of coordinates of atoms and electrons in that system. For simple systems, the PES resembles a surface in a classical and geometrically intuitive sense, but as the number of atoms in the systems increases, the problem becomes correspondingly multidimensional and complicated.¹³⁹ However, such visual interpretation is very useful for rationalisation of chemical phenomena, such as bond breaking, which often require activation energy. On the PES, example of which is presented in Figure 4, the minimum energy point linking the bonded

and unbonded system, *i.e.*, a transition state or activated complex, would be represented as a “saddle point”.^{139,140}

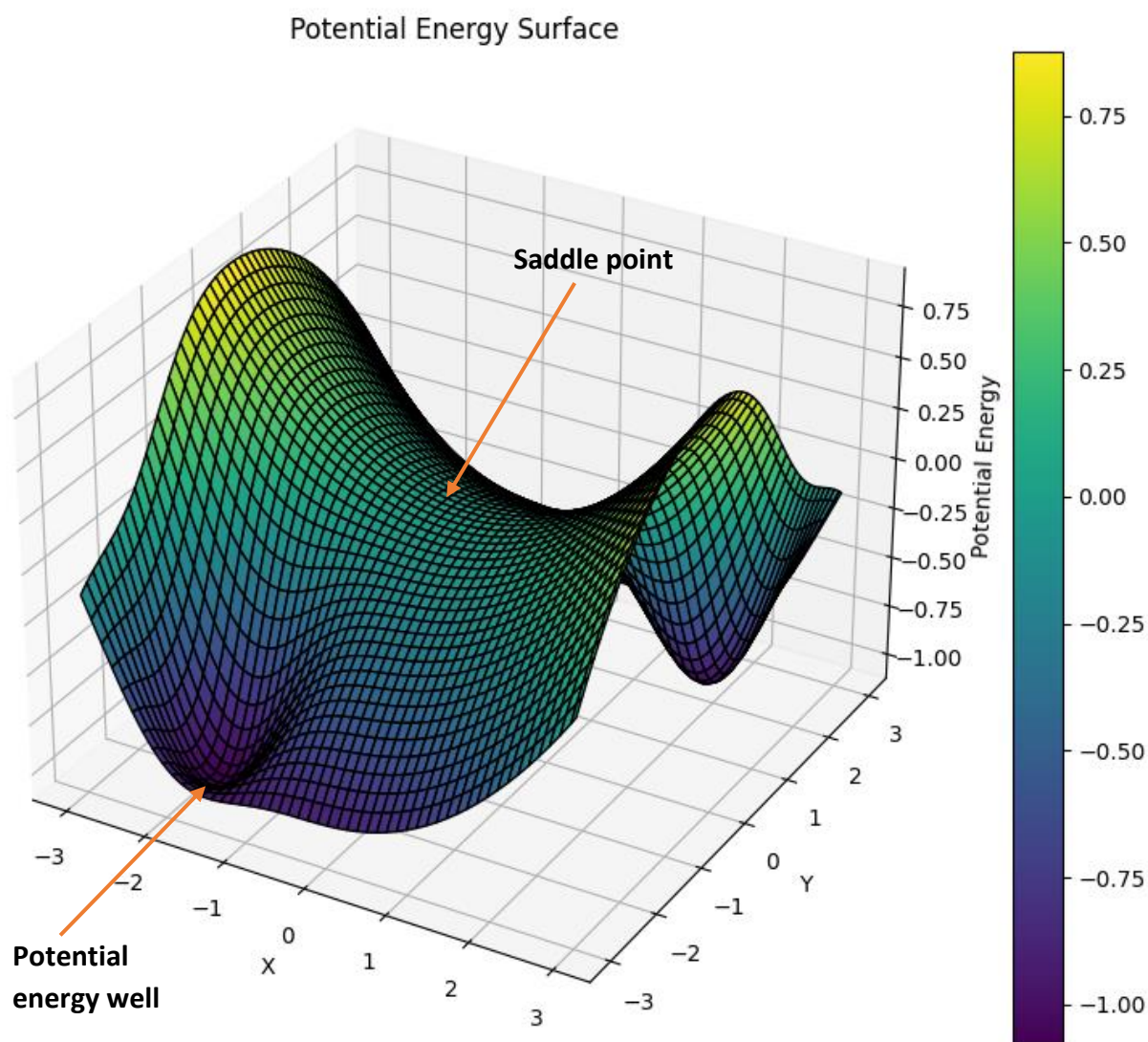


Figure 4. A visual representation of an example potential energy surface; labelled are the transition state at the saddle point, and the local minimum at the potential energy well; units on all axes are arbitrary.

The saddle is a very adequate description as thinking about a landscape: the transition state lies on a hill linking two local minima, or potential energy wells, while looking at the extrema perpendicular to it, the point lies in a valley linking two high energy conformations. The line which could be traced from the energy minima via a saddle point is called the minimum energy path (MEP).

When investigating geometries, the structures located in the local minima are particularly relevant for comparison against experimental results, because matter tends toward energy minimisation. The structures in local minima are referred to as "metastable" species, expected to have lifetimes significantly longer than other species lying on arbitrary points on the PES, and thus be detectable in spectroscopic experiments.¹⁴¹ The saddle point is useful for exploring the reaction energetics as the energy difference between the local minimum and the corresponding transition state is the activation energy required for advancing the reaction coordinate to the species in the second minimum (*e.g.*, bonded or unbonded atoms).

2.2.1. Geometry optimisation

A starting geometry for investigation of a molecular system will be commonly selected such that it is close to the structural local minimum. To find the potential energy well, an energy minimisation, or geometry optimisation procedure, must be performed. Geometry optimization procedures capitalise on a concept that is parallel to force minimisation in classical mechanics, where negative derivative of potential energy (U) with respect to position (x) is called force (F):

$$F = \frac{-dU}{dx}. \quad (2.5)$$

The force can be minimised to ensure that the energy is at an extremum. In quantum chemistry, the forces on each atom (i) can be minimised to find a minimum in the energy of the system (E) by iterative displacement of atomic position (x_i) in the direction of the lowest potential energy gradient (Equation 2.6) to build the multi-dimensional PES curvature and eventually based on the gradient find the energy minimum.¹⁴⁰

$$F_i = \frac{-dE}{dx_i} \quad (2.6)$$

Many methods for geometry optimisation have been proposed, but the one used throughout this work is the Broyden-Fletcher-Goldfarb-Shanno (BFGS) optimisation procedure, which has been shown to be reliable and stable for larger systems.¹⁴⁰

2.2.2. Vibrations and Thermodynamics

During exploration of the PES using DFT calculations, the electronic density of a particular static image of the molecular system can be measured in the ambience of pressure, temperature or motion of particles. Such representation might be necessary when relating computed quantities to experimental results, where effects of volume, pressure, and temperature collectively influence the energy of the system. In the context of thermodynamics, the internal energy (U) of a system is defined as the energy required to create the system, assuming no changes in temperature, volume, or pressure. This definition includes the contribution from the motion and configuration of particles within the system, which is mathematically expressed by the Hamiltonian operator (\hat{H}).

Zero point energy (ZPE) is the minimal amount of energy that persists in a system even when it is cooled to absolute zero, originating from the Heisenberg uncertainty principle, which asserts that certain pairs of physical properties, such as position and momentum, or energy and time, cannot be precisely determined and exhibit inherent uncertainty.¹⁴² Hence, even at absolute zero temperature, when classical thermodynamics predicts no energy, particles and fields still undergo fluctuations and oscillations in their ground state. ZPE can be calculated by considering the vibrational frequencies exhibited by the ground state of the system. The calculation of ZPE involves approximating the PES using the harmonic oscillator concept, *i.e.*, a system that, when displaced from its equilibrium position, experiences a restoring force proportional to the displacement. The vibrations of particles in a molecule are treated as small oscillations around an equilibrium position and Schrödinger equations are solved for the displaced geometries yielding ZPE for the ground state system. The harmonic oscillator approximation works well for small atomic displacements and short-range vibrations. Calculated geometries are used to fill the Hessian matrix, or second derivative of the PES, which captures the curvature of the PES and allows identification of previously introduced saddle points and minima. The Hessian matrix contains information about the energies associated with vibrational modes which are intricately linked to the system's position on the PES.

Imaginary vibrational modes are specifically tied to directions on the PES where the second energy derivative is less than zero. Information about the system's PES location can be

inferred from the number, displacement, and energy of these modes. When all vibrational modes are real, the system is at the PES minimum, which can further confirm the metastability of molecular species after geometry optimisation. Conversely, if there is one imaginary mode amongst real vibrational modes, the system is at a saddle point on the PES, while multiple imaginary modes suggest that there are multiple directions for energy minimisation and that the structure is at an arbitrary high energy lying point on the PES and is not chemically relevant in normal conditions.

In understanding the chemical behaviour of a system, the enthalpy (H) is often more informative than the total potential energy alone. Enthalpy describes the work done by the system on its surroundings. The work corresponds to the pressure (p) and volume (V) as:

$$H = U + pV, \quad (2.7)$$

where U represents the internal energy. The changes in internal energy (ΔU) can come from work done on the system or changes induced by chemical reactions. However, in DFT calculations are performed at 0 K, and only the ground state of particles is necessary for an accurate description of U , in such cases, the pV term can be assumed to be negligible. By removing the pV the ZPE contribution can be approximated and added to the total potential energy to obtain an approximate value for H in the absence of temperature. By calculating the enthalpy changes (ΔH) the derived enthalpies of adsorption are then relatable to experimental adsorption studies at ultra-high vacuum conditions.

On the other hand, the Gibbs free energy (G) measures the reversible work that can be performed by a system at given temperature and pressure conditions and is positively dependent on the H and negatively dependent on both temperature (T) and entropy (S):

$$G = H - TS. \quad (2.8)$$

A negative change in Gibbs free energy (ΔG) with reaction coordinate indicates spontaneity of a chemical reaction and a larger forward rate of reaction than the reverse rate and, conversely, a positive ΔG indicates the opposite as captured by the equation:

$$\Delta G = \Delta H - T\Delta S, \quad (2.9)$$

where ΔS is the change in entropy over the course of reaction. Considerations of ΔG are important for obtaining a complete picture of the chemical reaction favourability at experimentally relevant conditions.

2.2.3. Transition state calculations

For investigation of reaction energetics, often MEPs must be calculated to evaluate the relevant parts of the PES in terms a whole reaction pathway and find activation barriers along the reaction coordinate (x), *i.e.*, for all relevant reaction intermediates as the chemical reaction proceeds. Nudged elastic band (NEB) method is a popular way of evaluating the MEP and calculating the transition state.^{143–145} The NEB method implements the search for the MEP through construction of a set of images of the system between the initial and final states, *i.e.*, two relevant local metastable structures for which the activation energy must be found. To ensure the continuity of the path, a spring interaction is added between the images. Further, a geometry optimisation of the band is performed, *i.e.*, forces are minimised on each of the images and are placed closer and closer to the true MEP as the optimisation proceeds.¹⁴³ A necessary step for ensuring that the spring forces are not affecting the convergence of the elastic band to the MEP is the calculation of the tangent to the path at each of the images over the course of the geometry optimisation. Calculating the tangent to a path can help distinguish between the actual force and the spring force by decomposing them into components that are parallel and perpendicular to the path, respectively. An additional step for ensuring that the true transition state is included in the MEP involves the use of a climbing image (CI), where an additional force is included travelling upward along the gradient following the tangent of the MEP, resulting in improved convergence of the highest lying point on the MEP.¹⁴⁴ The act of force projection is commonly referred to as “nudging” of the band of images, hence the name of the nudged elastic band method.¹⁴⁴

The TS calculations involve optimising the whole “band” of images under specific conditions and therefore can be orders of magnitude more expensive than regular geometry optimisations involving a single structure. To ensure the tractability of modelling reaction energetics using NEB approaches on a complex system, modern machine learning approaches

can be used.^{146,147} One such solution is the low-scaling algorithm for NEB calculations using a surrogate machine learning model as proposed by Garrido Torres *et al.*¹⁴⁶ The algorithm involves building a surrogate PES model relying on Gaussian process regression (GPR), which estimates of images along the MEP in each iteration, thereby eliminating the need for recalculation of all images along the MEP per iteration, and only the currently evaluated image must be calculated using DFT.¹⁴⁶ GPR methods treat observables as finite realisations of a Gaussian distribution and the GPR in the work of Garrido Torres *et al.* is trained on atomic coordinates and corresponding structure energies as descriptors and returning predictions on the evaluated Gaussian distribution. GPR, as a probabilistic model, is capable of returning predictions of the target property along with fit uncertainty estimates, hence, the uncertainty of the fit is considered as a supplementary convergence criterion in combination with the force evaluation. The machine learning assisted NEB (MLNEB) utilising the CI approach enables a satisfactory estimation of the transition state structures, at a significantly lower cost than regular NEB.¹⁴⁶

2.3. Software details

Given the popularity of computational chemistry research, there is an abundance of software capable of performing quantum chemical simulations of materials. Similarly, when it comes to the choice of exchange-correlation functional, there is no single software combination that serves as a silver bullet for performing DFT material modelling. In this thesis, FHI-aims was used for evaluation of DFT energy and forces.¹³⁴ All structure preparation and manipulation and subsequent output data analysis was performed within the atomistic simulation environment (ASE) Python library developed by Larsen *et al.*¹⁴⁸ Transition state calculations using MLNEB were utilising the CatLearn Python library compatible with ASE.^{146,147} Additionally, to save computational time by shortening the MEP length, the input structures for transition state calculations in Chapter 5 were matched using periodic symmetry considerations using the Surface Science Modelling Toolkit (SuSMoST).¹⁴⁹

Chapter 3. A computational study of direct CO₂ hydrogenation to methanol on Pd surfaces

The work presented herein has previously been published in Physical Chemistry Chemical Physics under the same title in 2022 with Dr Lara Kabalan, Prof Sir Richard Catlow and Dr Andrew Logsdail as co-authors.¹²⁸

3.1. Introduction

The potential of direct CO₂ hydrogenation to methanol as a sustainable route for transport fuels and a circular fuel economy has been widely recognised by the chemical industry.¹⁵⁰ The industrial synthesis of methanol from syngas, *i.e.*, fossil-derived feedstock, is efficient and profitable, however, there is increasing pressure on the chemical industry to transition to a net-zero emissions economy by 2050.¹⁵¹ Bussche *et al.* demonstrated through a steady-state kinetic model that CO₂, rather than CO, is likely to be the primary carbon source in methanol synthesised from syngas, thereby encouraging the consideration of direct CO₂ hydrogenation using anthropogenic CO₂ from the atmosphere.^{21,44,151} However, a deeper understanding of the interaction between CO₂ and transition metal catalysts is necessary for the design of effective catalytic systems. The source of H₂ and other factors affect the "greenness" of direct methanol synthesis from CO₂, but the concept of using CO₂ as a feedstock for fuel synthesis and the generation of feedstock for further chemical synthesis, such as methanol, holds broad appeal.¹¹

A critical step in the direct hydrogenation of CO₂ to methanol on transition metals is the activation of CO₂ further reactivity which involves breaking one of the strong C-O bonds, donation of electrons to CO₂ and bending the molecule out of shape.^{152,153} The lowest unoccupied molecular orbital (LUMO) of CO₂ is a σ^* orbital which overlaps poorly with the accessible d orbitals of the metal.^{152,153} The second antibonding LUMO is the π^* molecular orbital, which overlaps well with the filled d orbitals of the transition metal allowing the transfer of electrons from the metal to the antibonding π^* orbital.^{152,153} Distortion of the CO₂ molecule requires high energy as it affects the integrity of the overlap of O and C orbitals but

lowers the energy of the π^* and allows for increased overlap with occupied d orbitals of the metal centre.¹⁵² The favourable electron donation offsets the distortion energy of the out-of-shape CO₂ molecule making the carbon more nucleophilic, thus, activating the CO₂ for subsequent reactivity with hydrogen dissociated on the metal surface.^{152,153}

On a heterogeneous catalyst, it is important to inhibit the reverse water-gas shift (RWGS) reaction while maintaining a strong interaction between CO₂ and the catalytic surface.^{48,154} Pd alone demonstrates poor selectivity for methanol in direct CO₂ hydrogenation, but its selectivity is significantly improved when alloyed with other transition metals like Zn.^{11,14,48,76,155,156} To fully understand the reactivity of Pd-based alloys, it is essential to investigate the nature of the CO₂-Pd interactions. Experimental data on the interaction between CO₂ and Pd facets is limited, but density functional theory (DFT) computations are providing valuable insights into the process.^{37,38,157,158} Burghaus *et al.* observed that CO₂ reactivity on clean Pd surfaces is weak, with dissociation to CO not favoured unless an alkali metal species is co-adsorbed. The weak interaction is primarily attributed to van der Waals physisorption, as supported by theoretical and experimental observations on the Pd (111) surface.^{157,159,160} CO₂ adsorption on Pd has been studied in the context of the RWGS reaction and syngas utilisation, and desorption of CO₂ from the Pd (111) surface was found to require an energy of 0.26 eV.¹⁵⁷ Solymosi *et al.* reported relatively low energy of 0.35 eV for CO₂ desorption from the Pd (100) surface, indicating a chemisorption process involving electron transfer from the metal to the empty CO₂ π^* orbital.³⁸ Brosseau *et al.* also reported evidence of CO₂ chemisorption on Pd (110) in the presence of water.⁴¹ Therefore, the nature of CO₂ interaction with Pd surfaces appears to depend on the surface structure. The variations in adsorption energies can be correlated with surface energies, where physisorption was exclusively observed on the lowest energy (111) surface, and experimental evidence of chemisorption was observed for CO₂ on the higher energy Pd (100) and (110) surfaces, with the latter occurring in the presence of water.^{37,38,41,157}

In addition to these findings, the catalytic hydrogenation rate of CO₂ on Pd is significantly enhanced when it is combined with suitable metal oxide supports like TiO₂ and ZnO, as they facilitate CO₂ adsorption and acid/base activation, where O of CO₂ donates electrons to the positively charged metal and O of the metal oxide donates electrons to the partially positively charged carbon.^{13,14,19,152} Using the dispersion-corrected PBE-D2 density functional, Ko *et al.*

investigated CO₂ adsorption on transition metal surfaces and reported two types of adsorption on Pd (111).¹⁵⁴ The first type is an exothermic physisorption (-0.33 eV) of undistorted CO₂ parallel to the surface. The second type is a less exothermic chemisorption (-0.18 eV) resulting in bent CO₂ geometry, accompanied by a partial negative charge. In contrast, Zhang *et al.*, using the PBE density functional, found CO₂ chemisorption on Pd (111) to be endothermic (0.06 eV), consistent with the results of Habas *et al.*, who used DFT with the B3LYP density functional and reported an adsorption energy of CO₂ at 0.22 eV above the dissociation limit.^{63,161} Additionally, Liu *et al.* demonstrated that the inclusion of the DFT-D2 correction significantly alters the adsorption energy of chemisorbed species on the Pd (111) surface when using the PBE density functional, shifting it from 0.30 to -0.18 eV.¹⁶⁰ Although there is no consensus regarding the endo- or exothermic nature of CO₂ chemisorption on Pd surfaces, the reported values are generally small, aligning with experimental reports indicating a weak interaction between CO₂ and Pd surfaces.

The proposed mechanism for direct CO₂ hydrogenation to methanol involves a surface formate intermediate (HCOO*) as opposed to carboxyl (COOH*), as the latter is active towards dissociation to CO* and OH*.⁹⁴ Medford *et al.* demonstrated that HCOO* could act as a poison for other reaction pathways due to its high thermodynamic stability on the catalyst surface.⁹⁴ Variations of the mechanism proposed by Grabow, which proceeds via formic acid (HCOOH), have been presented, as shown in Figure 5.⁹¹ For example, an initial Eley-Rideal type mechanism was proposed for Cu-based catalytic systems, where CO₂ in the gas phase reacts with surface-bound hydrogen to produce formate. More recently, Huš *et al.* suggested that dioxymethylene (H₂COO*) should be considered preferentially over formic acid (HCOOH*) on Cu-based catalysts, as the former exhibits stronger binding to the metallic surface and a lower activation energy towards hydroxymethoxy (H₂COOH*).¹⁶²

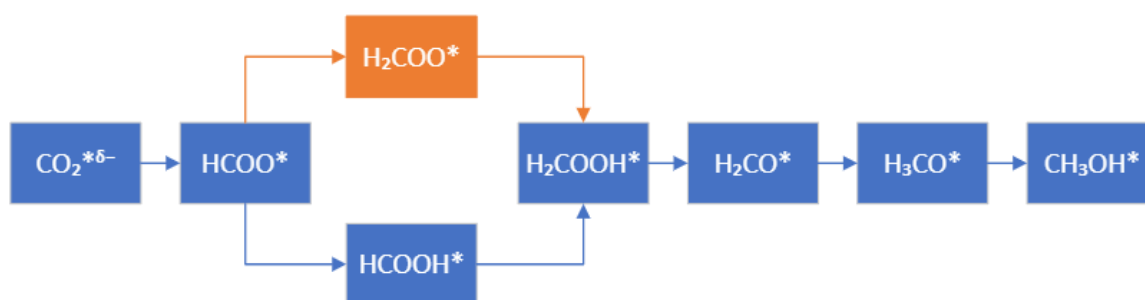


Figure 5. Formate pathway of direct CO₂ hydrogenation to methanol on metallic surfaces, as proposed by Grabow *et al.* (via HCOOH*, blue) and Huš *et al.* (via H₂COO*, orange). * indicates a surface-bound species and δ- indicates that CO₂ is partially charged (*i.e.*, activated).^{91,162}

Pd-based catalysts supported on ZnO have emerged as powerful alternatives for this reaction, attributed to the presence of Pd-Zn binary metallic phases that stabilise the HCOO* intermediate, similar to Cu-based catalysts.^{19,76} Zhang *et al.* conducted DFT studies on an alternative CO₂ formate mechanism, involving the dissociation of HCOOH into HCO and OH, followed by hydrogenations of HCO to produce CH₃OH.⁶³ In addition, in recent DFT work Brix *et al.* proposed that the initial CO₂ hydrogenation on Pd (111) proceeds via carboxylic acid (COOH) rather than formate, revealing a high energy barrier of 2.23 eV for CO₂ hydrogenation to formate on Pd (111), in contrast to the 0.85 eV barrier reported by Zhang *et al.*^{63,72}

Although binary metallic alloy catalysts may offer desirable selectivity, stability, and tunability compared to monometallic counterparts, the lack of fundamental understanding regarding the behaviour of monometallic materials hampers the design of emerging multi-component catalysts. To gain the necessary insights for CO₂ hydrogenation over Pd, it is essential to investigate the reactivity across all significant surface facets. Therefore, in this study, we present a comprehensive investigation of CO₂ interaction with low-energy Pd (111), (110), and (100) surfaces using DFT calculations. Subsequently, we explore the direct CO₂ hydrogenation to CH₃OH through the Grabow mechanism on the Pd (111), (110), and (100) surfaces. This research aims to elucidate CO₂ reactivity on Pd-based catalysts and provide a rational understanding of the process.

3.2. Methodology

The Fritz Haber Institute *ab initio* molecular simulations (FHI-aims) software package has been used for full potential all-electron DFT calculations, with the Pythonic Atomic Simulation Environment (ASE) used for management of calculation geometries.^{148,163} The default convergence criteria within FHI-aims for self-consistent field (SCF) calculations were used, i.e. the changes between the current and previous SCF iterations in charge density, sum of eigenvalues and total energy were below $N \times 1.67 \times 10^{-5} e \cdot a_0^{-3}$, 10^{-3} eV and 10^{-6} eV, respectively, where N is the number of atoms in the model. Scalar relativistic treatment of kinetic energy for all elements was achieved by the atomic zero-order regular approximation (ZORA), and a Gaussian-type broadening with width of 0.01 eV was applied to the occupation of electronic states. The Fritz Haber Institute *ab initio* molecular simulations (FHI-aims) software package has been used for full potential all-electron DFT calculations, with the Pythonic Atomic Simulation Environment (ASE) used for management of calculation geometries.^{148,163} The default convergence criteria within FHI-aims for self-consistent field (SCF) calculations were used, i.e. the changes between the current and previous SCF iterations in charge density, sum of eigenvalues and total energy were below $N \times 1.67 \times 10^{-5} e \cdot a_0^{-3}$, 10^{-3} eV and 10^{-6} eV, respectively, where N is the number of atoms in the model. Scalar relativistic treatment of kinetic energy for all elements was achieved by the atomic zero-order regular approximation (ZORA), and a Gaussian-type broadening with width of 0.01 eV was applied to the occupation of electronic states to effectively prevent the charge sloshing phenomenon hindering convergence of calculations involving metallic systems.¹⁶⁴

Due to the closed-shell electronic configuration of Pd ($[\text{Kr}] 4d^{10}$), spin-paired calculations were used in periodic calculations; gas-phase adsorbate structures were calculated both spin-paired and spin-unpaired, and the energy of the more stable system was considered for reference to periodic calculations. The effect of the spin-paired approximation has been assessed towards the activation energies in relevant surface hydrogenation reactions and was summarised in Table 1, with a spin-paired treatment shown to introduce small error bars of ± 0.05 eV.

Table 1. Comparison of activation energy (E_{act}) when using spin-paired or spin-collinear approximations, with impact considered across all intermediate steps in the CO₂ hydrogenation reaction over the FCC Pd (111), (110) and (100) surfaces. Species given in the Table are those at the start of the reaction step. All energies are in eV.

| Pd Surface | Species | E_{act} (spin-paired) | E_{act} (spin-collinear) | ΔE_{act} |
|------------|-------------------------------|-------------------------|----------------------------|------------------|
| (100) | CO ₂ ^{δ-} | 1.07 | 1.08 | -0.01 |
| | HCOO | 0.74 | 0.70 | 0.04 |
| | HCOOH | 1.26 | 1.29 | -0.04 |
| | H ₂ COOH | 0.80 | 0.77 | 0.03 |
| | H ₂ CO | 0.63 | 0.63 | 0.00 |
| | H ₃ CO | 0.70 | 0.69 | 0.01 |
| (110) | CO ₂ ^{δ-} | 0.83 | 0.82 | 0.02 |
| | HCOO | 0.65 | 0.62 | 0.03 |
| | HCOOH | 0.92 | 0.96 | -0.05 |
| | H ₂ COOH | 0.52 | 0.49 | 0.02 |
| | H ₂ CO | 0.65 | 0.64 | 0.01 |
| | H ₃ CO | 0.40 | 0.39 | 0.01 |
| (111) | CO ₂ ^{δ-} | 1.09 | 1.05 | 0.03 |
| | HCOO | 0.57 | 0.54 | 0.03 |
| | HCOOH | 1.35 | 1.34 | 0.01 |
| | H ₂ COOH | 0.50 | 0.51 | 0.00 |
| | H ₂ CO | 0.77 | 0.75 | 0.01 |
| | H ₃ CO | 0.49 | 0.48 | 0.01 |

3.2.1. Bulk models

A primitive Pd unit cell with side length (a) of between 2.47 Å and 2.97 Å (corresponding to a cubic lattice parameter of 3.5 and 4.2 Å, respectively) was used to test and converge the Monkhorst-Pack \mathbf{k} -grid (reciprocal space sampling) and basis functions on the bulk energy (E_{bulk}). Convergence of the \mathbf{k} -grid within 10 meV was achieved with a (9 x 9 x 9) \mathbf{k} -grid, as shown in Figure 6, and computational time increased beyond that point without significant accuracy gain. Thus, a (9 x 9 x 9) \mathbf{k} -grid was determined to be the most suitable choice for further calculations on the Pd primitive cell, with \mathbf{k} -space sampling adjusted appropriately for models with larger supercells (*i.e.*, slabs).

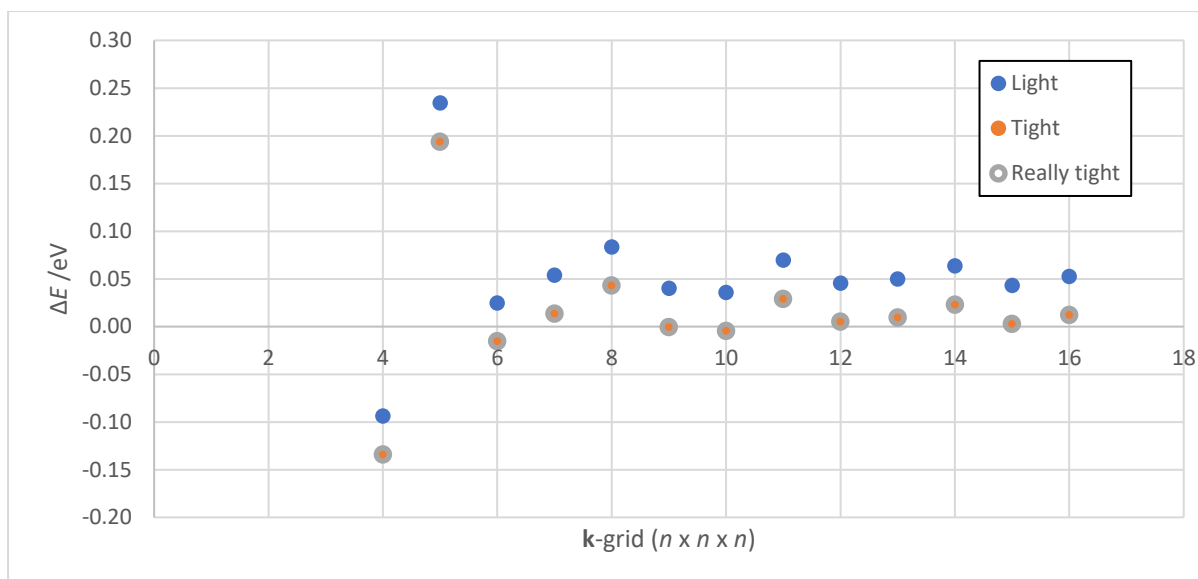


Figure 6. Convergence of energy with respect to \mathbf{k} -grid and basis set choice, sampled on a Pd primitive cell with a unit cell vector of 2.69 Å, where n corresponds to the \mathbf{k} -grid sampling. The energy difference (ΔE) is presented relative to that calculated with a “tight” basis set and a (9 x 9 x 9) \mathbf{k} -grid.

The standard basis sets that are distributed with the FHI-aims package were used, categorised as “light”, “tight” and “very tight”. A significant gain in energetic accuracy was observed when changing from the “light” to the “tight” settings; however, the calculations were twice as expensive. The “very tight” basis only marginally improved energetic accuracy, by on average 0.5 meV with respect to the “tight” settings; this increase in computational cost with little accuracy gain made further consideration of this setting inappropriate.

Using the outlined \mathbf{k} -grid and basis set choices, a_0 and the bulk modulus, B_0 , was calculated using the Birch-Murnaghan equation of state, with a range of common exchange-correlation (XC) functionals considered, and the results are shown in Table 2.¹⁶⁵ Selection of an appropriate exchange-correlation density functional was made based on accuracy, and computational time required for a single-point calculation. The PW-LDA XC functional underestimates the Pd bulk a_0 and overestimates B ; The PBE XC functional is inaccurate also, but introduction of a Van der Waals correction, represented using the Tkatchenko-Scheffler method, yields values of $a_0 = 3.914$ Å and $B_0 = 183.8$ GPa, with only a small error of +0.9 % and +1.8 % with respect to experiment.^{166,167} Furthermore, the cohesive energy (E_{coh}) of 4.00 eV agrees reasonably with literature.^{78,79} Therefore, the generalised gradient approximation (GGA) based on the Perdew-Burke-Ernzerhof exchange-correlation functional, with a

Tkatchenko-Scheffler van der Waals correction (PBE+vdW), was used for subsequent calculations.¹²⁵

Table 2. Screening of exchange correlation functionals with respect to accuracy for a_0 (Å), B_0 (GPa) and E_{coh} (eV), as acquired using a Birch-Murnaghan Equation of State, and the difference in each property with respect to experiment (Δ , given in %). PBE+MBD includes the many-body dispersion (MBD) correction of Tkatchenko *et al.*^{168,169}

| Settings | Basis | a_0 | Δa_0 | B_0 | ΔB_0 | E_{coh} | ΔE_{coh} |
|------------------------------|-------|-------|--------------|--------|--------------|-----------|------------------|
| Exp. ² (293.15 K) | - | 3.890 | - | - | - | 3.89 | - |
| Exp. ³ (0 K) | - | 3.878 | - | 180.40 | - | - | - |
| PW-LDA | Light | 3.841 | -1.0 % | 226.13 | 20.2 % | 5.08 | 30.6% |
| PBE | Light | 3.944 | 1.7 % | 168.60 | -7.0 % | 3.73 | -4.1% |
| PBE+TS | Light | 3.914 | 0.9 % | 183.77 | 1.8 % | 4.00 | 2.7 % |
| PBE+TS | Tight | 3.910 | 0.8 % | 186.39 | 3.2 % | 4.01 | 3.0 % |
| PBE+MBD | Light | 3.920 | 1.1 % | 179.59 | -0.4 % | 4.05 | 4.1% |
| B3LYP | Light | 3.989 | 2.9 % | 140.19 | -28.7 % | 2.50 | -35.7 % |

In summary, the Perdew-Burke-Ernzerhof exchange correlation (XC) density functional paired with the Tkatchenko-Scheffler Van der Waals dispersion correction (PBE+vdW) was used. A default “light” basis set (version: 2010) has been used for geometry optimisations, providing structural accuracy;^{124,163,170} energy calculations were then performed with a “tight” basis set (version: 2010) on the optimised geometries, providing greater electronic accuracy and mitigation of basis set superposition error.¹⁶³ For geometry optimisations, convergence was deemed complete when forces on all unconstrained atoms were less than $0.01 \text{ eV } \text{Å}^{-1}$. For sampling of the Brillouin zone of face-centred cubic (FCC) Pd in a primitive unit cell, a $(9 \times 9 \times 9)$ Monkhorst–Pack \mathbf{k} -grid provides converged accuracy.¹³³ The lattice constant ($a_0 = 3.914 \text{ Å}$), bulk modulus ($B_0 = 183.37 \text{ GPa}$) and cohesive energy ($E_{coh} = 3.996 \text{ eV}$) calculated for bulk FCC Pd match closely with the experimental observations of 3.88 Å , 180.40 GPa and 3.89 eV , respectively.^{122,166}

3.2.2. Surface models

Using the optimised model of bulk FCC Pd, a surface supercell was created with dimensions of $(3 \times 3 \times n)$, where n is the number of atomic layers in the z -direction perpendicular to the material surface. The x - and y -dimensions were chosen such that the adsorbates are significantly separated (7.5 Å), and a vacuum layer of 40 Å was added in the z -direction. The \mathbf{k} -grid sampling was reduced appropriately for altered cell dimensions, with a \mathbf{k} -grid of $(3 \times 3 \times 1)$ applied. Due to the one-sided nature of the slab models considered, a dipole-correction was used in all calculations.

The energy penalty for breaking chemical bonds at the surface of a material (E_{cleave}) is calculated as:

$$E_{\text{cleave}} = \frac{E_{\text{Slab}}^{\text{Unrelaxed}} - N \cdot E_{\text{bulk}}}{2A} \quad (3.1)$$

where the DFT total energy of an unrelaxed surface slab model ($E_{\text{Slab}}^{\text{Unrelaxed}}$), the bulk energy per atom (E_{bulk}), the number of atoms in the model (N), and the surface area (A), are needed. E_{cleave} converges for the Pd (111), (100) and (110) facets when E_{cleave} ceases to fluctuate as a function of slab thickness, as can be seen for $n \geq 5$ in Figure 7; thus, 5-layer models are used for all subsequent calculations in Chapter 3.

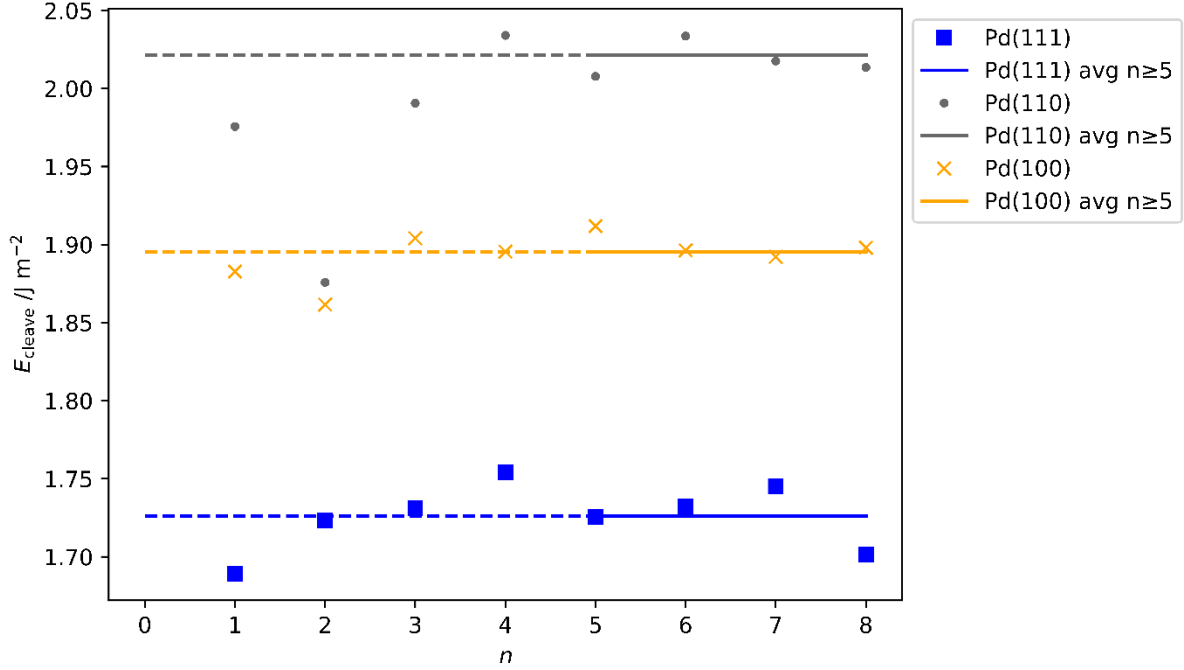


Figure 7. E_{cleave} calculated for Pd FCC (111), (110) and (100) surfaces as a function of increasing model thickness, n . A key is provided to identify the symbols and linear fits; the average cleave energy (solid horizontal line) was taken from $n \geq 5$, to avoid bias from inaccurate thin slabs (dashed lines). The oscillations between the odd and even n can be attributed to the quantum size effect.¹⁷¹

To calculate the surface energy (E_{surf}), the energy of stabilisation provided by geometry relaxation (E_{relax}) needs to be obtained from the difference in total DFT energy of the optimised slab ($E_{\text{Slab}}^{\text{Relaxed}}$) and $E_{\text{Slab}}^{\text{Unrelaxed}}$:

$$E_{\text{relax}} = \frac{E_{\text{Slab}}^{\text{Relaxed}} - E_{\text{Slab}}^{\text{Unrelaxed}}}{A} \quad (3.2)$$

where a single-sided model of the surface is considered, hence the denominator is A only. Constraints were used to maintain the bulk structure for Pd atoms distant from the adsorption site, *i.e.*, the bottom layers of the slab model. $E_{\text{Slab}}^{\text{Relaxed}}$ was calculated for all three surface facets with one, two or three layers of surface atoms unconstrained, with E_{relax} converging only when the top three surface layers are unconstrained.

In summary, accurate results has been achieved herein with a 3 x 3 x 5 supercell surface model, with the bottom two layers constrained to their bulk positions and the three top surface layers unconstrained. The surface energies (E_{surf}) can subsequently be calculated as follows:

$$E_{\text{surf}} = E_{\text{cleave}} + E_{\text{relax}} \quad (3.3)$$

with these settings, and are presented in Table 3. The calculated Pd (111), (100) and (110) E_{surf} match previous computation and experiments, thus supporting the validity of our approach.

Table 3. Pd FCC (111), (100) and (110) surface energies calculated using the outlined settings. Literature and experiment are provided for comparison.

| Reference | XC | $E_{\text{surf}} / (\text{J}\cdot\text{m}^{-2})$ | | |
|---|----------------|--|-------------|-------------|
| | | Pd (111) | Pd (100) | Pd (110) |
| This work | PBE+vdW | 1.72 | 1.91 | 1.99 |
| Methfessel <i>et al.</i> ¹⁷² | LDA | 1.64 | 1.86 | 1.97 |
| Vitos <i>et al.</i> ¹⁷³ | GGA | 1.92 | 2.33 | 2.23 |
| Patra <i>et al.</i> ¹⁷⁴ | LDA | 1.88 | 2.43 | 2.25 |
| | PBE | 1.36 | 1.79 | 1.61 |
| | PBEsol | 1.63 | 2.15 | 1.93 |
| | SCAN | 1.54 | 2.03 | 1.83 |
| | SCAN+rVV10 | 1.77 | 2.29 | 2.05 |
| Singh-Miller <i>et al.</i> ¹⁷⁵ | PBE | 1.31 | 1.49 | 1.55 |
| Da Silva <i>et al.</i> ¹⁷⁶ | LDA | 1.87 | - | - |
| | PBE | 1.33 | - | - |
| Skriver <i>et al.</i> ¹⁷⁷ | LDA | 1.88 | - | - |
| Tyson <i>et al.</i> ¹⁷⁸ | Experiment | 2.00 | - | - |
| Boer <i>et al.</i> ¹⁷⁹ | Experiment | 2.01 | - | - |

3.2.3. Surface adsorption

For catalytic surface reactions, the adsorption energy (E_{ads}) measures the interaction between a surface and reactant, and is deduced from comparison of the energies of the optimised gas-phase adsorbate (E_A), optimised surface (E_S) and the combined system (E_{A-S}).

$$E_{\text{ads}} = E_{A-S} - (E_A + E_S) \quad (3.4)$$

where a negative value indicates favourable adsorption. Due to basis set incompleteness when using an atom centred basis, a Boys-Bernardi counterpoise correction is necessary for surface-adsorbate interactions to account for the basis set superposition error (BSSE).¹³⁵ In our work, the BSSE for CO₂ adsorbed on Pd (111) was assessed on an aperiodic model with all Pd atoms within 7.0 Å of the adsorbed CO₂ molecule included (*i.e.*, all atoms within the distance of the atom-centred basis cut-off, including those in neighbour cells). The energy of the CO₂ in the presence and absence of Pd basis functions ($E_{A(A-S)}$ and $E_{A(A)}$, respectively) were compared, and the equivalent comparison of the energy of the slab model in the presence and absence of the basis functions of the CO₂ adsorbate ($E_{S(A-S)}$ and $E_{S(S)}$, respectively) was also performed.¹³⁵ The BSSE energy (E_{BSSE}) was then calculated as:¹³⁵

$$E_{\text{BSSE}} = [E_{A(A-S)} - E_{A(A)}] + [E_{S(A-S)} - E_{S(S)}] \quad (3.5)$$

A more negative the E_{BSSE} indicates a greater overbinding error; however, by subtracting E_{BSSE} from E_{ads} , the counterpoise corrected adsorption energy can be established ($E_{\text{ads}}^{\text{CP}}$) as:

$$E_{\text{ads}}^{\text{CP}} = E_{\text{ads}} - E_{\text{BSSE}} \quad (3.6)$$

With the “light” basis set, E_{BSSE} is -0.08 eV for CO₂ on Pd (111), but E_{BSSE} was reduced to -0.02 eV with the “tight” basis set. Considering the low BSSE with the “tight” basis, which is used subsequently throughout this work, the E_{BSSE} contribution to E_{ads} was deemed negligible and was not subsequently calculated for species other than CO₂.

3.2.4. Transition state structures

For kinetic studies, we have used a machine learning nudged elastic band (MLNEB) method to identify saddle points and minimum energy paths (MEPs).^{144,147} A spring constant of 0.05 eV Å⁻¹ has been used throughout; the convergence criterion of forces on all unconstrained atoms of below 0.05 eV Å⁻¹, with energy uncertainty below 0.03 eV, was deemed sufficiently accurate for CO₂ adsorption. Comparison with a more stringent force criterion of 0.01 eV Å⁻¹ altered the activation energy for CO₂ adsorption on FCC (111) surface by 5 meV only as shown

in Figure 8. The MLNEB method also utilizes climbing image (CI) calculation routine, resulting in well converged TS, but the intermediate points along the MEP are of much less significance.

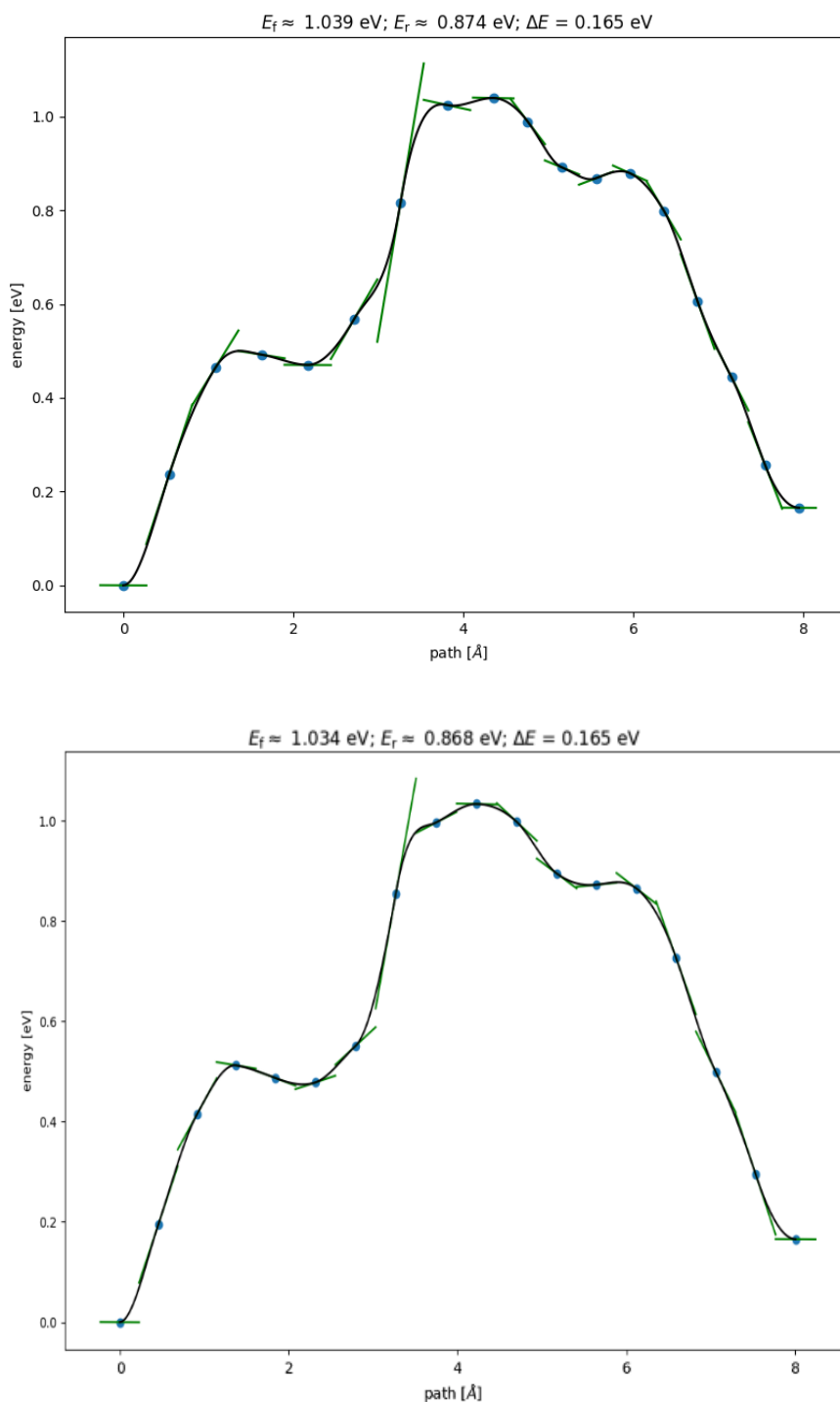


Figure 8. Energy profile of the initial CO₂ hydrogenation step towards HCOO on the Pd (111) surface, as calculated using the MLNEB approach. Top: Results with $f_{\max} = 0.05 \text{ eV}\text{\AA}^{-1}$, fit uncertainty = 0.03 eV; Bottom: $f_{\max} = 0.01 \text{ eV}\text{\AA}^{-1}$ and fit uncertainty = 0.03 eV. Activation energy forward along the reaction coordinate and the activation energy in the reverse direction are denoted as E_f and E_r , respectively, and ΔE is the overall reaction energy.

3.2.5. Vibrations and Thermodynamics

Vibration frequency calculations have been performed for structures in the reaction pathway using the ASE vibrations module and the Frederiksen method.¹⁸⁰ To reduce the computational cost, the number of vibrating Pd atoms in the structures was tested as a function of adsorbate nearest Pd neighbours based on the connectivity matrix. The vibrational energy converged at first Pd neighbours of the adsorbate, and this approximation has been applied throughout. The vibration frequencies were also calculated for transition state structures, and the saddle points were confirmed by the presence of a single imaginary frequency. Where multiple imaginary frequencies occurred on the transition state structure, the transition state was deemed converged if none of the other imaginary frequencies exceeded 10i meV. Free energies of gas components were calculated using an ideal gas-phase approximation, whereas the energies of periodic surface structures with adsorbates were calculated using a harmonic approximation. Once the zero-point energy (ZPE) was established, the contribution of ZPE was added to E_{ads} yielding enthalpy of adsorption, H_{ads} .

3.3. Results and discussions

3.3.1. Hydrogen adsorption

Prior to investigating the reaction steps in CO₂ hydrogenation, an understanding of hydrogen behaviour on Pd is crucial as the interaction of H with CO₂ is integral to the reaction profile. Thus, a survey was conducted of E_{ads} for H, $E_{\text{ads}}(\text{H})$, on the Pd surfaces; the H atom was positioned at various locations on the surface and optimised, with constraints in the xy -plane. $E_{\text{ads}}(\text{H})$ on the Pd (111), (100), and (110) surfaces was calculated with respect to the gas-phase diatomic hydrogen molecule and is plotted across the xy -plane in Figure 9(i), Figure 10(i), and Figure 11(i), respectively. The ZPE-correction was not applied in these scans and all energies presented in this section are based on differences in total electronic energy. The most stable adsorption site for H on the Pd (111) surface is the FCC hollow position, which is site A in Figure 9(ii), with $E_{\text{ads}}(\text{H})$ of -0.67 eV; similar stability over high coordination sites is observed

on the (100) surface, where the hollow site (Figure 11(ii), site C) has lower energy with $E_{\text{ads}}(\text{H})$ of -0.54 eV, and the “FCC” site (Figure 11(ii), site B) is of lower energy in the case of the (110) surface, with $E_{\text{ads}}(\text{H})$ of -0.56 eV. The least stable adsorption site for H on all surfaces is atop, with $E_{\text{ads}}(\text{H})$ of -0.12, -0.08 and 0.00 eV on the (111), (100) and (110) Pd surfaces, respectively. The typical reactant feed for CO₂ hydrogenation is between 1:3 to 1:9 molar ratio of CO₂ and H₂, and thus dissociated hydrogen would be readily available on the catalyst surface.^{14,19} High hydrogen mobility can be deduced from Figures 8(i), 9(i), and 10(i), as differences in favourable E_{ads} are low along specific channels, highlighted in red. The adsorption energies for H on the Pd (111) surface (-0.67 eV) and the (110) surface (-0.56 eV) compare reasonably with the experimental work of Conrad *et al.*, who report initial heats of adsorption for ½ H₂ of -0.45 and -0.53 eV for Pd (111) and (110) surfaces, respectively.¹⁸¹ There is also good agreement with previous theoretical research as Herron *et al.* calculated atomic hydrogen adsorption energies on Pd (111) using PW91 and reported them to be -0.59, -0.56 and 0.00 eV on FCC hollow, HCP hollow and atop positions, respectively.¹⁸² Similarly, Fonseca *et al.* used PBE in their DFT study of hydrogen adsorption on Pd (111) and observed -0.66, -0.61 and -0.50 eV adsorption energies of hydrogen atom on FCC hollow, HCP hollow and bridge position, respectively.^{183,183} In literature, there are conflicting perspectives on the impact of hydrogen coverage on the E_{ads} of H on Pd surfaces, which is there is a negligible³¹ or a significant¹⁸⁴ positive contribution to E_{ads} as H coverage increases up to 0.9 ML. Therefore, the effect of hydrogen coverage on E_{ads} is not elaborated upon in detail at this point.

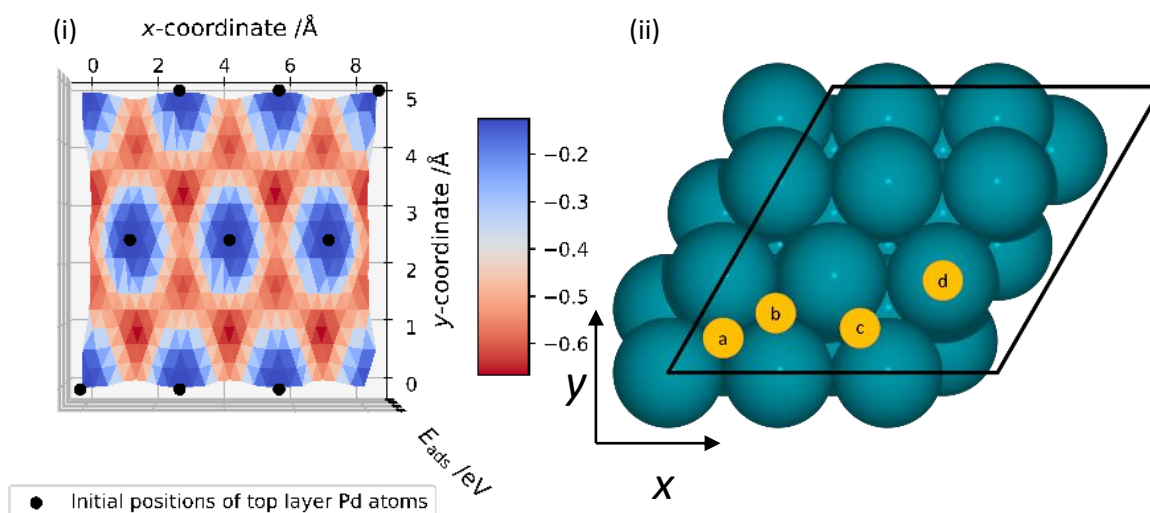


Figure 9. (i) Adsorption energy (E_{ads}) of a hydrogen atom on Pd (111) surface, calculated as a function of x - and y -coordinate; the H atom remained constrained in the xy -plane during each geometry optimisation. A key is provided for the adsorption energies, in units of eV. (ii) Top-down view of the FCC Pd (111) surface with a $3 \times 3 \times 5$ atoms simulation cell. Blue spheres represent Pd atoms and yellow circles represent unique adsorption sites: a) hollow-FCC, b) hollow-HCP, c) bridge, d) atop. Black lines represent the x - and y -direction cell boundaries.

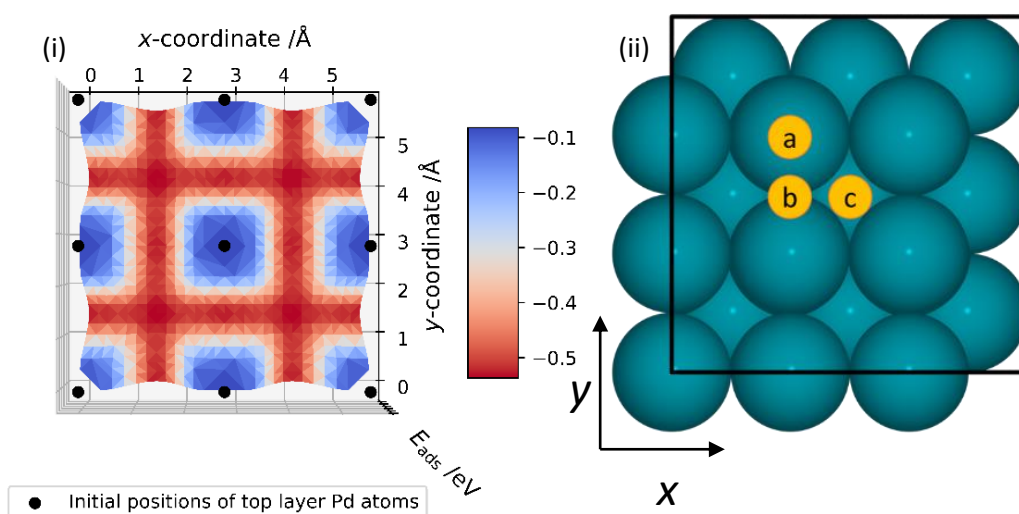


Figure 10. (i) Adsorption energy (E_{ads}) of hydrogen atom on Pd (100) surface calculated as a function of x - and y -coordinate; the H atom remained constrained in the xy -plane during each geometry optimisation. A key is provided for the adsorption energies, in units of eV. (ii) Top-down view of the FCC Pd (100) surface with a $3 \times 3 \times 5$ atoms simulation cell. Blue spheres represent Pd atoms and yellow circles represent unique adsorption sites: a) atop, b) bridge c) hollow. Black lines represent the x - and y -direction cell boundaries.

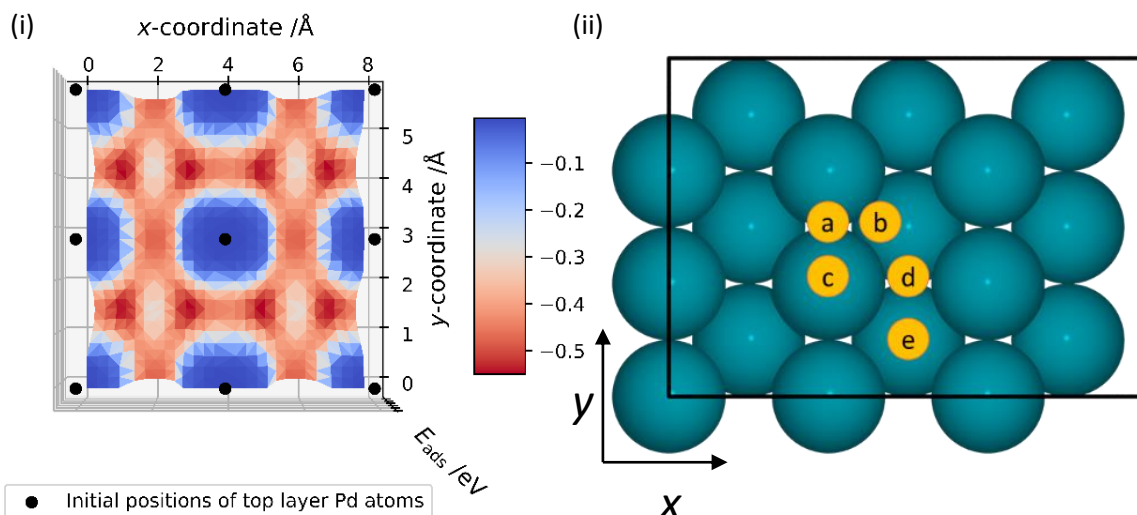


Figure 11. (i) Adsorption energy (E_{ads}) of hydrogen atom on Pd (110) surface calculated as a function of x- and y-coordinate; the H atom remained constrained in the xy-plane during each geometry optimisation. A key is provided for the adsorption energies, in units of eV. (ii) Top-down view of the FCC Pd (110) surface with a 3 x 3 x 5 atoms simulation cell. Blue spheres represent Pd atoms and yellow circles represent unique adsorption sites: a) short bridge, b) “FCC” c) atop, d) long bridge, e) hollow. Black lines represent the x- and y-direction cell boundaries.

3.3.2. CO₂ adsorption

The adsorption energies and structures for CO₂ on the Pd (111), (100) and (110) surfaces are reported in Table 4. The undistorted CO₂ geometry is the most stable adsorption configuration with a C-Pd bond distance, $d(\text{C-Pd})$, of 3.454 Å, which agrees with the physisorbed species observed by Habas *et al.*¹⁶¹ $H_{\text{ads}}(\text{CO}_2)$ is strongest on the close-packed (111) surface, and is found to relate linearly with the number of Pd atoms that neighbour the surface adsorption site; when $H_{\text{ads}}(\text{CO}_2)$ is plotted as a function of surface atom coordination number (CN), which are 9, 8, and 7 for the Pd (111), (100), and (110) surfaces, respectively, a linear fit returns $R^2 = 0.998$. It is noted that the Pd (110) is not considered a flat surface and has both metal atoms with CN of 11 and 7, however the less coordinated atoms are more exposed, hence preferably considered in the interaction between the (110) facet and the physisorbed adsorbate.

The strongest physisorption, rather than chemisorption, observed for CO₂ on the Pd (111) surface ($E_{\text{ads}}(\text{CO}_2)$ of -0.21 eV) was reported previously by Ko *et al.*¹⁶¹ (-0.33 eV); they also identify a chemisorbed state CO₂^{δ-} with E_{ads} of -0.16 eV,¹⁷ which is in contrast with our observation of endothermic $H_{\text{ads}}(\text{CO}_2^{\delta-})$ of 0.09 eV. Huš *et al.* observed that on Cu catalysts, CO₂ binds to the metal surface in a bent geometry, where one of the oxygens binds to a secondary metal atom and the carbon binds to a metal atom underneath.¹⁶² Higham *et al.* observed an endothermic CO₂ chemisorption on Cu (100) and (110) surfaces, similarly to our result on Pd (111).⁵⁵ Energy differences between our results and those of Ko *et al.* are probably due to the choice of van der Waals correction;¹⁵⁴ never-the-less, the observed trends are similar, and the stability of the physisorbed CO₂ implies that there is an energy barrier on the Pd (111) surface for the activation of CO₂.

Table 4. Geometric and energetic observations for CO₂ and CO₂^{δ-} physisorbed and chemisorbed species on low-index Pd surfaces, respectively; CO₂^{TS} is the transition state geometry between these stable local minima. H_{ads} is the ZPE-corrected species adsorption energy, given in eV; $d_{(\text{C-Pd}^1)}$ is the distance between the carbon and the nearest neighbouring Pd given in Å, and $\angle_{\text{O-C-O}}$ is the angle between the oxygen, carbon and oxygen, given in °.

| Species | Pd surface | | | | | | | | |
|-------------------------------|------------------|-----------------------|-------------------------|------------------|-----------------------|-------------------------|-------------------|-----------------------|-------------------------|
| | (111) | | | (100) | | | (110) | | |
| | H_{ads} | $d_{(\text{C-Pd}^1)}$ | $\angle_{\text{O-C-O}}$ | H_{ads} | $d_{(\text{C-Pd}^1)}$ | $\angle_{\text{O-C-O}}$ | H_{ads} | $d_{(\text{C-Pd}^1)}$ | $\angle_{\text{O-C-O}}$ |
| CO ₂ | -0.21 | 3.45 | 179.5 | -0.18 | 3.28 | 179.1 | -0.16 | 3.26 | 179.2 |
| CO ₂ ^{TS} | 0.12 | 2.37 | 154.8 | 0.00 | 2.45 | 160.6 | No energy barrier | | |
| CO ₂ ^{δ-} | 0.09 | 2.10 | 140.3 | -0.09 | 2.06 | 140.6 | -0.19 | 2.06 | 140.2 |

$H_{\text{ads}}(\text{CO}_2^{\delta-})$ is endothermic (0.09 eV) on the Pd (111) surface, matching the work of Zhang *et al.*⁶³, and then exothermic (-0.09 and -0.19 eV) on the Pd (100) and (110) surfaces, respectively.²⁷ Reduction of the size of the model surface, such that 1/4 monolayer (ML) coverage of CO₂ is achieved on Pd (111), (100) and (110) surfaces, results in $H_{\text{ads}}(\text{CO}_2^{\delta-})$ of 0.12 eV, -0.03 eV and -0.16 eV, respectively. The higher (less favourable) $H_{\text{ads}}(\text{CO}_2^{\delta-})$ values for 1/4 ML coverage, when compared to the $\frac{1}{9}$ ML coverage presented in Table 4, is intuitively linked to unfavourable interactions between neighbouring adsorbates. $H_{\text{ads}}(\text{CO}_2^{\delta-})$ is noted as increasingly negative (*i.e.*, strengthens) with increasing E_{surf} for the Pd facets, and the energy difference between surface-bound CO₂ and CO₂^{δ-} also decreases; these observations agree

with experimental data that show an absence of chemisorption on the Pd (111) surface, and both physisorption and chemisorption on the Pd (100) surface.^{37,38,157} The adsorbed geometries of $\text{CO}_2^{\delta-}$ are similar across all surfaces (Table 4); only a small difference in angles (0.4°) is calculated for the chemisorbed geometries when compared across the three facets, but $H_{\text{ads}}(\text{CO}_2^{\delta-})$ varies with 0.09, -0.09 and -0.19 eV on Pd (111), (100) and (110), respectively. The impact of steric interactions for adsorbed CO_2 can be quantified via the distortion energy, i.e., the gas-phase energy of the bent adsorbed $\text{CO}_2^{\delta-}$ geometry relative to the preferred linear CO_2 configuration, which is 1.35, 1.33 and 1.33 eV for Pd (111), Pd (110), and (100) facets, respectively. Given that the overall adsorption energies are exothermic on Pd (100) and (110) surface facets, it can be concluded that the binding energy between surface Pd atoms and the CO_2 is significant and offsets the distortion energy arising from the unfavourable bending and poor overlap of C and O orbitals in the CO_2 molecule.

Mulliken charge analysis of the CO_2 and $\text{CO}_2^{\delta-}$ species adsorbed on the Pd (111), (110) and (100) facets provides insight into the electronic charge of the surface species, and the data acquired are reported in Table 5. The notation used for describing charges on atoms of interest is shown in Figure 12: O^1 and O^2 are oxygen atoms on CO_2 molecule; the two closest Pd atoms interacting with CO_2 are labelled Pd^1 and Pd^2 , where Pd^1 is closest to O^1 and Pd^2 is closest to O^2 ; and Pd_{surf} , $\text{Pd}_{\text{sublayer}}$, and Pd_{slab} refer to the first, second and all layers of Pd atoms in the model, respectively.

Table 5. Net Mulliken charges, in units of e , on relevant atoms for CO_2 physisorption and chemisorption on the Pd (111), (110) and (100) surfaces; the charges (q) over Pd atoms have been averaged in the first surface layer surface (Pd_{surf}) and sublayer ($\text{Pd}_{\text{sublayer}}$), and summated over the whole slab (Pd_{slab}).

| | Pristine surfaces | | | CO_2 | | | | $\text{CO}_2^{\delta-}$ | | |
|----------------------------|-------------------|-------------|-------------|---------------|-------------|-------------|-------------|-------------------------|-------------|-------------|
| | Pd (111) | Pd (110) | Pd (100) | Gas | Pd (111) | Pd (110) | Pd (100) | Pd (111) | Pd (110) | Pd (100) |
| q_C | - | - | - | +0.48 | +0.47 | +0.45 | +0.44 | +0.39 | +0.38 | +0.38 |
| q_{O^1} | - | - | - | -0.24 | -0.22 | -0.22 | -0.22 | -0.19 | -0.26 | -0.23 |
| q_{O^2} | - | - | - | -0.24 | -0.23 | -0.22 | -0.22 | -0.23 | -0.24 | -0.25 |
| q_{Pd^1} | - | - | - | - | -0.02 | -0.05 | -0.05 | -0.32 | -0.10 | -0.15 |
| q_{Pd^2} | - | - | - | - | -0.01 | -0.02 | 0.00 | -0.30 | +0.04 | -0.07 |
| $q_{Pd_{\text{sublayer}}}$ | +0.03 | +0.02 | +0.02 | - | +0.02 | +0.05 | 0.00 | -0.02 | +0.03 | 0.00 |
| $q_{Pd_{\text{surf}}}$ | -0.03 | -0.03 | -0.02 | - | 0.00 | -0.01 | 0.00 | -0.07 | 0.00 | -0.02 |
| $q_{Pd_{\text{slab}}}$ | 0.00 | 0.00 | 0.00 | - | -0.02 | -0.01 | 0.00 | +0.04 | +0.11 | +0.10 |

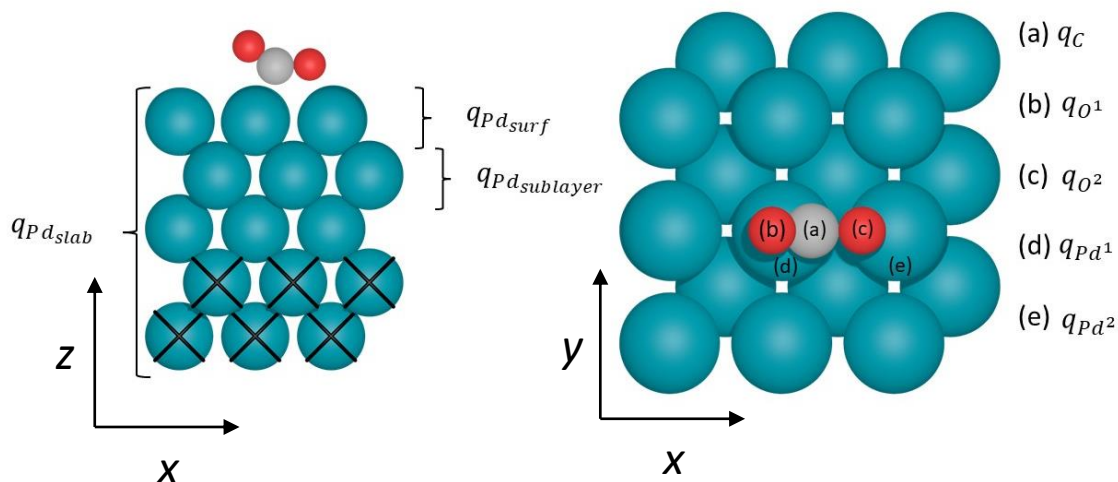


Figure 12. Side- and top-view of CO_2 chemisorbed on the FCC Pd (100) surface, illustrating notations used for Mulliken analysis. Blue, red, and grey spheres represent Pd, O, and C atoms, respectively. Black crosses mark constrained bulk Pd layers.

For CO_2 physisorption on the Pd (111) surface (Figure 13a), the charge of the carbon (q_C) is +0.47 e , very similar to the gas phase CO_2 ($q_C = +0.48 e$), and only small changes are observed on the surface Pd. For $\text{CO}_2^{\delta-}$ on the Pd (111) surface (Figure 13b), negatively charged Pd atoms bond to an oxygen and carbon ($q_{Pd^1} = -0.30 e$, $q_{Pd^2} = -0.32 e$). The distance $d(\text{C-Pd}^2)$ is 2.85

Å, and there is a direct electronic interaction between Pd² and the carbon atom of CO₂. The average charge on the second layer of Pd atoms, $q_{Pd_{sublayer}}$, decreases from +0.03 to +0.02 e upon physisorption and decreases further to -0.02 e upon chemisorption. The average charge on the first surface atomic layer of Pd, $q_{Pd_{surf}}$, is -0.03 e, 0.00 e and -0.07 e for pristine Pd (111) surface, Pd (111) slab with CO₂ and Pd (111) slab with CO₂^{δ-}, respectively, suggesting that the electron density has been pulled to the first two layers of Pd, and to the CO₂^{δ-} adsorbate via Pd¹ and Pd². q_C has decreased from +0.47 e to +0.39 e, indicating some metal (Pd¹) to empty CO₂ π* orbital electron transfer.³⁸ The negatively charged oxygen close to the negative q_{Pd^1} and q_{Pd^2} will result in electrostatic repulsion, and thus are likely to contribute in the decreased stability of CO₂^{δ-} on the Pd (111) surface.^{6,161}

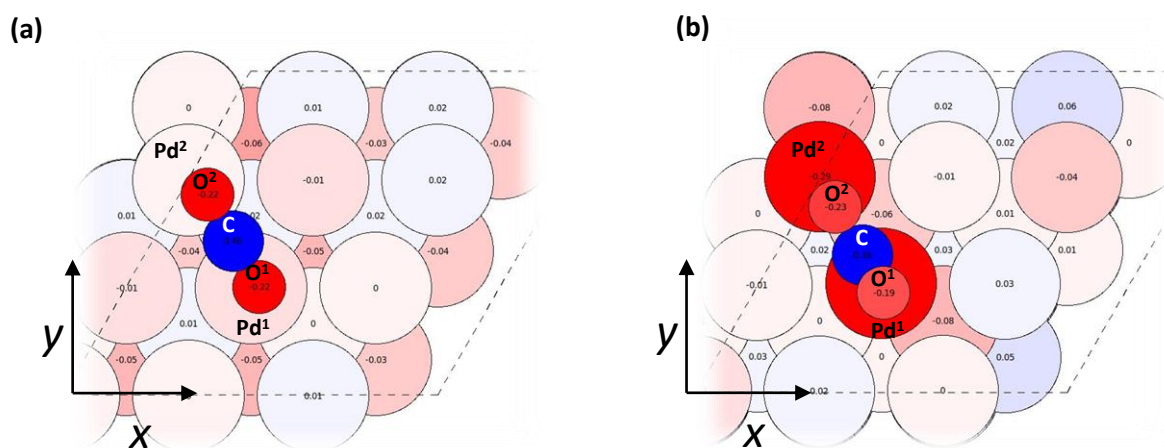


Figure 13. A red-white-blue (negative-neutral-positive charges) color-coded visualisation of the net Mulliken charge on atoms for (a) CO₂ physisorbed and (b) CO₂^{δ-} chemisorbed on the Pd (111) surface.

In contrast, for CO₂^{δ-} on Pd (110) the q_C reduction by 0.07 e upon chemisorption, higher electron density on the oxygens and much lesser charge redistribution on the surface Pd atoms compared to the Pd (111) surface (q_{Pd^1} of -0.10 e and -0.30 e, respectively) contribute to the overall stability (*i.e.*, lower H_{ads}). For CO₂^{δ-} on a Pd (100) facet, the charges calculated are intermediary between the results on the Pd (111) and (110) surfaces, and H_{ads} also falls between the values observed for Pd (111) and (110) surfaces.

The overall charge transfer from the metal to CO₂^{δ-} is -0.04, -0.10 and -0.11 e on Pd (111), (100) and (110) surfaces, respectively, which is small but correlates directly with adsorption strength. In the previous literature, Bader charge analysis has been considered for CO₂

chemisorption on Pd (111) surfaces, and the transfer to $\text{CO}_2^{\delta-}$ reported as -0.28 and -0.43 e by Tang *et al.* and Habas *et al.*, respectively;^{161,185} the direction of charge transfer is consistent with our own observations, with the quantitative difference attributed to methodological differences, *i.e.*, Mulliken charge analysis has a strong basis set dependency than Bader analysis.^{186,187} Importantly, we show qualitatively that the charge transfer to $\text{CO}_2^{\delta-}$ increases over Pd (111), (100), and (110) surfaces, indicating that Pd (100) and (110) surfaces are more suitable for CO_2 activation than the most stable Pd (111) surface.

3.3.3. Interactions of intermediates with Pd surfaces

Reaction intermediates from the Grabow mechanism, as introduced in Section 3.2, have been optimised on the pristine Pd (111), (100) and (110) surfaces, in each case starting from an atop position, which ensured that adsorbates were starting at a proximity allowing metal-adsorbate bond formation during the geometry optimisation process. For example, in the case of CO_2 , the chemisorbed species could easily be missed starting from the gas phase due to an energy barrier for the chemisorption of CO_2 on Pd (111) and (100) surfaces. The calculated values of H_{ads} are presented in Figure 14 and tabulated in Table 22.

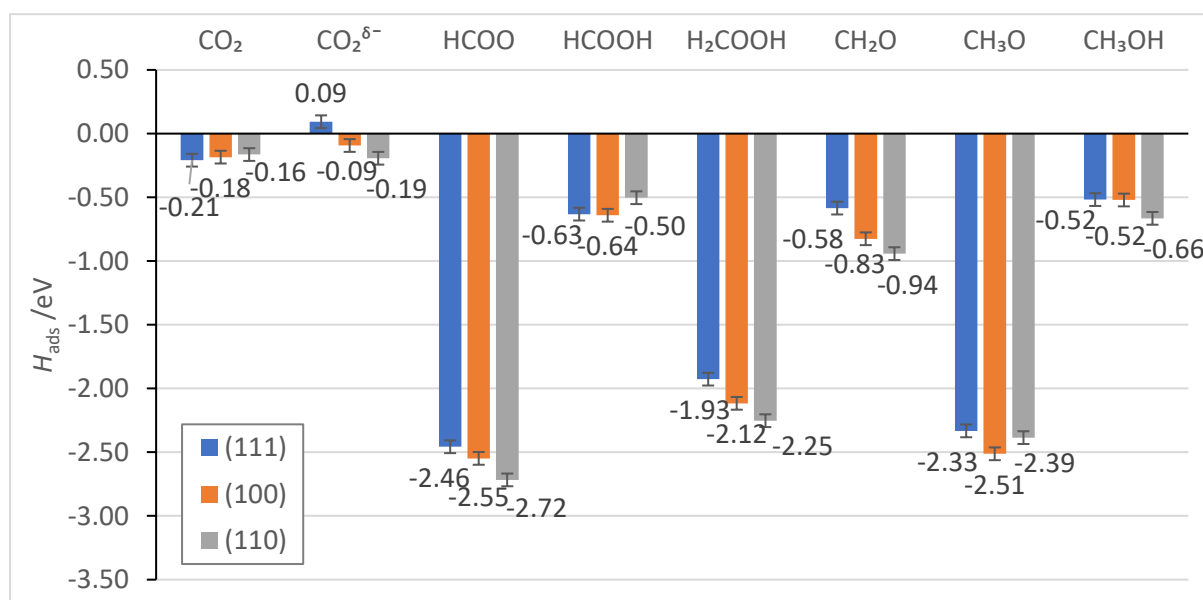


Figure 14. H_{ads} of the intermediates in the direct CO_2 hydrogenation to methanol, as studied on the low-index Pd surfaces, presented in order of increasing E_{surf} : (111), (100) and (110),⁹¹ in blue, orange and grey, respectively. Error bars of ± 0.05 eV are provided to account for the spin-paired approximation applied to the adsorbed species, as described in Section 3.2.3.

For the intermediates considered, the average difference between the highest and lowest H_{ads} across the three surfaces is 0.22 eV; the smallest difference is for the CO_2 molecule (0.05 eV), and the largest for H_2CO , H_2COOH and $\text{CO}_2^{\delta-}$ (0.36, 0.33 and 0.29 eV, respectively). Plotting the surface energy (E_{surf}) of the low-index Pd surfaces against the adsorption enthalpy (H_{ads}) of these intermediates on the corresponding surfaces (Figure 15) illustrates where surface properties associate with these observations. In particular, H_{ads} of CO_2 , $\text{CO}_2^{\delta-}$, H_2COOH and H_2CO present clear linear correlations with the stability of the surface facets, giving R^2 of 0.988, 0.997, 0.987 and 1.000, respectively. HCOO , HCOOH , H_3CO and CH_3OH give a poor linear fit, which indicates that other factors, such as steric effects, should be considered for rationalising the strength of these adsorbate interactions with the Pd surfaces. For example, due to additional space on the long-bridge site on the Pd (110) surface, the HCOOH can be accommodated in a different orientation from that on the Pd (111) and (100) surfaces (*i.e.*, C-H atoms facing down, rather than up), which makes the resulting structures more difficult to compare directly.

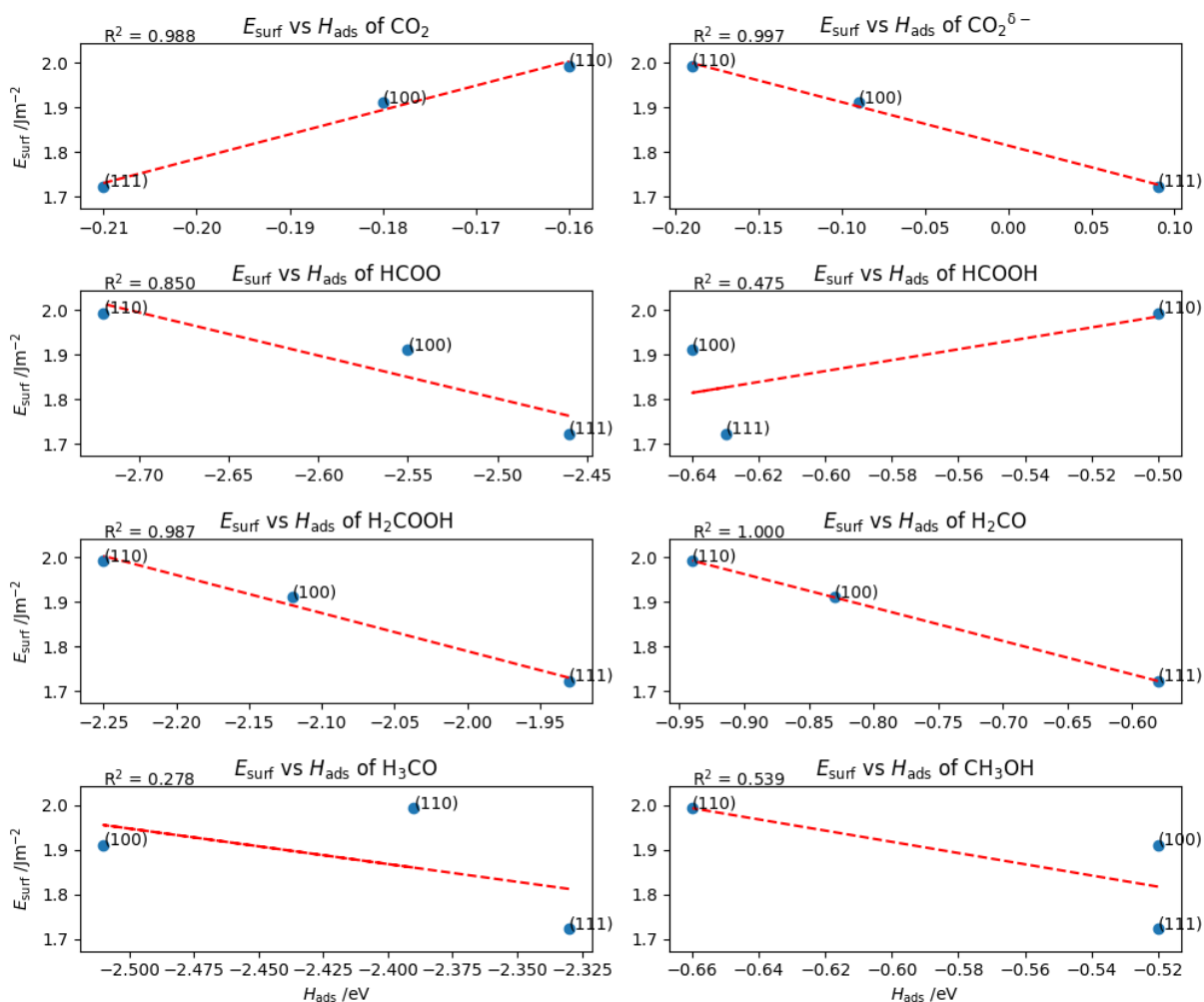


Figure 15. E_{surf} of the Pd (111), (100) and (110) surfaces plotted against H_{ads} of intermediates in the mechanism of CO_2 hydrogenation to methanol. The red dashed line is the linear fit of the data points, and R^2 is the linear coefficient of determination showing the quality of the fit.

3.3.4. Transition states and reaction profile

In order to gain insight into reaction mechanisms, activation energies were calculated. Here, for each reaction step that involved a hydrogenation, it was necessary to set the transition state (TS) starting geometry such that a hydrogen atom was positioned near to the intermediate; optimisation of these starting models with proximal hydrogen in some instances led to instability of the intermediate adsorption structures, which, however, did not cause problems when directly applied to the TS calculations. Once a transition state structure was confirmed, the ZPE-corrected activation energy (H_{act}) was calculated for each reaction step as:

$$H_{\text{act}} = H_{\text{TS}}(\text{species}) - H_{\text{ads}}(\text{species}). \quad (3.7)$$

The reference initial state for the calculation of H_{act} is the species adsorbed on the surface, and for hydrogenation steps a hydrogen atom is also adsorbed, but the two adsorbates have a very limited interaction between them. The resulting H_{act} are presented in Figure 16 and structures are tabulated in Table 22 in the Appendix. Here, $\text{CO}_2^{\delta-}$ was considered as the starting point, *i.e.*, proceeding via a Langmuir-Hinshelwood mechanism, and *not* a physisorbed CO_2 .⁹¹ As part of the reaction pathway via formate, the decomposition of H_2COOH^* into H_2CO^* and OH^* was included, as previously considered for metal catalysts containing Cu, Pd and Zn.^{47,72,91,162} All TS have also been validated by vibrational analysis, displaying only one imaginary frequency each. The elementary step towards which each energy barrier refers are presented in Table 6.

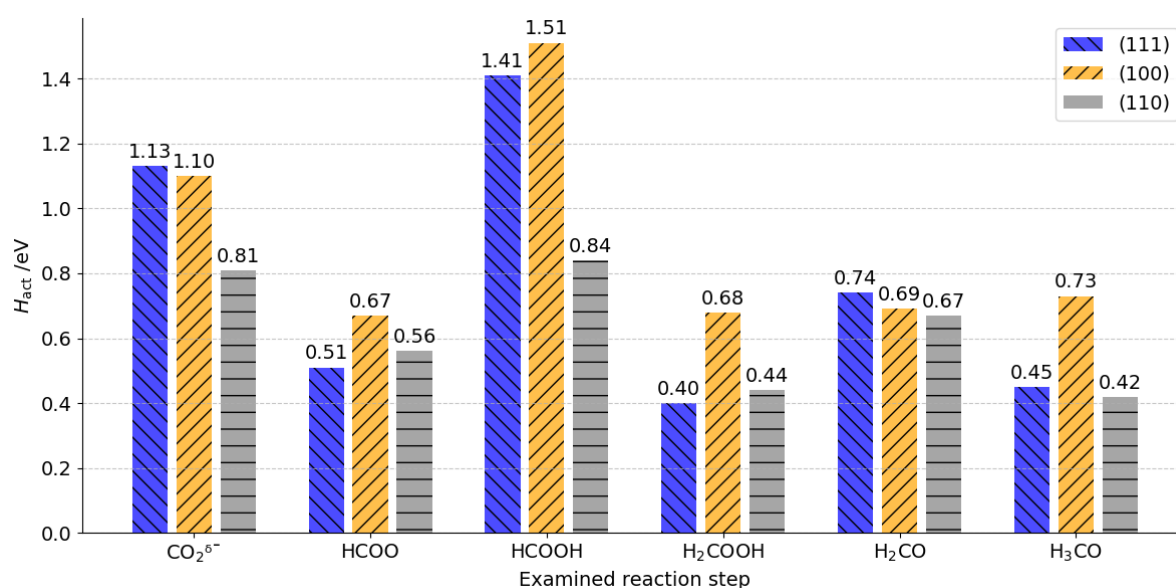


Figure 16. The ZPE-corrected activation energies (H_{act} , eV) of reaction steps in the pathway for CO_2 hydrogenation to methanol, presented for Pd surfaces in order of increasing E_{surf} , *i.e.*, (111), (100), and (110), given in blue, orange, and grey, respectively. In each case, the label refers to the initial reaction species, and the activation energies are also tabulated.

Table 6. Detailed reaction steps towards which the $H_{\text{act}}(\text{species})$ abbreviations refer to in Figure 16.

| | | | |
|---|--|---|--|
| $H_{\text{act}}(\text{CO}_2^{\delta-})$ | $2.5\text{H}_2 + \text{H}^* + \text{CO}_2^*_{\text{chem}}$ $\rightarrow \text{TS1} + 2.5\text{H}_2$ | $H_{\text{act}}(\text{H}_2\text{COOH})$ | $1.5\text{H}_2 + \text{H}_2\text{COOH}^*$ $\rightarrow \text{TS4} + 1.5\text{H}_2$ |
| $H_{\text{act}}(\text{HCOO})$ | $2\text{H}_2 \rightarrow \text{HCOO}^* + \text{H}^*$ $\rightarrow \text{TS2} + 2\text{H}_2$ | $H_{\text{act}}(\text{H}_2\text{CO})$ | $0.5\text{H}_2 + \text{H}_2\text{CO}^* + \text{H}^* + \text{H}_2\text{O}$ $\rightarrow \text{TS5} + 0.5\text{H}_2 + \text{H}_2\text{O}$ |
| $H_{\text{act}}(\text{HCOOH})$ | $1.5 \text{H}_2 + \text{HCOOH}^* + \text{H}^*$ $\rightarrow \text{TS3} + 1.5 \text{H}_2$ | $H_{\text{act}}(\text{H}_3\text{CO})$ | $\text{CH}_3\text{O}^* + \text{H}^* + \text{H}_2\text{O}$ $\rightarrow \text{TS6} + \text{H}_2\text{O}$ |

The activation energy for $\text{CO}_2^{\delta-}$ hydrogenation, $H_{\text{act}}(\text{CO}_2^{\delta-})$, is 1.13 eV, 1.10 eV and 0.81 eV on the Pd (111), (100) and (110) surfaces, respectively. The observation that $H_{\text{act}}(\text{CO}_2^{\delta-})$ is lowest on the Pd (110) surface can be attributed to the additional space underneath the $\text{CO}_2^{\delta-}$ on the preferred long-bridge site, which facilitates the hydrogen atom binding to the carbon. The $H_{\text{act}}(\text{CO}_2^{\delta-})$ on the Pd (111) surface (1.13 eV) matches the work of Zhang *et al.* (0.85 eV), though differs somewhat from the results of Brix *et al.* (2.23 eV); we consider that this difference stems from the use of a physisorbed CO_2 geometry in their calculations, with a chemisorbed structure considered in our work and the calculations by Zhang *et al.*^{63,72}

$H_{\text{act}}(\text{HCOOH})$ is observed to follow the trend (100) > (111) > (110), i.e. different from the E_{surf} trend. The $H_{\text{act}}(\text{HCOOH})$ of 1.41 eV evaluated for the most commonly studied Pd (111) surface, is larger than 1.13 eV reported by Brix *et al.* Given that the adsorption energy of HCOOH on the Pd (111) surface is calculated as -0.58 eV, and desorption is considered as the reverse process, the high $H_{\text{act}}(\text{HCOOH})$ observed (1.41 eV) for the Pd (111) surface suggests that HCOOH is more likely to desorb than react further. The high activation barrier for HCOOH hydrogenation agrees with work by Huš *et al.* on Cu-based catalysts; however, formic acid is not amongst the product stream observed when using Pd catalysts experimentally, with CH_3OH , CO and trace to significant amounts of CH_4 reported.^{11,14,17,19,162} Thus, another intermediate, such as H_2COO , might be of importance in leading to the experimental products, as was determined for Cu-based catalysts.¹⁶² In our work, the $H_{\text{act}}(\text{HCOOH})$ on the Pd (110) surface is about 40 % lower than on Pd (111) and almost 45% lower than on the Pd (100). The reduction of

$H_{\text{act}}(\text{HCOOH})$ might stem from lower stability of the HCOOH, and reduced stability of the hydrogen atom on Pd (110), which translates into a more accessible transition state.

The activation enthalpy for dissociation of H_2COOH species, $H_{\text{act}}(\text{H}_2\text{COOH})$, is highest on the Pd (100) surface, where the H_2COOH intermediate is stabilised. Brix *et al.* reported a very high $H_{\text{act}}(\text{H}_2\text{COOH})$ of 2.01 eV on Pd (111), while we calculate $H_{\text{act}}(\text{H}_2\text{COOH})$ to be only 0.40 eV. The significant discrepancy of 1.61 eV for dissociation of H_2COOH on Pd (111) arises from a considerable difference in the transition state geometry, i.e., our transition state involves breaking of a single C-O bond, whereas both C-O bonds were broken to yield H_2C and two O in the transition state found by Brix *et al.*, with one of the C-O bonds subsequently reformed later along the minimum energy path. For hydrogenation of formaldehyde, $H_{\text{act}}(\text{H}_2\text{CO})$ is similarly low (0.67 – 0.74 eV) on the three surfaces; however, on the (111) surface, it is higher than H_{ads} of H_2CO (-0.58 eV), whilst on Pd (100) and (110) surfaces, H_2CO is stabilised more (-0.83 and -0.94 eV) than on Pd (111). The stronger H_{ads} on (100) and (110) surfaces means that H_2CO desorption is less likely, and reactivity favoured, whilst on the (111) surface desorption would be a competitive process. Desorption of H_2CO during CO_2 hydrogenation to methanol on Pd catalysts is a major concern in experiment, and thus the Pd (100) and (110) surfaces may be preferable in catalyst design.¹¹

In most hydrogenation steps examined on the three Pd surfaces, the reaction pathway favoured migration of the hydrogen atom towards the least stable on-top site before bonding to the intermediate. Therefore, the relative stability of the hydrogen adsorption sites, as shown in Section 3.3.1, has a major impact on the H_{act} for most hydrogenation reactions on the Pd (111), (100) and (110) surfaces. Reducing the difference in stability for hydrogen atoms on the possible surface sites might be an important factor in the design of catalysts for CO_2 hydrogenation to methanol, as it could lead to reduction of H_{act} for species reacting on a Pd-based catalyst.

A reaction profile based on the energy of initial, TS and final geometries, relative to the energy of isolated Pd (111), (100) and (110) surfaces and gas-phase reactants, is plotted in Figure 17, with each individual step balanced stoichiometrically by energies of gas-phase molecules.

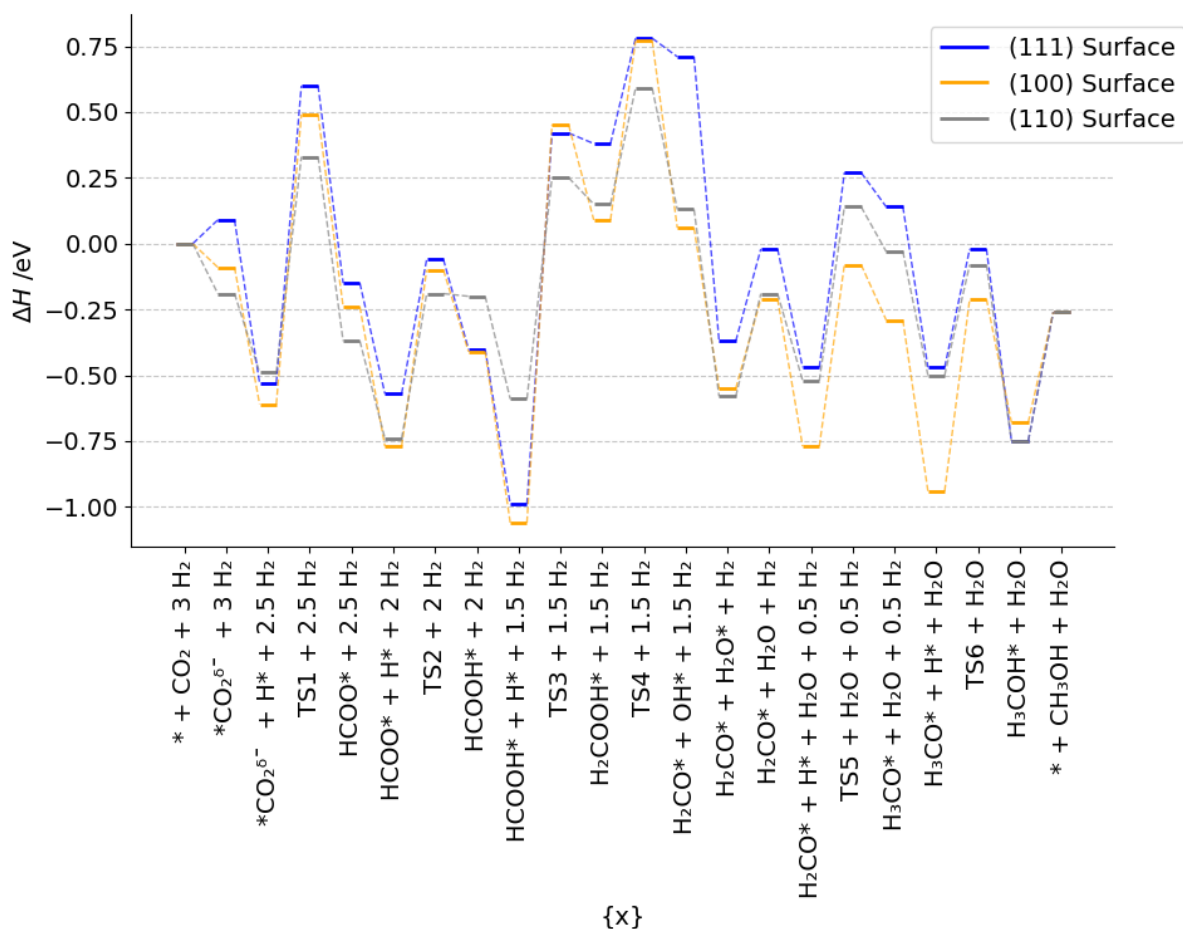


Figure 17. The ZPE-corrected energy profile of CO₂ hydrogenation to methanol, via the formate pathway, on Pd (111), (100), and (110) surfaces, plotted in blue, orange, and grey, respectively, relative to the energy of pristine surface and gas phase reactants.⁹¹ Energies of intermediate structures and transition state geometries have been stoichiometrically balanced with energies of gas phase reactants; * indicates surface bound species.

Based on total electronic energy, which is presented in Table 22 in the Appendix, for all the surfaces, the reaction energy for the conversion of CO₂ to methanol is exothermic (-1.05 eV) relative to gas phase reactants, which agrees with reaction energy (-1.17 eV) derived from atomization energies.^{11,132,188} The gas-phase reaction enthalpy presented above (-0.26 eV) is underestimated by 0.26 eV with respect to experimental values reported in literature,¹¹ and the magnitude of the error in gas-phase energies of molecules is typical for gradient corrected functionals, such as PBE.¹⁸⁹ The highest H_{act} in the CO₂ hydrogenation reaction across the Pd (100), (111) and (110) surfaces is $H_{act}(\text{HCOOH})$, with values of 1.51, 1.41, and 0.84 eV, respectively, which is therefore a likely rate determining step (RDS) for the reaction. However, in an experimental study by Aas *et al.* the decomposition of HCOOH on Pd (110) was shown

to require 0.42 eV, which is only 50% of formic acid hydrogenation, $E_{\text{act}}(\text{HCOOH})$, on Pd (110), and therefore much more likely.¹⁹⁰ An important feature of the reaction energy profile is that TS1 remains endothermic on all three surfaces, with respect to the gas phase reactants, which would inevitably influence the rate of the reaction. All transition states on Pd (110) remain either below net zero energy of the reaction or significantly lower than Pd (111) and Pd (100) when above, which indicates that Pd (110) is the most active among the surfaces investigated here. As highlighted in Section 3.1, the hydrogen atoms are stabilised strongly on the Pd (111), (100), and (110) surfaces; the binding energies of intermediates with a neighbouring hydrogen atom do not vary significantly from the sum of binding energies of the adsorbates calculated separately, which suggests that the presence of hydrogen neither stabilises nor destabilises the intermediates at the low $\frac{1}{9}$ ML coverage of hydrogen considered.⁹¹ However, presence of a hydrogen atom at the nearest neighbouring site to chemisorbed CO_2 was observed to result in CO_2 desorption during geometry optimisation, to form a linear physisorbed species, which may indicate a lower stability of chemisorbed CO_2 with increasing hydrogen ML coverage. Experimentally, the presence of H_2 appears to induce a larger CO_2 intake, but this phenomenon was linked to CO_2 dissociation.³⁶

3.3.5. Gibbs free energy analysis

Gibbs free energy changes (ΔG , eV) between the reaction steps a-v in Table 7 across Pd (111), (110) and (100) were calculated and are shown in Figure 18-19. The pressure (p) used was 1 atm (1013125 Pa), which was applied to gas components. The temperatures (T) considered were 0 K (*i.e.*, enthalpy), 300 K for ambient conditions, and 500 K as typical experimental conditions for CO_2 hydrogenation over Pd catalysts.¹⁹ A comparison of results for 500 K presented in Figure 21.

Table 7. Calculated reaction steps in CO₂ hydrogenation reaction via formate on Pd.

| | |
|--|--|
| a) $3\text{H}_2 + \text{CO}_2^*_{\text{phys}} \rightarrow \text{TS0} + 3\text{H}_2$ | b) $3\text{H}_2 + \text{TS0} \rightarrow \text{CO}_2^*_{\text{chem}} + 3\text{H}_2$ |
| c) $3\text{H}_2 + \text{CO}_2^*_{\text{chem}} \rightarrow \text{CO}_2^*_{\text{chem}} + \text{H}^* + 2.5\text{H}_2$ | d) $2.5\text{H}_2 + \text{H}^* + \text{CO}_2^*_{\text{chem}} \rightarrow \text{TS1} + 2.5\text{H}_2$ |
| e) $2.5\text{H}_2 + \text{TS1} \rightarrow \text{HCOO}^* + 2.5\text{H}_2$ | f) $2.5\text{H}_2 + \text{HCOO}^* \rightarrow \text{HCOO}^* + \text{H}^* + 2\text{H}_2$ |
| g) $2\text{H}_2 + \text{HCOO}^* + \text{H}^* \rightarrow \text{TS2} + \text{H}_2$ | h) $2\text{H}_2 + \text{TS2} \rightarrow \text{HCOOH}^* + 2\text{H}_2$ |
| i) $2\text{H}_2 + \text{HCOOH}^* \rightarrow \text{HCOOH}^* + \text{H}^* + 1.5\text{H}_2$ | j) $1.5\text{H}_2 + \text{HCOOH}^* + \text{H}^* \rightarrow \text{TS3} + 1.5\text{H}_2$ |
| k) $1.5\text{H}_2 + \text{TS3} \rightarrow \text{H}_2\text{COOH}^* + 1.5\text{H}_2$ | l) $1.5\text{H}_2 + \text{H}_2\text{COOH}^* \rightarrow \text{H}_2\text{COOH}^*_{\text{rotated}} + 1.5\text{H}_2$ |
| m) $1.5\text{H}_2 + \text{H}_2\text{COOH}^*_{\text{rotated}} \rightarrow \text{TS4} + 1.5\text{H}_2$ | n) $1.5\text{H}_2 + \text{TS4} \rightarrow \text{H}_2\text{CO}^* + \text{OH}^* + 1.5\text{H}_2$ |
| o) $1.5\text{H}_2 + \text{H}_2\text{CO}^* + \text{OH}^* \rightarrow \text{H}_2\text{CO}^* + \text{H}_2\text{O}^* + \text{H}_2$ | p) $\text{H}_2 + \text{H}_2\text{CO}^* + \text{H}_2\text{O}^* \rightarrow \text{H}_2\text{CO}^* + \text{H}_2 + \text{H}_2\text{O}$ |
| q) $\text{H}_2 + \text{H}_2\text{CO}^* + \text{H}_2\text{O} \rightarrow \text{H}_2\text{CO}^* + \text{H}^* + 0.5\text{H}_2 + \text{H}_2\text{O}$ | r) $0.5\text{H}_2 + \text{H}_2\text{CO}^* + \text{H}^* + \text{H}_2\text{O} \rightarrow \text{TS5} + 0.5\text{H}_2 + \text{H}_2\text{O}$ |
| s) $0.5\text{H}_2 + \text{TS5} + \text{H}_2\text{O} \rightarrow \text{CH}_3\text{O}^* + 0.5\text{H}_2 + \text{H}_2\text{O}$ | t) $\text{CH}_3\text{O}^* + 0.5\text{H}_2 + \text{H}_2\text{O} \rightarrow \text{CH}_3\text{O}^* + \text{H}^* + \text{H}_2\text{O}$ |
| u) $\text{CH}_3\text{O}^* + \text{H}^* + \text{H}_2\text{O} \rightarrow \text{TS6} + \text{H}_2\text{O}$ | v) $\text{H}_2\text{O} + \text{TS6} \rightarrow \text{CH}_3\text{OH}^* + \text{H}_2\text{O}$ |

On Pd (111) in Figure 18 as T increases, formation of species from respective TS structure shows more negative (favourable) ΔG for formation of H₂COOH (k), H₂CO* (n) and H₃CO* (s), and less negative for CO₂^{δ-} (b) and HCOOH* (h), while HCOO* (e) and CH₃OH* (v) are not significantly affected. On Pd (100) in Figure 19, formation of species from respective TS structure shows similar trends to Pd (111) with an increase of T , but formation of H₂CO* (n) and CH₃OH* (v) is increasingly more favourable also. On Pd (110), elevated T facilitates formation of CO₂^{δ-} (b), HCOO* (e), H₂COOH (k) and CH₃OH* (v), but formation of HCOOH* (h) shows a ΔG increase, while H₂CO (n) and H₃CO* (s) are not significantly affected. Overall, the changes are subtle and are most prominent for processes involving H adsorption, which becomes less favourable as T increases. The H₂O desorption is more favourable as T increases.

Large positive ΔG is observed for all reaction steps involving breaking of Pd-H bonds and attaching of the hydrogen to the adsorbates, *i.e.*, formation of TS1 (d), TS2 (g), TS3 (j), TS5(r) and TS6 (u), which indicates that the very strong Pd-H interaction at $\frac{1}{9}$ ML hydrogen coverage is impeding the reaction on Pd (111), (100) and (110) surfaces even at the first hydrogenation step to formate.

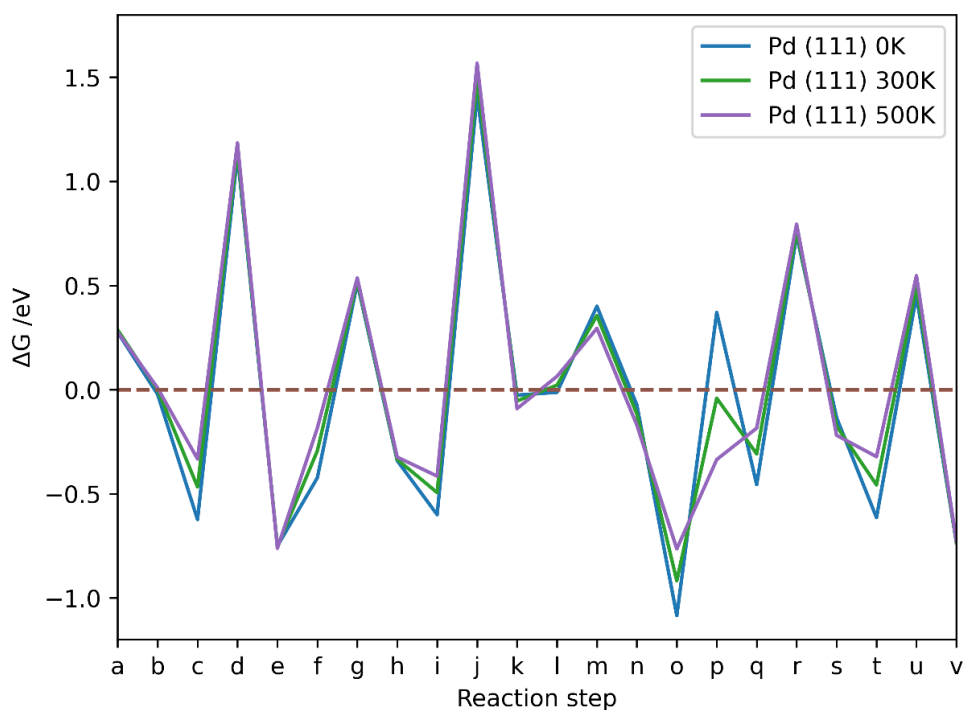


Figure 18. The Gibbs free energy changes between reaction steps in CO₂ hydrogenation reaction via formate on Pd (111) at p of 1 atm and T of 0, 300 and 500K; reaction steps a-v are explained in Table 7.

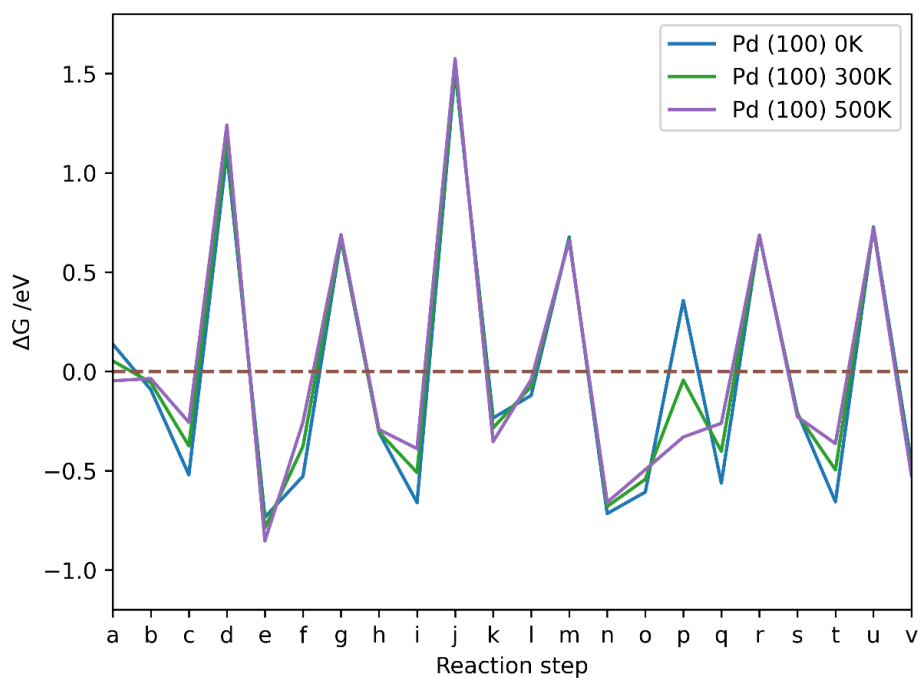


Figure 19. The Gibbs free energy changes between reaction steps in CO₂ hydrogenation reaction via formate on Pd (100) at p of 1 atm and T of 0, 300 and 500 K; reaction steps a-v are explained in Table 7.

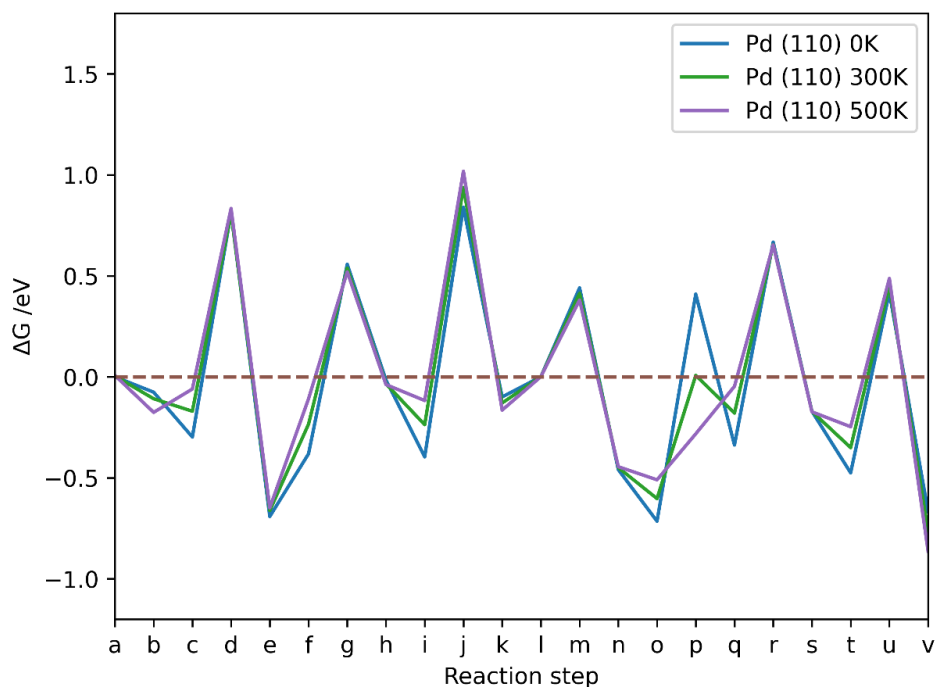


Figure 20. The Gibbs free energy changes between reaction steps in CO₂ hydrogenation reaction via formate on Pd (110) at p of 1 atm and T of 0, 300 and 500 K; reaction steps a-v are explained in Table 7.

On Pd (111) as T increases, formation of species from respective TS structure shows more negative (favourable) ΔG for formation of H_2COOH (k), H_2CO^* (n) and H_3CO^* (s), and less negative for $\text{CO}_2^{\delta-}$ (b) and HCOOH^* (h), while HCOO^* (e) and CH_3OH^* (v) are not significantly affected.

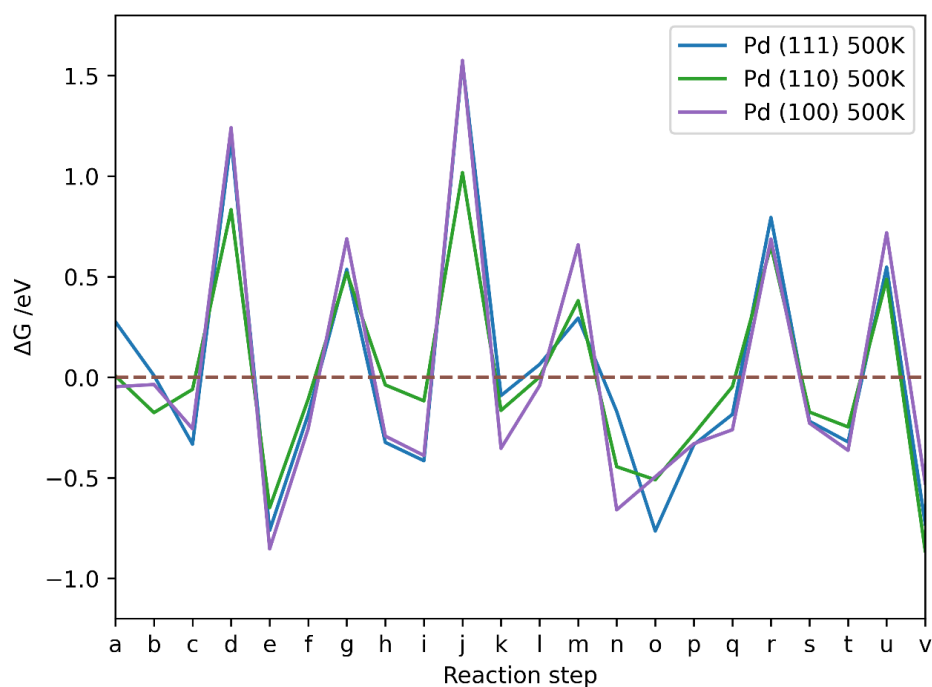


Figure 21. The Gibbs free energy changes between reaction steps in CO_2 hydrogenation reaction via formate on Pd (111), (100) and (110) at p of 1 atm and T of 500 K; reaction steps a-v are explained in Table 7.

The Pd (110) surface has the lowest ΔG values for TS formations, except for dissociation of H_2COOH (m), which is more favourable on the Pd (111) surface. The ΔG associated with TS formation are not strongly affected by T , which suggests that the flat low-index surfaces of Pd are not the likely source of methanol formation in supported metallic Pd catalysts. The conclusion is in agreement with experiment showing that pure unsupported Pd does not produce methanol at 463 K and atmospheric pressure.¹⁴ Moreover, changing T was shown to have a very limited effect on formation of TS structures in CO_2 hydrogenation on Pd catalysts at the studied temperature range of 0 to 500 K at 1 atm of pressure, implying that the kinetics of the reaction are dominated by the observed activation energy barriers and the $T\Delta S$ term does not significantly contribute to the ΔG . Adsorbing hydrogen on Pd surfaces is less

favourable at higher T , but formation of TS structures remains largely unaffected, thus rendering the process less feasible at high T ; however, elevated T is necessary to activate CO_2 on Pd (100), showing that low T CO_2 activation is key for CO_2 hydrogenation to be kinetically viable on the catalytic surfaces.

3.4. Summary and conclusions

Direct hydrogenation of CO_2 to methanol on transition metal catalysts is a promising approach for green energy storage, and to make the technology viable, new and more efficient catalysts need to be designed. Here, we have investigated the CO_2 hydrogenation reaction via the formate pathway on Pd (111), (100), and (110) surfaces.

Firstly, we investigated the stability of H on the Pd surfaces, showing that high coordination sites have the largest adsorption energy, and these high stability sites are interlinked via channels with low diffusion barriers; we also show for CO_2 adsorption that the preference of physical or chemical adsorption is dependent on the stability of the Pd surface facet. For the CO_2 hydrogenation reaction, the transition state for $\text{CO}_2^{\delta-}$ hydrogenation (TS1), to form formate, is endothermic, which will influence the overall rate of the reaction. $H_{\text{act}}(\text{HCOOH})$ is the highest energy step in the reaction profile on the Pd (111), (100), and (110) surfaces (TS3), and it can be considered as the likely rate determining step of this reaction on the surfaces examined. Based on thermodynamical analysis, the formation of TS1 has a high barrier that is not significantly influenced by reaction conditions, which indicates that flat surfaces of metallic Pd are unlikely to be the source of formate, and subsequently, methanol in product streams of reactions using supported monometallic Pd catalysts. Increased temperature was found to facilitate CO_2 chemisorption on Pd (100) and (110), but has an adverse effect on multiple other reaction steps, including the free energy of hydrogen adsorption. Novel Pd-based polymetallic nanoparticle catalysts for direct CO_2 hydrogenation to methanol could be designed to lower the barrier to initial CO_2 hydrogenation, TS1, and lower the barrier for formic acid hydrogenation (TS3) or facilitate a mechanism that proceeds via an alternative intermediate, such as H_2COO . Importantly, a Pd-based CO_2 hydrogenation catalyst should have lower Pd-H binding strength to facilitate the reaction.

Overall, we show that the most stable geometry of CO₂ adsorbed on Pd surface varies across (111), (100) and (110) facets and future studies should not be limited to consideration of the lowest energy (111) surface facet. Inclusion of zero-point energy has shown the Pd (100) surface to be unsuitable for CO₂ hydrogenation, highlighting that consideration of enthalpy is important for accuracy in computational catalysis. Low-index Pd surfaces are therefore unlikely to be the source of methanol formation on supported monometallic Pd catalysts, which indicates the potential importance of low-coordination metallic sites and metal-support interfacial sites. The H₂COO surface-bound intermediate could be alternatively considered as part of the formate pathway, and future work will entail detailed modelling of the initial hydrogenation to formate considered on multi-component Pd-based catalytic systems, which have been shown to manifest great selectivity to CH₃OH in direct CO₂ hydrogenation.^{19,50,71,191}

Chapter 4. Hydrogen coverage on low-index Pd surfaces

The following work was performed in collaboration with Prof David J. Willock (Cardiff Catalysis Institute, Cardiff, United Kingdom) and Dr Herzain Rivera-Arrieta (Fritz Haber Institute, Berlin, Germany) as part of the international Centre-to-Centre (C2C) collaboration project under the Max Planck Centre on the Fundamentals of Heterogeneous Catalysis (FUNCAT) banner.¹⁹²

Dr Rivera performed a significant portion of the geometry optimisations of Pd (111) structures. Prof Willock developed methods for the enumeration of significant structures and reduction of the dataset via symmetry considerations. The contents shown herein are constituents of a manuscript, which is currently in preparation for publication.

4.1. Introduction

Palladium metal is a widely used heterogeneous hydrogenation catalyst due to a high efficiency for hydrogen molecule dissociation at its surface, even under mild reaction conditions.¹⁹³ Indeed, Engel *et al.* have used molecular-beam experiments to show that adsorption of H₂ on Pd is barrierless at coverages up to $\theta = 0.9$ monolayer (ML), with θ , defined as the ratio of the number of H atoms adsorbed per unit area and the number of surface Pd atoms per unit surface area.¹⁹³ The spontaneous hydrogen dissociation reaction can be stoichiometrically represented as:



where “*” is used to represent an adsorption site on the Pd surface, H₂(g) is the gas-phase dihydrogen molecule and H(ads) is an adsorbed hydrogen atom.

Pd nanoparticle catalysts have been successfully used in industrially relevant chemical reactions, such as reverse water-gas shift and selective hydrogenation reactions.^{11,15,19,25,56,71} To reach optimal efficiency, the hydrogenation reaction must often be performed at high temperature and hydrogen gas pressure, which enhances the catalytic performance.¹¹ However, operating at such conditions can be detrimental to the catalyst’s long-term stability due to changes occurring in surface morphology of the material, resulting in inadvertent

alteration of the active sites that determine surface reactivity.²⁵ Since heterogeneous catalysis is a phenomenon occurring at phase boundary, an understanding of the effect of experimental conditions on the catalytic materials surface is key for the design of novel catalysts.

To understand the chemical properties of a catalytic material and optimise reaction conditions, surface phase diagrams can be constructed by carefully assessing the material structure under various temperature, pressure and chemical environments either experimentally or by simulation.^{54,194,195} Phase diagrams provide vital information on the material's structure and morphology under specified conditions, which is crucial for ensuring desired reactivity and preventing catalytic activity loss due to material degradation; in the context of hydrogenation catalysis, hydrogen adsorption itself can induce structural changes of the surface and bulk of transition metals, such as Pd, which are observable on a macroscale as a loss of mechanical stability under tensile stress, a phenomenon known as hydrogen embrittlement, with important implications in space technology.¹⁹⁶ Hydrogen-induced changes in a material's surface morphology are equally important for chemical reactivity of nanoparticle-based catalytic materials, as formation of surface metal hydrides is known to affect the intermetallic spacing and extent of alloying in binary transition metal catalysts which reflects upon the catalytic activity.^{197,198} To understand the chemical properties of a catalytic material and optimise reaction conditions, surface phase diagrams can be constructed by carefully assessing the material structure under various temperature, pressure and chemical environments either experimentally or by simulation.^{54,194,195} Phase diagrams provide vital information on the material's structure and morphology under specified conditions, which is crucial for ensuring desired reactivity and preventing catalytic activity loss due to material degradation; in the context of hydrogenation catalysis, hydrogen adsorption itself can induce structural changes of the surface and bulk of transition metals, such as Pd, which are observable on a macro scale as a loss of mechanical stability under tensile stress, a phenomenon known as hydrogen embrittlement, with important implications in space technology.¹⁹⁶ Hydrogen-induced changes in a material's surface morphology are equally important for chemical reactivity of nanoparticle-based catalytic materials, as formation of surface metal hydrides is known to affect the intermetallic spacing and extent of alloying in binary transition metal catalysts which reflects upon the catalytic activity.^{197,198}

In 1974, Conrad and Ertl reported that the work function of Pd single crystal surfaces increases with the partial pressure of hydrogen, for Pd (111) by up to 17 kJ mol^{-1} .³¹ The change of work function was then used as a direct measurement of the surface coverage (θ) with the highest value of the work function observed as taken to correspond to $\theta = 1 \text{ ML}$. Using a combination of temperature programmed desorption (TPD) under ultrahigh vacuum conditions and θ vs $p(\text{H}_2)$ isotherms in the range 10^{-9} to 10^{-5} torr, they were then able to deduce the adsorption enthalpy as a function of coverage using the Clausius-Clapeyron equation. Their desorption enthalpy value for H_2 on Pd (111) of $89 \pm 4 \text{ kJ mol}^{-1}$ was found to be practically independent of θ . In the same paper, low energy electron diffraction (LEED) was used to identify a (1×2) pattern for Pd (100) with H(ads), suggesting that the repeat pattern of H(ads) atoms is doubled in the surface b -direction with respect to the surface atom 2D lattice. No such changes were seen for Pd (111), although changes in LEED spot intensity were observed, consistent with the H(ads) atoms having a repeat lattice with the same geometry as the surface atoms. The suggestion that H atoms on the Pd(111) occupy threefold hollow sites was later confirmed by the photoelectron spectroscopy studies of Eberhardt *et al.*¹⁹⁹. Ever since, the work of Conrad and Ertl has been used as a benchmark study by modelling groups to compare the reliability of different DFT methods.

In recent years, computational models have been successfully used to aid experimental studies, and the methodology now provides a platform for sampling physical and chemical properties at a range of conditions *in silico*.^{195,200,201} Thus, careful modelling of the material surfaces can be used to understand the energy landscape, and surface coverage phase diagrams can be constructed to visualise the change of chemical environment on the surfaces of materials under reaction conditions.

4.1.1. Simulation of surface compositions of transition metal hydrides and oxides

In the case of palladium, which is a late 4d transition metal with a face-centred cubic lattice structure, interaction with gas adsorbates can alter the surface morphology. Experimental studies, complemented by *ab initio* density functional theory (DFT) calculations, were performed by Lundgren *et al.* who considered formation of oxide on Pd and Rh low-index

surfaces.⁵⁴ The structures observed in scanning tunnelling microscopy (STM) were used to build atomistic computer models that could then be used in a search for the most stable structures using DFT calculations, allowing comparison of stable surface oxide formations to the metal oxide bulk.⁵⁴ The candidate structures showing most favourable energy of oxygen adsorption were compared to the quantitative low-energy electron microscope and SXRD results, confirming the existence of surface oxides on late 4d transition metals, which is an important consideration for Pd- and Rh-based modern catalyst design.⁵⁴

As early as 1927, Linde and Borelius showed experimentally that palladium can absorb large volumes of hydrogen without significant changes in the lattice structure²⁰²; later, in 1937, Lacher followed with a theoretical formula for the solubility of hydrogen in palladium.²⁰³ The macroscale bulk studies gave rise to the study of hydrogen storage; however, the surface chemistry of late transition metals and hydrogen at nanoscale levels still remains challenging to establish and more insight is needed. Recent advances in computational chemistry now allow studies of the intricate H surface chemistry on transition metals.¹⁹⁵

4.1.2. Hydrogen on late transition metals

Low Miller index facets, especially the (111) and (100) surfaces of FCC metals, are often chosen for theoretical studies of surface chemistry of nanoparticle-based catalysts due to availability of comparable experimental data. Skúlason *et al.* show that, at coverages above 1 ML at a temperature of 300 K, the H atoms are most stable in an atop adsorption site in their study of H₂ interaction with Pt (111) in the context of the hydrogen evolution reaction.²⁰⁴ Work of Skúlason *et al.* matched the experimental findings of Källén *et al.*, showing that the difference in adsorption energy of H atom at the FCC and atop site is only 10 kJ mol⁻¹. Therefore, the second most favourable adsorption site is occupied once the FCC sites are saturated with hydrogen atoms.²⁰⁵ Moreover, Jerkiewicz observed in cyclic voltammetry experiments that the interaction of H atoms in neighbouring sites are weak (4 kJ mol⁻¹) on Pt.¹⁸⁴ Such information can be used in the design of modern catalytic processes; operating conditions can be tuned to ensure that an active site of the catalyst is enabled, *e.g.*, an exposed hydrogen atom on the atop position of Pt.

Johansson *et al.* performed experiments and atomistic DFT simulations in tandem to compare the adsorption of H₂ on Pd and on Pd hydride. They experimentally determined a greater sticking probability of H₂ on Pd hydride than on metallic Pd, by a factor of 1.4 at 140 °C; however, no apparent changes in the desorption energy were observed, suggesting that hydrogen is utilised more efficiently on Pd once the surface hydride had formed.²⁰⁶ Johansson *et al.* also performed DFT calculations using a GGA-RPBE exchange correlation functional on the (111) surfaces of Pd hydride and Pd metal at 1 ML coverage and they observed a stronger H atom binding energy on Pd than on Pd hydride.²⁰⁶ Additionally, in the case of the α -phase of surface Pd hydride, they found that representing the bulk as pure Pd without hydrogen atoms adsorbed into the metal provides a good approximation that aligns well with experiments conducted under ultra-high vacuum conditions, where hydrogen is also normally present in the bulk.²⁰⁶ In the simulation work of Johansson *et al.*, the Pd/H ratio in surface Pd hydride was assumed to be 0.75, based on the works of Teschner *et al.* and Nelin *et al.*, and the lattice constant of 4.15 Å matched the experimental expansion of 3.3% with respect to their calculated Pd lattice parameter of 4.02 Å (3.89 Å in experiment).^{207–209} Johansson *et al.* calculated the initial adsorption energy of -81 kJ mol_{H₂}⁻¹ on Pd (111) surface, with reasonable match to the experimentally derived value of -90 kJ mol_{H₂}⁻¹³¹, and found the adsorption energy to decrease at 1 ML coverage of hydrogen to -50.9 kJ per mol of H₂ in contrast to the findings of Conrad *et al.*^{31,206} The zero point energy (ZPE) for H adsorbed state was reported as 31.8 kJ mol⁻¹ per 2H* and had a small impact on hydrogen adsorption activation energy of up to 3.9 kJ mol_{H₂}⁻¹ and deemed insignificant with respect to the energies without the ZPE correction.

To minimise error, comparisons between theory and experiment should cover surface compositions that can strongly influence reactivity *in-situ*, which might differ from the catalyst structure *ex-situ*. For example, the level of hydrogen coverage and arrangement of H atoms will affect the surface active sites, hence an appropriate surface coverage should be used when calculating the potential energy surface for hydrogenation reactions. In this study, an *ab initio* thermodynamics approach is used to calculate effective adsorption energies of chemically adsorbed hydrogen to Pd (111) and Pd (100) surfaces at industrially relevant temperature and pressure as a function of hydrogen coverage. The work complements the

comprehensive surveys conducted in Chapter 3, which investigate the adsorption energy of low coverage hydrogen on Pd (111), (100), and (110) surfaces.

4.2. Computational Methods

4.2.1. Density functional theory (DFT) calculations

Full potential all-electron periodic DFT calculations have been performed with the Fritz-Haber Institute *ab initio* materials simulations (FHI-aims) package, coupled with the LibXC density functional library, and Pythonic Atomic Simulation Environment (ASE) used for management of calculated geometries.^{163,210,148} It has been previously shown that the meta-generalised gradient approximation (MGGA) semi-local Bayesian error estimation (mBEEF) exchange-correlation functional accurately represents both low and high Miller index surfaces of Cu, Pd and Zn metals, giving us confidence in the results generated using mBEEF throughout this work, while ensuring compatibility of future work on Pd-based alloy surfaces.^{132,171} The default convergence criteria within FHI-aims for self-consistent field (SCF) calculations were used, *i.e.* the changes between the current and previous SCF iterations in charge density, sum of eigenvalues and total energy were below $N \times 1.67 \times 10^{-5} e a_0^{-3}$, 10^{-3} eV and 10^{-6} eV, respectively, where N is the number of atoms in the model; and a spin-paired configuration was used due to the closed-shell electronic configuration of Pd ([Kr] 4d¹⁰), with scalar relativity included via the atomic zero order regular approximation (ZORA). The “light” basis set from the FHI-aims 2020 default setting and a k -grid density of minimum one k -point per $(0.018 \times 2\pi) \text{ \AA}^{-1}$ were used throughout.

4.2.2. Adsorption enthalpy

A single-sided slab model was used to investigate H adsorption. The pristine Pd (111) and (100) surfaces were obtained by cutting the bulk Pd structure using ASE functionality, where the optimal lattice parameter of 3.888 Å was previously obtained via an equation-of-state on the primitive cell.^{211,212} The surface slab consists of 5 atomic layers, which is a sufficient approximation for low-index Pd facets^{128,154,171}, and the top 4 and 3 layers are unconstrained

during geometry optimisation of the Pd (111) and Pd (100) surfaces, respectively, while the bottom layers remain constrained to mimic the bulk material at long distance.

As a result of the single-sided adsorption model, a dipole correction must be applied in the z-direction to eliminate any electrostatic effects that result from asymmetric slab relaxation. Geometry optimisations were performed using the Broyden–Fletcher Goldfarb–Shanno (BFGS) algorithm with a force convergence criterion of $1 \times 10^{-2} \text{ eV \AA}^{-1}$. To accelerate the geometry relaxations and save computational resources, part of the structures was computed taking advantage of the Hartree potential force correction functionality as implemented in FHI-aims.²¹³ The correction to the forces allows the loosening of the SCF threshold for the electron density accuracy without modifying the quality of the geometric and energetic results. For example, for the 1, 2, 4, and 6 hydrogen atom structures, the difference in the average adsorption energies ($\langle \Delta E_{ads} \rangle$) obtained with the FHI-aims defaults ($N \times 1.67 \times 10^{-5} \text{ e} a_0^{-3}$, where N is the number of atoms) and an electron density convergence criterion of $10^{-3} \text{ e} a_0^{-3}$ is less than 0.4 kJ mol^{-1} , as can be seen in Table 8. As will be later discussed in more detail, many symmetry-unique configurations are accessible at 293 K at 4-atom and 6-atom coverages, hence the higher chance of the error affecting the weighted average adsorption energy.

Table 8. Average adsorption energy with and without Hartree potential correction at different H coverages and 293 K. The addition of the Hartree potential force correction (column 3) provides a reliable way to save computational resources without affecting the rationalization of the results. All the energies are reported in kJ mol^{-1} .

| Number of H atoms | $\langle E_{ads} \rangle^{293K}$ in eV $N \times 1.67 \times 10^{-5} \text{ e} a_0^{-3}$ | $\langle E_{ads} \rangle^{293K}$ in eV $10^{-3} \text{ e} a_0^{-3}$ | $\Delta \langle E_{ads} \rangle^{293K}$ in eV |
|-------------------|---|--|---|
| 1 | -100.78 | -100.75 | -0.03 |
| 2 | -99.48 | -99.49 | 0.01 |
| 4 | -98.91 | -99.27 | 0.36 |
| 6 | -95.84 | -96.05 | 0.21 |

Vibration frequency calculations have been performed for geometry optimised structures using the ASE vibrations module employing the Frederiksen method, consistently with the method used in Chapter 3.¹⁸⁰ The large number of structures considered makes a full

vibrational analysis unfeasible; a reduction in computational cost was achieved by assuming that the large difference in atomic masses implies that only H(ads) atoms need be included in the calculation of frequencies for adsorbed state structures. By exclusion of the surface Pd atoms contributions, the number of degrees of freedom remains constant between the gas phase reference and adsorbed structure geometries, since only the hydrogen atoms are vibrating.

The adsorption energy, ΔE_{ads} , measures the change in energy per hydrogen molecule (hence the factor of 2 for two hydrogen atoms in a diatomic hydrogen molecule) on adsorption to the surface from the gas phase. An estimation of ΔE_{ads} is calculated by placing a number of H atoms on a periodic surface model and calculating the energy difference between the surface with H atoms adsorbed and the reference states of the clean surface and free H₂ molecules:

$$\Delta E_{\text{ads}} = 2 \left(E_{\text{surf-H}} - \left(\frac{n_{\text{H}}}{2} E_{\text{H}_2} + E_{\text{surf}} \right) \right) / n_{\text{H}} \quad (4.2)$$

where n_{H} is the number of H atoms on the Pd surface, $E_{\text{surf-H}}$, the calculated energy of the surface with H atoms adsorbed, E_{H_2} , is the calculated energy for an optimised gas-phase H₂ molecule, and E_{surf} is the calculated energy of the pristine Pd surface. The definition of ΔE_{ads} means that a negative value corresponds to exothermic adsorption. It is emphasised that this definition and all thermodynamic relations defined in this work are per H₂ molecule, with relevant literature values also converted to kJ per mol of H₂.

The calculated ΔE_{ads} is an estimate of one contribution to the change of internal energy that occurs when dissociative adsorption takes place. There are other contributions that ought to be included in order to make comparison with experiment. If frequency calculations have been carried out, the adsorption enthalpy, ΔH_{ads} , can also be defined as:

$$\Delta H_{\text{ads}} = \Delta E_{\text{ads}} + U_{\text{ads}}^{\text{sup}} - \frac{7}{2} k_{\text{B}} T - \frac{1}{2} h \nu_{\text{gas}} \quad (4.3)$$

Here, k_{B} , h and T are the Boltzmann constant, the Planck constant and the temperature, respectively. ν_{gas} is the vibrational frequency of the bond stretch in H₂(g), which is taken from the experimental value of 4401.21 cm⁻¹.²¹⁴ The final two terms in equation (3) are from the H₂(g) reference state: $5k_{\text{B}}T/2$ is from the equipartition of energy in the translation and rotational states, and a further $k_{\text{B}}T$ that replaces the pV term in the gas phase enthalpy; and

the final term represents the vibrational ZPE of $H_2(g)$, $\frac{1}{2}h\nu_{gas}$. U_{ads}^{sup} are supplementary terms that appear in the internal energy of the adsorbed state. These terms depend on the modelling approach used to treat the adsorbed state. Three approaches have been considered here: firstly, the lattice gas model treats H(ads) as a set of independent simple harmonic oscillators with three degrees of freedom per atom. In this case,

$$U_{ads}^{sup} = U_{ads}^{vib} = U_{ads}^{zpe} + U_{ads}^{exc}, \quad (4.4)$$

which shows that the supplementary contribution to the internal energy of the adsorbed state due to vibrations, U_{ads}^{vib} , is the sum of the ZPE of each mode, U_{ads}^{zpe} :

$$U_{ads}^{zpe} = \frac{2}{n_H} \sum_{j=1}^{n_H} \sum_{k=1}^3 \frac{1}{2} h\nu_{j,k} \quad (4.5)$$

and a term to estimate the thermal excitation of oscillators to higher states, U_{ads}^{exc} which can become important at higher temperatures:

$$U_{ads}^{exc} = \frac{2}{n_H} \sum_{j=1}^{n_H} \sum_{k=1}^3 \frac{h\nu_{j,k}}{\left(\exp\left(\frac{h\nu_{j,k}}{k_B T}\right) - 1\right)} \quad (4.6)$$

In these equations, $\nu_{j,k}$ is the vibrational frequency calculated for the k^{th} mode of H(ads) atom j . It is noted that vibrationally excited states need not be included for the gas phase as the stretching frequency is high.

The second approach that has been used is to assume that surface diffusion of adsorbates is sufficiently fast that the adsorbed state is effectively a two-dimensional ideal gas. In this case,

$$U_{ads}^{sup} = U_{ads}^{2Dgas} = 2k_B T + \frac{2}{n_H} \sum_{j=1}^{n_H} h\nu_{j,z} \left(\frac{1}{2} + \frac{1}{\left(\exp\left(\frac{h\nu_{j,z}}{k_B T}\right) - 1\right)} \right) \quad (4.7)$$

Now, the degrees of freedom for motion parallel to the surface each contribute $\frac{1}{2}k_B T$, while motion perpendicular to the surface is treated as a harmonic oscillator using $\nu_{j,z}$ to represent the vibrational frequency of the j^{th} atom in the surface normal direction.

The lattice gas model assumes that H(ads) atoms are localised at specific adsorption sites while the 2D ideal gas assumes free motion parallel to the surface plane. For intermediate cases, Sprowl *et al.*²¹⁵ proposed a hindered translator model of surface adsorption. In this

model, the adsorbate moves in a periodic potential so that at low temperatures the system behaves like a lattice gas but at higher temperatures translation around the surface becomes important. The periodic potential is approximated as sinusoidal with barriers between minima of ϵ_k , where the subscript “k” allows for different barriers in different surface directions, x or y, for example. The surfaces treated here are highly symmetric and so ϵ_k is assumed to be single valued but expressions are written in a general way. These hindered translator degrees of freedom contribute to the internal energy in a similar way to the lattice gas but with an additional term accounting for translation:

$$U_{\text{ads}}^{\text{sup}} = U_{\text{ads}}^{\text{hind}} = U_{\text{ads}}^{\text{zpe}} + U_{\text{ads}}^{\text{exc}} + 2k_B T \sum_{j=1}^{n_H} \sum_{k=x,y} \left(-\frac{1}{2} - \frac{h\nu_{j,k}}{(2k_B T + 16\epsilon_k)} + p_k \left(1 - \frac{I_1[p_k]}{I_0[p_k]} \right) \right) \quad (4.8)$$

Here $I_1[p_k]$ and $I_0[p_k]$ are the first and zero-order modified Bessel function of the first kind, with:

$$p_k = \frac{\epsilon_k}{2k_B T} \cdot \quad (4.9)$$

In this expression, the treatment of atomic motion perpendicular to the surface is again treated in the harmonic oscillator approximation through the use of equations (4.5) and (4.6) for $U_{\text{ads}}^{\text{zpe}}$ and $U_{\text{ads}}^{\text{exc}}$.

The vibrational states of a configuration will also contribute to the entropy of the adsorbed state. In the lattice gas model, all modes for surface vibrations are taken to be simple harmonic in form:

$$S_{\text{ads}}^{\text{sup}} = S_{\text{ads}}^{\text{harm}} = \frac{2k_B}{n_H} \sum_{j=1}^{n_H} \sum_{k=1}^3 \frac{h\nu_{j,k}}{k_B T \left(\exp\left(\frac{h\nu_{j,k}}{k_B T}\right) - 1 \right)} - \ln \left(1 - \exp\left(-\frac{h\nu_{j,k}}{k_B T}\right) \right) \quad (4.10)$$

In the 2D-gas model, the entropy is taken as 4/3 that of the values calculated for the standard equations for a 3-D ideal gas, as suggested by Campbell *et al.*²¹⁶ The use of 4/3 occurs as one mole of H₂(g) will generate two moles of H(ads) that are prevented from desorption in the z-direction, hence, H(ads) contribute 2/3 each. Finally, the hindered translator model changes

the entropy for the modes parallel to the surface to reflect the sinusoidal potential assumed in the x and y directions:²¹⁵

$$S_{\text{ads}}^{\text{sup}} = S_{\text{ads}}^{\text{harm}} - \frac{2k_B}{n_H} \sum_{j=1}^{n_H} \sum_{k=x,y} \frac{1}{2} + p_k \frac{I_1[p_k]}{I_0[p_k]} - \ln \left(-(2\pi p_k)^{\frac{1}{2}} I_0[p_k] \right), \quad (4.11)$$

where I_0 and I_1 are Bessel functions of the first kind in the 0th and 1st order, respectively.²¹⁷ These terms are correction factors for the harmonic result given in equation (4.11) and so $S_{\text{ads}}^{\text{harm}}$ is calculated using that equation for all modes.

As alluded to in Section 4.1, calculations regularly show differences in the adsorption energy between H(ads) atoms adsorbed at different surface sites. Herein, the possible arrangements or configurations of H(ads) atoms at a given surface coverage are considered, which allows thermodynamic averaging of ΔE_{ads} and ΔH_{ads} over all possible arrangements within a defined set of adsorption sites. In the next section, the use of symmetry to enumerate the unique H(ads) configurations at a particular surface coverage is covered in detail before discussion of the calculation of the adsorption entropy in the alternative models, which allows evaluation of the free energy of adsorption.

4.2.3. Enumeration of unique surface hydrogen arrangements

Palladium has a face centred cubic (FCC) structure. The close packed (111) surface has the lowest surface energy (1.32 J m^{-2}) of the pure metal and the higher energy (1.50 J m^{-2}) (100) typically forms the secondary faces of the supported metal nanoparticles used in hydrogenation catalysis.¹⁷¹ Dissociation of H_2 places H(ads) atoms on any of the adsorption sites on (111) and (100) surfaces shown in Figure 22. Table 9 compares data from previous studies on hydrogen adsorption to these surfaces. There is general agreement that on Pd (111) the most favourable adsorption sites are the three-fold hollow sites (Figure 22a, A and B) with the FCC hollow being 9 to 16 kJ mol^{-1} lower in energy than the HCP.^{128,182,183,218} The atop and bridge sites (Figure 22a, C and D, respectively) have much weaker adsorption energies for low coverage H(ads) atoms.^{31,128,183,218} On Pd (100), the hydrogen atom can be adsorbed in three distinct adsorption sites: 1E – hollow, 1F – bridge and 1G – atop, where the hollow site is considered as the most stable one.^{29,128,219,220}

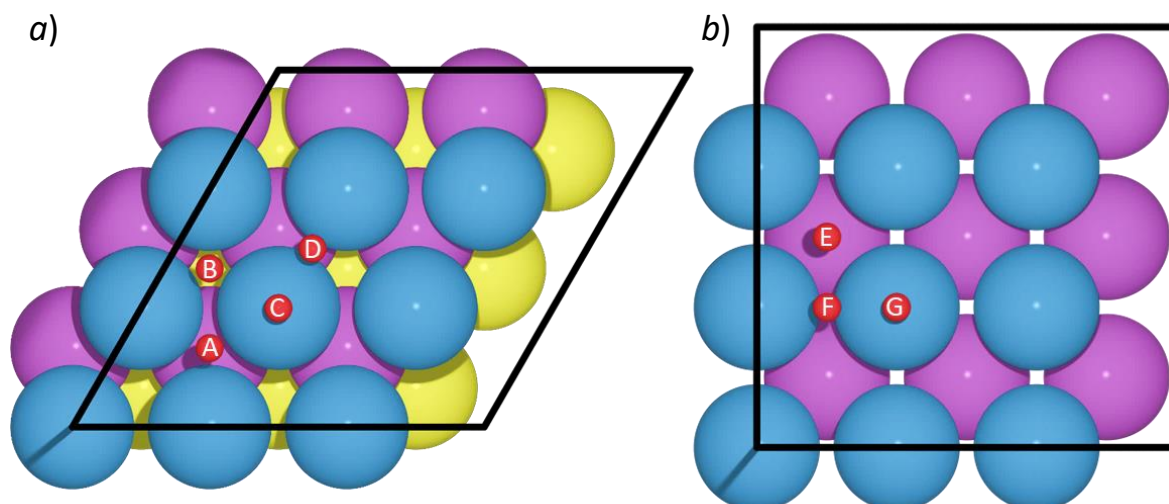


Figure 22. Top view of FCC a) (111) and b) (100) surfaces, with blue, purple and yellow spheres indicating the 1st, 2nd and 3rd atomic layers of the surface, respectively. Black lines are unit cell boundaries as viewed along the z-axis; red spheres mark the positions of the adsorption sites: the (111) surface: A) HCP, B) FCC, C) atop, D) bridge; and Pd (100) surface: E) hollow, F) bridge and G) atop.

Table 9. Pd FCC (111) and (100) hydrogen adsorption energies calculated using the outlined settings; literature and experiment are provided for comparison, with energies normalised to H_{ads} in units of kJ mol^{-1} , and the adsorption site description follows the naming convention summarised in Figure 22. Abbreviations of experimental methods are: TPD – temperature programmed desorption, LEED – low energy electron diffraction, MB – molecular beam.

| Method | Ref. | Year | Method | Surface (site) | Coverage (ML) | H_{ads} per $\text{H}_2 / \text{kJ mol}^{-1}$ |
|-----------------|-------------------------------------|------|-----------|----------------------------------|---------------|---|
| Expt: TPD, LEED | Conrad <i>et al.</i> ¹⁸¹ | 1974 | | 111 | < 0.5 | -87 |
| | | | | 100 | Low | -102 |
| Expt: MB | Engel <i>et al.</i> ¹⁹³ | 1979 | | 111 | Low | -89 |
| | | | | 111 | High | -77 |
| Expt: | Behm <i>et al.</i> ²⁹ | 1980 | TPD, LEED | 100 | < 0.9 | -102 |
| Theory | Hennig ²¹⁹ | 1993 | LMTO | 100 ($O_{h,sub}$) ^a | 1.0 | -68 |
| | | | | 100 (hollow +) | 2.0 | -76 |

| | | | | | | |
|--------|--|------|------------|------------------------|----------------|------|
| | | | | subsurface octahedral) | | |
| | | | | 100 (hollow) | 1.0 | -95 |
| Theory | Watson <i>et al.</i> ²¹⁸ | 2000 | PW91 | 111 (FCC) | Low | -97 |
| | | | | 111 (HCP) | Low | -87 |
| | | | | 111 (bridge) | Low | -72 |
| | | | | 111 (atop) | Low | -6 |
| Theory | Gladys <i>et al.</i> ²²⁰ | 2010 | PBE | 100 (hollow) | $\frac{9}{16}$ | -95 |
| | | | | 100 (hollow) | 0.25 p(2x2) | -100 |
| | | | | 100 (hollow) | 0.25 c(2x2) | -97 |
| Theory | ^b Herron <i>et al.</i> ¹⁸² | 2012 | PW91 | 111 (FCC) | Low | -114 |
| | | | | 111 (HCP) | Low | -108 |
| | | | | 111 (atop) | Low | 0 |
| Theory | Maark <i>et al.</i> ²²¹ | 2014 | RPBE | 111 (FCC) | 0.25 | -83 |
| Theory | Fonseca <i>et al.</i> ¹⁸³ | 2018 | PBE | 111 (FCC) | 0.25 | -127 |
| | | | | 111 (HCP) | 0.25 | -118 |
| | | | | 111 (bridge) | 0.25 | -96 |
| Theory | Sherada ²²² | 2019 | PBE | 111 | 0.125 | -116 |
| | | | RBPE | 111 | 0.125 | -85 |
| | | | optPBE-vdw | 111 | 0.125 | -106 |
| | | | BEEF-vdw | 111 | 0.125 | -70 |
| | | | MS2 | 111 | 0.125 | -135 |
| | | | SCAN | 111 | 0.125 | -139 |
| | | | SCAN+rVV10 | 111 | 0.125 | -141 |

| | | | | | | |
|--------|--------------------------------------|------|--------|--------------|---------------|------|
| | | | HSE06 | 111 | 0.125 | -140 |
| Theory | Kowalec <i>et al.</i> ¹²⁸ | 2022 | PBE+TS | 111 (FCC) | $\frac{1}{9}$ | -129 |
| | | | | 111 (atop) | $\frac{1}{9}$ | -23 |
| | | | | 100 (hollow) | $\frac{1}{9}$ | -104 |
| | | | | 100 (atop) | $\frac{1}{9}$ | -15 |
| Theory | This work | 2023 | mBEEF | 111 (FCC) | $\frac{1}{9}$ | -97 |
| | | | | 111 (HCP) | $\frac{1}{9}$ | -84 |
| | | | | 111 (atop) | $\frac{1}{9}$ | -18 |
| | | | | 100 (hollow) | $\frac{1}{9}$ | -84 |
| | | | | 100 (bridge) | $\frac{1}{9}$ | -81 |
| | | | | 100 (atop) | $\frac{1}{9}$ | -7 |

Notes: *a*) subsurface octahedral, *b*) RPBE values from the work of Herron *et al.* cannot be scaled as they are reported in H binding energy without H₂ energy for reference.¹⁸²

4.2.4. Adsorption on Pd (111)

The energies of adsorption (E_{ads}) of hydrogen on the Pd (111) surface for a single H atom in the $p(3\times 3)$ supercell are -103, -89 and -21 kJ mol⁻¹ on the FCC, HCP, and atop sites, respectively. After inclusion of the ZPE, the enthalpy of adsorption at 0 K ($H_{\text{ads}}(0)$) of hydrogen on the Pd (111) surface are weaker than E_{ads} at -97, -84 and -18 kJ mol⁻¹ on the FCC, HCP, and atop sites, respectively. The calculated values compare well with previous studies, summarised in Table 9. The low coordination atop site is the least stable, while no metastable structure for the bridge site was found at $\frac{1}{9}$ ML of hydrogen, presumably due to proximity of the high coordination favourable FCC and HCP hollow sites. Fonseca *et al.* had similar observations using the PW91 and RPBE exchange correlation functionals.¹⁸³

The FCC hollow site is most stable and the difference between the FCC and HCP hollow sites is only 14 kJ mol⁻¹ per H₂, hence the FCC and HCP hollow sites were predicted to be the dominant adsorption sites and were selected for subsequent surface enumeration. The supercell surface slab has been constructed from a cut of the crystallographic structure by making an $p(m \times n)$ repeating structure, which means that inherent translation symmetry exists within the supercell; for example, the Pd (111) slab $p(3 \times 3)$ supercell has 9 equivalent FCC hollow sites and 9 equivalent HCP hollow sites. The surface vectors are also equivalent for this surface, *i.e.*, a H atom adsorbed on the hollow sites of this surface has only 2 symmetry-inequivalent choices for the first atom (HCP or FCC).

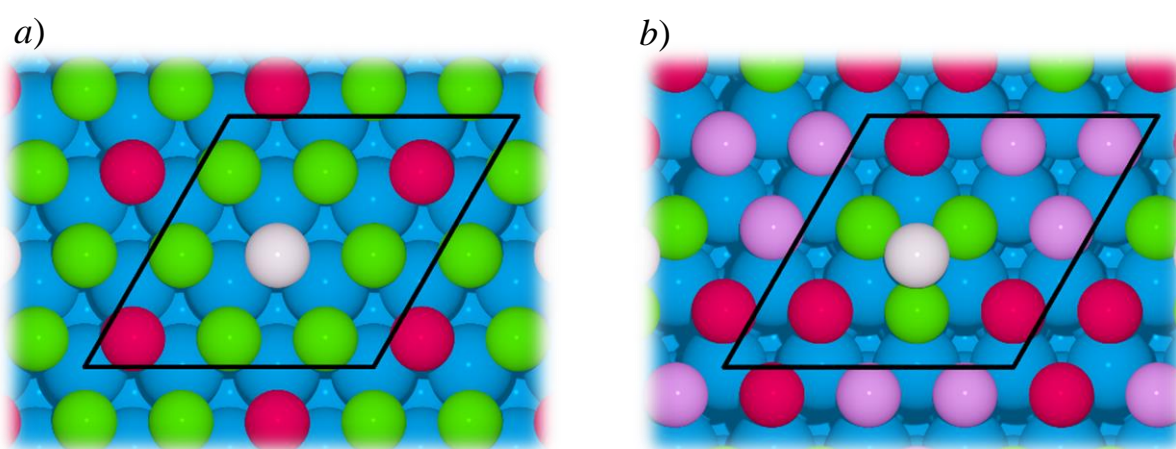


Figure 23. Effect of supercell symmetry on the placement of two H atoms on a Pd (111) $p(3 \times 3)$ slab surface in a) FCC sites and b) FCC site followed by a HCP site. The first H atom placed is coloured white with equivalent 1st, 2nd and 3rd neighbour placements shown in green, red and purple, respectively; Pd atoms are coloured blue; black lines represent the unit cell boundaries; atoms in neighbouring cells are included to aid visualisation of equivalent positions.

Considering the addition of a second H atom in the same type of hollow site, Figure 23a illustrates the two possible choices in the nearest and second-nearest neighbour sites of that sub-lattice, resulting in two FCC only and two HCP only symmetrically inequivalent configurations. The two H atoms could be positioned on different types of hollow sites, and there are thus 3 configurational options on a $p(3 \times 3)$ supercell surface (Figure 23b), bringing the total number of unique configurations to consider to 7. In contrast, considering all configurations without symmetry considerations would result in choosing configurations based on 18 possible sites. For two atoms this gives ${}^{18}C_2 = 153$ possible configurations. Table 10 provides a detailed breakdown of the resulting number of configurations, totalling

262,143, obtained without the use of symmetry, within coverages ranging from $\frac{1}{9}$ to 2 ML. Additionally, the table also includes the count of configurations after removing symmetry equivalent arrangements, which amounts to 2,895 configurations. To identify distinct configurations and document the corresponding degeneracy values for H(ads) atoms at a specific coverage, arrangements are created based on binary number representations of site occupancies. Upon generating each configuration, all distances between pairs of H(ads) atoms are computed and logged. The lists of inter-pair distances are then cross-referenced with previously generated configurations. In the event of a match in the distance lists, the degeneracy for the corresponding configuration is incremented, obviating the need for further action on the structure. Conversely, if no match is found, the configuration is appended to the unique list and subsequently optimised to determine the adsorption energy.

Table 10. Enumeration of possible adsorption patterns on a $p(3 \times 3)$ Pd (111) surface with and without symmetry consideration, and the number of unique metastable configurations found after relaxation for each calculated hydrogen coverage.

| Number of H atoms on a $p(3 \times 3)$ Pd (111) supercell surface | Number of configurations in full enumeration | Number of symmetry-inequivalent configurations |
|---|--|--|
| 1 | 18 | 2 |
| 2 | 153 | 7 |
| 3 | 816 | 24 |
| 4 | 3060 | 69 |
| 5 | 8568 | 144 |
| 6 | 18564 | 212 |
| 7 | 31824 | 356 |
| 8 | 43758 | 435 |
| 9 | 48620 | 396 |
| 10 | 43758 | 435 |
| 11 | 31824 | 356 |
| 12 | 18564 | 212 |
| 13 | 8568 | 144 |
| 14 | 3060 | 69 |
| 15 | 816 | 24 |

| | | |
|--------------|---------------|-------------|
| 16 | 153 | 7 |
| 17 | 18 | 2 |
| 18 | 1 | 1 |
| Total | 262143 | 2895 |

4.2.5. Adsorption on Pd (100)

The E_{ads} of the hydrogen atom on the Pd (100) $p(3\times 3)$ supercell surface slab is -64, -86, and -7 kJ mol⁻¹ on the hollow, bridge and atop sites, respectively. The results differ from previous studies^{128,223} where the hollow site is reported as more stable than the bridge; however, after inclusion of the ZPE, H_{ads} of hydrogen on the Pd (100) surface was calculated to be -84, -81 and -9 kJ mol⁻¹ on the hollow, bridge and atop sites, respectively, upholding the trend previously calculated using PBE+TS and ZPE corrections presented in Chapter 3. The H_{ads} values compare well with previous work, though calculations with the mBEEF functional give a value for H_{ads} on Pd (100) that is lower by 18 kJ mol⁻¹ with respect to experiment. Similar differences can be observed between the H_{ads} of H₂ on Pd (111) calculated using other meta-GGA functionals^{221,222}, while calculations using the GGA functionals tend overestimate the strength of hydrogen interaction with Pd with respect to experiment.^{128,183,222}

The $\frac{1}{9}$ ML hydrogen atom adsorption calculations showed that the hollow and bridge sites have high stability and so were included in the enumeration of possible arrangements. There are 9 hollow and 18 bridge sites in the supercell, leading to a much larger number of possible configurations than obtained for Pd (111), even when symmetry is considered. The total number of configurations for coverages from 1 to 7 H atoms (up to $\frac{7}{9}$ ML), without symmetry taken into account, is 1,285,623, while the inclusion of symmetry lowers this to 10,155 as shown in Table 11. Even so, to make the number of calculations tractable for coverages up to 9 atoms (1 ML), focus must be on the H atom arrangements that significantly contribute to the adsorption free energy. At the higher coverages on Pd (111), H atoms in neighbouring adsorption sites often were either forced sub-surface, or combined with neighbours to form H₂(g) on optimisation; on the Pd (100) surface the minimum inter-site distance for

neighbouring sites (bridge-hollow = 1.52 Å) is smaller than on Pd (111) (FCC-HCP = 1.60 Å) and so a constraint was imposed on acceptable initial configurations such that no H-H distance should be less than 2.0 Å, which also eliminates placing H atoms in neighbouring bridge sites (bridge-bridge distance is 1.94 Å). Thereby, the number of structures to consider for coverages between $\frac{1}{9}$ and 1 ML was reduced to 1,393 symmetry unique configurations.

Table 11. Enumeration of possible configurations of H atoms on a $p(3 \times 3)$ Pd (100) supercell surface with and without symmetry considerations at coverages between $\frac{1}{9}$ and $\frac{7}{9}$ ML.

| Number of H atoms on a $p(3 \times 3)$ Pd (100) supercell surface | Number of configurations in full enumeration | Number of symmetry-inequivalent configurations |
|---|--|--|
| 1 | 27 | 2 |
| 2 | 351 | 11 |
| 3 | 2925 | 55 |
| 4 | 17550 | 227 |
| 5 | 80730 | 857 |
| 6 | 296010 | 2456 |
| 7 | 888030 | 6547 |
| Total | 1,285,623 | 10,155 |

4.2.6. Vibrations and Thermodynamics

The calculation of the free energy of adsorption from electronic structure calculation energies has been discussed in detail by Rogal and Reuter.²²⁴ Applying their approach to a surface with a particular coverage of n_H hydrogen atoms under experimental conditions of hydrogen partial pressure, p and temperature T , starts with an expression for the free energy of adsorption, $\Delta G_{\text{ads}}(T, p)$, per unit surface area:

$$\Delta G_{\text{ads}}(T, p) = \frac{1}{A} \left(G(T, p, n_H) - G(T, p, 0) - \frac{n_H}{2} \mu_{H_2}(T, p) \right), \quad (4.12)$$

where $G(T, p, n_H)$ is the free energy for the surface with n_H H(ads) atoms present, $G(T, p, 0)$ is the free energy for the clean surface and A is the area of the simulation cell. The gas phase chemical potential per H_2 molecule, $\mu_{H_2}(T, p)$, is simply the absolute free energy per H_2 molecule for the gas phase, which can be obtained from standard thermodynamic relations for indistinguishable molecules:

$$\mu_{H_2}(T, p) = E_{H_2} + \frac{1}{2}hc\nu_{H_2} - \frac{1}{N} \left[k_B T \ln \left(\frac{(q_t q_R q_v q_e)^N}{N!} \right) - pV \right] + k_B T \ln \left(\frac{p}{p^\ominus} \right), \quad (4.13)$$

where, E_{H_2} is the electronic ground state energy for a H_2 molecule using the same electronic structure method as the surface calculations and the second term is the molecular zero-point energy. V is the volume of the gas and q_t , q_R , q_v and q_e are the translational, rotational, vibrational and electronic molecular partition functions for $H_2(g)$, respectively, and N the number of molecules. For the partition functions relating to molecular motion, standard equations are employed and assumed for the ideal gas and harmonic approximations:

$$q_t = V \left(\frac{2\pi m k_B T}{h^2} \right)^{\frac{3}{2}}, \quad q_R = \frac{k_B T}{2hcB}, \quad q_v = \left(1 - \exp \left(-\frac{hc\nu_{H_2}}{k_B T} \right) \right)^{-1} \quad (4.14)$$

In which m is the molecular mass ($m_{H_2} = 2.016$ amu). For B , the experimental rotational constant ($B_{H_2} = 60.86 \text{ cm}^{-1}$)⁶ is used, and for ν_{H_2} , the experimentally derived wavenumber for the diatomic stretching vibration, 4401.21 cm^{-1} is used.²¹⁴ The factor of 2 in the denominator of q_R is the symmetry factor for a diatomic molecule, and the physical constants h and c are the Planck constant and speed of light, respectively. The $H_2(g)$ electronic ground state is a singlet and so $q_e = 1$, however, the value should be adjusted accordingly for non-hydrogen.

Making use of the ideal gas equation and Stirling's approximation, Equation (4.14) reduces to:

$$\mu_{H_2}(T, p) = E_{H_2} + \frac{1}{2}hc\nu_{H_2} + \Delta\mu_{H_2}(T, p^\ominus) + k_B T \ln \left(\frac{p}{p^\ominus} \right), \quad (4.15)$$

with,

$$\Delta\mu_{H_2}(T, p^\ominus) = -k_B T \left[\ln \left(\left(\frac{2\pi m k_B T}{h^2} \right)^{\frac{3}{2}} \frac{(k_B T)^{\frac{5}{2}}}{p^\ominus} \right) + \ln(q_R) - \ln(q_v) \right]. \quad (4.16)$$

The standard pressure, p^\ominus , is taken as 1 atm. The free energy of the clean surface, $G(T, p, 0)$ is taken to be the calculated DFT energy for the Pd slab, E_{Pd} . The free energy contribution due to motion of Pd atoms is assumed to be unaffected by H₂ adsorption and so can be set to zero.

In terms of the quantities defined earlier, where the adsorption energy per H₂ molecule is used, expression (12) can be rewritten as:

$$\Delta G_{\text{ads}}(T, p) = \frac{n_H}{2A} \left(\langle \Delta H_{\text{abs}} \rangle - (\langle S_{\text{ads}}^{\text{sup}} \rangle + \langle S_{\text{ads}}^{\text{conf}} \rangle) T + S_{\text{H}_2}(T, p) \right) \quad (4.17)$$

where $S_{\text{H}_2}(T, p)$ is the absolute entropy for gas phase H₂ taken from thermodynamic relations.

The free energy for the surface at a particular hydrogen coverage, $G(T, p, n_H)$ requires consideration of the configurational entropy of the H atoms in the available low energy surface sites and the enthalpy and entropy contributions of the H atoms on the surface due to their vibrational states. When more than a single configuration exists for any given H coverage, a temperature dependant configurational partition function can be defined for the set of structures, $q_c(T)$:

$$q_c(T) = \sum_{i=1}^{N_c} g_i \exp \left(- \frac{\Delta H_{\text{ads},i} - \Delta H_{\text{ads},\text{min}}}{k_B T} \right) \quad (4.18)$$

where $\Delta H_{\text{ads},i}$ is the adsorption enthalpy for configuration i , and $\Delta H_{\text{ads},\text{min}}$ is the minimum adsorption enthalpy found for any configuration in the set. The summation is over all symmetry unique configurations, N_c , and the degeneracy level, g_i , is taken to be the number of symmetry related configurations of type i . Once $q_c(T)$ is calculated, the weight, $w_i(T)$, for the importance of any configuration in calculating thermodynamic averages will be:

$$w_i(T) = \frac{g_i}{q_c(T)} \exp \left(- \frac{\Delta H_{\text{ads},i} - \Delta H_{\text{ads},\text{min}}}{k_B T} \right) \quad (4.19)$$

The configuration average for the adsorption enthalpy then becomes:

$$\langle \Delta H_{\text{ads}} \rangle = \sum_{i=1}^{N_c} w_i(T) \Delta H_{\text{ads},i} \quad (4.20)$$

The use of configuration weights, $w_i(T)$, in this way is akin to the Monte Carlo approach developed by Wang and Landau^{225, 226} in which the density of states for configurations is built

over the course of Monte Carlo sampling calculations. In this work, the definition of the supercell and adsorption site allows for the calculation of the density of states of energy levels of the adsorbate directly based on reducing the number of calculations required using symmetry arguments.

4.3. Results and discussion

4.3.1. Adsorption on Pd (111)

The $p(3 \times 3)$ Pd (111) structures have been geometrically classified by comparing the optimised configurations with the given input structures. Relaxation of configurations to different arrangements implies small barriers for H diffusion, as seen for low coverage calculations.¹²⁸ The analysis procedure for confirming structure stability was applied to all calculated hydrogen coverages on the $p(3 \times 3)$ Pd (111) surface, *i.e.*, 1-, 2-, 4-, 6-, 8-, 9-, 10-, 13-, 14- and 18-atom arrangements for a total of 1770 configurations with symmetry considerations, as was shown in Table 10.

The for each optimised structure in the $\frac{8}{9}$ ML coverage are shown in Figure 24, with visualised common structures resulting from optimised unique arrangements. The $\frac{8}{9}$ ML coverage has the most symmetry inequivalent initial configurations, as was shown in Table 10, but after relaxation 67 unique final structures were observed. To illustrate the dataset reduction, the configurations have been ranked by calculated ΔE_{ads} , grouped into sets of structures sharing common traits and within 20 kJ mol⁻¹ of the lowest energy configuration. The resulting energies were shown in Figure 24.

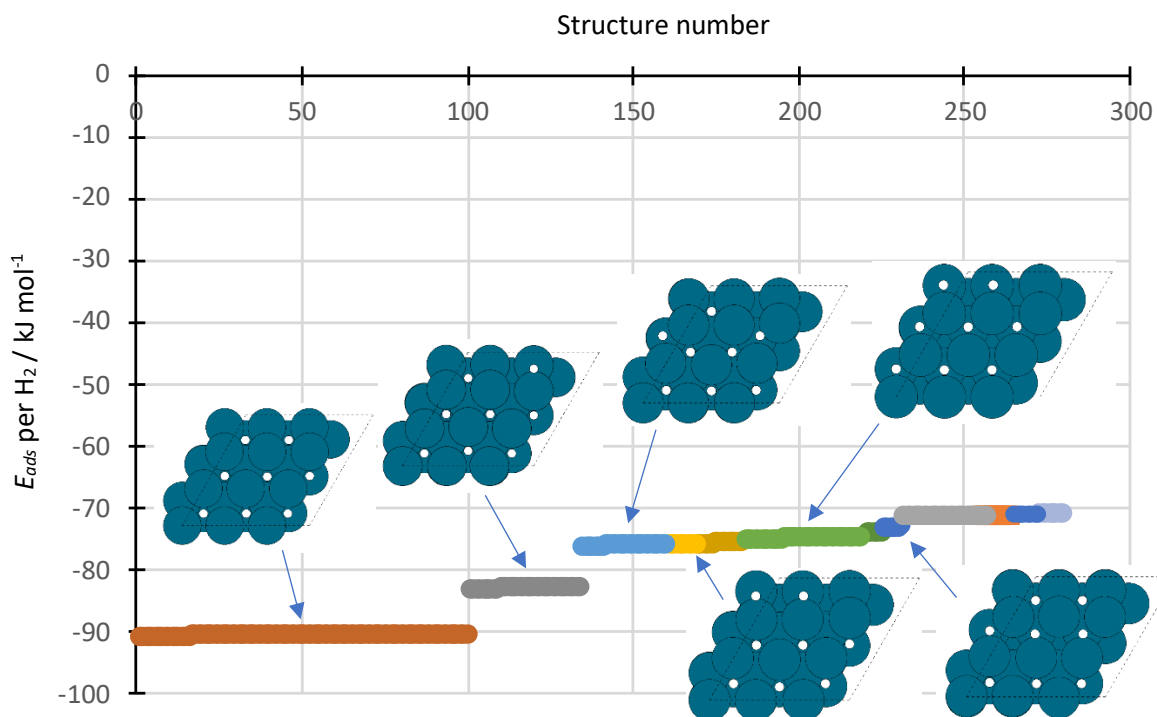


Figure 24. E_{ads} per H_2 for structures enumerated in the $\frac{8}{9}$ ML coverage on Pd (111) surface; the coloured lines represent sets of structures which relaxed to a common structure; blue and white circles correspond to Pd and H atoms of the $\frac{8}{9}$ ML hydrogen covered $p(3 \times 3)$ Pd (111) surface; representative examples of structures with common features are also provided for relevant coloured lines.

The total number of metastable structures found after pattern matching was 336, *i.e.*, 5.3% of the symmetry inequivalent configurations and only 0.20% of possible arrangements enumerated through simple exhaustion.

The most stable configuration has all H atoms in FCC sites and is obtained from 100 of the configuration optimisations. The average energy across these is -96 kJ mol^{-1} per H_2 molecule, with a standard deviation of only 0.04 kJ mol^{-1} , and is very close (4 kJ mol^{-1}) to that obtained for a single H atom in the same unit cell, confirming that the interaction between H atoms in all FCC configuration is very low.

The second most favourable configuration, shown in Figure 25, has 7 FCC H atoms and 1 H atom at an HCP site. The average adsorption energy for this set of structures is -89 kJ mol^{-1} per H_2 molecule, which is 10 kJ mol^{-1} higher than if the H atoms were adsorbed independently at the sites. Inspection of the geometries shows that, in these configurations, the H atoms

occupying neighbouring HCP and FCC sites are displaced from the site centres to increase the H-H separation for the pair, as discussed further below.

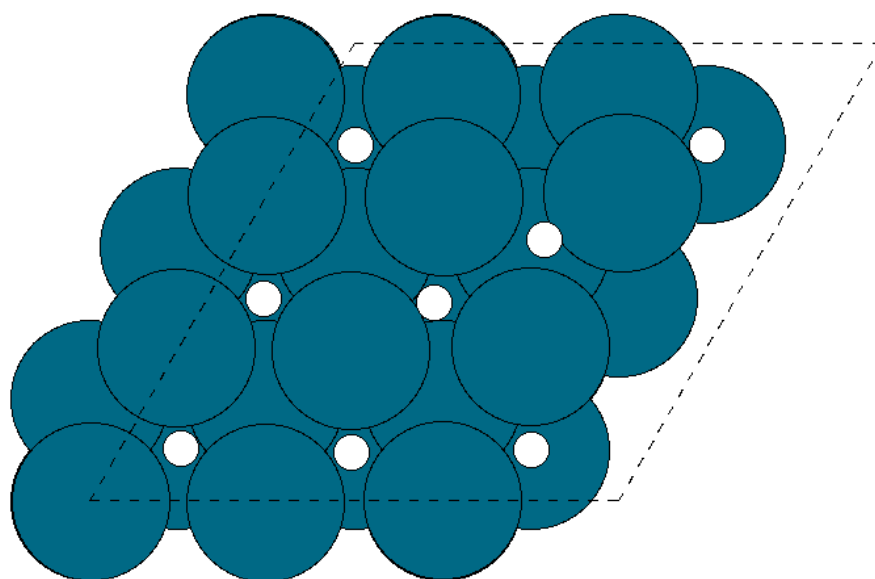


Figure 25. Second most favourable configuration of H atoms (white circles) on the Pd (111) surface (blue circles) at $\frac{8}{9}$ ML coverage of hydrogen, with 7 atoms in the FCC site and one atom in the HCP site; the view is in the xy-plane and dotted lines represent the unit cell boundaries.

The next three groups of structures contain 6 FCC H atoms and 2 HCP, with a corresponding increase in the average energy of 7 kJ mol^{-1} per H_2 ; the structures differ in the relative positions of the two HCP atoms and the FCC adsorbates, which has only a minor influence on the calculated adsorption energy.

The following structure (Figure 24, green) has all the H atoms in HCP sites with a calculated $\langle E_{\text{ads}} \rangle$ of -81 kJ mol^{-1} per H_2 . The value is only 6 kJ mol^{-1} above that for a single atom in the same site and a similar difference is seen for the FCC hollow sites. At between 3 and 7 HCP H atoms, the unfavourable neighbouring interactions in mixed FCC/HCP configurations are more significant than the difference in adsorption energies between the two types of sites.

Overall, the calculated $\langle E_{\text{ads}} \rangle$ of H_2 is only very weakly affected by coverage up to 1 ML, as can be seen in Figure 26. Temperature most strongly affects coverages between $\frac{4}{9}$ and $\frac{6}{9}$ ML where there are many metastable configurations accessible at elevated temperatures. The effect is most pronounced for the 6-atom configurations (0.67 ML), where the $\langle E_{\text{ads}} \rangle$ at 293 K is 6.1 kJ

mol⁻¹ stronger than at 523 K. Above 1 ML, the magnitude of $\langle E_{\text{ads}} \rangle$ decreases and $\langle E_{\text{ads}} \rangle$ becomes endothermic at 15 H atoms (1.67 ML).

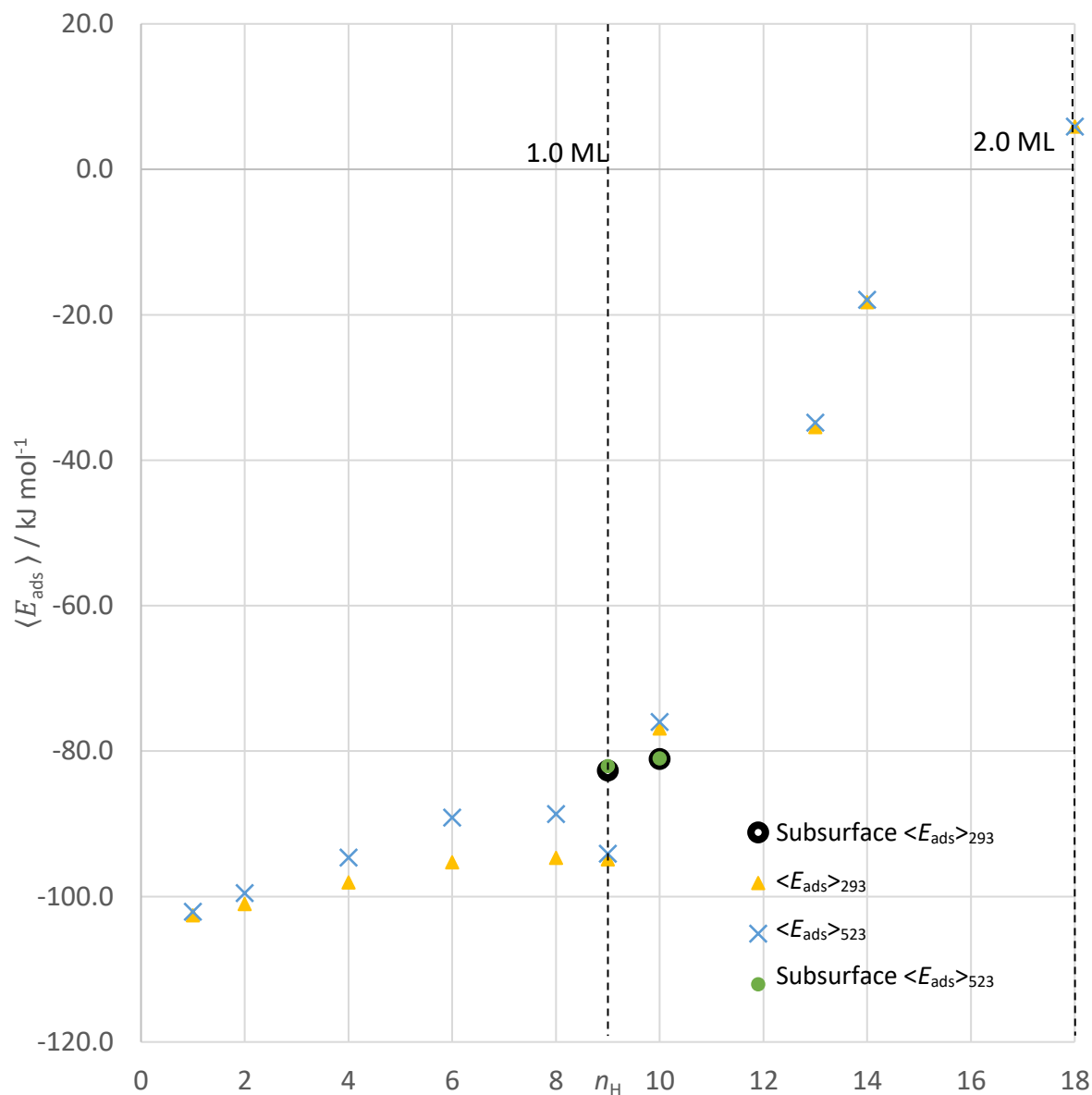


Figure 26. The average adsorption energy ($\langle E_{\text{ads}} \rangle$) per H₂ molecule on the Pd (111) surface at 293 K (triangles) and at 523 K (crosses). $\langle E_{\text{ads}} \rangle$ for configurations with a single sub-surface H atom included at 293 K and 523 K is shown by open and green circles, respectively. Dotted lines show the position of 1 ML and 2 ML coverage levels for this $p(3 \times 3)$ supercell.

Once the sharp increase in $\langle E_{\text{ads}} \rangle$ between the 9-atom and 10-atom configurations was observed, the subsurface hydrogen adsorption sites were considered these coverages by placing a hydrogen atom in symmetry inequivalent sites, starting from 8- and 9-atom

configurations. In all cases, the starting configurations were fully decorated with hydrogen located in the most stable FCC adsorption site. The procedure resulted in 8 and 3 unique configurations for the 1 and $\frac{10}{9}$ ML structures, respectively. The effect of the full enumeration was also studied for the 1 ML coverage under the assumption that the subsurface hydrogen has only a limited interaction with the surface atoms, hence limiting the number of configurations to one per atom site per metastable $\frac{8}{9}$ ML structure, *i.e.*, 201 structures. The comparison of resulting $\langle E_{\text{ads}} \rangle$ and $\langle H_{\text{ads}} \rangle$ at 293 K and 523 K is presented in Table 12. Consideration of only the lowest structure results in overestimation of $\langle E_{\text{ads}} \rangle$ at 293 K and both $\langle H_{\text{ads}} \rangle_{293}$ and $\langle H_{\text{ads}} \rangle_{523}$ by around 2-3 kJ mol⁻¹, which does not alter the gap between surface and subsurface adsorption significantly enough to change conclusions.

Table 12. Comparison of $\langle E_{\text{ads}} \rangle$ and $\langle H_{\text{ads}} \rangle$ at temperature of 293 K and 523 K for 1 ML of hydrogen, with 8 atoms on the surface and 9th atom in a subsurface site: full enumeration and results for the lowest structure from the $\frac{8}{9}$ ML dataset used as starting point.

| 1 ML | $\langle E_{\text{ads}} \rangle_{293}$ | $\langle E_{\text{ads}} \rangle_{523}$ | $\langle H_{\text{ads}} \rangle_{293}$ | $\langle H_{\text{ads}} \rangle_{523}$ |
|-----------------------|--|--|--|--|
| Enumerated | -82.7 | -82.1 | -78.2 | -77.8 |
| From lowest structure | -85.4 | -82.3 | -80.1 | -79.9 |

Once the surface hydrogen coverage reaches $\frac{8}{9}$ ML, putting the next hydrogen atom subsurface has an energy penalty of 12 kJ mol⁻¹; however, with the 1 ML hydrogen present at the surface, placing the next atom of hydrogen subsurface is more favourable than $\frac{10}{9}$ ML by 5 kJ mol⁻¹. Thus, once a full monolayer of hydrogen saturation is reached, the hydrogen is predicted to start occupying the subsurface octahedral holes in preference over the surface adsorption sites.

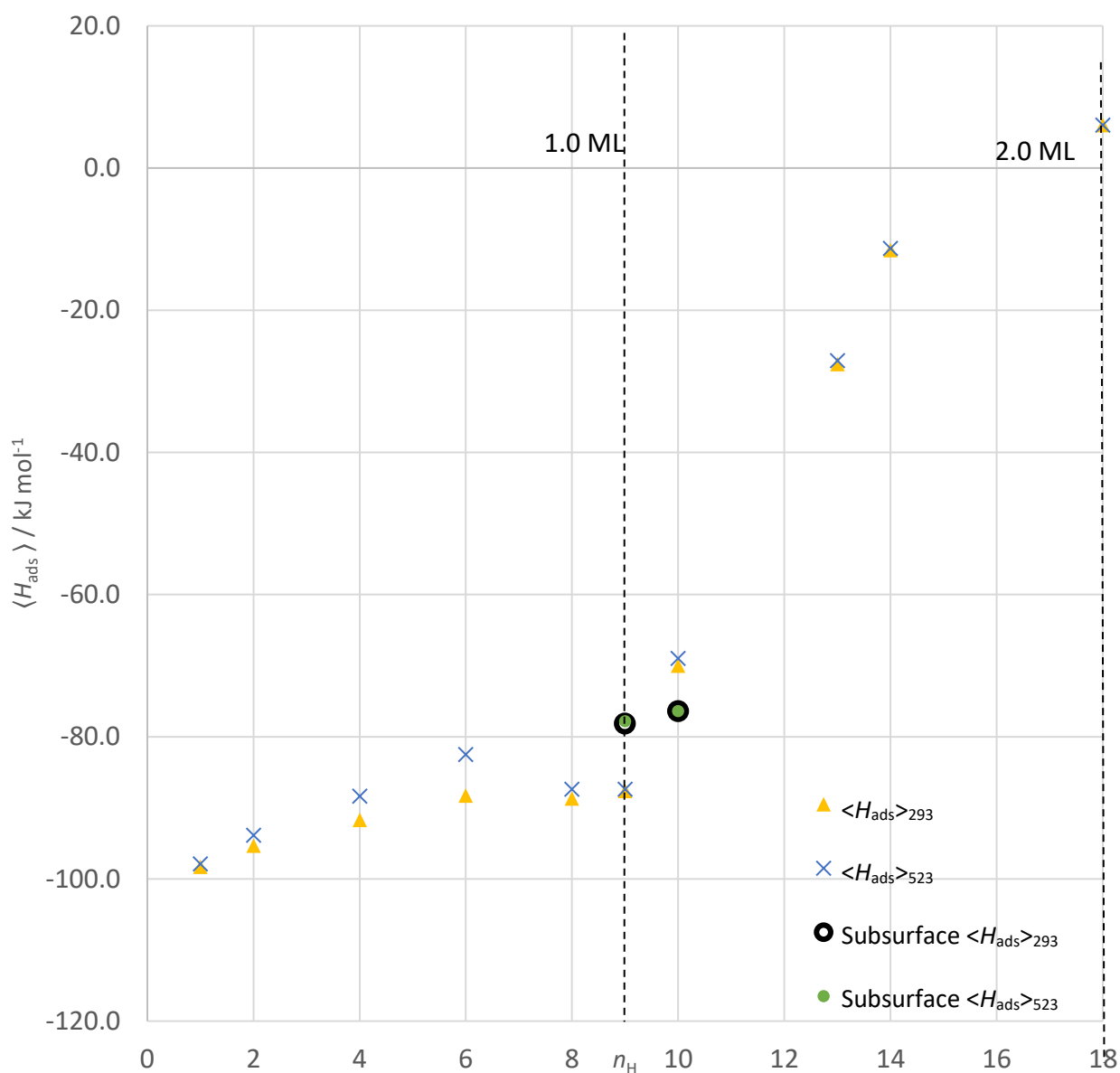


Figure 27. The average adsorption enthalpy ($\langle H_{\text{ads}} \rangle$) per H_2 molecule on the Pd (111) surface at 293 K (triangles) and at 523 K (crosses). $\langle H_{\text{ads}} \rangle$ for configurations with a single sub-surface H atom included at 293K and 523K is shown by open and green circles, respectively. Dotted lines show the position of 1 ML and 2 ML coverage levels for the $p(3 \times 3)$ used.

After inclusion of the ZPE in Figure 27, the resulting $\langle H_{\text{ads}} \rangle$ are higher than $\langle E_{\text{ads}} \rangle$ by about 7 kJ mol^{-1} for all corresponding coverages. However, the shape of the plot is largely maintained. The number of metastable states accessible at 523 K for $\frac{8}{9}$ ML decreases, resulting in a much smaller discrepancy between the $\langle H_{\text{ads}} \rangle$ at 293 K and 523 K, which is reduced to 1.3 kJ mol^{-1} from 6.0 kJ mol^{-1} . As a result, the $\langle H_{\text{ads}} \rangle$ at 523K becomes stronger at $\frac{8}{9}$ ML than $\frac{6}{9}$ ML by 4.9 kJ mol^{-1} . Moreover, the subsurface octahedral sites are favoured at $\frac{10}{9}$ ML coverage by 10 kJ mol^{-1} .

mol⁻¹, as compared to 5 kJ mol⁻¹ when only $\langle E_{\text{ads}} \rangle$ is considered. At 293 K and coverage up to 1 ML, the $\langle H_{\text{ads}} \rangle$ is between -97.9 and -87.4 kJ mol⁻¹, matching the enthalpy of desorption at 87 and 89 kJ mol⁻¹ observed by Conrad *et al.* and Engel *et al.* for Pd (111) at low hydrogen coverages.^{31,193}

4.3.2. Adsorption on Pd (100)

Possible hydrogen configurations on a $p(3 \times 3)$ Pd (100) surface supercell have been enumerated as described in Chapter 4.2.3 and calculated for 1- (0.11 ML) to 9-atom (1 ML) configurations. Wilke *et al.* observed that the interaction between subsurface H and H adsorbed in the FCC hollow site is weak in the study of hydrogen adsorption on Pd (100), reporting ΔE_{ads} of 71-78 kJ mol⁻¹ at coverages close to saturation, *i.e.*, 0.9 ML.²²⁷

The results in Figure 28 show that the average enthalpy increased with increasing coverage, up to 1 ML on both. The largest effect of temperature was observed at 0.4-0.6 monolayer for both Pd (111) and Pd (100) facets. At both low ($\frac{1}{9}$ ML) and high ($\frac{8}{9}$ ML) coverage on the Pd (100) surface the hollow site is the preferred adsorption site.

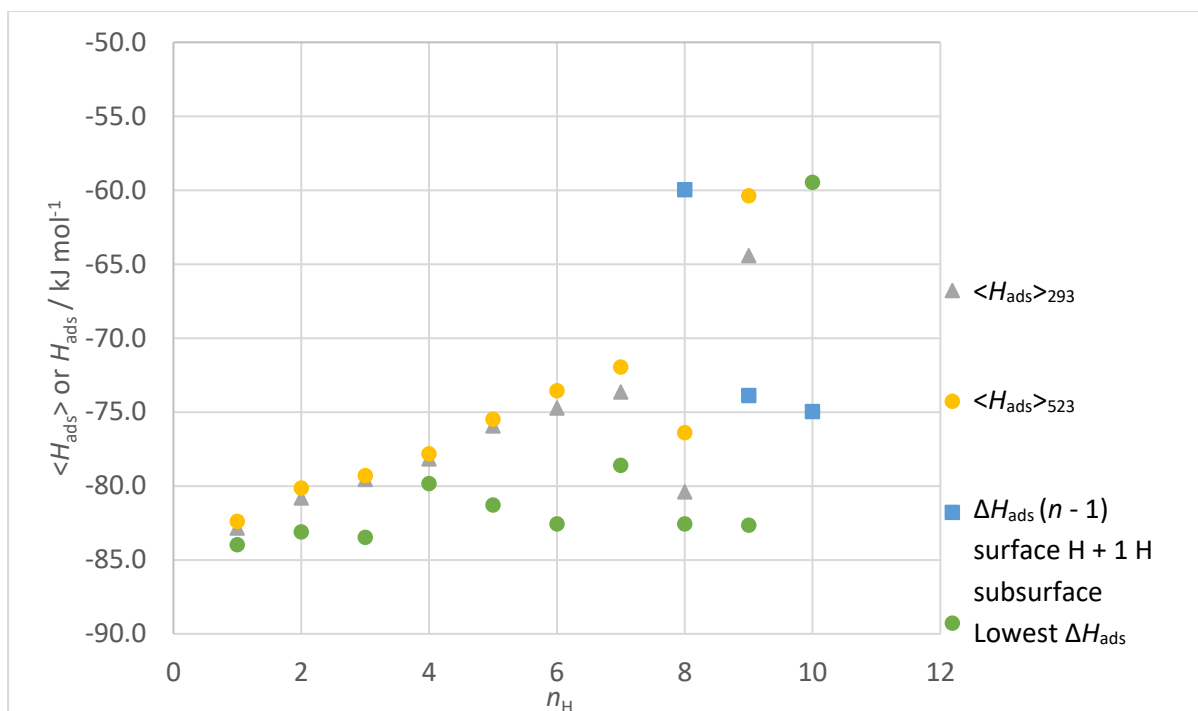


Figure 28. The average adsorption enthalpy ($\langle H_{\text{ads}} \rangle$) per H₂ molecule on the Pd (100) surface calculated using equation (3) at 293 K (grey triangles) and at 523 K (yellow circles). The ΔH_{ads} without vibrational energy contributions (*i.e.*, $\Delta E_{\text{ads}} + \Delta ZPE$) for configurations with a single sub-surface H atom is shown by blue squares, and ΔH_{ads} of the most stable configuration of surface hydrogen atoms at coverages between $\frac{1}{9}$ and $\frac{10}{9}$ are shown using green circles.

The $\langle E_{\text{ads}} \rangle$ of H₂ steadily increases from -86 kJ mol^{-1} at $\frac{1}{9}$ ML coverage to -74 kJ mol^{-1} at $\frac{8}{9}$ ML and 293 K, and the temperature has a very limited effect on its strength. However, the calculated $\langle E_{\text{ads}} \rangle$ values should be treated with caution due to erroneously 22 kJ mol^{-1} lower ΔE_{ads} at the bridge adsorption site compared to the hollow site, as discussed in Chapter 4.2.5. The $\langle H_{\text{ads}} \rangle$ of H₂ on Pd (100) starts from $-82.4 \text{ kJ mol}^{-1}$ at $\frac{1}{9}$ ML coverage to -74 kJ mol^{-1} at $\frac{8}{9}$ ML coverage at 293 K, matching the work of Wilke *et al.*²²⁷ Increasing the temperature to 523 K weakens the $\langle H_{\text{ads}} \rangle$ at $\frac{7}{9}$ ML by only 1.6 kJ mol^{-1} . The inclusion of the ZPE energy has significant effect on $\langle H_{\text{ads}} \rangle$ at $\frac{8}{9}$ ML, strengthening the adsorption by 6.8 kJ mol^{-1} at 293 K and 3.3 kJ mol^{-1} at 523 K with respect to $\langle E_{\text{ads}} \rangle$ for the same coverage, instead of the expected weakening. The resulting observable kink in $\langle H_{\text{ads}} \rangle$ at $\frac{8}{9}$ ML stems from the low ΔZPE for the Pd (100) structure with all 8 H atoms occupying hollow sites, leading to proportionally stronger H_{ads} , thereby dominating the partial contributions of the all-hollow structure to the $\langle H_{\text{ads}} \rangle$ at $\frac{8}{9}$ ML

coverage, which had just 9 other structures considered. It is noted that there is a similarly strengthened $\langle H_{\text{ads}} \rangle$ on the Pd (111) surface going from $\frac{6}{9}$ ML to $\frac{8}{9}$ ML, though the phenomenon is only observed at a temperature of 523 K and not 293 K.

However, at around 0.5 ML coverage the most stable structure includes a mix of bridge and hollow sites, with 3 bridge and 1 hollow site occupied at $\frac{4}{9}$ ML, and 2 bridge and 3 hollow sites occupied at $\frac{5}{9}$ ML, as shown in Figure 29. The finding contrasts with the Pd (111) surface, where the preferred structure at any coverage up to 1 ML involved only FCC sites, suggesting that, on the Pd (100) surface, the hydrogen might be more likely to occupy the lower coordination bridge site at coverages of around 0.5 ML, which carries important implications for surface chemistry.

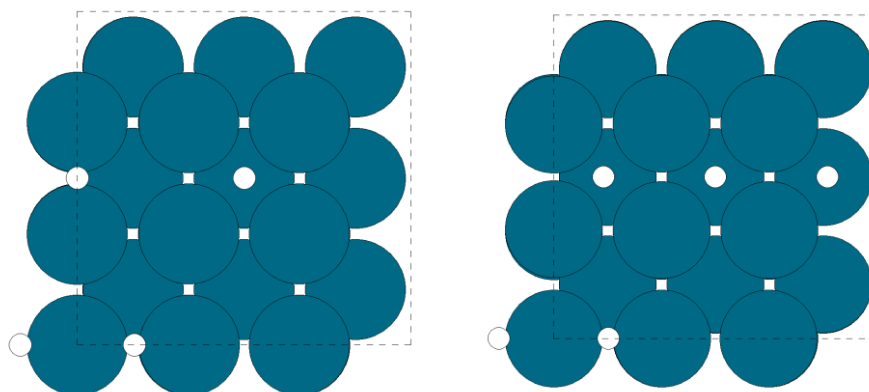


Figure 29. Most favourable configuration of H atoms (white circles) on the Pd (100) surface (blue circles) at $\frac{4}{9}$ and $\frac{5}{9}$ ML (left and right, respectively) coverage of hydrogen; the view is in the xy -plane and dotted lines are representing the unit cell boundaries.

At 1 ML coverage, a significant difference exists between the lowest energy structure in the data set and the effective average adsorption enthalpy on Pd (100). The latter was 18.3 kJ mol^{-1} and 22.3 kJ mol^{-1} higher than the lowest ΔH_{ads} at 293 K and 523 K, respectively, implying that subsurface hydrogen could affect the adsorption on Pd (100), even at coverages close to 1 ML, as the subsurface hydrogen had an adsorption enthalpy of only 8.8 kJ mol^{-1} higher than the most stable configuration. When all the hollow sites were occupied by hydrogen, adding the 10th hydrogen atom either on a bridge site above the surface or in the subsurface site yielded adsorption enthalpies of $-59.5 \text{ kJ mol}^{-1}$ and $-75.0 \text{ kJ mol}^{-1}$, respectively. The observed

difference suggests that subsurface hydrogen is strongly preferred over surface hydrogen above 1 ML coverage of hydrogen on Pd (100).

4.3.3. Pd (111) – Gibbs free energy

Once $\langle H_{\text{ads}} \rangle$ was evaluated on Pd (111) surfaces at coverages between $\frac{1}{9}$ up to 2 ML, at temperatures of 293 K and 523 K, the vibrational energy and the entropy contributions to the enthalpy of adsorption were considered using the harmonic oscillator (open circles and dotted line in Figure 30 and hindered translator models (closed circles and solid line in Figure 30) to calculate the free energy of adsorption, *i.e.*, the Gibbs free energy change (ΔG_{ads}) as a result of the dissociation of the hydrogen molecule on the Pd (111) surface.

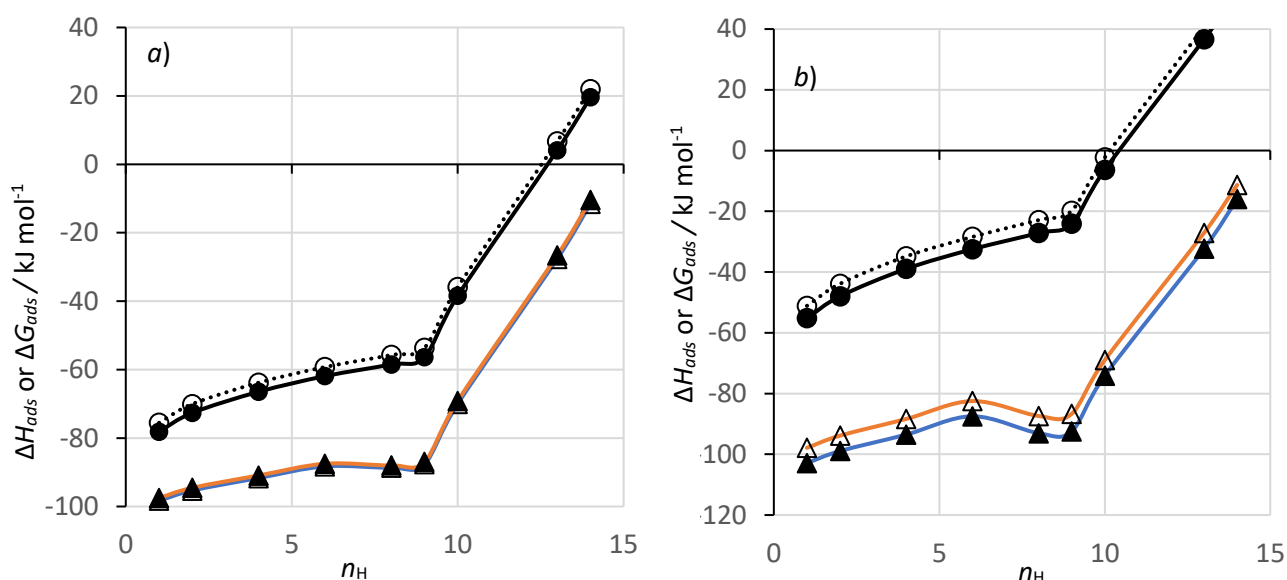


Figure 30. Enthalpy and free energy of adsorption for $\text{H}_2(\text{g}) \rightarrow 2\text{H}(\text{ads})$ on Pd (111) as a function of number of adsorbates on the $p(3 \times 3)$ supercell, $n_{\text{H}} = 9$ corresponds to 1 ML coverage. At a) $T = 293$ K and b) $T = 523$ K. In both cases, $\Delta H_{\text{ads}} = \Delta E_{\text{DFT}} + \Delta \text{ZPE}$: open triangles and orange line, $\Delta H_{\text{ads}} = \Delta E_{\text{DFT}} + \Delta \text{ZPE} + U_{\text{vib}}$: closed triangles and blue line, $\Delta G_{\text{ads}} = \Delta E_{\text{DFT}} + \Delta \text{ZPE} + U_{\text{vib}} - T\Delta S_{\text{HO}}$: Open circles and dotted line, $\Delta G_{\text{ads}} = \Delta E_{\text{DFT}} + \Delta \text{ZPE} + U_{\text{vib}} - T(\Delta S_{\text{hindxy}} + \Delta S_{\text{HOz}})$: Closed circles and solid line.

The use of the hindered translator model results in around 2 and 4 kJ mol^{-1} lower ΔG_{ads} curves at 293 K and 523 K, respectively. The free energy curve is higher than the enthalpy curve by about 20 kJ mol^{-1} and 30 kJ mol^{-1} at 293 K and 523 K, respectively. The ΔG_{ads} curve results do not contain any kink at low coverages, unlike the $\langle H_{\text{ads}} \rangle$ curve; instead, a smooth increase in

the ΔG_{ads} is observed from coverages of $\frac{1}{9}$ up to 1 ML, followed by a sharp rise at higher hydrogen coverages. At 293 K, the expected coverage was around 1.25 monolayer, as the 13-atom coverage is just above 0 kJ mol⁻¹. However, at 523 K, the ΔG_{ads} is below 0 kJ mol⁻¹ at $\frac{10}{9}$ ML coverage and positive afterwards. The results suggest that subsurface hydrogen is important as it will be present at the expected coverages of around $\frac{10}{9}$ ML at 523 K. At low coverages of $\frac{1}{9}$ ML, the ΔG_{ads} is -75.6 and -51.1 kJ mol⁻¹ at 293 K and 523 K, respectively, therefore single hydrogen atom desorption in mechanistic studies of hydrogenation processes on Pd (111) contributes makes a significant contribution to free energy change in hydrogenation ΔG barriers. Correspondingly, a correction of around 38 kJ mol⁻¹ and -26 kJ mol⁻¹ per hydrogen atom could be imposed on the ΔG barriers at 293 K and 523 K, respectively, due to considering an unrealistically low coverage of $\frac{1}{9}$ ML.

4.4. Conclusions

The adsorption of hydrogen is a phenomenon of great importance to the field of heterogeneous catalysis and general surface science, as shown by the detail with which the reaction has been studied both experimentally and theoretically over the years. The work here fully enumerates the possible adsorption configurations of hydrogen atoms on $p(3 \times 3)$ supercells of Pd (111) and Pd (100) at coverages from of $\frac{1}{9}$ to 2 ML and $\frac{1}{9}$ to 1 ML, respectively, and uses symmetry to reduce the number of relevant structures by orders of magnitude. By calculating the energy of each selected configuration using the mBEEF functional, changes of hydrogen adsorption energy have been evaluated as a function of surface coverage. Further, vibrational frequency calculations have been performed to evaluate the ZPE contributions and include the vibrational energy factors in free energy calculations. The work shows that consideration of ZPE is important for accurate representation of hydrogen adsorption energy on Pd surfaces in contrast to views present in literature.

For Pd (111) at 293 K and coverage of hydrogen of up to 1 ML, the average adsorption enthalpy is between -97.9 and -87.4 kJ mol⁻¹, matching well the experimentally derived enthalpy of desorption of 89 ± 4 kJ mol⁻¹. Moreover, subsurface hydrogen adsorption is

thermodynamically unfavourable at coverages of up to 1 ML but is thermodynamically preferable as the next adsorption, resulting in a coverage of $\frac{10}{9}$ ML by around 10 kJ mol⁻¹ on both Pd (111) and Pd (100) surfaces. Subsurface hydrogen is expected to be present in Pd (111) and (100) surfaces at temperatures of up to 523 K at 1 atm pressure, and therefore can contribute to the reactivity exhibited by these facets.

Average free energy of adsorption of hydrogen on the Pd (111) surface shows that simulations involving hydrogenation of adsorbed species assuming a low $\frac{1}{9}$ ML coverage of hydrogen likely overestimate the free energy barriers involving hydrogen desorption at 293 K and 523 K by around 38 and 26 kJ mol⁻¹, respectively, due to operating at unrealistically low coverages of hydrogen. The effect of the hydrogen coverage on transition metal surfaces on the free energy landscape is significant and should be considered in detail for simulated reactions involving low hydrogen concentration, as it has the potential to significantly alter the calculated free energy barriers.

The thermodynamics of the recently calculated Pd (100) configurations require further extensive analysis. Future work will involve deriving ΔG_{ads} for the Pd (100) surface and combining the results from Pd (111) and (100) surfaces to build an effective surface phase diagram of surface Pd hydride under industrially relevant conditions.

Chapter 5. CO₂ hydrogenation to formate on Cu, Pd, Zn and PdZn and CuPd alloy surfaces

In Chapter 3, the free energy change of initial hydrogenation of CO₂ to the formate intermediate on the Pd (111), (100) and (110) surfaces is shown to be highly positive due to the strong Pd-H interaction, which inhibits further hydrogenation to methanol. Then, in Chapter 4, the interaction of hydrogen with low-index Pd surfaces was explored in detail and the effect of the low hydrogen coverage used for mechanistic studies on free energy barriers was substantial. However, the free energy change required to form the transition state in CO₂ hydrogenation to formate remains high even with consideration of hydrogen coverage effects on the free energy surface. Further understanding of the initial hydrogenation of CO₂ to formate on Pd-based alloy surfaces is required to provide insight into the underlying reasons for the observed changes in the reactivity of Pd-based catalysts.

5.1. Introduction

As discussed in Chapter 1, CuPd and PdZn alloys have been explored in the context of CO₂ hydrogenation to methanol and were found to be more effective than Pd catalysts. In CO₂ hydrogenation using heterogeneous Pd-based supported catalysts only C₁ products can be observed: CO, methanol and methane.^{39,40} In electrochemical catalytic hydrogenation of CO₂ on PdZn alloy catalysts only CO and methanol are detected, while in thermal hydrogenation methane is observed only above a temperature of 500 K at ambient pressure.^{50,98} Using combined X-ray/Neutron powder diffraction data analysis, Peterson *et al.* precisely described the nature of the tetragonal β_1 -PdZn and showed that, despite the complicated PdZn phase diagram, it is the most prevalent phase.²²⁸ Friedrich *et al.*, Heggen *et al.* and Miyazaki *et al.* in their studies of the PdZn nanoparticle catalysts were able to identify the structure as tetragonal with (101) surfaces as the most abundant facets using various microscopy methods.^{45,229,230} Similarly, the tetragonal PdZn was shown to be the most abundant in the nanoalloy particles synthesised by Nowicka *et al.* with the (110) facets being especially prominent.²³¹ The PdZn alloy shows features of a perfectly ordered (o-) material with a pattern of alternating stripes of Pd and Zn on the surfaces as shown in Figure 31.^{45,229–231}

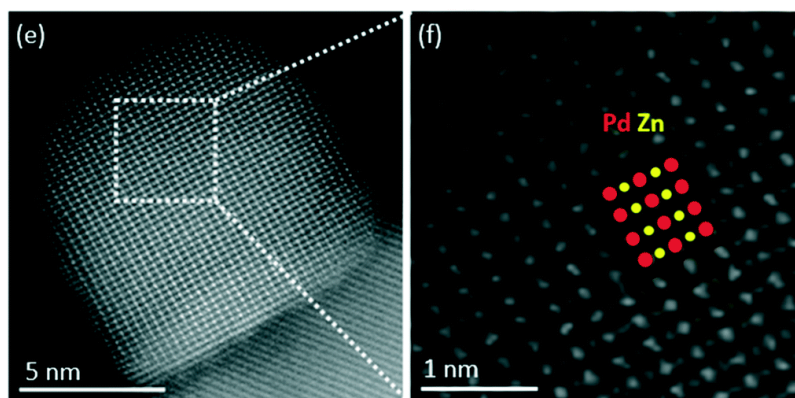


Figure 31. Adapted from Nowicka *et al.*²³¹: high angle annular dark field scanning transmission electron microscopy (STEM-HAADF) imaging of the C_{imp} 3% PdZn/ZnO catalyst. (e) A higher magnification STEM-HAADF image of a PdZn particle, showing the tetragonal PdZn phase. (f) A higher magnification HAADF image of a [001] projection of a PdZn, with Pd and Zn atoms highlighted in red and yellow, respectively.

Moreover, the 1:1 composition of the alloy appears to be obtained regardless of the starting Pd and Zn precursor ratio owing to the very large heat of mixing of Pd and Zn metals in the 1:1 alloy.²⁰ Recent theoretical studies of the PdZn alloy at varying composition done by Kabalan *et al.* confirmed the PdZn at 1:1 ratio as most favourable and identified the structure as body-centred tetragonal, in line with experiment.²³² Similarly, the distinct ordering on the most abundant (110) surface of the ordered body-centred cubic (BCC) 1:1 alloy of CuPd was reported in the nanoalloy synthesised by Yamauchi *et al* and the BCC crystal structure is reported as particularly stable for the 1:1 CuPd alloy.²³³ Preliminary studies on BCC CuPd alloy done by Dr Lara Kabalan, currently pending publication, confirmed the (110) facet to be the lowest energy and highest coverage surface on a 11 nm Wulff-shaped nanoparticle at equilibrium. Following the naming convention of Crawley *et al.*, due to the specific highly symmetric ordering the 1:1 PdZn and 1:1 CuPd alloys, the catalysts could be name body-centred tetragonal (BCT) o-Pd_{0.5}Zn_{0.5} and body-centred cubic (BCC) o-Cu_{0.5}Pd_{0.5}.²² To simplify the naming convention, in subsequent text the alloys are referred to as PdZn and CuPd with crystal structure, composition and ordering implied.

The research here delves into the computational analysis of CO₂, CO, and hydrogen behaviour on PdZn (101) and (110), as well as CuPd (110) alloy surfaces. The primary focus is on the hydrogenation of CO₂ to produce the formate intermediate, and the performance of alloys is

referenced against their monometallic counterparts. It has been shown that the most studied lowest energy face-centred-cubic (FCC) (111) surfaces of Cu and Pd are not suitable catalyst candidates for reactivity involving carbon dioxide and formate, hence particular focus is on the more reactive and catalytically versatile (110) surfaces.^{55,128,171} The metastable intermediates considered are based on previous computational studies of Cu surfaces by Higham *et al.*, and Pd surfaces from our previous work.^{55,128} Herein, the higher efficiency of CO₂ hydrogenation to methanol on Pd-based alloy materials as compared to Pd catalysts is investigated by modelling the initial stages of CO₂ hydrogenation to formate using periodic DFT techniques.

5.2. Computational methods

The Fritz Haber Institute *ab initio* molecular simulations (FHI-aims) software package, has been used for full potential all-electron DFT calculations, with the Pythonic Atomic Simulation Environment (ASE) used for management of calculation geometries.^{148,163} The default convergence criteria within FHI-aims for self-consistent field (SCF) calculations were used, *i.e.*, the changes between the current and previous SCF iterations in charge density, sum of eigenvalues and total energy were below $N \times 1.67 \times 10^{-5} e a_0^{-3}$, 10^{-3} eV and 10^{-6} eV, respectively, where N is the number of atoms in the model. Scalar relativistic treatment of kinetic energy for all elements was achieved by the atomic zero-order regular approximation (ZORA), and a Gaussian-type broadening with width of 0.01 eV was applied to the occupation of electronic states. In the work of Kabalan *et al.*,¹⁷¹ the accurate semi-local Bayesian error estimation density functional (mBEEF)¹³² exchange correlation density functional (DF) as implemented in the LibXC DF library²¹⁰ was highlighted as a suitable choice for modelling Cu and Pd surfaces. A \mathbf{k} -grid density of one \mathbf{k} -point per $(0.018 \times 2\pi) \text{ \AA}^{-1}$ and a default “light” basis set (version: 2020) have been used for geometry optimisations, providing structural accuracy and electronic accuracy in Mulliken charge population analysis.^{163,171,186} For geometry optimisations, convergence was deemed complete when forces on all unconstrained atoms were less than 0.01 eV \AA^{-1} . Spin-paired calculations were used in periodic calculations; gas-phase adsorbate structures were calculated both spin-paired and spin-unpaired, and the energy of the more stable system was considered for reference to periodic calculations. The

Fritz Haber Institute *ab initio* molecular simulations (FHI-aims) software package, has been used for full potential all-electron DFT calculations, with the Pythonic Atomic Simulation Environment (ASE) used for management of calculation geometries.^{148,163} The default convergence criteria within FHI-aims for self-consistent field (SCF) calculations were used, *i.e.*, the changes between the current and previous SCF iterations in charge density, sum of eigenvalues and total energy were below $N \times 1.67 \times 10^{-5} e a_0^{-3}$, 10^{-3} eV and 10^{-6} eV, respectively, where N is the number of atoms in the model. Scalar relativistic treatment of kinetic energy for all elements was achieved by the atomic zero-order regular approximation (ZORA), and a Gaussian-type broadening with width of 0.01 eV was applied to the occupation of electronic states. In the work of Kabalan *et al.*,¹⁷¹ the accurate semi-local Bayesian error estimation density functional (mBEEF)¹³² exchange correlation density functional (DF) as implemented in the LibXC DF library²¹⁰ was highlighted as a suitable choice for modelling Cu and Pd surfaces. A k -grid density of one k -point per $(0.018 \times 2\pi) \text{ \AA}^{-1}$ and a default “light” basis set (version: 2020) have been used for geometry optimisations, providing structural accuracy and electronic accuracy in Mulliken charge population analysis.^{163,171,186} For geometry optimisations, convergence was deemed complete when forces on all unconstrained atoms were less than 0.01 eV \AA^{-1} . Spin-paired calculations were used in periodic calculations; gas-phase adsorbate structures were calculated both spin-paired and spin-unpaired, and the energy of the more stable system was considered for reference to periodic calculations.

Monometallic surfaces were constructed from face-centred cubic (FCC) Cu, Pd and hexagonal close-packed (HCP) Zn bulk structures optimised based on the outcomes of the work by Kabalan *et al.*¹⁷¹ In summary, supercells of Pd (111), (110), (110), Cu (111), (100) and (110) and Zn (0001) surfaces were created with cell dimensions of $(3 \times 3 \times 7)$, and a vacuum layer of 40 \AA added in the z -direction. The bottom three atomic layers were constrained to their bulk positions and the 4 top surface layers were unconstrained; and, due to the one-sided nature of the slab models considered, a dipole-correction was used in all calculations. The alloy surfaces were prepared similarly to the monometallic surfaces; however, as BCT and BCC primitive cells contained two atoms, the $(2 \times 3 \times 7)$ supercells were used instead. For the body-centred tetragonal (BCT) PdZn (101) and (110), the bimetallic alloy ordering was obtained from experimental studies by Peterson *et al.* and Nowicka *et al.*^{228,231} The ordering of the body-centred cubic (BCC) CuPd (110) surface was based on a study by Yamauchi *et al.*²³³

Henceforth, whenever the metallic and alloy systems are mentioned, the crystal structure is implied as the following: Cu and Pd – FCC, Zn – HCP, CuPd – BCC and PdZn – BCT.

For catalytic surface reactions, the adsorption energy (E_{ads}) measures the interaction between a surface and adsorbate, and is deduced from comparison of energies of optimised gas-phase adsorbate, pristine surface and the optimised combined system. The definition used here is such that negative E_{ads} indicates exothermic interactions. The adsorption energy (E_{ads}) of formate species is considered in bidentate (HCOO^{b*}) or monodentate (HCOO^{m*}) form; carbon dioxide is considered either as chemisorbed ($\text{CO}_2^{\delta-*}$) or physisorbed (CO_2^*); and hydrogen as dissociated only (H^*), where * indicates a surface-bound species. For kinetic studies, we have used the MLNEB method to identify saddle points and MEPs.^{144,147} In line with our previous work, a spring constant of 0.05 eV \AA^{-1} has been used throughout; the convergence criterion of forces on all unconstrained atoms of below 0.05 eV \AA^{-1} , with energy uncertainty below 0.03 eV .¹²⁸

5.3. Results and discussion

5.3.1. Hydrogen adsorption on Cu, Pd and Zn, CuPd and PdZn surfaces

It is essential to understand the behaviour of hydrogen on the Cu, Pd and Zn before delving into the reaction steps of CO_2 hydrogenation on surfaces of these metals and their alloys. Hydrogen adsorption on Pd (111) and (100) using the mBEEF density functional was previously investigated in detail in Chapter 4, hence only the new Pd (110) results are shown below. Higham *et al.* highlighted the Cu (110) surface as the best candidate for CO_2 hydrogenation to methanol, hence the hydrogen adsorption energetics were included in the study. The hydrogen adsorption strength on the metal surfaces was probed by placing a hydrogen atom at 1 \AA above the in the symmetry unique adsorption and subsequent relaxation of the structures.

The symmetry unique adsorption sites on the FCC Cu and Pd (110) surfaces are shown in Figure 31 and the corresponding hydrogen adsorption energies are tabulated in Table 13. Given the well known low affinity of Zn metal towards hydrogen, no extensive adsorption survey was performed, and the highly endothermic E_{ads} of H on Zn (0001) was calculated as 0.72 eV , in agreement with previously reported value of 0.76 eV .²³⁴

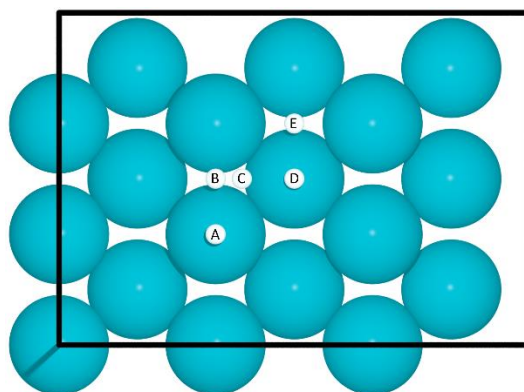


Figure 32. Top-down view of unique adsorption sites (white circles) on the FCC (110) surface of Pd (blue circles): (A) atop, (B) short-bridge, (C) 'FCC', (D) hollow, (E) long-bridge. The black lines represent boundaries of the model simulation cell.

Table 13. $E_{\text{ads}}(\text{H})$ on FCC Cu and Pd (110) surfaces, relative to the energy of $\frac{1}{2}\text{H}_2(\text{g})$. Unstable adsorption sites are marked as hyphens only.

| Adsorption site | $E_{\text{ads}}(\text{H}) / \text{eV}$ | |
|-----------------|--|----------|
| | Cu (110) | Pd (110) |
| A. atop | 0.49 | -0.06 |
| B. short-bridge | -0.02 | -0.38 |
| C. 'FCC' | -0.04 | -0.47 |
| D. hollow | - | -0.17 |
| E. long-bridge | 0.01 | -0.29 |

The calculated most stable hydrogen adsorption site on Cu (110) matches closely previous observations of Wang *et al.*²³⁵ (RPBE) (-2.30 eV H atom binding energy on the short-bridge site) and deviate from the work of Leny *et al.*³⁴ (-2.11 eV H atom binding energy), which we attribute to differences in methodology (PBE-D2). Assuming H_2 bond energy of 4.48 eV, the hydrogen atom binding energy of -2.30 eV reported by Wang *et al.* is equivalent to E_{ads} of -0.06 eV relative to gas H_2 and very close to the -0.02 eV reported here.²³⁵ However, here the 'FCC' site situated between the short-bridge and hollow sites was also considered and was found to be more stable by -0.02 eV. Overall, the hydrogen dissociation is determined to be a mildly exothermic process on Cu in agreement with observations of others.⁵⁵

The adsorption of the hydrogen atom on the Pd (110) 'FCC' adsorption site was previously reported by Dong *et al.* and their observed E_{ads} was only -0.03 eV more stable than E_{ads} of

-0.47 eV calculated in this work. The value calculated with the mBEEF exchange correlation functional compares well to the -0.56 eV predicted in our previous work using PBE exchange correlation functional with a Tkatchenko-Scheffler van der Waals correction in Chapter 3.^{125,128,170} Conrad *et al.* have experimentally derived the initial heat of hydrogen adsorption of -0.53 on Pd (110), *i.e.*, 0.06 eV lower than the E_{ads} of H atom on the ‘FCC’ site, indicating that mBEEF mildly underpredicts the strength of the interaction of hydrogen with the Pd surfaces as previously discussed in detail in Chapter 4.¹⁸¹ The adsorption of the hydrogen atom on the Pd (110) ‘FCC’ adsorption site was previously reported by Dong *et al.* and their observed E_{ads} was only -0.03 eV more stable than E_{ads} of -0.47 eV calculated here. The value calculated with the mBEEF exchange correlation functional compares well to the -0.56 eV predicted in our previous work using PBE exchange correlation functional with a Tkatchenko-Scheffler van der Waals correction in Chapter 3.^{125,128,170} Conrad *et al.* have experimentally derived the initial heat of hydrogen adsorption of -0.53 on Pd (110), *i.e.*, 0.06 eV lower than the E_{ads} of H atom on the ‘FCC’ site, indicating that mBEEF mildly underpredicts the strength of the interaction of hydrogen with the Pd surfaces as previously discussed in detail in Chapter 4.¹⁸¹

Once the hydrogen adsorption energies were calculated for monometallic Cu, Pd and Zn surface, unique adsorption sites on the CuPd (110) surface were identified in Figure 33 and the E_{ads} was calculated for the corresponding sites in Table 14.

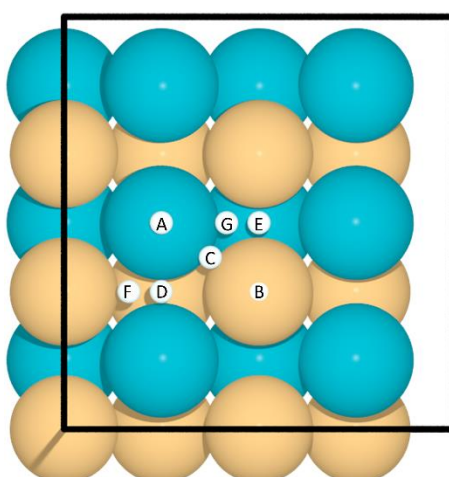


Figure 33. Top-down view of unique adsorption sites (white circles) on BCC (110) surface of CuPd alloy (Pd: blue circles; Cu: yellow circles): (A) Pd atop, (B) Cu atop, (C) Pd-Cu bridge, (D) Pd-Pd bridge, (E) Cu-Cu bridge, (F) Cu hollow and (G) Pd hollow. The black lines represent boundaries of the simulation cell.

Table 14. $E_{\text{ads}}(\text{H})$ on BCC CuPd (110) surface, relative to the energy of $\frac{1}{2}\text{H}_2(\text{g})$. Unstable adsorption sites are marked as hyphens only.

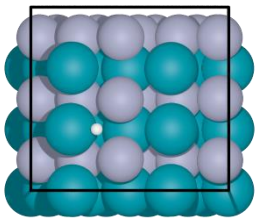
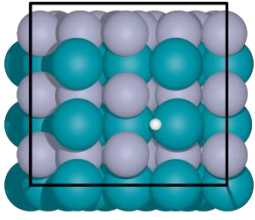
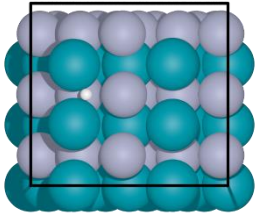
| Adsorption site | $E_{\text{ads}}(\text{H})$ /eV |
|-----------------|--------------------------------|
| | CuPd (110) |
| A. Pd atop | 0.05 |
| B. Cu atop | 0.39 |
| C. Cu-Pd bridge | - |
| D. Pd-Pd bridge | -0.43 |
| E. Cu-Cu bridge | -0.23 |
| F. Cu Hollow | -0.49 |
| G. Pd Hollow | -0.28 |

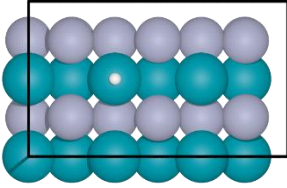
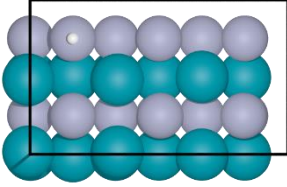
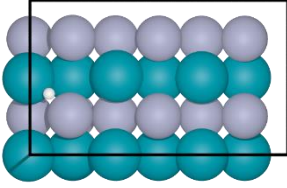
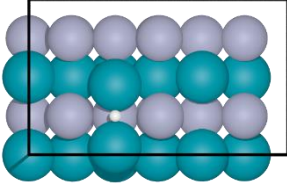
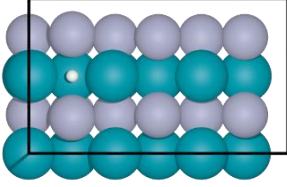
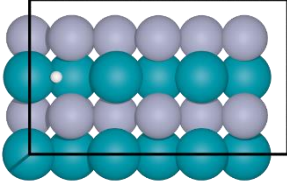
On the CuPd (110) surface, the hydrogen atom adsorbs stronger (*i.e.*, has a lower energy of adsorption) on Pd atom rather than Cu atoms; and the hydrogen atom is most stable when it interacts with two Pd atoms at the surface layer, which is the case both on the Pd-Pd bridge site (D in Figure 33) and the Cu hollow site (F in Figure 33), with exothermic E_{ads} of -0.43 and -0.49 eV, respectively. Furthermore, it is noted that the Cu hollow site for the alloy adsorbs H stronger than the most stable ‘FCC’ site of Pd (110) (-0.49 eV and, -0.47 eV, respectively). The Cu and Pd atop positions on the alloy are endothermic, due to the reduced coordination of H, and adsorption on both positions are around 0.1 eV less stable than on monometallic FCC (110) surfaces, which give E_{ads} of 0.49 and -0.06 eV for Cu and Pd, respectively. The E_{ads} on the Cu-Cu bridge site of the BCC CuPd (110) surface is exothermic, and lower than on the FCC Cu (110) by 0.21 eV, meaning higher accessibility of hydrogen around surface Cu atoms of the alloy than on the monometallic Cu (110) surface. The hydrogen atoms are also predicted to be more labile than on the Pd surfaces, which show much stronger adsorption energies.

Further, hydrogen atom adsorption energies are evaluated on the alloy PdZn (101) and (110) surfaces. A single hydrogen atom is placed at symmetry inequivalent positions on PdZn (101) and (110) and a geometry optimisation is performed, resulting in three metastable geometries on PdZn (101) and six metastable geometries on PdZn (110). On PdZn (101) the hydrogen atom is most stable in a Pd-Pd off-bridge position with a Zn atom in the sublayer (Table 15.iii) with E_{ads} of -0.25 eV. On PdZn (110) the hydrogen atom adsorption is observed

to be endothermic on all adsorption sites, and most stable on the Pd-Pd bridge site (Table 15.vii) with E_{ads} of 0.05 eV. The adsorption of hydrogen on PdZn is less favourable than on the Pd metal and CuPd alloy, but more favourable than on either Cu or Zn metals. Overall, the hydrogen atom adsorbs stronger to the high Pd-coordinated sites and minimised Zn-coordination. In Chapter 3, the high E_{ads} of H on Pd surfaces was highlighted as an inhibitor of the CO₂ hydrogenation on Pd catalysts, therefore the considerably weaker adsorption might facilitate the reaction.¹²⁸ Interestingly, a significant part of the activation energy barrier for hydrogenation of CO₂ on metallic Pd at low H coverage comes from moving the hydrogen from the highly coordinated hollow sites to the atop sites.¹²⁸ The small energy differences between in E_{ads} of H on Pd-rich regions on PdZn surfaces indicate low diffusion barriers which are also observed on metallic Pd.^{128,218}

Table 15. E_{ads} of a hydrogen atom on PdZn (101) and (110) surfaces; blue, grey and white spheres represent Pd, Zn and H atoms, respectively; the black lines represent the simulation cell boundaries as viewed in the xy-plane.

| Structure | Surface | Visualization | Sites | $E_{\text{ads}} / \text{eV}$ |
|-----------|------------|---|------------------|------------------------------|
| i | PdZn (101) |  | Pd off-top 1 | -0.01 |
| ii | PdZn (101) |  | Pd off-top 2 | 0.17 |
| iii | PdZn (101) |  | Pd-Pd off-bridge | -0.25 |

| | | | | |
|------|------------|---|--|------|
| iv | PdZn (110) |  A 3D model of a PdZn (110) surface. The surface is composed of two layers of atoms: a top layer of grey spheres (Pd) and a bottom layer of teal spheres (Zn). A single grey sphere is shown on top of the Pd layer, highlighted by a white dot and a black box. | Pd atop | 0.31 |
| v | PdZn (110) |  A 3D model of a PdZn (110) surface. The surface is composed of two layers of atoms: a top layer of grey spheres (Pd) and a bottom layer of teal spheres (Zn). A single teal sphere is shown on top of the Zn layer, highlighted by a white dot and a black box. | Zn atop | 0.61 |
| vi | PdZn (110) |  A 3D model of a PdZn (110) surface. The surface is composed of two layers of atoms: a top layer of grey spheres (Pd) and a bottom layer of teal spheres (Zn). A grey sphere and a teal sphere are shown bridging between the two layers, highlighted by a white dot and a black box. | Pd-Zn bridge | 0.16 |
| vii | PdZn (110) |  A 3D model of a PdZn (110) surface. The surface is composed of two layers of atoms: a top layer of grey spheres (Pd) and a bottom layer of teal spheres (Zn). Two grey spheres are shown bridging between the two layers, highlighted by a white dot and a black box. | Pd-Pd bridge | 0.05 |
| viii | PdZn (110) |  A 3D model of a PdZn (110) surface. The surface is composed of two layers of atoms: a top layer of grey spheres (Pd) and a bottom layer of teal spheres (Zn). A white dot is located in the center of a four-fold hollow formed by four atoms in the top layer, highlighted by a black box. | Pd ₂ Zn ₂ four-fold hollow | 0.23 |
| ix | PdZn (110) |  A 3D model of a PdZn (110) surface. The surface is composed of two layers of atoms: a top layer of grey spheres (Pd) and a bottom layer of teal spheres (Zn). A grey sphere is shown off-top, bridging between the two layers, highlighted by a white dot and a black box. | Pd off-top | 0.22 |

5.3.2. CO adsorption

The binding of CO on the Pd metal and PdZn alloy surfaces was calculated to rationalise the product streams observed in CO₂ hydrogenation to formate. The calculated E_{ads} of CO tabulated in Table 16 indicate that the CO binding energy on PdZn alloy is weaker compared to pure Pd. Moreover, the 1:1 PdZn alloy has limited viable CO adsorption sites, as CO reacts preferentially with Pd.

Table 16. E_{ads} of CO on FCC Pd (111), (100) and (110), and BCT PdZn (101) and (110) across the unique metastable adsorption sites; energy units are provided in eV.

| structure | surface | Site | E_{ads} /eV |
|-----------|------------|--|-------------------------|
| i | Pd (100) | atop | -1.51 |
| ii | | bridge | -1.99 |
| iii | | hollow | -1.89 |
| iv | Pd (110) | hollow | -1.19 |
| v | | atop | -1.50 |
| vi | | long-bridge | -1.74 |
| vii | | short-bridge | -1.99 |
| viii | Pd (111) | FCC hollow | -2.02 |
| ix | | atop | -1.38 |
| x | | HCP hollow | -1.99 |
| xi | PdZn (101) | Pd atop | -1.08 |
| xii | | Pd-Pd bridge | -1.10 |
| xiii | PdZn (110) | Pd atop | -1.10 |
| xiv | | Pd-Pd bridge (over Zn) | -0.88 |
| xv | | Pd ₂ Zn ₂ four-fold hollow | -0.28 |

Any geometries containing CO placed in a Zn-rich adsorption site on the PdZn alloy (101) and (110) surface are not stable and lead to Pd coordinated atop- and bridge-like adsorption sites, instead of the hollow sites as is the case across Pd (111), (100) and (110) facets. Weakening of the CO adsorption is consistent with the observations of Jeroro *et al.* who using low energy

electron diffraction (LEED), temperature programmed desorption (TPD) and high resolution electron energy loss spectroscopy (HREELS), which have shown weakening of the carbon monoxide binding to the Zn-covered FCC Pd (111) surface as a function of Zn coverage.²³⁶ The effect of Zn addition to Pd on CO binding energy can be rationalised as the interpolation of the metallic properties of Pd and Zn, as the interaction of CO and metallic Zn is very weak.²³⁷ A linear relationship exists between the E_{ads} of CO on PdZn alloys and the concentration of Zn in the alloy, *i.e.*, the more Zn there is, the weaker the adsorption energy.⁷²

Brix *et al.* reported a E_{ads} of CO of -1.82 eV for atop, -2.22 eV for hollow, and -2.09 eV on the bridge adsorption site of the Pd (111).⁷² The values reported here are weaker by about 0.2 eV for the atop and hollow sites, while the bridge adsorption site is not metastable using the mBEEF functional at the investigated 0.08 ML coverage. Jeroro *et al.* observed a preferential binding site alteration resulting from Zn coverage increase, *i.e.*, the preferred site on FCC Pd (111) surface with an atomic monolayer of Zn is the atop position instead of the three-fold hollow or bridge sites, matching our observations of the change in CO preferential adsorption sites on Pd (111) and PdZn (110) surfaces. On the most stable PdZn (101) surface, however, we observed that the Pd-Pd bridge CO adsorption site is preferred slightly by -0.02 eV. In any case, the three-fold hollow positions on the PdZn (101) surface and four-fold hollow position on the PdZn (110) surface remain either high in energy or not metastable, with hydrogen tending to move closer to the Pd-Pd bridging sites. Our work considers a low coverage of one CO molecule per 12 surface metals atoms, *i.e.*, 0.08 ML and the preference of CO towards the Pd-Pd bridge site was previously reported in a theoretical study by Brix *et al.* on the tetragonal PdZn (111) surface at a 0.11 ML coverage with an E_{ads} of -1.19 eV which qualitatively agrees with the results on the BCT PdZn alloy presented here.⁷² Bakó *et al.* calculated a CO binding energy of -1.14 eV on a 1:1 PdZn overlayer on Pd (111) using a PBE functional, which qualitatively agrees with the values of -1.10 eV observed here on the (110) and (101) surfaces of the PdZn alloy.²³⁸

On Pd, the hydrogenation of CO is facilitated due to it being energetically favourable compared to desorption.⁷² In addition, on PdZn, CO competes with hydrogen for adsorption sites on the (101) and (110) surfaces as both of H and CO avoid binding to Zn sites, which can affect the CO coverage at high H₂ partial pressure. However, the reduced binding energy of

CO combined with higher activation energies towards hydrogenation observed previously suggest that CO desorbs from PdZn surfaces instead of hydrogenating further.⁷²

5.3.3. CO₂ adsorption

CO₂ was previously shown to adsorb on Cu and Pd in two distinctive ways, which are referred to herein as physisorption (yielding CO₂) and chemisorption (yielding CO₂^{δ-}).^{55,128} Physisorbed CO₂ is positioned parallel to the surface at a distance of over 3 Å, and no chemical bond forming between the metal and the adsorbate; the interaction is marginally exothermic.^{55,128} In contrast, the chemisorbed CO₂^{δ-} assumes a bidentate geometry with a C-metal and O-metal bond formation, and electron density is pushed from the metal surface to the π* orbital of the carbon atom, resulting in a distortion of the O-C-O bond angle and stabilisation of the negatively charged (δ-), distorted geometry.^{55,128} On Zn (0001) surfaces, only the physisorbed CO₂ species with a weak E_{ads} of -0.10 eV was considered, as CO₂ does not show signs of chemisorption on Zn surfaces in the absence of surface oxygen or high electrostatic potential.^{237,239–242}

Here, it is recognised that the CO₂ hydrogenation to formate requires a H* species in the vicinity of the carbon dioxide; therefore, the relative stability of the CO₂ and CO₂^{δ-} were assessed both in the presence and the absence of hydrogen at the most stable adsorption sites. The resulting E_{ads} of the CO₂ and CO₂^{δ-} species on the monometallic Cu (110) and Pd (110) are presented in Table 17. The CuPd and PdZn alloys only have shown a single chemisorbed structure CO₂^{δ-}, hence no detailed breakdown of adsorption survey is provided and the E_{ads} of CO₂ and CO₂^{δ-}, with and without co-adsorbed H, for all investigated surfaces are presented in Figure 34 and tabulated in Table 27 the Appendix.

Table 17. E_{ads} of CO_2 and $\text{CO}_2^{\delta-}$ with and without co-adsorbed H atom on FCC Cu and Pd (110) surfaces; the energies are relative to the gas-phase $\frac{1}{2}\text{H}_2$ and CO_2 . Unstable adsorption sites are marked as hyphens only.

| | Adsorption Site | Surface | |
|---|-----------------|----------|----------|
| | | Cu (110) | Pd (110) |
| $E_{\text{ads}}(\text{CO}_2^*) / \text{eV}$ | long-bridge | -0.17 | -0.18 |
| | short-bridge | -0.15 | -0.17 |
| $E_{\text{ads}}(\text{CO}_2^{\delta-*}) / \text{eV}$ | long-bridge | 0.30 | -0.18 |
| | short-bridge | - | -0.25 |
| $E_{\text{ads}}(\text{CO}_2^* + \text{H}^*) / \text{eV}$ | long-bridge | - | - |
| | short-bridge | -0.18 | -0.67 |
| $E_{\text{ads}}(\text{CO}_2^{\delta-*} + \text{H}^*) / \text{eV}$ | long-bridge | 0.34 | -0.51 |
| | short-bridge | - | -0.66 |

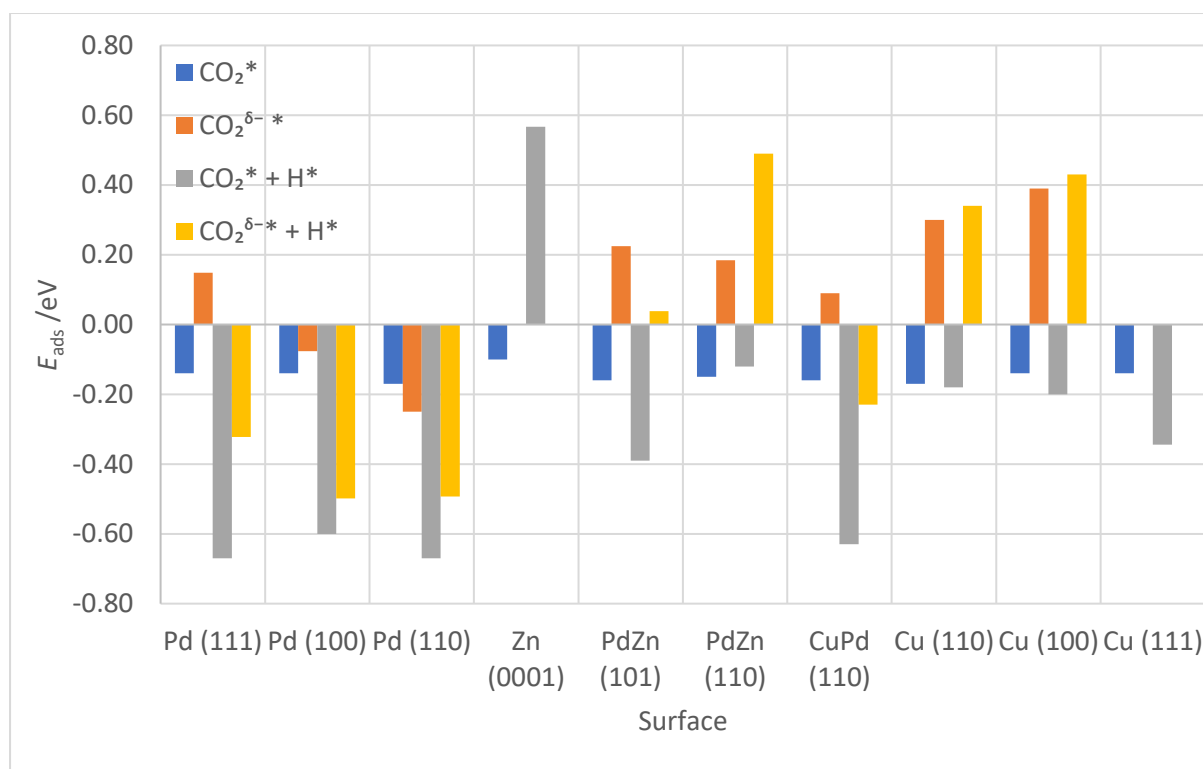


Figure 34. E_{ads} of CO_2 , $\text{CO}_2^{\delta-}$ in units of eV, with and without co-adsorbed hydrogen atom in the most favourable adsorption position, across Pd (111), (100), (110), Zn (0001), Cu (111), (100), (110), CuPd (110) and PdZn (101) and (110) surfaces. No metastable structures of $\text{CO}_2^{\delta-}$ were found on Cu (111) and Zn (0001) surfaces.

The horizontally positioned physisorbed CO₂ species has a very similar stability across all investigated surfaces, with E_{ads} of between -0.17 and -0.10 eV; therefore, the physisorption strength of the CO₂ species is not the root cause of differences in reactivity of the surfaces towards CO₂ hydrogenation. The stability of the chemisorbed CO₂^{δ-} species is more indicative for reactivity, as was previously shown in the study of CO₂ hydrogenation on Pd surfaces in Chapter 3. The most stable geometries of CO₂^{δ-} on Cu (110), Pd (110) and CuPd (110) shown an E_{ads} of 0.30 eV, -0.25 eV and 0.09 eV, respectively; thus, the surface of the 1:1 alloy of Cu and Pd shows stability of CO₂^{δ-} at the intermediate of the monometallic surfaces. The E_{ads} of the chemisorbed CO₂^{δ-} species was also investigated across other lower-index surfaces of Cu and Pd, but without an extensive adsorption energy survey. The E_{ads} of CO₂^{δ-} was calculated as 0.39 eV, 0.15 eV and -0.08 eV on Cu (100), Pd (111) and Pd (100), respectively, and no CO₂^{δ-} structure was observed on Cu (111), in line with observations of Higham *et al.*⁵⁵ The E_{ads} of CO₂^{δ-} on Cu (110) reported here is less stable than observed by Higham *et al.*, which can be attributed to the methodological differences – the PBEsol and mBEEF exchange-correlation functionals only share the exchange energy in their derivation, but not the correlation energy, which causes a different treatment of dispersion forces resulting in energy differences. E_{ads} of CO₂^{δ-} on PdZn (101) and (110) is 0.22 eV and 0.18 eV, respectively, weaker than Pd (111) that shows the highest E_{ads} of CO₂^{δ-} on low-index Pd surfaces.

On the Pd (110) surface, the chemisorbed CO₂^{δ-} species with co-adsorbed hydrogen atom in the ‘FCC’ position (C in Figure 31) shows almost identical stability as the physisorbed CO₂ (-0.67 eV and -0.66 eV, respectively), further highlighting the importance of the CO₂^{δ-} intermediate on Pd. CO₂^{*} and H^{*} co-adsorption yields an almost identical E_{ads} as the sum of E_{ads} of the separate species on the respective surfaces, signifying a limited interaction of co-adsorbed CO₂^{*} and H^{*}. In contrast, the co-adsorbed CO₂^{δ-*} and H^{*} are less stable than the isolated CO₂^{δ-} and H adsorbates, by 0.06, 0.08, and 0.17 eV on the FCC Pd (110), FCC Cu (110) and BCC CuPd (110) surfaces, respectively.

The exothermicity of CO₂^{δ-} adsorption on Pd (100) and (110) surfaces implies that chemical activation of CO₂ is possible on Pd, but the interaction is weak, and therefore short-lived, matching our previous calculations performed using a different method in Chapter 3.¹²⁸ Conversely, CO₂^{δ-} adsorption on investigated Cu (100), (110), Pd (111), CuPd (110) and PdZn

(101) and (110) surfaces is exothermic, hence $\text{CO}_2^{\delta-}$ on these surfaces is a rare and transient intermediate.

On PdZn surfaces the bidentate $\text{CO}_2^{\delta-}$ species binds on intermetallic bridging sites, with C more strongly bound at Pd and O at Zn. Similarly, the $\text{CO}_2^{\delta-}$ structure on CuPd (110) has a Pd-C bond and Cu-O bond, and non-intermetallic adsorption sites were not metastable. Therefore, on pristine PdZn (101), (110) and CuPd (110) surfaces, the preferred CO_2 chemisorption sites are more accessible than on metallic Pd, since the Cu or Zn sites are not covered by adsorbed hydrogen allowing oxygen-metal interaction. PdZn catalysts for CO_2 hydrogenation include an excess of ZnO support material from which the Zn alloys into the Pd nanoparticles. When in excess, the ZnO forms an overlayer on top of the PdZn alloy nanoparticles over the course of the first few hours of CO_2 hydrogenation reaction after which point the catalyst reaches maximum activity.^{45,230,231,243} In fact, many researchers have previously proposed that the ZnO is responsible for the adsorption of CO_2 in PdZn catalysts, and that CO_2 hydrogenation happens either at the metal-support interface (MSI) or on the ZnO support via hydrogen spillover.^{19,20,45,230,231,243,244} The claims have been further corroborated by theoretical work of Song *et al.* who observed a significant promotion of CO_2 adsorption strength at the MSI (-0.37 eV on PdZn compared to -0.86 eV on the MSI) on simulated 3 atomic layers thick PdZn nanowires on ZnO.²⁴⁴

In the work of Nowicka *et al.*, after 10 h on stream, the removed supported PdZn/ZnO catalyst sample showed the PdZn surfaces in-tact with around a 2 ML on top with weaker signals in energy-dispersive X-ray spectroscopy, which were attributed to the ZnO formation.²³¹ The presence of ZnO islands on the surface of PdZn particles aligns completely with earlier studies from Armbrüster *et al.*, who linked such structure to highly active catalysts.^{45,230} Moreover, the duration required to form the ZnO overlayer on PdZn is in line with the induction period needed for the PdZn/ZnO catalyst to achieve maximum effectiveness.²³¹ The induction period observed by Freidrich *et al.* was 2 hours and the catalyst was showing signs of ZnO on PdZn during characterisation after the period. Such observations bear resemblance to the activity of Cu/ZnO- Al_2O_3 catalysts being attributed to ZnO nanoparticles on Cu surfaces in the work of Kattel *et al.*⁴⁷ It is noted that CO_2 chemisorption is a process more endothermic than physisorption on Cu (100) and (110) surfaces by 0.47 and 0.53 eV, respectively. PdZn alloy alone has a higher selectivity than Pd catalysts, but shows a lower selectivity than the mixed

PdZn/ZnO active catalyst where ZnO is in high excess.²³⁰ However, there is only a small and negative dependence of the yield on the ZnO support surface area, as shown in the work of Lawes *et al.*, where the ZnO support surface area is varied by an order of magnitude with little changes in catalytic activity, meaning that the catalyst activity is still correlated to the PdZn nanoparticles themselves.²⁰

5.3.4. CO₂ dissociation

To assess the how competitive the RWGS reaction is to CO₂ hydrogenation, the dissociation of carbon dioxide was modelled on FCC Cu, FCC Pd, HCP Zn, BCC CuPd and BCT PdZn surfaces. The CO₂ dissociation reaction was initiated from a chemisorbed CO₂ structure (CO₂^{δ-}); the Cu (111) and Zn (0001) surfaces were not considered as no chemisorbed CO₂ state was found.

From the results of CO₂ dissociation studies in Figure 35, the Pd (100) surface had the lowest overall energy barrier (0.78 eV) for CO₂ dissociation, $E_a(\text{CO}_2)$, where the energy of the physisorbed species is considered as the initial state and also the lowest activation energy barrier of 0.72 eV of the modelled CO₂^{δ-} dissociation reaction step, $E_a(\text{CO}_2^{\delta-})$. On Pd the $E_a(\text{CO}_2)$ followed the trend of Pd (100) < Pd (111) < Pd (110), which is not correlated to either the surface energies or coordination number of surface metal atoms. However, as Pd (100) is one of the most abundant facets on Pd nanoparticles, based on the energetics, majority of the CO₂ dissociation occurs on Pd (100).

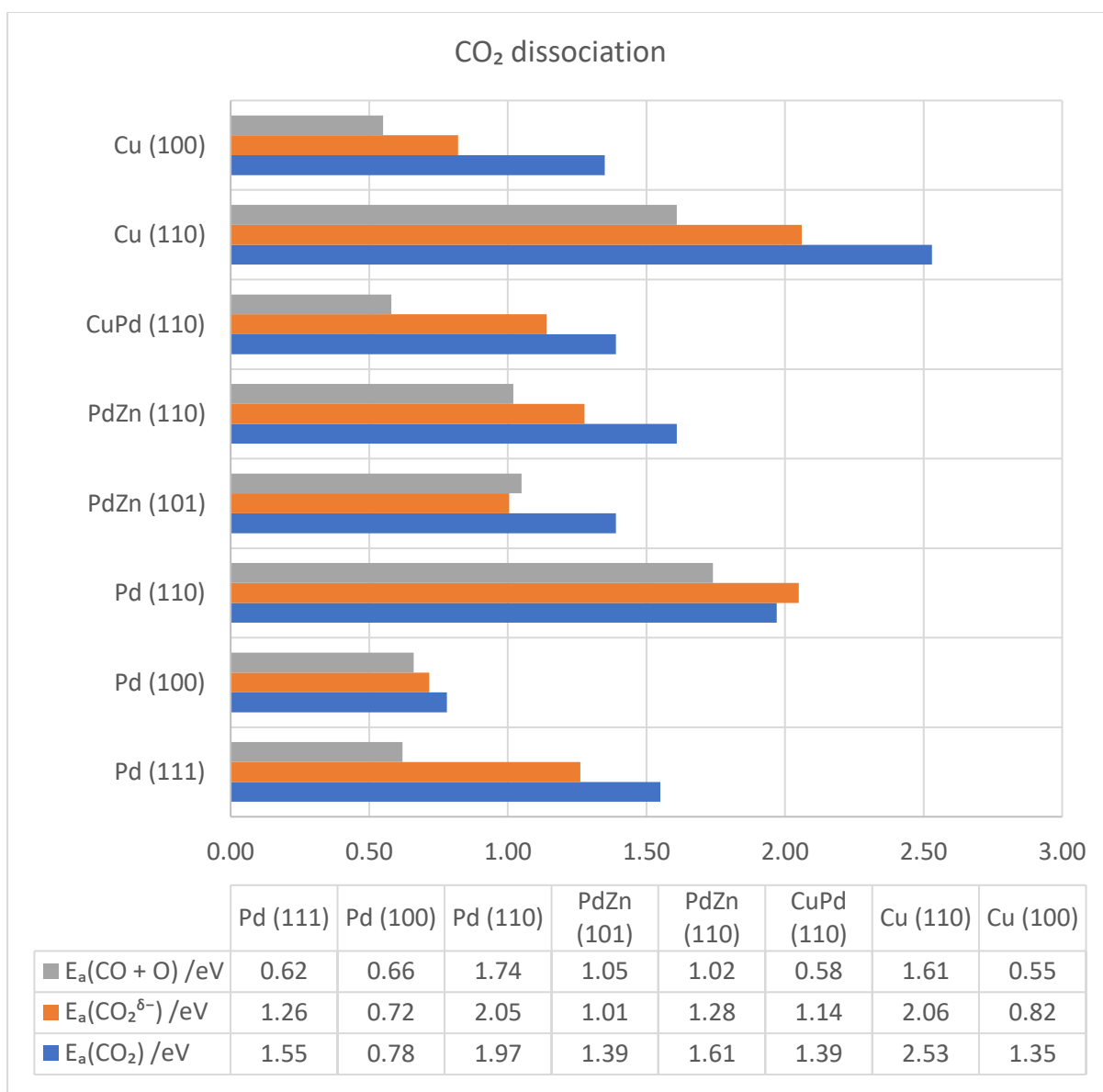


Figure 35. CO₂ dissociation reaction energetics across Pd (111), (100), (110), Cu (100), (110), CuPd (110) and PdZn (101) and (110) surfaces; $E_a(\text{CO}_2^{\delta-})$ is the activation barrier for C-O bond dissociation of chemisorbed CO₂^{δ-}; $E_a(\text{CO}_2)$ constitutes of $E_a(\text{CO}_2^{\delta-})$ with included the difference between E_{ads} of CO₂ and CO₂^{δ-}; $E_a(\text{CO} + \text{O})$ is the activation energy towards the formation of CO₂^{δ-} from co-adsorbed CO and O species.

The activation barriers are low on Pd (100), but still substantially higher than the energy of CO₂ physisorption (5 times) and chemisorption (10 times). The $E_a(\text{CO}_2)$ were lower on the most stable surface of the PdZn alloy, *i.e.*, PdZn (101) < PdZn (110). The highest $E_a(\text{CO}_2)$ and $E_a(\text{CO}_2^{\delta-})$ were observed on Pd (110) and were almost tripled with respect to barriers observed on Pd (100), which emphasises the role of surface structure in the dissociative reactivity of CO₂ on transition metal surfaces.

Brix *et al.* observed a C-O bond dissociation energy of 1.56 eV for CO₂ on Pd (111) and 1.67 eV on PdZn (111), and the $E_a(\text{CO}_2)$ on Pd (111) calculated here matches their results with just a 0.01 eV difference.⁷² Here, the $E_a(\text{CO}_2^{\delta-})$ is 1.01 eV and $E_a(\text{CO}_2)$ is 1.39 eV on PdZn (101), qualitatively matching the $E_a(\text{CO}_2)$ of 1.67 eV for the PdZn (111) reported by Brix *et al.*⁷² The PdZn (111) surface is higher in energy than PdZn (101) and (110), and has a different surface morphology, hence the observed differences in $E_{\text{act}}(\text{CO}_2)$.

The activation energy required for the reverse reaction of co-adsorbed CO* and O* to form CO₂, $E_a(\text{CO} + \text{O})$, is an important aspect of the WGS reaction. The $E_a(\text{CO} + \text{O})$ on Pd (111) is 0.62 eV and compares well with the value of 0.75 eV evaluated with a GGA PW-91 exchange correlation functional in the work of Clay *et al.*⁵⁶ $E_a(\text{CO} + \text{O})$ is higher on PdZn (101) and (110) surfaces than on Pd (111) by 0.43 and 0.40 eV, respectively. The $E_a(\text{CO} + \text{O})$ on the CuPd (110) surface is 0.04 eV lower than on Pd (111) facet and 0.03 eV higher than on Cu (100) surface. On Pd (111), the E_{ads} of CO is -2.02 eV in the FCC hollow site, *i.e.*, over three times higher than the $E_a(\text{CO} + \text{O})$, thus the desorption of CO is not a competitive process to the WGS. In contrast, $E_a(\text{CO} + \text{O})$ is 1.05 and 1.02 eV on PdZn (101) and (110), respectively, meaning that CO desorption (1.10 eV) is a competitive process to WGS on PdZn. Brix *et al.* investigated a part of the WGS reaction on Pd (111) and observed $E_a(\text{CO} + \text{O})$ of 2.32 eV on Pd (111) and 0.62 eV on PdZn (111) and $E_a(\text{CO}_2)$ of 2.46 eV on Pd (111) and 1.42 on PdZn (111). In the transition state structure calculated on PdZn (111), the oxygen atom is reported to be orientated towards the bridging Zn position, whereas the CO resides on the Pd atop site in similarity to the observation here. While their PdZn (111) results qualitatively match our calculated result from PdZn (101) and (110), the $E_a(\text{CO}_2)$ and $E_a(\text{CO} + \text{O})$ on Pd (111) are 0.91 eV and 1.7 eV higher, respectively. Here, a shorter minimum energy path is considered thanks to CO₂ being already chemisorbed on the surface in the initial structure, which might lead to a different result, as previously observed for CO₂ hydrogenation in Chapter 3.¹²⁸ It is noted that the differences between the results are higher than simply the difference between the adsorption energies of physisorbed and chemisorbed CO₂ species.

CuPd (110) shows similar $E_a(\text{CO}_2)$ and $E_a(\text{CO} + \text{O})$ to Cu (100), surface, but a higher $E_a(\text{CO}_2^{\delta-})$ simply due to a more stable CO₂^{δ-} chemisorbed species on the CuPd (110) surface. The Cu (110) and Pd (110) surfaces shows similarly very high $E_a(\text{CO}_2)$ and $E_a(\text{CO} + \text{O})$, implying that both RWGS and WGS do not significantly contribute to the CO₂ reactivity on these surfaces.

Overall, the energetics of CO₂ dissociation and CO adsorption on PdZn surfaces suggest that the Pd-based catalyst upon alloying with Zn becomes a more potent reverse water-gas shift (RWGS) catalyst, which helps to explain substantial amounts of CO being produced as part of the reaction.^{11,19,20} In contrast, the CuPd (110) surface WGS and RWGS reactivity remains largely unchanged with respect to the Cu (100), but the barrier towards CO₂ dissociation is nearly doubled with respect to Pd (100).

5.3.5. HCOO

Two binding modes of the HCOO* intermediate have previously been identified on Cu surfaces – the bidentate and monodentate formates.^{245–249} Their relevance in CO₂ hydrogenation to formate was investigated by placing the HCOO* intermediate on the Cu, Pd and CuPd (110) surfaces at a height of 2 Å from the unique adsorption sites, with either one oxygen (to facilitate monodentate geometry, HCOO^{m*}, Figure 36C) or both oxygen atoms (to facilitate bidentate geometry, HCOO^{b*}, Figure 36D) facing towards the surface, and a geometry optimisation was performed to determine relative energetics.

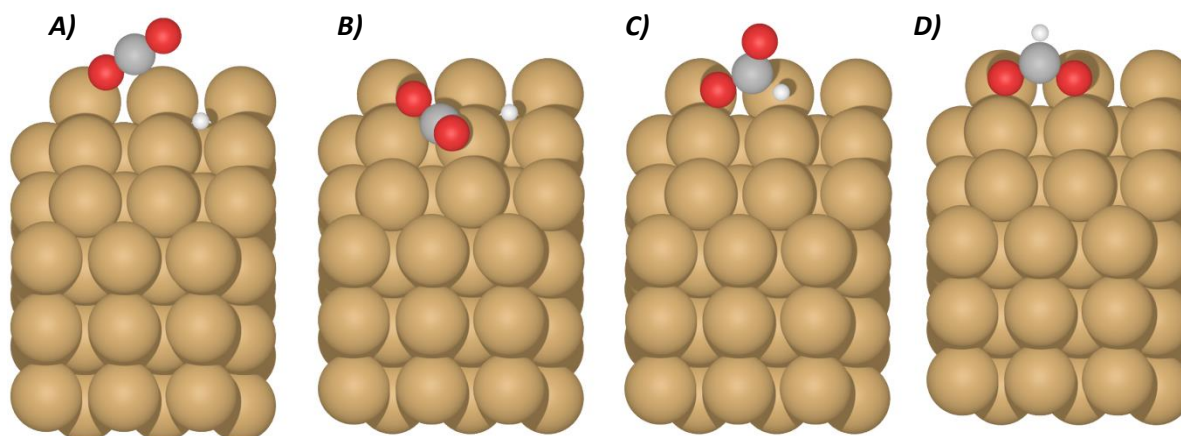


Figure 36. Intermediates considered in CO₂ hydrogenation to formate shown on the Cu (110) surface: A) co-adsorbed CO₂* and H*, B) co-adsorbed CO₂^{δ-*} and H*, C) HCOO^{m*}, D) HCOO^{b*}; brown, red, grey and white spheres represent Cu, O, C and H atoms, respectively.

The E_{ads} of all adsorption modes of HCOO^{b*} and HCOO^{m*} found on Cu, Pd and CuPd (110) surfaces are tabulated in Table 18 and

Table 19.

Table 18. $E_{\text{ads}}(\text{HCOO})$ on FCC Cu and Pd (110) surfaces, relative to gas-phase $\frac{1}{2}\text{H}_2$ and CO_2 ; $^{\text{m}*}$ represents monodentate geometry and $^{\text{b}*}$ corresponds to the bidentate geometry. Unstable adsorption sites are marked as hyphens only.

| Adsorption site | $E_{\text{ads}}(\text{HCOO}^{\text{m}*}) / \text{eV}$ | | $E_{\text{ads}}(\text{HCOO}^{\text{b}*}) / \text{eV}$ | |
|----------------------------|---|----------|---|----------|
| | Cu (110) | Pd (110) | Cu (110) | Pd (110) |
| short-bridge (H-M present) | -0.40 | 0.14 | -1.08 | -0.81 |
| short-bridge (H-M absent) | 0.09 | 0.17 | - | - |
| long-bridge | - | - | -1.02 | -0.65 |

Table 19. E_{ads} of HCOO on BCC CuPd (110) surface, relative to gas-phase $\frac{1}{2}\text{H}_2$ and CO_2 ; $^{\text{m}*}$ represents monodentate geometry and $^{\text{b}*}$ corresponds to the bidentate geometry.

| Adsorption site | $E_{\text{ads}}(\text{HCOO}^{\text{m}*}) / \text{eV}$ | $E_{\text{ads}}(\text{HCOO}^{\text{b}*}) / \text{eV}$ |
|----------------------------|---|---|
| | CuPd (110) | |
| Pd-Pd bridge (H-M present) | 0.58 | -0.34 |
| Pd-Cu bridge (H-M present) | 0.50 | -0.43 |
| Cu-Cu bridge (H-M absent) | 0.15 | -0.50 |

Notably, monodentate adsorption of HCOO ($\text{HCOO}^{\text{m}*}$) is endothermic on FCC Pd (110) and BCC CuPd (110) surfaces, while an exothermic adsorption was calculated for the FCC Cu (110) surface. The bidentate geometry ($\text{HCOO}^{\text{b}*}$) is more stable, especially on the short-bridge site of the FCC (110) surfaces of Cu and Pd with E_{ads} of -1.08 eV and -0.81 eV, respectively; and is most stable at the Cu-Cu bridge adsorption site of BCC CuPd (110) surface, with E_{ads} of -0.50 eV. $\text{HCOO}^{\text{b}*}$ is more stable on Cu (110) than it is on Pd (110), and the preferable adsorption of $\text{HCOO}^{\text{b}*}$ on the Cu atoms of BCC CuPd (110) surface layer matches this observation: E_{ads} of $\text{HCOO}^{\text{b}*}$ is only -0.34 eV when both oxygens are bound to Pd, while -0.43 eV and -0.50 when bound to one and two Cu atoms, respectively. While the stability of the $\text{HCOO}^{\text{b}*}$ on the Pd-Cu

bridge is intermediary when comparing E_{ads} for adsorption sites on the BCC CuPd (110) surface, even the most stable site on the alloy surface (Cu-Cu bridge) is significantly less stable than the $\text{HCOO}^{\text{b}*}$ on the monometallic Cu and Pd surfaces, by 0.58 eV and 0.31 eV, respectively.

The stability of formates was explored further and $\text{HCOO}^{\text{b}*}$ and $\text{HCOO}^{\text{m}*}$ intermediates were modelled on the FCC Pd (111), (100), FCC Cu (111), (100), HCP Zn (0001), BCC CuPd (110) and BCT PdZn (101) and (110) surfaces. The E_{ads} of the most stable $\text{HCOO}^{\text{b}*}$ and $\text{HCOO}^{\text{m}*}$ intermediates on each surface were calculated, ensuring that the $\text{HCOO}^{\text{m}*}$ contains an oxygen-metal bond and a significant hydrogen-metal interaction, and are shown in Figure 37. No metastable $\text{HCOO}^{\text{m}*}$ structure has been identified on Cu (111) and Zn (0001) surfaces, in similarity to the structures $\text{CO}_2^{\delta-}$ modelled before.

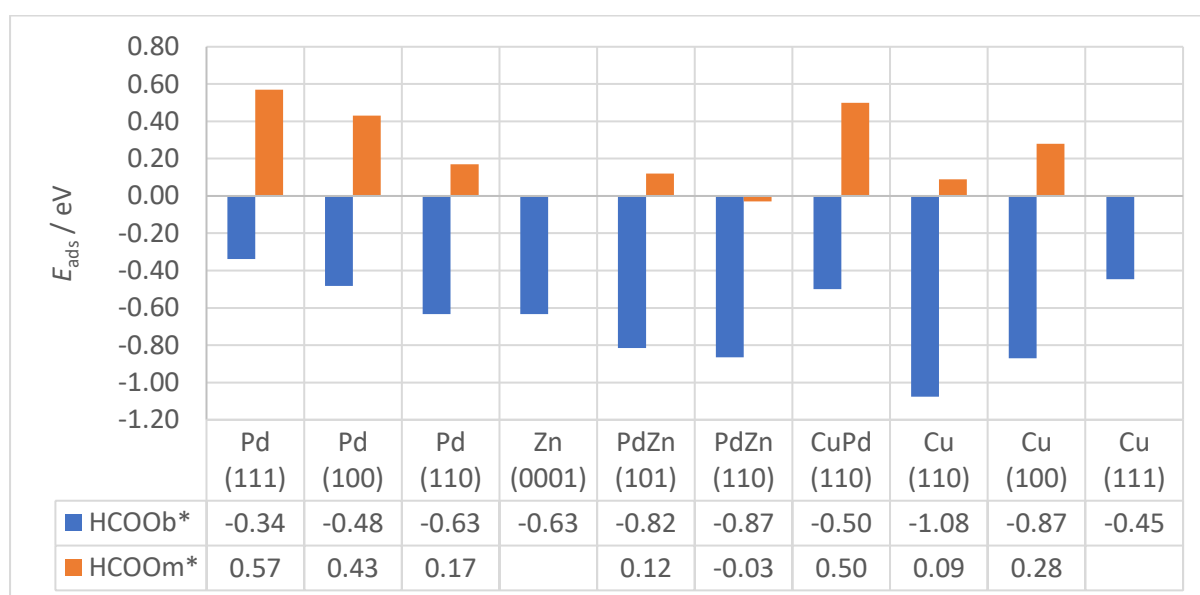


Figure 37. E_{ads} of surface-bound (*) monodentate (m) and bidentate (b) formate (HCOO) intermediates on FCC Pd (111), (100), (110), Cu (111), (100), (110), HCP Zn (0001), BCC CuPd (110) and PdZn (101) and (110) surfaces. $\text{HCOO}^{\text{b}*}$ is in the most stable conformation with both oxygen atoms bound to metal atoms, while the $\text{HCOO}^{\text{m}*}$ is bound to the surface via a single oxygen atom and a short hydrogen-metal bond allowing a significant electronic interaction. No metastable $\text{HCOO}^{\text{m}*}$ structure has been identified on Cu (111) and Zn (0001) surfaces.

Metastable monodentate formate structure was previously reported by Li *et al.* who calculated its adsorption energy to be 0.76 eV and 0.78 eV weaker than the bidentate species

on Pd (111) and Pd (100) surface, respectively, and the values match reasonably the energy differences of 0.91 eV for both surfaces calculated here.²⁵⁰ The relative energy difference between $\text{HCOO}^{\text{b}*}$ and $\text{HCOO}^{\text{m}*}$ Cu (110) is calculated as 0.99 eV, *i.e.*, higher than 0.78 eV from the angle-resolved analysis of desorbed products done by Quan *et al.*²⁴⁸ The only exothermic $\text{HCOO}^{\text{m}*}$ species containing a M-O and M-H bond was found for the PdZn (110) surface with E_{ads} of -0.03 eV.

5.3.6. Mulliken charge analysis of Cu, Pd and CuPd (110) surfaces

Mulliken charge analysis was performed for the relevant intermediates in the CO_2 hydrogenation to formate on FCC Cu, FCC Pd and BCC CuPd (110) surfaces to rationalise observed trends in E_{ads} of intermediates in the context of electronic charge transfers. The changes in atomic charges (Δq) in electrons (e) with respect to the atomic charges on the pristine surfaces were calculated; summation of Δq over the whole slab (Δq_{slab}), average of Δq per atom in the first surface layer (Δq_{surf}), and maximum Δq of a single atom in the surface layer ($\Delta q_{\text{surf_max}}$) were tabulated in Table 7. The contents of Table 7 were also complemented with the oxygen-carbon-oxygen angles ($\angle\text{OCO}$) of the adsorbates to compare structural features with Δq .

Table 20. Net change in Mulliken charges, in units of e, on relevant surface atoms of CO₂, CO₂^{δ-}, HCOO^b and HCOO^m adsorbed on Cu (110), Pd (110) and CuPd (110) surfaces relative to the atomic charges on the pristine surface; the charge differences (Δq) have been averaged over the first surface layer (Δq_{surf}), summated over the whole slab (Δq_{slab}); the maximum change in the atomic surface atomic layer charge ($\Delta q_{\text{surf_max}}$) and the OCO angle ($\angle\text{OCO}$) in degrees are also shown.

| Surface | Structure | $\Delta q_{\text{slab}} / e$ | $\Delta q_{\text{surf}} / e$ | $\Delta q_{\text{surf_max}} / e$ | $\angle\text{OCO} / ^\circ$ |
|------------|-------------------------------|------------------------------|------------------------------|-----------------------------------|-----------------------------|
| Cu (110) | CO ₂ ^{δ-} | 0.48 | 0.06 | 0.19 | 127.3 |
| | CO ₂ | 0.01 | 0.01 | 0.03 | 179.8 |
| | HCOO ^b | 0.47 | 0.06 | 0.20 | 127.2 |
| | HCOO ^m | 0.54 | 0.07 | 0.24 | 124.7 |
| Pd (110) | CO ₂ ^{δ-} | 0.31 | 0.05 | 0.21 | 137.4 |
| | CO ₂ | 0.01 | 0.00 | 0.02 | 179.7 |
| | HCOO ^b | 0.43 | 0.06 | 0.21 | 128.8 |
| | HCOO ^m | 0.54 | 0.07 | 0.24 | 125.4 |
| CuPd (110) | CO ₂ ^{δ-} | 0.26 | 0.03 | 0.17 | 140.4 |
| | CO ₂ | 0.01 | 0.00 | 0.04 | 179.8 |
| | HCOO ^b | 0.43 | 0.04 | 0.17 | 128.5 |
| | HCOO ^m | 0.54 | 0.05 | 0.19 | 124.1 |

Both Δq_{slab} and Δq_{surf} of CO₂ were negligible across FCC Cu, FCC Pd and BCC CuPd (110) surfaces, which agrees with the expectations for the physisorbed species as possible electronic interaction is limited due to the long surface-adsorbate distance of over 3 Å. The lack of significant charge transfer also correlates with the limited change of up to 0.3 ° in $\angle\text{OCO}$ across all surfaces with respect to the $\angle\text{OCO}$ of 180 ° of the gas phase CO₂. The more positive Δq_{slab} the higher the charge transfer of e into the adsorbate, therefore 0.48, 0.31 and 0.26 e were transferred to CO₂^{δ-} on the FCC Cu, FCC Pd and BCC CuPd (110) surfaces, respectively. The higher the Δq_{slab} the lower the $\angle\text{OCO}$ of the adsorbed CO₂^{δ-}, with $\angle\text{OCO}$ of 127.3, 137.4 and 140.4 °, respectively.

The Δq_{slab} of 0.31 e of Pd (110) facet with CO₂^{δ-} adsorbate is similar to the calculated value of 0.28 e on the Pd (111) surface in a study by Tang *et al.*¹⁸⁵ and much higher than our previously reported value of 0.11 e on Pd (110), which is attributed to significant differences in exchange correlation functional choice and the depth of the surface slab model.^{128,171} In the optimised

pristine BCC CuPd (110) surface Cu atoms have a $\delta+$ charge (q) due to charge transfer into Pd, which is stronger in the bulk with q of between 0.15 and 0.18 e, than q of 0.08 e at the surface.

Upon $\text{CO}_2^{\delta-}$ adsorption on BCC CuPd the charge donation to the adsorbate originates from the surface Cu atoms, while the changes in net Mulliken charges of Pd atoms in the initial surface layer are negligible, including the Pd atom to which the carbon atom of $\text{CO}_2^{\delta-}$ binds, which is analogous to the FCC Cu (110) surface where the Cu atoms in the Cu-O bonds show a net positive Δq , while the Δq of Cu atom in Cu-Pd bond remains almost unchanged. In the monometallic FCC Pd (110) the surface atom binding to $\text{CO}_2^{\delta-}$ has a net positive Δq , whereas in the BCC CuPd (110) surface the charge on the Pd atom involved in a Pd-C bond is compensated by the surrounding Cu atoms, which become more positively charged and more akin to the Cu atoms in the bulk of the material, making the overall structure more stable than on the FCC Cu (110) surface.

The charge transfer to HCOO^m leaves all investigated surfaces with identical Δq_{slab} of 0.54 e and small differences in $\angle\text{OCO}$ of up to 1.3° , which is caused by steric effects and not due to electronic transfer. However, the Δq_{slab} is higher by 0.04 e for FCC Cu (110) with HCOO^b adsorbate than on the FCC Pd (110) and BCC CuPd (110), which might contribute to relatively higher stability of HCOO^b on the monometallic Cu surface, although the structure geometry is not strongly affected with discrepancies of $\angle\text{OCO}$ in HCOO^b of up to 1.6° between the three surfaces.

Therefore, the differences in E_{ads} of the intermediates in CO_2 hydrogenation to formate are linked to the relative stability of the surface upon donation of the charge at the low 1/12 ML (alloy surfaces) or 1/9 ML (metal surfaces) coverage of species studied here; while effects of the species coverage on the charge donation would yield more insight into the electronic structure, such investigation is beyond the scope of this work. For a monodentate species like HCOO^m the BCC CuPd (110) facet is more akin to the FCC Pd (110) surface, but for bidentate $\text{CO}_2^{\delta-}$ and HCOO^b the limited ability of electron donation via the bonding metal atoms or compensation of charge to the surrounding metal atoms at the surface layer results in E_{ads} higher than observed on the FCC Pd (110) surface. Further analysis is required to assess the effects of charge transfer on PdZn (101) and (110) surfaces.

5.3.7. Transition states

Wang *et al.* proposed a mechanism of CO₂ hydrogenation on Cu (110) involving the monodentate HCOO^{m*} species from which the HCOO^{b*} is formed. They observed that the transition state energy of initial CO₂ hydrogenation to formate is closely related to that of the HCOO^{m*} species. Effect of the carbon dioxide and formate geometry on the resulting transition state was assessed by performing a TS search on the PdZn (110) surface from CO₂ or CO₂^{δ-} and co-adsorbed hydrogen atom as the initial geometry to HCOO^{b*} or HCOO^{m*} as the final geometries. The influence of the chosen starting geometry on the final TS was then tabulated in Table 21.

Table 21. Comparison of the effect of starting geometries in CO₂ hydrogenation to formate on the resulting transition state (TS) energy and geometry, and the length of the minimum energy path (MEP); - denotes lack of data for a calculation which failed to converge.

| Starting species | Final species | MEP length /Å | TS energy /eV | <i>d</i> _{TS(M-C)} /Å | <i>d</i> _{TS(C-H)} /Å | ∠TS(O-C-O) /° |
|-------------------------------------|--------------------|---------------|---------------|--------------------------------|--------------------------------|---------------|
| *CO ₂ + *H | HCOO ^{b*} | 11.5 | 0.54 | 3.30 | 1.64 | 151.1 |
| *CO ₂ + *H | HCOO ^{m*} | 5.4 | 0.49 | 3.30 | 1.68 | 153.1 |
| *CO ₂ ^{δ-} + *H | HCOO ^{m*} | 7.1 | 0.50 | 2.95 | 1.71 | 152.2 |
| *CO ₂ ^{δ-} + *H | HCOO ^{b*} | - | - | - | - | - |

Starting from physisorbed CO₂ results in C-Pd distance in the TS elongated by 0.35 Å compared to starting with the chemisorbed geometry CO₂^{δ-}, but there are overall very small differences in C-H of up to 0.07 Å and of up to 0.05 eV in TS adsorption energy between the TS structures estimated using the different approaches. Starting from the CO₂^{δ-} and HCOO^{b*} resulted in a long and convoluted MEP involving multiple rotations in the initial path approximation and the calculation has ultimately failed to converge. In the longest converged MEP, the CO₂ first forms a monodentate HCOO^{m*} species as it is hydrogenated and rotates in an energy descent to give the bidentate HCOO^{b*} species, similarly to the mechanism on Cu (110) proposed by Wang *et al.*²⁴⁹ Based on the results in Table 21, the simultaneous Pd-H bond breaking and C-H formation appears to define the TS shape; hence the shortest MEP

length can be chosen to monitor the energetics of the process on PdZn at a reduced cost, *i.e.*, the CO₂ and HCOO^{m*} species.

5.3.8. Reaction energetics

To rationalise the changes in reactivity upon alloying the metals, CO₂ hydrogenation to formate was modelled using the shortest initially approximated MEPs and the most stable TS states found and the aspects of their geometry have been tabularised in Table 27 in the Appendix. The resulting activation energy for hydrogenation of physisorbed CO₂ to formate, $E_a(\text{CO}_2 + \text{H})$, activation energy for CO₂^{δ-} hydrogenation to formate, $E_a(\text{CO}_2^{\delta-} + \text{H})$, and the activation energy for decomposition of bidentate formate, $E_a(\text{HCOOb})$, were calculated in Figure 38. Formation of HCO and ½O₂ has been previously shown to require a high energy on Cu (110)⁵⁵, and on the more stable (111) facet of Pd^{63,72}. Hence, the dissociation of C–H in formate is thought to be preferred over C–O bond scission.

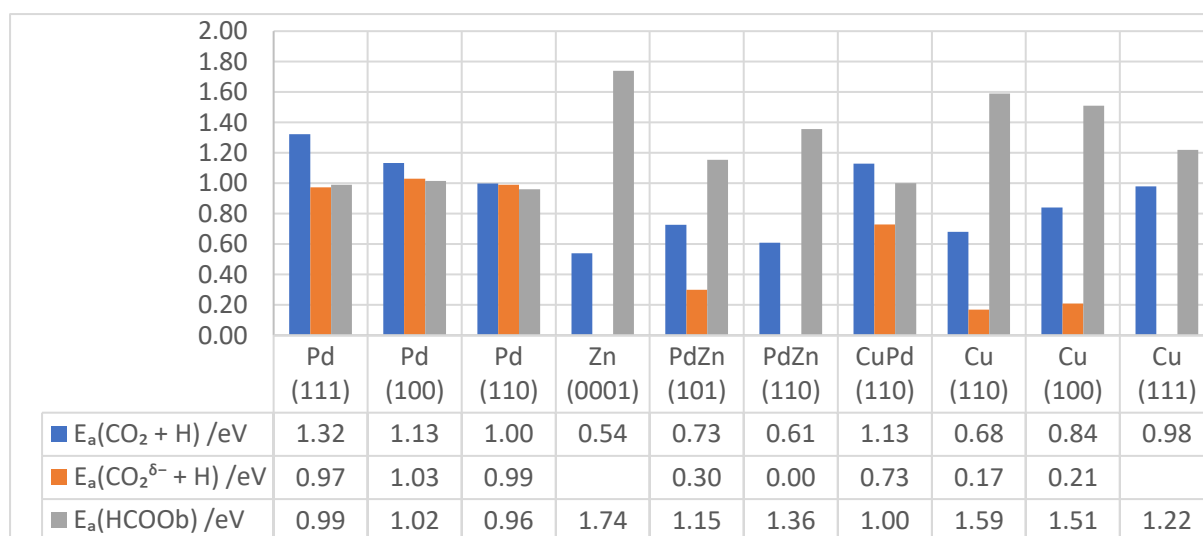


Figure 38. Activation energy of CO₂ and CO₂^{δ-} hydrogenation to HCOO and the reverse reaction on FCC Pd (111), (100), (110), FCC Cu (111), (100), (110), HCP Zn (0001), BCT PdZn (101), (110) and BCC CuPd (110) surfaces. Values missing for $E_a(\text{CO}_2^{\delta-} + \text{H})$ are due to lack of a metastable CO₂^{δ-} species on the Cu (111) and Zn (0001) surfaces.

Considering all the lowest energy TS structures obtained across the investigated Pd, Zn and PdZn surfaces, the metal-carbon bond ($d_{\text{TS}}(\text{C-M})$) is longer on PdZn than on Pd and the C-H

distance in the TS changes significantly from 1.15 - 1.23 Å on Pd to 1.60 - 1.68 Å on PdZn surfaces, similarly to the 1.63 Å observed on the monometallic Zn surface. Similarly, the C–H distance on Cu surfaces spans from 1.61 – 1.63 Å and on CuPd (110) is intermediary to Cu and Pd with C–H distance of 1.43 Å. The results imply that on Pd and CuPd surfaces the most energy intensive aspect of the TS formation is the cleavage of the bond between the H atom and the surface. On Cu, Zn and PdZn surfaces, the CO₂ activation and bending contributes more to the hydrogenation energy barrier. Further, both HCOO^{b*} and HCOO^{m*} species show stronger E_{ads} on surfaces with higher energies. The HCOO^{m*} species is less stable than CO₂^{δ-} on Pd and CuPd surfaces, but it is more stable than CO₂^{δ-} on PdZn and Cu surfaces. The observations are hinting a possible change in mechanism of CO₂ hydrogenation towards the formate species. Since the H atom is more exposed on the PdZn surfaces than on Pd, the adsorbing CO₂ can react with it directly from the gas phase, *i.e.*, an Eley-Rideal type mechanism instead of a Langmuir-Hinshelwood, where the CO₂^{δ-} and H species co-exist adsorbed on the surface prior to bonding.

$E_{\text{a}}(\text{CO}_2 + \text{H})$, is 0.33, 0.11 and 0.04 eV less favourable than the reverse process on Pd (111), (100) and (110), respectively, meaning that the formate decomposition process is competitive to CO₂ hydrogenation on Pd. Moreover, the $E_{\text{a}}(\text{CO}_2 + \text{H})$ is 0.35 eV (45%) higher than $E_{\text{a}}(\text{CO}_2)$ on the Pd (110) surface, hence the majority of the CO₂ substrate forms CO rather than undergoing direct hydrogenation. The Pd (110) surface was previously highlighted as the most suitable low-index Pd surface for CO₂ hydrogenation to methanol in Chapter 3, and here $E_{\text{a}}(\text{CO}_2)$ was shown to be almost double that of $E_{\text{a}}(\text{CO}_2 + \text{H})$, indicating that on the Pd (110) surface the CO chemistry is limited in favour of CO₂ hydrogenation. In contrast, $E_{\text{a}}(\text{CO}_2 + \text{H})$ on Cu surfaces is much lower than $E_{\text{a}}(\text{HCOO}_b)$, hence formate remains stable once formed. On CuPd (110) surface hydrogenation of CO₂ towards formate is preferred by 0.26 eV over CO₂ dissociation, but as previously shown, the HCOO^{b*} species shows an E_{ads} 0.58 eV higher than on Cu (110), which can facilitate the reaction by limiting the poisoning effect of formate observed on Cu surfaces. The low $E_{\text{a}}(\text{CO}_2 + \text{H})$ of 0.54 eV on the Zn (0001) surface is an artifact of the definition of activation energy of CO₂ hydrogenation used in this work, which assumes a chemisorbed H in the initial stage of the reaction. Hydrogen adsorption is very unfavourable on Zn, hence the initial configuration is already a high energy state, and the TS on Zn (0001)

is the highest in energy with respect to gas substrates across all modelled surfaces as can be seen in the reaction energy profiles in Figure 39.

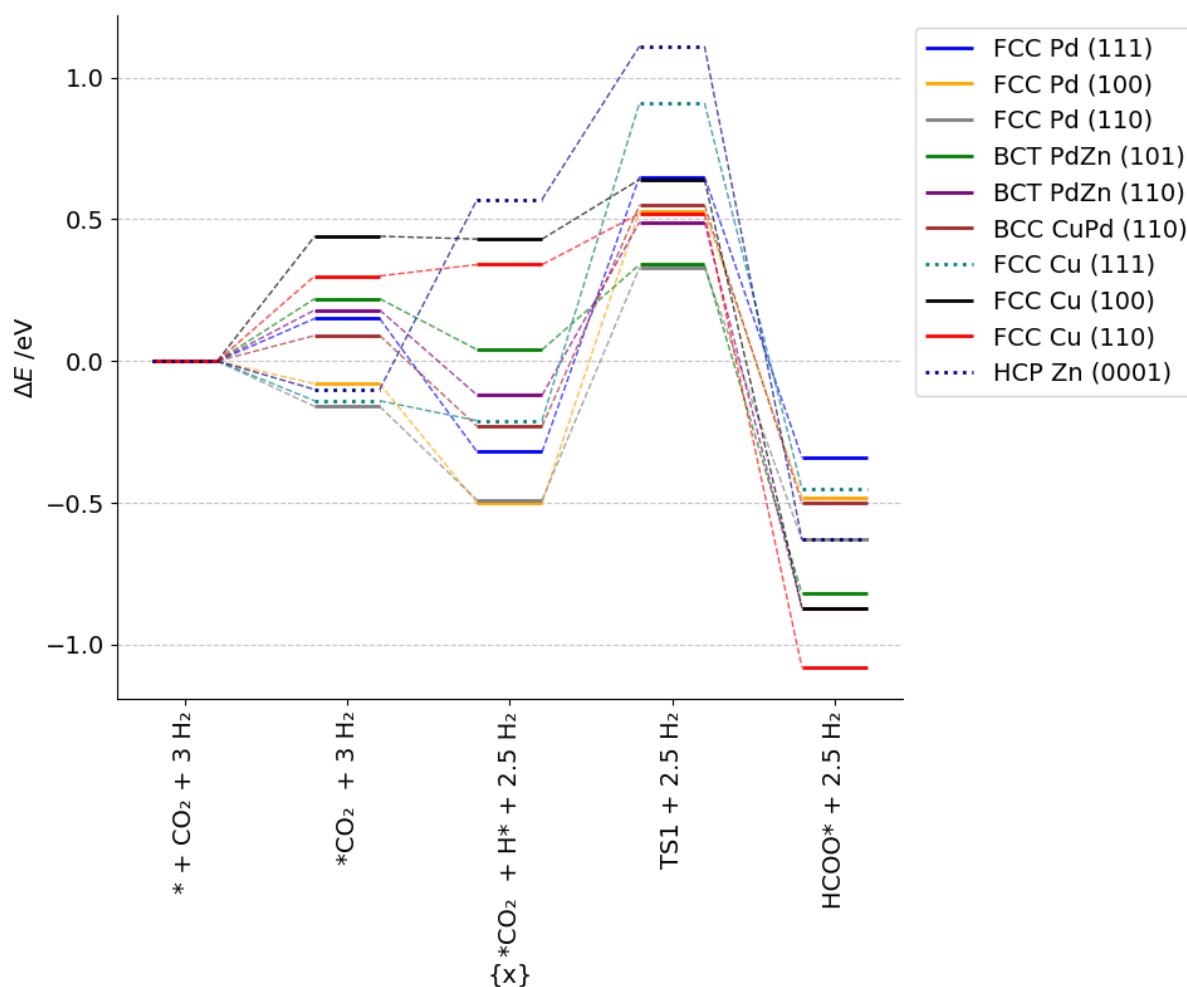


Figure 39. Reaction energy profiles of initial hydrogenation of CO_2 to HCOO on FCC Cu, Pd, HCP Zn, BCT PdZn and BCC CuPd surfaces in units of eV. The preferred adsorbed CO_2 geometry for the transition state calculation was the bent chemisorbed $\text{CO}_2^{\delta-}$ (solid line). Metastable $\text{CO}_2^{\delta-}$ geometry was not found on FCC Cu (111) and HCP Zn (0001), thus the physisorbed CO_2 was used instead (dotted lines); * denotes a surface and surface-bound intermediates.

The $E_a(\text{CO}_2^{\delta-} + \text{H})$ of 0.30 eV on PdZn (101) the barrierless $E_a(\text{CO}_2^{\delta-} + \text{H})$ on PdZn (110) indicate that removal of the H atom from the surface to form a C-H bond requires less energy than on Pd, and the relative E_{ads} of CO_2 and $\text{CO}_2^{\delta-}$ constitutes most of the barrier. Thus, the CO_2 activation remains challenging on the surface of the pristine PdZn surfaces, but hydrogenating $\text{CO}_2^{\delta-}$ is much more efficient than on Pd. The trends observed help explain the initially low reactivity of these catalysts or overall lower activity of PdZn supported on materials other

than ZnO, where ZnO is not in excess.²⁰ An induction period is required for ZnO islands to form on the surface of the PdZn catalyst, which aids CO₂ binding via oxygen vacancies in strongly reducing environment.^{45,230,231} Once CO₂ is chemically activated and in the vicinity of H activated on PdZn, the hydrogenation to the methanol precursor, *i.e.*, formate, can occur on the alloy surface, thereby enabling the reaction. However, this thesis does not encompass the calculations necessary to validate the hypothesis of a change in mechanism from Eley-Rideal to Langmuir-Hinshelwood at the MSI, such as the CO₂ hydrogenation on ZnO clusters situated on periodic PdZn surfaces.

Further, Pearson correlation was calculated for quantities derived from relevant carbon dioxide, formate and transition state structures tabulated in Table 27 in the Appendix. No clear correlation was found between the geometries of TS structures or their energies and properties of the initial structures taking part in the reactions modelled. However, sets of derived quantities based on the HCOO^{m*} intermediates clearly correlated with the initial CO₂ hydrogenation energy have been identified and plotted in Figure 40-42.

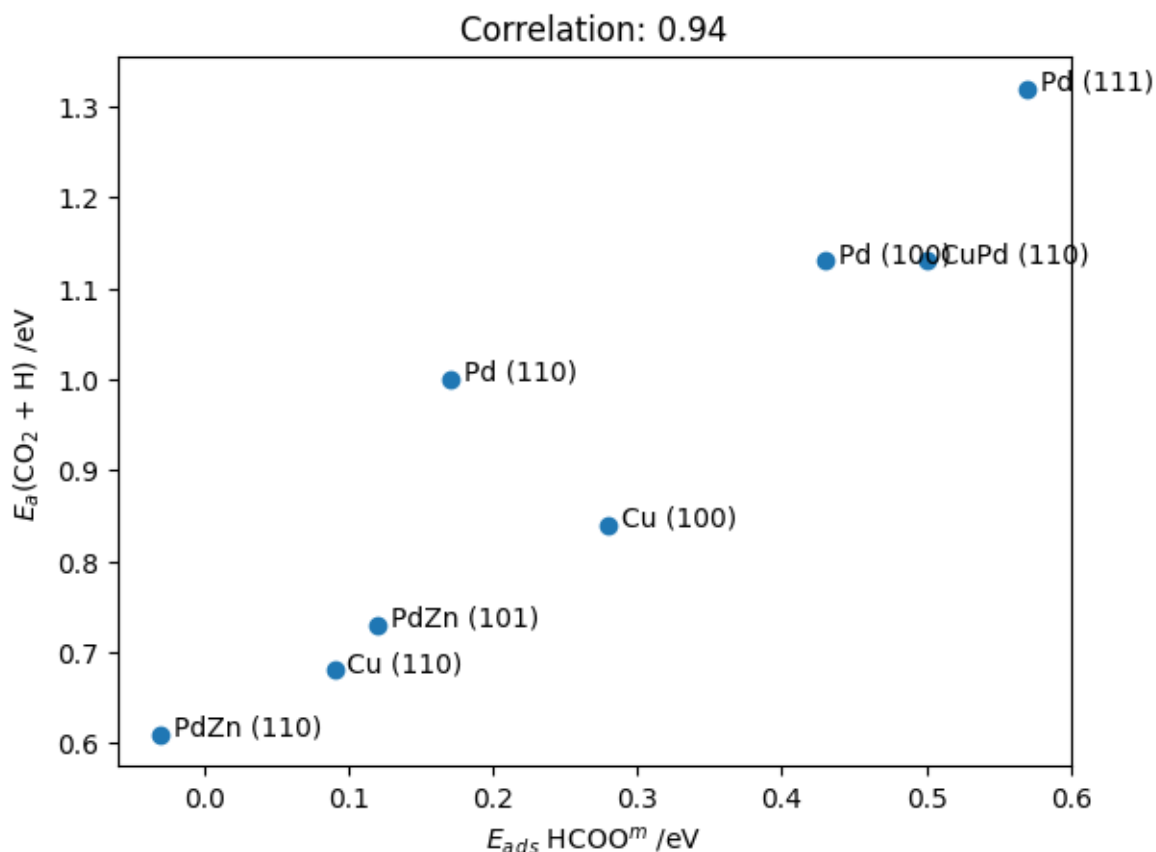


Figure 40. Pearson correlation of $E_a(\text{CO}_2 + \text{H})$ and E_{ads} of HCOO^m across Pd (111), (100), (110), Cu (100), (110), CuPd (110), PdZn (101) and (110) surfaces. A positive Pearson correlation of 0.94 was found, the linear coefficient of determination, R^2 , is 0.88.

Figure 40 shows the positive linear correlation of $E_a(\text{CO}_2 + \text{H})$ and E_{ads} of HCOO^{m*} across Pd (111), (100), (110), Cu (100), (110), CuPd (110), PdZn (101) and (110) surfaces. Figure 41 and Figure 42 show that the size of the O-C-O bond angle is linearly and positively correlated to $E_a(\text{CO}_2^{\delta-} + \text{H})$ and the ratio of $E_a(\text{CO}_2 + \text{H})$ and $E_a(\text{HCOOb})$, abbreviated as E_f/E_r (ratio of E_a of the forward reaction step : E_a of the reverse reaction step). Such simplistic relationships of adsorbed intermediates and trends in reaction energetics have previously been proposed in the work of Hansen *et al.*, who mapped the electrocatalytic activity of metals in CO_2 reduction by comparing the binding energies of COOH and CO intermediates and has shown a scaling relation of electrocatalytic activity with E_{ads} of COOH and CO.²⁵¹

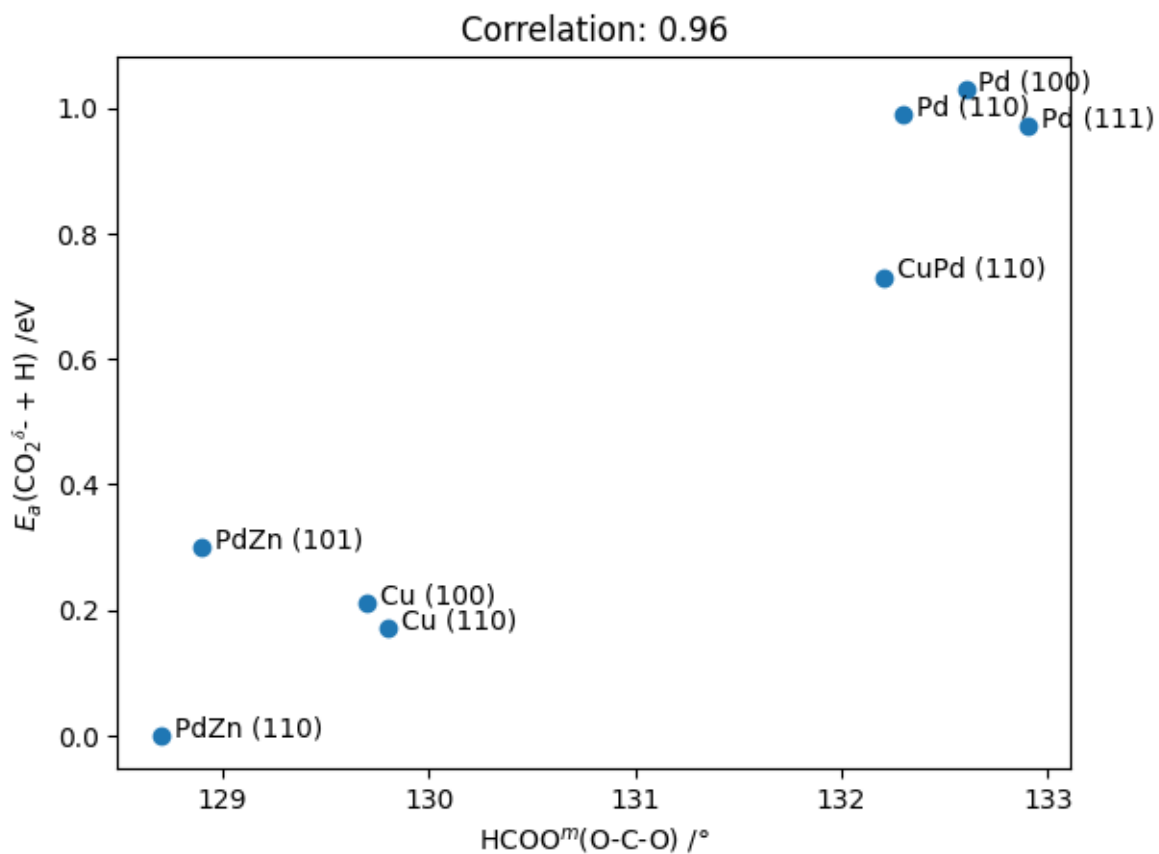


Figure 41 Pearson correlation of $E_a(\text{CO}_2^{\delta-} + \text{H})$ and HCOO^m O-C-O angle across Pd (111), (100), (110), Cu (100), (110), CuPd (110), PdZn (101) and (110) surfaces. A positive Pearson correlation of 0.94 was found, the linear coefficient of determination, R^2 , is 0.92.

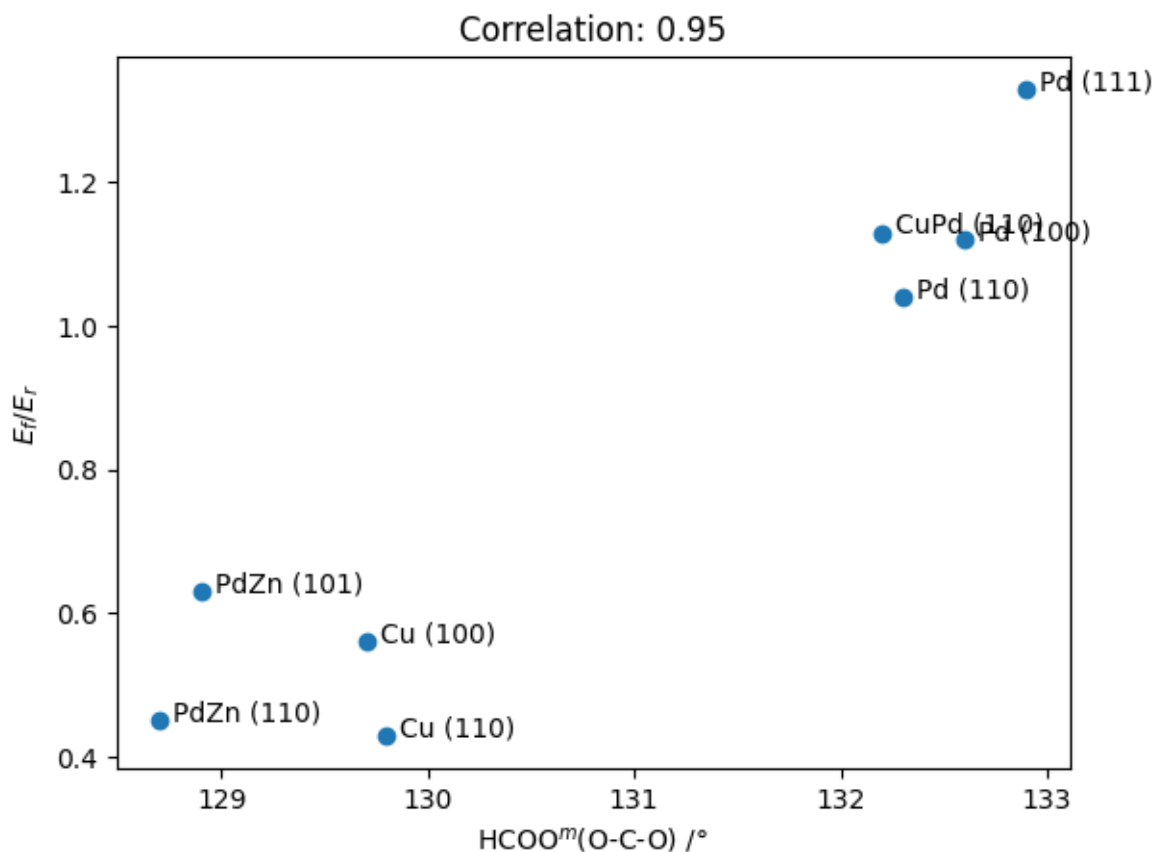


Figure 42. Pearson correlation of E_f/E_r , *i.e.*, the ratio of the activation energy of the forward and reverse reaction of CO_2 hydrogenation to formate ($E_a(\text{CO}_2 + \text{H})$ divided by $E_a(\text{HCOOb})$), and HCOO^m O-C-O bond angle across Pd (111), (100), (110), Cu (100), (110), CuPd (110), PdZn (101) and (110) surfaces. A positive Pearson correlation of 0.95 was found, the linear coefficient of determination, R^2 , is 0.90.

The properties of monodentate formate intermediate, especially the E_{ads} , O-C-O angle and C-H bond distance, emerge as a suitable descriptors of reaction energies. If the trends hold on other Pd-based alloys, modelling HCOO^{m*} species could be used to efficiently estimate the $E_a(\text{CO}_2 + \text{H})$ without running expensive NEB calculations for transition state search. Moreover, based on HCOO^{m*} geometry, the $E_a(\text{CO}_2^{\delta-} + \text{H})$ could be deduced and give access to relative differences between adsorption of CO_2 and $\text{CO}_2^{\delta-}$. Further, the E_f/E_r ratio could be deduced, thus giving a broad overview of the reaction energetics from simple calculations of HCOO^{m*} geometry.

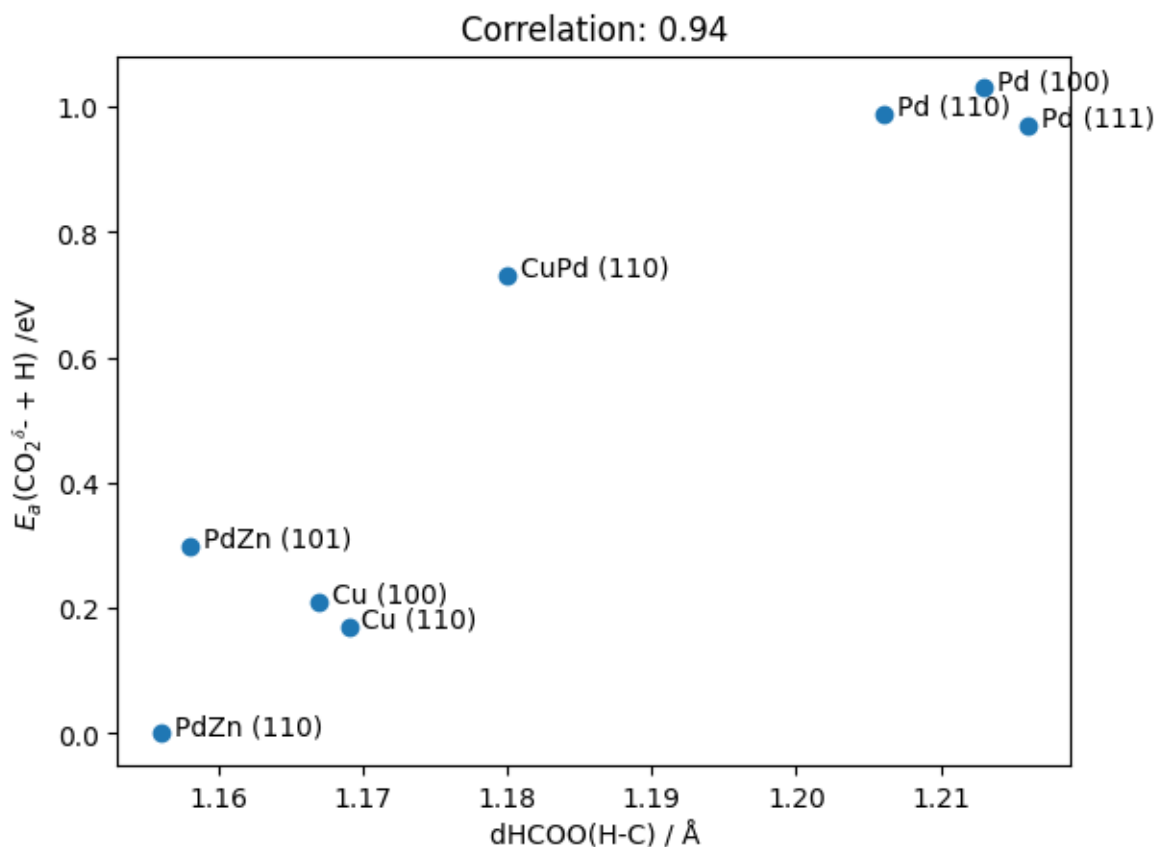


Figure 43. Pearson correlation of $E_a(\text{CO}_2^{\delta-} + \text{H})$ and hydrogen-carbon bond distance in $\text{HCOO}^{\text{m*}}$, $d\text{HCOO(H-C)}$, across Pd (111), (100), (110), Cu (100), (110), CuPd (110), PdZn (101) and (110) surfaces. A positive Pearson correlation of 0.94 was found, the linear coefficient of determination, R^2 , is 0.88.

Across the investigated surfaces, $\text{HCOO}^{\text{m*}}$ shows significant changes in the hydrogen-carbon bond distance, $d\text{HCOO(H-C)}$, which is linearly correlated to $E_a(\text{CO}_2^{\delta-} + \text{H})$ as shown in Figure 43. Ghiringelli *et al.* postulated that exploration of scaling relations is a promising approach for rational material design, but care must be taken for machine-learned descriptors with unclear causality of their property predictions.²⁵² $\text{HCOO}^{\text{m*}}$ structure captures the interaction of the surface with hydrogen and with the oxygen atoms in the intermediates, hence the information deduced from the correlations is logical. The surfaces on which no metastable $\text{HCOO}^{\text{m*}}$ was found, *i.e.*, the Cu (111) and Zn (0001) surface also have shown no $\text{CO}_2^{\delta-}$ and overall large $E_a(\text{CO}_2 + \text{H})$. Therefore, the absence of the metastable geometry is also informative, however, further work is required to confirm whether the $\text{HCOO}^{\text{m*}}$ intermediate can be used in high throughput analysis of trimetallic alloy surfaces for CO_2 hydrogenation.

5.4. Conclusions and future work

The synthesis of methanol from CO₂ and hydrogen using Pd-based alloy catalysts holds great potential for sustainable energy storage. Gaining deeper understanding of the initial stages of CO₂ hydrogenation on Pd-based catalysts is essential for understanding the reactivity variations observed upon alloying and facilitating the strategic design of novel catalysts. Here, we have investigated the initial CO₂ hydrogenation to formate and CO₂ dissociation reactions across monometallic FCC Pd (111), (100), (110), FCC Cu (111), (100), (110), HCP Zn (0001) surfaces and BCC CuPd (110) and BCT PdZn (101) and (110) alloy facets.

Firstly, we modelled the hydrogen adsorption, showing that upon alloying Pd with Zn, the preferential adsorption sites of hydrogen atoms on PdZn (101) and (110) are the Pd-Pd bridging sites instead of the hollow sites as is the case for Pd (111), (100) and (110). The CuPd (110) strongly adsorbs hydrogen in the hollow position, but the Cu atop sites, similarly to Zn atop sites on PdZn, are strongly endothermic. We show that CO adsorption on PdZn facets is less favourable than on Pd surfaces, and preferred adsorption sites are identical with those of the adsorbing hydrogen. Then, the physisorption of CO₂ and chemisorption of CO₂^{δ-} was modelled, and the chemisorption on CuPd (110) and PdZn (101) and (110) surfaces is endothermic, and no chemisorbed species was found on the Cu (111) and Zn (0001) surfaces. Hydrogen co-adsorbed on the surfaces next to CO₂^{δ-} results in destabilisation as compared to separate adsorption of the species. A lower activation barrier towards CO₂ dissociation was observed on PdZn (101) and CuPd (110) as compared to lowest energy Pd (111) surface, however, the Pd (100) has overall the lowest activation energy towards CO₂ dissociation. The reverse reaction proceeds with lowest barriers on Pd (111), (100) and Cu (110) and (100) surfaces.

The thermodynamically more stable bidentate formate (HCOO^b) species adsorbs the strongest on Cu and PdZn surfaces, while the monodentate formate (HCOO^m) shows an exothermic adsorption on the PdZn (110) surface, and adsorption of both species is stronger on higher energy surfaces. Using Mulliken charge analysis, we show that more electron density is transferred from the surface onto the HCOO^m than onto the HCOO^b across Cu, Pd

and CuPd (110) surfaces. Further, we show that on Pd-based alloy surfaces, the choice of the initial geometries from CO_2 , $\text{CO}_2^{\delta-}$, HCOO^m and HCOO^b influences the calculation complexity and length of the minimum energy path but has little effect on the final TS energy. Cu and PdZn surfaces have shown lowest hydrogenation barriers. CuPd (110) has a similar activation energy to Pd surfaces, but the formate adsorption energy is halved. CO_2 activation constitutes a major part of the CO_2 hydrogenation barrier on PdZn and Cu surfaces, suggesting an Eley-Rideal mechanism as opposed to the Langmuir-Hinshelwood model. Finally, adsorption energy of the HCOO^m was found to linearly correlate with the energy required for hydrogenation of the CO_2 species, while the geometry of HCOO^m correlates well with the energy required for activation of the chemisorbed $\text{CO}_2^{\delta-}$ species towards formate.

Overall, we investigated the initial stages of CO_2 hydrogenation and CO_2 dissociation reactions on FCC Pd (111), (100), (110), FCC Cu (111), (100), (110), HCP Zn (0001), BCC CuPd (110), and BCT PdZn (101) and (110) surfaces. Our findings indicate that Cu and PdZn surfaces exhibit lower hydrogenation barriers, CuPd (110) shows similar reactivity to Pd surfaces with reduced formate adsorption energy resulting in alleviation of the poisoning effect of the formate on the reaction as compared to Cu surfaces. The high CO_2 activation energy plays a crucial role in the CO_2 hydrogenation barrier on PdZn and Cu surfaces, suggesting an Eley-Rideal mechanism. Future work will entail a comprehensive investigation of the HCOO^m species across diverse Pd-based alloy surfaces, aiming to thoroughly explore the initial energetics of CO_2 hydrogenation, which are strongly correlated to the characteristics of the HCOO^m species.

Chapter 6. Summary, Conclusions and Future Prospects

In this thesis, we investigated the process of CO₂ hydrogenation to methanol on Pd-based catalysts with the aim of advancing sustainable energy storage technologies. Through state-of-the-art density functional theory calculations, we explored the reactivity of CO₂ and hydrogen on Pd and Pd-based alloy surfaces in the context of CO₂ hydrogenation to methanol. Additionally, we investigated the effects of alloying Cu and Zn into Pd on the activation energy barriers for CO₂ activation and hydrogenation. The analyses provided valuable insights into the fundamental aspects of the reaction and the design principles for efficient catalysts. Here, a summary of the key findings from each chapter is presented, highlighting their significance in CO₂ hydrogenation and offering directions for future research.

Chapter 3 focused on the hydrogenation of CO₂ to methanol on Pd (111), (100) and (110) surfaces as catalysts. We demonstrated the stability of hydrogen on Pd surfaces and showed that high coordination sites exhibit the strongest hydrogen adsorption energy. Moreover, we observed that hydrogen is mobile on the surfaces, facilitated by the connection of adsorption sites through low-energy diffusion channels. The transition state for CO₂ hydrogenation to form formate was found to be endothermic with respect to the gas-phase substrates on Pd (111), (100) and (110) surfaces, suggesting its negative influence on the overall reaction rate. We showed that increased temperature facilitated CO₂ chemisorption on Pd (100) and (110) surfaces but had adverse effects on other reaction steps. Finally, Gibbs free energy analysis showed that CO₂ hydrogenation on Pd surfaces is inhibited at the first hydrogenation step towards formate, and Pd-based CO₂ hydrogenation catalysts should possess a lower Pd-H binding strength to enhance the reaction.

In Chapter 4, we explored the adsorption of hydrogen on Pd (111) and (100) surfaces, considering a fully enumerated, statistically significant number of configurations of hydrogen atoms on Pd surfaces at coverages from $\frac{1}{9}$ up to 2 monolayers. Our calculations revealed that the inclusion of zero-point energy is crucial for accurate representation of hydrogen adsorption energy on Pd surfaces. We observed that subsurface hydrogen adsorption becomes thermodynamically favourable as the next adsorption once Pd (111) and (100) surfaces are covered with one monolayer of hydrogen. At mild conditions of 500 K

temperature and pressure of 1 atm, the free energy of hydrogen adsorption is negative up to $\frac{13}{9}$ and $\frac{10}{9}$ monolayer of hydrogen on Pd (111) and (100), respectively; thus, subsurface hydrogen is present on Pd surfaces at conditions typical for CO₂ hydrogenation to methanol and can contribute to the reactivity of the Pd facets. Importantly, the coverage of hydrogen significantly influenced the free energy landscape, emphasising the necessity of considering hydrogen concentration when simulating hydrogenation reactions. Based on this result, a correction to the free energy barriers of hydrogenation steps is applicable to the results presented in Chapter 3 for the Pd (111) surface to account for the low hydrogen coverage, though the free energy barriers in CO₂ hydrogenation to methanol on Pd (111) are 3 to 5 times higher than the contribution and qualitative conclusions from Chapter 3 remain unaffected. Further analysis of Pd (100) configurations and the derivation of an effective surface phase diagram under industrially relevant conditions were identified as essential future research directions.

Chapter 5 delved into the initial stages of CO₂ hydrogenation on Pd-based catalysts, considering both low Miller index monometallic FCC Cu, FCC Pd and HCP Zn, and alloy BCC CuPd and BCT PdZn surfaces. Our investigations revealed that alloying Pd with Zn had a notable impact on the adsorption behaviour of hydrogen and CO species. The preferential adsorption sites for hydrogen shifted upon alloying Pd with Zn from the hollow sites to the Pd-Pd bridge sites, and CO adsorption on PdZn surfaces became less favourable compared to Pd surfaces. PdZn surfaces have lower barriers for CO₂ hydrogenation than Pd facets, and the CO₂ activation energy constitutes a significant portion of the barrier, suggesting an Eley-Rideal mechanism of CO₂ hydrogenation, as opposed to the Langmuir-Hinshelwood mechanism proposed for Pd surfaces. Additionally, the adsorption of formate species differed across surfaces, with stronger adsorption observed on Cu and PdZn surfaces. In contrast, the adsorption of formate on CuPd surface was substantially weakened with respect to low-index Cu surfaces, and the CuPd (110) surface had a significantly higher CO₂ dissociation energy than that on Pd (100). Finally, the activation energy barriers of CO₂ hydrogenation to formate were found to correlate linearly with the energy of adsorption, size of the O-C-O bond angle and C-H bond length of the monodentate formate intermediate, suggesting that the species can be used for efficient benchmarking of the Pd-based alloy surfaces without performing complex calculations of transition states. The findings provide valuable insights for the

strategic design of Pd-based alloy catalysts and shed light on the reaction mechanisms involved in CO₂ hydrogenation. Future work will entail Gibbs free energy analysis of the hydrogen adsorption on Pd-based alloy surfaces akin to the research in Chapter 4, and the use of the monodentate formate species as a descriptor for high-throughput computational analysis of Pd-based alloy surfaces.

The research can be further expanded by considering trimetallic Pd-based alloys containing Cu, Zn, and other metals that have been identified as capable of CO₂ activation, either on their metal surfaces or their oxides. Additional metals include gold, cerium, gallium, and indium among others.^{253–256} The search for stable trimetallic nanoalloys can be efficiently complemented by high-throughput analysis of such Pd-alloy surfaces.

Future research would benefit from machine learning approaches, such as subgroup discovery or hierarchical symbolic regression, for rationalisation of chemical activity of the Pd-based alloy materials.^{81,257} These approaches allow searching trends in vast amounts of data and formulation of complex descriptors without any expert bias. Subgroup discovery can be used for identification of subgroups of active Pd-based alloy surfaces sharing common intrinsic properties, thus helping to narrow down the vast search space of trimetallic catalysts suitable for CO₂ hydrogenation to methanol.⁸¹ The hierarchical symbolic regression could be applied to the data obtained in the thesis combined with experimental data on the efficiency of the catalysts to identify the underlying causes of increased activity across a broad range of Pd-alloy nanoparticle catalysts. Using hierarchical symbolic regression, origins of the improved chemical reactivity can be expressed in a human-comprehensible mathematical expression relating materials properties and key physical parameters, which would further improve the understanding of underlying material properties resulting in desired activity in CO₂ hydrogenation to methanol.²⁵⁷

Finally, the combination of theoretical and experimental data in the literature suggests that the most important chemical reactivity occurs at the metal-support interface on metal oxide-covered surfaces. The hypothesis can be validated by modelling of metal oxide clusters, *e.g.*, ZnO, on periodic surfaces of Pd-based alloy surfaces and investigating the reactivity of CO₂ hydrogenation at the metal-support interface.

In conclusion, this thesis contributes to the understanding of CO₂ hydrogenation to methanol on Pd-based catalysts by means of detailed investigation of the identified key mechanistic steps. The findings underscore the importance of designing efficient catalysts with lower barriers for initial CO₂ hydrogenation. Additionally, the influence of hydrogen coverage on the reaction thermodynamics and the impact of alloying on the adsorption behaviour were highlighted. By combining the insights from this thesis and emerging new data analysis approaches, we can strive towards the development of highly efficient catalysts for the sustainable synthesis of methanol from CO₂ and hydrogen, contributing to the advancement of green energy storage technologies.

References

- 1.) IEA (2021), *Global Energy Review 2021*, IEA, Paris <https://www.iea.org/reports/global-energy-review-2021>, License: CC BY 4.0.
- 2.) P. Anastas and N. Eghbali, *Chem. Soc. Rev.*, 2009, **39**, 301–312.
- 3.) P. T. Anastas and M. M. Kirchhoff, *Acc. Chem. Res.*, 2002, **35**, 686–694.
- 4.) IEA (2019), *World Energy Outlook 2019*, IEA, Paris <https://www.iea.org/reports/world-energy-outlook-2019>, License: CC BY 4.0.
- 5.) IEA (2013), *Technology Roadmap - Energy and GHG Reductions in the Chemical Industry via Catalytic Processes*, IEA, Paris <https://www.iea.org/reports/technology-roadmap-energy-and-ghg-reductions-in-the-chemical-industry-via-catalytic-processes>, License: CC BY 4.0
- 6.) P. Atkins and J. de Paula, *Physical Chemistry*, Oxford University Press, 10th edn., 2014.
- 7.) A. Bhargava, S. Shelke, M. Dilkash, N. S. Chaubal-Durve, P. D. Patil, S. S. Nadar, D. Marghade and M. S. Tiwari, *Reviews in Chemical Engineering, Reviews in Chemical Engineering*, 2023, **39**, 7, p. 1187-1226.
- 8.) M. K. Gupta, in *Practical Guide to Vegetable Oil Processing (Second Edition)*, ed. M. K. Gupta, AOCS Press, 2017, p. 171–215.
- 9.) S. Kraft, K. Ryan and R. B. Kargbo, *J. Am. Chem. Soc.*, 2017, **139**, 11630–11641.
- 10.) E. R. Nesbitt, *Industrial Biotechnology*, 2020, **16**, 147–163.
- 11.) M. Bowker, *ChemCatChem*, 2019, **11**, 4238–4246.
- 12.) L. Wang, Y. Yi, H. Guo and X. Tu, *ACS Catal.*, 2018, **8**, 1, 90–100
- 13.) A. Erdöhelyi, M. Pásztor and F. Solymosi, *Journal of Catalysis*, 1986, **98**, 166–177.
- 14.) N. Iwasa, H. Suzuki, M. Terashita, M. Arai and N. Takezawa, *Catalysis Letters*, 2004, **96**, 75–78.
- 15.) N. Lawes, I. E. Gow, L. R. Smith, K. J. Aggett, J. S. Hayward, L. Kabalan, A. J. Logsdail, T. J. A. Slater, M. Dearg, D. J. Morgan, N. F. Dummer, S. H. Taylor, M. Bowker, C. R. A. Catlow and G. J. Hutchings, *Faraday Discuss.*, 2023, **242**, 193–211.
- 16.) H. Lorenz, C. Rameshan, T. Bielez, N. Memmel, W. Stadlmayr, L. Mayr, Q. Zhao, S. Soisuwan, B. Klötzer and S. Penner, *ChemCatChem*, 2013, **5**, 1273–1285.
- 17.) T. Fujitani, M. Saito, Y. Kanai, T. Watanabe, J. Nakamura and T. Uchijima, *Applied Catalysis A: General*, 1995, **125**, L199–L202.
- 18.) N. Aas, Y. Li and M. Bowker, *J. Phys.: Condens. Matter*, 1991, **3**, S281.
- 19.) H. Bahruji, M. Bowker, G. Hutchings, N. Dimitratos, P. Wells, E. Gibson, W. Jones, C. Brookes, D. Morgan and G. Lalev, *Journal of Catalysis*, 2016, **343**, 133–146.

- 20.) M. Bowker, N. Lawes, I. Gow, J. Hayward, J. R. Esquiús, N. Richards, L. R. Smith, T. J. A. Slater, T. E. Davies, N. F. Dummer, L. Kabalan, A. Logsdail, R. C. Catlow, S. Taylor and G. J. Hutchings, *ACS Catal.*, 2022, **12**, 5371–5379.
- 21.) M. Bowker, R. A. Hadden, H. Houghton, J. N. K. Hyland and K. C. Waugh, *Journal of Catalysis*, 1988, **109**, 263–273.
- 22.) J. W. M. Crawley, I. E. Gow, N. Lawes, I. Kowalec, L. Kabalan, C. R. A. Catlow, A. J. Logsdail, S. H. Taylor, N. F. Dummer and G. J. Hutchings, *Chem. Rev.*, 2022, **122**, 6795–6849.
- 23.) A. J. Medford, A. Vojvodic, J. S. Hummelshøj, J. Voss, F. Abild-Pedersen, F. Studt, T. Bligaard, A. Nilsson and J. K. Nørskov, *Journal of Catalysis*, 2015, **328**, 36–42.
- 24.) V. Dubois, D. Desmecht, L. Rkiouak, A.-S. Jacquet, T. Hoshinoo, K. Nakagawa and S. Hermans, *Reac Kinet Mech Cat*, 2019, **126**, 399–415.
- 25.) P. H. Jen, Y. H. Hsu and S. D. Lin, *Catalysis Today*, 2007, **123**, 133–141.
- 26.) D. Allam, S. Bennici, L. Limousy and S. Hocine, *Comptes Rendus Chimie*, 2019, **22**, 227–237.
- 27.) G. C. Chinchén, P. J. Denny, D. G. Parker, M. S. Spencer and D. A. Whan, *Applied Catalysis*, 1987, **30**, 333–338.
- 28.) M. Van den Bossche, C. Rose-Petruck and H. Jónsson, *J. Phys. Chem. C*, 2021, **125**, 25, 13802–13808
- 29.) R. J. Behm, K. Christmann and G. Ertl, *Surface Science*, 1980, **99**, 320–340.
- 30.) X. Zhao, Y. Chang, W.-J. Chen, Q. Wu, X. Pan, K. Chen and B. Weng, *ACS Omega*, 2022, **7**, 17–31.
- 31.) H. Conrad, G. Ertl and E. E. Latta, *Surface Science*, 1974, **41**, 435–446.
- 32.) W. Dong, V. Ledentu, Ph. Sautet, A. Eichler and J. Hafner, *Surface Science*, 1998, **411**, 123–136.
- 33.) M. G. Cattania, V. Penka, R. J. Behm, K. Christmann and G. Ertl, *Surface Science*, 1983, **126**, 382–391.
- 34.) L. Álvarez-Falcón, F. Viñes, A. Notario-Estévez and F. Illas, *Surface Science*, 2016, **646**, 221–229.
- 35.) Yin and J. Liebscher, *Chem. Rev.*, 2007, **107**, 133–173.
- 36.) F. Solymosi, A. Erdöhelyi and M. Lancz, *Journal of Catalysis*, 1985, **95**, 567–577.
- 37.) F. Solymosi, *Journal of Molecular Catalysis*, 1991, **65**, 337–358.
- 38.) F. Solymosi and A. Berkó, *Journal of Catalysis*, 1986, **101**, 458–472.
- 39.) W. Wang, S. Wang, X. Ma and J. Gong, *Chemical Society Reviews*, 2011, **40**, 3703–3727.
- 40.) M. D. Porosoff, B. Yan and J. G. Chen, *Energy Environ. Sci.*, 2016, **9**, 62–73.
- 41.) R. Brosseau, T. H. Ellis and H. Wang, *Chemical Physics Letters*, 1991, **177**, 118–122.
- 42.) A. Beck, M. Zabilskiy, M. A. Newton, O. Safonova, M. G. Willinger and J. A. van Bokhoven, *Nat Catal*, 2021, **4**, 488–497.

- 43.) M. Zabilskiy, V. L. Sushkevich, D. Palagin, M. A. Newton, F. Krumeich and J. A. van Bokhoven, *Nat Commun*, 2020, **11**, 2409.
- 44.) K. M. V. Bussche and G. F. Froment, *Journal of Catalysis*, 1996, **161**, 1–10.
- 45.) M. Heggen, S. Penner, M. Friedrich, R. E. Dunin-Borkowski and M. Armbrüster, *J. Phys. Chem. C*, 2016, **120**, 10460–10465.
- 46.) J. Schumann, M. Eichelbaum, T. Lunkenbein, N. Thomas, M. C. Álvarez Galván, R. Schlögl and M. Behrens, *ACS Catal.*, 2015, **5**, 3260–3270.
- 47.) S. Kattel, P. J. Ramírez, J. G. Chen, J. A. Rodriguez and P. Liu, *Science*, 2017, **355**, 1296–1299.
- 48.) J. Xu, X. Su, X. Liu, X. Pan, G. Pei, Y. Huang, X. Wang, T. Zhang and H. Geng, *Applied Catalysis A: General*, 2016, **514**, 51–59.
- 49.) J. Wang, B. Hokkanen and U. Burghaus, *Surface Science*, 2005, **577**, 158–166.
- 50.) J. Díez-Ramírez, J. L. Valverde, P. Sánchez and F. Dorado, *Catal Lett*, 2016, **146**, 373–382.
- 51.) E. Nowicka, S. M. Althahban, Y. Luo, R. Kriegel, G. Shaw, D. J. Morgan, Q. He, M. Watanabe, M. Armbrüster, C. J. Kiely and G. J. Hutchings, *Catal. Sci. Technol.*, 2018, **8**, 5848–5857.
- 52.) A. Arandia, J. Yim, H. Warraich, E. Leppäkangas, R. Bes, A. Lempelto, L. Gell, H. Jiang, K. Meinander, T. Viinikainen, S. Huotari, K. Honkala and R. L. Puurunen, *Applied Catalysis B: Environmental*, 2023, **321**, 122046.
- 53.) R. M. Palomino, P. J. Ramírez, Z. Liu, R. Hamlyn, I. Waluyo, M. Mahapatra, I. Orozco, A. Hunt, J. P. Simonovis, S. D. Senanayake and J. A. Rodriguez, *J. Phys. Chem. B*, 2018, **122**, 794–800.
- 54.) E. Lundgren, A. Mikkelsen, J. N. Andersen, G. Kresse, M. Schmid and P. Varga, *J. Phys.: Condens. Matter*, 2006, **18**, R481–R499.
- 55.) M. D. Higham, M. G. Quesne and C. R. A. Catlow, *Dalton Trans.*, 2020, **49**, 8478–8497.
- 56.) J. P. Clay, J. P. Greeley, F. H. Ribeiro, W. Nicholas Delgass and W. F. Schneider, *Journal of Catalysis*, 2014, **320**, 106–117.
- 57.) Z. Jiang, B. Wang and T. Fang, *Applied Surface Science*, 2014, **320**, 256–262.
- 58.) A. Luthfi Maulana, R. I. Dwi Putra, A. Gandaryus Saputro, M. Kemal Agusta, Nugraha and H. Kresno Dipojono, *Physical Chemistry Chemical Physics*, 2019, **21**, 20276–20286.
- 59.) P. Makkar and N. N. Ghosh, *RSC Adv.*, 2021, **11**, 27897–27924.
- 60.) D. Smykowski, B. Szyja and J. Szczygieł, *Journal of Molecular Graphics and Modelling*, 2013, **41**, 89–96.
- 61.) G.-C. Wang, L. Jiang, Y. Morikawa, J. Nakamura, Z.-S. Cai, Y.-M. Pan and X.-Z. Zhao, *Surface Science*, 2004, **570**, 205–217.
- 62.) J. Ye, C. Liu, D. Mei and Q. Ge, *Journal of Catalysis*, 2014, **317**, 44–53.
- 63.) M. Zhang, Y. Wu, M. Dou and Y. Yu, *Catal Lett*, 2018, **148**, 2935–2944.

- 64.) T. Engel and G. Ertl, *The Journal of Chemical Physics*, 2008, **69**, 1267–1281.
- 65.) M. Sankar, N. Dimitratos, P. J. Miedziak, P. P. Wells, C. J. Kiely and G. J. Hutchings, *Chem. Soc. Rev.*, 2012, **41**, 8099–8139.
- 66.) S. E. Collins, J. J. Delgado, C. Mira, J. J. Calvino, S. Bernal, D. L. Chiavassa, M. A. Baltanás and A. L. Bonivardi, *Journal of Catalysis*, 2012, **292**, 90–98.
- 67.) P. Lu, T. Teranishi, K. Asakura, M. Miyake and N. Toshima, *J. Phys. Chem. B*, 1999, **103**, 9673–9682.
- 68.) R. M. Navarro, B. Pawelec, J. M. Trejo, R. Mariscal and J. L. G. Fierro, *Journal of Catalysis*, 2000, **189**, 184–194.
- 69.) A. G. Nabi, A. Aman-ur-Rehman, A. Hussain, G. A. Chass and D. Di Tommaso, *Nanomaterials*, 2023, **13**, 87.
- 70.) L. Liu and A. Corma, *Chem. Rev.*, 2023, **123**, 8, 4855–4933.
- 71.) H. Bahruji, M. Bowker, W. Jones, J. Hayward, J. Ruiz Esquius, D. J. Morgan and G. J. Hutchings, *Faraday Discuss.*, 2017, **197**, 309–324.
- 72.) F. Brix, V. Desbuis, L. Piccolo and É. Gaudry, *J. Phys. Chem. Lett.*, 2020, **11**, 7672–7678.
- 73.) S. Hermans, R. Raja, J. M. Thomas, B. F. G. Johnson, G. Sankar and D. Gleeson, *Angewandte Chemie International Edition*, 2001, **40**, 1211–1215.
- 74.) M. Armbrüster, K. Kovnir, M. Behrens, D. Teschner, Y. Grin and R. Schlögl, *J. Am. Chem. Soc.*, 2010, **132**, 14745–14747.
- 75.) K. P. Reddy, D. Kim, S. Hong, K.-J. Kim, R. Ryoo and J. Y. Park, *ACS Appl. Mater. Interfaces*, 2023, **15**, 9373–9381.
- 76.) N. Iwasa, T. Mayanagi, N. Ogawa, K. Sakata and N. Takezawa, *Catalysis Letters*, 1998, **54**, 119–123.
- 77.) R. Ferrando, J. Jellinek and R. L. Johnston, *Chem. Rev.*, 2008, **108**, 845–910.
- 78.) L. O. P. Borbón, *Computational Studies of Transition Metal Nanoalloys*, Springer Science & Business Media, 2011.
- 79.) C. Massen, T. V. Mortimer-Jones and R. L. Johnston, *J. Chem. Soc., Dalton Trans.*, 2002, 4375–4388.
- 80.) Y. Ustinovshikov, *Advances in Materials Physics and Chemistry*, 2015, **5**, 244–270.
- 81.) L. Foppa and L. M. Ghiringhelli, *Top. Catal.*, 2022, **65**, p. 196–206.
- 82.) L. Foppa, L. M. Ghiringhelli, F. Girgsdies, M. Hashagen, P. Kube, M. Hävecker, S. J. Carey, A. Tarasov, P. Kraus, F. Rosowski, R. Schlögl, A. Trunschke and M. Scheffler, *MRS Bulletin*, 2021, **46**, 1016–1026.

- 83.) M. A. Laughton, *Renewable Energy Sources: Watt Committee: report number 22*, CRC Press, 1990.
- 84.) BP. (2019). BP Energy Outlook 2019. BP, <https://www.bp.com/content/dam/bp/business-sites/en/global/corporate/pdfs/energy-economics/energy-outlook/bp-energy-outlook-2019.pdf>, (accessed 28 November 2019).
- 85.) P. Gao, L. Zhang, S. Li, Z. Zhou and Y. Sun, *ACS Cent. Sci.*, 2020, **6**, 1657–1670.
- 86.) R.-P. Ye, J. Ding, W. Gong, M. D. Argyle, Q. Zhong, Y. Wang, C. K. Russell, Z. Xu, A. G. Russell, Q. Li, M. Fan and Y.-G. Yao, *Nat Commun*, 2019, **10**, 5698.
- 87.) M. Liu, Y. Yi, L. Wang, H. Guo and A. Bogaerts, *Catalysts*, 2019, **9**, 275.
- 88.) W. M. Haynes, Ed., in *CRC Handbook of Chemistry and Physics*, CRC Press, 95th edn., 2014.
- 89.) Statista Research Department, *Global production capacity of methanol 2018-2021*, <https://www.statista.com/statistics/1065891/global-methanol-production-capacity/>, (accessed 10 March 2023).
- 90.) M. Huš, D. Kopač, N. S. Štefančič, D. L. Jurković, V. D. B. C. Dasireddy and B. Likozar, *Catal. Sci. Technol.*, 2017, **7**, 5900–5913.
- 91.) L. C. Grabow and M. Mavrikakis, *ACS Catal.*, 2011, **1**, 365–384.
- 92.) H. Ahouari, A. Soualah, A. Le Valant, L. Pinard, P. Magnoux and Y. Pouilloux, *Reac Kinet Mech Cat*, 2013, **110**, 131–145.
- 93.) J. Hu, W. Guo, Z.-H. Liu, X. Lu, H. Zhu, F. Shi, J. Yan and R. Jiang, *J. Phys. Chem. C*, 2016, **120**, 20181–20191.
- 94.) A. J. Medford, J. Sehested, J. Rossmeisl, I. Chorkendorff, F. Studt, J. K. Nørskov and P. G. Moses, *Journal of Catalysis*, 2014, **309**, 397–407.
- 95.) B. Hu, Y. Yamaguchi and K. Fujimoto, *Catalysis Communications*, 2009, **10**, 1620–1624.
- 96.) J. Wu, M. Saito, M. Takeuchi and T. Watanabe, *Applied Catalysis A: General*, 2001, **218**, 235–240.
- 97.) D. Liuzzi, C. Peinado, M. A. Peña, J. van Kampen, J. Boon and S. Rojas, *Sustainable Energy Fuels*, 2020, **4**, 5674–5681.
- 98.) J. Díez-Ramírez, P. Sánchez, J. L. Valverde and F. Dorado, *Journal of CO₂ Utilization*, 2016, **16**, 375–383.
- 99.) C. Rameshan, W. Stadlmayr, C. Weilach, S. Penner, H. Lorenz, M. Hävecker, R. Blume, T. Rocha, D. Teschner, A. Knop-Gericke, R. Schlögl, N. Memmel, D. Zemlyanov, G. Rupprechter and B. Klötzer, *Angewandte Chemie International Edition*, 2010, **49**, 3224–3227.
- 100.) O. A. Ojelade, S. F. Zaman, M. A. Daous, A. A. Al-Zahrani, A. S. Malik, H. Driss, G. Shterk and J. Gascon, *Applied Catalysis A: General*, 2019, **584**, 117185.
- 101.) Y. Li, Z. Tian and L. Chen, *J. Phys. Chem. C*, 2021, **125**, 21381–21389.

- 102.) S. Ma, M. Sadakiyo, M. Heima, R. Luo, R. T. Haasch, J. I. Gold, M. Yamauchi and P. J. A. Kenis, *J. Am. Chem. Soc.*, 2017, **139**, 47–50.
- 103.) H. Pan, B. Ma, L. Zhou, Y. Hu, M. Shakouri, Y. Guo, X. Liu and Y. Wang, *ACS Sustainable Chem. Eng.*, 2023, **11**, 7489–7499.
- 104.) R. Qiu, Z. Ding, Y. Xu, Q. Yang, K. Sun and R. Hou, *Applied Surface Science*, 2021, **544**, 148974.
- 105.) W. J. Wang, S. Hwang, T. Kim, S. Ha and L. Scudiero, *Electrochimica Acta*, 2021, **387**, 138531.
- 106.) C. Azenha, T. Lagarteira, C. Mateos-Pedrero and A. Mendes, *International Journal of Hydrogen Energy*, 2021, **46**, 17490–17499.
- 107.) R. G. Lerner and G. L. Trigg, *Encyclopedia of Physics*, VCH, 1991.
- 108.) F. Schwabl, *Quantum Mechanics*, Springer Science & Business Media, 2007.
- 109.) J. M. Combes, P. Duclos and R. Seiler, in *Rigorous Atomic and Molecular Physics*, eds. G. Velo and A. S. Wightman, Springer US, Boston, MA, 1981, p. 185–213.
- 110.) M. Born and R. Oppenheimer, *Annalen der Physik*, 1927, **389**, 457–484.
- 111.) D. R. Hartree, *Mathematical Proceedings of the Cambridge Philosophical Society*, 1928, **24**, 89–110.
- 112.) V. Fock, *Z. Physik*, 1930, **61**, 126–148.
- 113.) J. A. Pople, *Rev. Mod. Phys.*, 1999, **71**, 1267–1274.
- 114.) E. van Lenthe, J. G. Snijders and E. J. Baerends, *The Journal of Chemical Physics*, 1996, **105**, 6505–6516.
- 115.) J. Townsend, J. K. Kirkland and K. D. Vogiatzis, in *Mathematical Physics in Theoretical Chemistry*, eds. S. M. Blinder and J. E. House, Elsevier, 2019, p. 63–117.
- 116.) P. Hohenberg and W. Kohn, *Phys. Rev.*, 1964, **136**, B864–B871.
- 117.) J. P. Perdew, A. Ruzsinszky, L. A. Constantin, J. Sun and G. I. Csonka, *J. Chem. Theory Comput.*, 2009, **5**, 902–908.
- 118.) W. Kohn and L. J. Sham, *Phys. Rev.*, 1965, **140**, A1133–A1138.
- 119.) M. Levy, *Proceedings of the National Academy of Sciences*, 1979, **76**, 6062–6065.
- 120.) PubMed, <https://pubmed.ncbi.nlm.nih.gov/>, (accessed 23 May 2023).
- 121.) J. P. Perdew and K. Schmidt, *AIP Conference Proceedings*, 2001, **577**, 1–20.
- 122.) P. Janthon, S. (Andy) Luo, S. M. Kozlov, F. Viñes, J. Limtrakul, D. G. Truhlar and F. Illas, *J. Chem. Theory Comput.*, 2014, **10**, 3832–3839.
- 123.) J. P. Perdew, K. Burke and M. Ernzerhof, *Phys. Rev. Lett.*, 1996, **77**, 3865–3868.
- 124.) A. Tkatchenko and M. Scheffler, *Phys. Rev. Lett.*, 2009, **102**, 073005.
- 125.) T. Bucko, S. Lebègue, J. Hafner and J. Ángyán, *Physical Review B*, 2013, **87**, 064110.
- 126.) J. Li and K. Yoshizawa, *Catalysis Today*, 2015, **248**, 142–148.

- 127.) O. Mohan, Q. T. Trinh, A. Banerjee and S. H. Mushrif, *Molecular Simulation*, 2019, **45**, 1163–1172.
- 128.) I. Kowalec, L. Kabalan, C. R. A. Catlow and A. J. Logsdail, *Phys. Chem. Chem. Phys.*, 2022, **24**, 9360–9373.
- 129.) S. Grimme, *Journal of Computational Chemistry*, 2004, **25**, 1463–1473.
- 130.) S. Grimme, *J. Comput. Chem.*, 2006, **27**, 1787–1799.
- 131.) J. Tao, J. P. Perdew, V. N. Staroverov and G. E. Scuseria, *Phys. Rev. Lett.*, 2003, **91**, 146401.
- 132.) J. Wellendorff, K. T. Lundgaard, K. W. Jacobsen and T. Bligaard, *J. Chem. Phys.*, 2014, **140**, 144107.
- 133.) H. J. Monkhorst and J. D. Pack, *Phys. Rev. B*, 1976, **13**, 5188–5192.
- 134.) V. Blum, M. Rossi, S. Kokott and M. Scheffler, 2022.
- 135.) S. S. Xantheas, *J. Chem. Phys.*, 1996, **104**, 8821–8824.
- 136.) C. D. Sherrill, 6.
- 137.) R. S. Mulliken, *The Journal of Chemical Physics*, 2004, **23**, 1833–1840.
- 138.) S. C. North, K. R. Jorgensen, J. Pricetolstoy and A. K. Wilson, *Frontiers in Chemistry*.
- 139.) R. N. Porter and M. Karplus, *The Journal of Chemical Physics*, 2004, **40**, 1105–1115.
- 140.) J. D. Head and M. C. Zerner, *Chemical Physics Letters*, 1985, **122**, 264–270.
- 141.) Y. Harada, S. Masuda and H. Ozaki, *Chem. Rev.*, 1997, **97**, 1897–1952.
- 142.) P. Busch, T. Heinonen and P. Lahti, *Physics Reports*, 2007, **452**, 155–176.
- 143.) G. Henkelman and H. Jónsson, *The Journal of Chemical Physics*, 2000, **113**, 9978–9985.
- 144.) G. Henkelman, B. P. Uberuaga and H. Jónsson, *J. Chem. Phys.*, 2000, **113**, 9901–9904.
- 145.) H. Jónsson, G. Mills and K. W. Jacobsen, in *Classical and Quantum Dynamics in Condensed Phase Simulations*, WORLD SCIENTIFIC, 1998, p. 385–404.
- 146.) J. A. Garrido Torres, P. C. Jennings, M. H. Hansen, J. R. Boes and T. Bligaard, *Phys. Rev. Lett.*, 2019, **122**, 156001.
- 147.) M. H. Hansen, J. A. G. Torres, P. C. Jennings, Z. Wang, J. R. Boes, O. G. Mamun and T. Bligaard, *arXiv:1904.00904 [physics]*.
- 148.) A. H. Larsen, J. J. Mortensen, J. Blomqvist, I. E. Castelli, R. Christensen, M. Dulak, J. Friis, M. N. Groves, B. Hammer, C. Hargus, E. D. Hermes, P. C. Jennings, P. B. Jensen, J. Kermode, J. R. Kitchin, E. L. Kolsbjerg, J. Kubal, K. Kaasbjerg, S. Lysgaard, J. B. Maronsson, T. Maxson, T. Olsen, L. Pastewka, A. Peterson, C. Rostgaard, J. Schiøtz, O. Schütt, M. Strange, K. S. Thygesen, T. Vegge, L. Vilhelmsen, M. Walter, Z. Zeng and K. W. Jacobsen, *J. Phys.: Condens. Matter*, 2017, **29**, 273002.

- 149.) S. S. Akimenko, G. D. Anisimova, A. I. Fadeeva, V. F. Fefelov, V. A. Gorbunov, T. R. Kayumova, A. V. Myshlyavtsev, M. D. Myshlyavtseva and P. V. Stishenko, *Journal of Computational Chemistry*, 2020, **41**, 2084–2097.
- 150.) G. J. Hutchings, M. Davidson, P. Atkins, P. Collier, N. Jackson, A. Morton, M. Muskett, M. Rosseinsky, P. Styring, P. Thornley and C. Williams, *Sustainable synthetic fuels for transport*, Royal Society, 2019.
- 151.) S. Roy, A. Cherevotan and S. C. Peter, *ACS Energy Lett.*, 2018, **3**, 1938–1966.
- 152.) A. Álvarez, M. Borges, J. J. Corral-Pérez, J. G. Olcina, L. Hu, D. Cornu, R. Huang, D. Stoian and A. Urakawa, *ChemPhysChem*, 2017, **18**, 3135–3141.
- 153.) U. J. Etim, C. Zhang and Z. Zhong, *Nanomaterials*, 2021, **11**, 3265.
- 154.) J. Ko, B.-K. Kim and J. W. Han, *J. Phys. Chem. C*, 2016, **120**, 3438–3447.
- 155.) I. Melián-Cabrera, M. L. Granados and J. L. G. Fierro, *Journal of Catalysis*, 2002, **210**, 285–294.
- 156.) R. Manrique, R. Jiménez, J. Rodríguez-Pereira, V. G. Baldovino-Medrano and A. Karelavic, *International Journal of Hydrogen Energy*, 2019, **44**, 16526–16536.
- 157.) T. Matsushima and H. Asada, *The Journal of Chemical Physics*, 1986, **85**, 1658–1668.
- 158.) U. Burghaus, *Progress in Surface Science*, 2014, **89**, 161–217.
- 159.) C.-L. Kao, A. Carlsson and R. J. Madix, *Surface Science*, 2002, **497**, 356–372.
- 160.) X. Liu, L. Sun and W.-Q. Deng, *J. Phys. Chem. C*, 2018, **122**, 8306–8314.
- 161.) M.-P. Habas, F. Mele, M. Sodupe and F. Illas, *Surface Science*, 1999, **431**, 208–219.
- 162.) M. Huš, D. Kopač, N. S. Štefančič, D. L. Jurković, V. D. B. C. Dasireddy and B. Likozar, *Catal. Sci. Technol.*, 2017, **7**, 5900–5913.
- 163.) V. Blum, R. Gehrke, F. Hanke, P. Havu, V. Havu, X. Ren, K. Reuter and M. Scheffler, *Computer Physics Communications*, 2009, **180**, 2175–2196.
- 164.) G. Kresse and J. Furthmüller, *Phys. Rev. B*, 1996, **54**, 11169–11186.
- 165.) M. Hebbache and M. Zemzemi, *Phys. Rev. B*, 2004, **70**, 224107.
- 166.) J. W. Arblaster, *Platinum Metals Review*, 2012, **56**, 3, p. 181-189(9).
- 167.) A. K. Giri and G. B. Mitra, *J. Phys. D: Appl. Phys.*, 1985, **18**, L75.
- 168.) A. Tkatchenko, R. A. DiStasio, R. Car and M. Scheffler, *Phys. Rev. Lett.*, 2012, **108**, 236402.
- 169.) A. Tkatchenko, A. Ambrosetti and R. A. DiStasio, *J. Chem. Phys.*, 2013, **138**, 074106.
- 170.) M. Ernzerhof and G. E. Scuseria, *J. Chem. Phys.*, 1999, **110**, 5029–5036.
- 171.) L. Kaban, I. Kowalec, C. R. A. Catlow and A. J. Logsdail, *Phys. Chem. Chem. Phys.*, 2021, **23**, 14649–14661.
- 172.) M. Methfessel, D. Hennig and M. Scheffler, *Physical Review B*, 1992, **46**, 4816–4829.
- 173.) L. Vitos, A. V. Ruban, H. L. Skriver and J. Kollár, *Surface Science*, 1998, **411**, 186–202.

- 174.) A. Patra, J. E. Bates, J. Sun and J. P. Perdew, *PNAS*, 2017, **114**, E9188–E9196.
- 175.) N. E. Singh-Miller and N. Marzari, *Phys. Rev. B*, 2009, **80**, 235407.
- 176.) J. L. F. Da Silva, C. Stampfl and M. Scheffler, *Surface Science*, 2006, **600**, 703–715.
- 177.) H. L. Skriver and N. M. Rosengaard, *Physical Review B*, 1992, **46**, 7157–7168.
- 178.) W. R. Tyson and W. A. Miller, *Surface Science*, 1977, **62**, 267–276.
- 179.) F. R. de Boer, W. C. M. Mattens, R. Boom, A. R. Miedema and A. K. Niessen, .
- 180.) T. Frederiksen, M. Paulsson, M. Brandbyge and A.-P. Jauho, *Phys. Rev. B*, 2007, **75**, 205413.
- 181.) H. Conrad, G. Ertl and E. E. Latta, *Surface Science*, 1974, **41**, 435–446.
- 182.) J. A. Herron, S. Tonelli and M. Mavrikakis, *Surface Science*, 2012, **606**, 1670–1679.
- 183.) S. Fonseca, G. Maia and L. M. C. Pinto, *Electrochemistry Communications*, 2018, **93**, 100–103.
- 184.) G. Jerkiewicz, *Progress in Surface Science*, 1998, **57**, 137–186.
- 185.) Q. Tang, F. Shi, K. Li, W. Ji, J. Leszczynski, A. G. Russell, E. G. Eddings, Z. Shen and M. Fan, *Fuel*, 2020, **280**, 118446.
- 186.) J. S. Gómez-Jeria, *Journal of the Chilean Chemical Society*, 2009, **54**, 482–485.
- 187.) J. Dobado, H. Martinez, J. Molina and M. Sundberg, 2000, p. 337–353.
- 188.) R. Haunschild and W. Klopper, *J. Chem. Phys.*, 2012, **136**, 164102.
- 189.) A. Posada-Borbón and H. Grönbeck, *ACS Catal.*, 2021, **11**, 9996–10006.
- 190.) N. Aas, Y. Li and M. Bowker, *J. Phys.: Condens. Matter*, 1991, **3**, S281.
- 191.) J. Díez-Ramírez, J. A. Díaz, P. Sánchez and F. Dorado, *Journal of CO₂ Utilization*, 2017, **22**, 71–80.
- 192.) Max Planck Centre on the Fundamentals of Heterogeneous Catalysis (FUNCAT), <https://www.cardiff.ac.uk/cardiff-catalysis-institute/research/mpc-funcat>, (accessed 15 May 2023).
- 193.) T. Engel and H. Kuipers, *Surface Science*, 1979, **90**, 162–180.
- 194.) H. Zhang, J. Gromek, G. W. Fernando, H. L. Marcus and S. Boorse, *JPE*, 2002, **23**, 246.
- 195.) A. van de Walle and G. Ceder, *JPE*, 2002, **23**, 348.
- 196.) W. Zhong, Y. Cai and D. Tománek, *Nature*, 1993, **362**, 435–437.
- 197.) J.-D. Grunwaldt, M. Caravati, S. Hannemann and A. Baiker, *Phys. Chem. Chem. Phys.*, 2004, **6**, 3037–3047.
- 198.) E. M. Fiordaliso, I. Sharafutdinov, H. W. P. Carvalho, J.-D. Grunwaldt, T. W. Hansen, I. Chorkendorff, J. B. Wagner and C. D. Damsgaard, *ACS Catal.*, 2015, **5**, 5827–5836.
- 199.) W. Eberhardt, S. G. Louie and E. W. Plummer, *Phys. Rev. B*, 1983, **28**, 465–477.
- 200.) L. Cao, C. Li and T. Mueller, *J. Chem. Inf. Model.*, 2018, **58**, 2401–2413.

- 201.) B. J. Berne, G. Ciccotti and D. F. Coker, *Classical And Quantum Dynamics In Condensed Phase Simulations: Proceedings Of The International School Of Physics*, World Scientific, 1998.
- 202.) J. O. Linde and G. Borelius, *Annalen der Physik*, 1927, **389**, 747–774.
- 203.) J. R. Lacher and R. H. Fowler, *Proceedings of the Royal Society of London. Series A - Mathematical and Physical Sciences*, 1937, **161**, 525–545.
- 204.) E. Skúlason, G. S. Karlberg, J. Rossmeisl, T. Bligaard, J. Greeley, H. Jónsson and J. K. Nørskov, *Physical Chemistry Chemical Physics*, 2007, **9**, 3241–3250.
- 205.) G. Källén and G. Wahnström, *Phys. Rev. B*, 2001, **65**, 033406.
- 206.) M. Johansson, E. Skúlason, G. Nielsen, S. Murphy, R. M. Nielsen and I. Chorkendorff, *Surface Science*, 2010, **604**, 718–729.
- 207.) E. Wicke, H. Brodowsky and H. Züchner, in *Hydrogen in Metals II: Application-Oriented Properties*, eds. G. Alefeld and J. Völkl, Springer, Berlin, Heidelberg, 1978, p. 73–155.
- 208.) D. Teschner, J. Borsodi, A. Wootsch, Z. Révay, M. Hävecker, A. Knop-Gericke, S. D. Jackson and R. Schlögl, *Science*, 2008, **320**, 86–89.
- 209.) G. Nelin, *physica status solidi (b)*, 1971, **45**, 527–536.
- 210.) S. Lehtola, C. Steigemann, M. J. T. Oliveira and M. A. L. Marques, *SoftwareX*, 2018, **7**, 1–5.
- 211.) M. Hebbache and M. Zemzemi, *Phys. Rev. B*, 2004, **70**, 224107.
- 212.) L. Kabalan, I. Kowalec, C. R. A. Catlow and A. J. Logsdail, *NOMAD repository*, DOI:10.17172/NOMAD/2021.05.21-1.
- 213.) C. T. Chan, K. P. Bohnen and K. M. Ho, *Phys. Rev. B*, 1993, **47**, 4771–4774.
- 214.) K. P. Huber and G. Herzberg, in *Molecular Spectra and Molecular Structure: IV. Constants of Diatomic Molecules*, eds. K. P. Huber and G. Herzberg, Springer US, Boston, MA, 1979, p. 8–689.
- 215.) L. H. Sprowl, C. T. Campbell and L. Árnadóttir, *J. Phys. Chem. C*, 2016, **120**, 9719–9731.
- 216.) C. T. Campbell, L. H. Sprowl and L. Árnadóttir, *J. Phys. Chem. C*, 2016, **120**, 10283–10297.
- 217.) F. Bowman, *Introduction to Bessel Functions*, Courier Corporation, 2012.
- 218.) G. W. Watson, R. P. K. Wells, D. J. Willock and G. J. Hutchings, *Chem. Commun.*, 2000, 705–706.
- 219.) D. Hennig, S. Wilke, R. Löber and M. Methfessel, *Surface Science*, 1993, **287–288**, 89–93.
- 220.) M. J. Gladys, I. Kambali, M. A. Karolewski, A. Soon, C. Stampfl and D. J. O’Connor, *J. Chem. Phys.*, 2010, **132**, 024714.
- 221.) T. Adit Maark and A. A. Peterson, *J. Phys. Chem. C*, 2014, **118**, 4275–4281.
- 222.) S. Mallikarjun Sharada, R. K. B. Karlsson, Y. Maimaiti, J. Voss and T. Bligaard, *Phys. Rev. B*, 2019, **100**, 035439.
- 223.) E. W. Hansen and M. Neurock, *Journal of Catalysis*, 2000, **196**, 241–252.

- 224.) J. Rogal and K. Reuter, in *Experiment, Modeling and Simulation of Gas-Surface Interactions for Reactive Flows in Hypersonic Flights*, NATO RTO, 2007, p. 2.1-2.18.
- 225.) F. Wang and D. P. Landau, *Phys. Rev. Lett.*, 2001, **86**, 2050–2053.
- 226.) F. Wang and D. P. Landau, *Phys. Rev. E*, 2001, **64**, 056101.
- 227.) S. Wilke, D. Hennig, R. Löber, M. Methfessel and M. Scheffler, *Surface Science*, 1994, **307–309**, 76–81.
- 228.) E. J. Peterson, B. Halevi, B. Kiefer, M. N. Spilde, A. K. Datye, J. Peterson, L. Daemen, A. Llobet and H. Nakotte, *Journal of Alloys and Compounds*, 2011, **509**, 1463–1470.
- 229.) M. Miyazaki, S. Furukawa, T. Takayama, S. Yamazoe and T. Komatsu, *ACS Appl. Nano Mater.*, 2019, **2**, 3307–3314.
- 230.) M. Friedrich, S. Penner, M. Heggen and M. Armbrüster, *Angewandte Chemie International Edition*, 2013, **52**, 4389–4392.
- 231.) E. Nowicka, S. M. Althahban, Y. Luo, R. Kriegel, G. Shaw, D. J. Morgan, Q. He, M. Watanabe, M. Armbrüster, C. J. Kiely and G. J. Hutchings, *Catal. Sci. Technol.*, 2018, **8**, 5848–5857.
- 232.) L. Kabalan, I. Kowalec, S. Rigamonti, M. Troppenz, C. Draxl, R. Catlow and A. Logsdail, *J. Phys.: Condens. Matter*, 2023, **35**, 405402.
- 233.) M. Yamauchi and T. Tsukuda, *Dalton Trans.*, 2011, **40**, 4842–4845.
- 234.) P. Cremaschi, G. F. Tantardini, J. Muilu and T. A. Pakkanen, *Vacuum*, 1990, **41**, 260–264.
- 235.) R. Wang, B. Zhu, G. Zhang and Y. Gao, *J Mol Model*, 2020, **26**, 202.
- 236.) E. Jeroro, V. Lebarbier, A. Datye, Y. Wang and J. M. Vohs, *Surface Science*, 2007, **601**, 5546–5554.
- 237.) K. P. Kuhl, T. Hatsukade, E. R. Cave, D. N. Abram, J. Kibsgaard and T. F. Jaramillo, *J. Am. Chem. Soc.*, 2014, **136**, 14107–14113.
- 238.) I. Bakó, R. Schennach and G. Pálinkás, *J. Phys.: Conf. Ser.*, 2008, **100**, 052067.
- 239.) M. W. Roberts, *Journal of Molecular Catalysis*, 1992, **74**, 11–22.
- 240.) P. R. Davies and M. W. Roberts, *J. Chem. Soc., Faraday Trans.*, 1992, **88**, 361–368.
- 241.) A. F. Carley, S. Yan and M. W. Roberts, *J. Chem. Soc., Faraday Trans.*, 1990, **86**, 2701–2710.
- 242.) K. Blaziak, D. Tzeli, S. S. Xantheas and E. Uggerud, *Physical Chemistry Chemical Physics*, 2018, **20**, 25495–25505.
- 243.) C. Quilis, N. Mota, B. Pawelec, E. Millán and R. M. Navarro Yerga, *Applied Catalysis B: Environmental*, 2023, **321**, 122064.
- 244.) J. Song, S. Liu, C. Yang, G. Wang, H. Tian, Z. Zhao, R. Mu and J. Gong, *Applied Catalysis B: Environmental*, 2020, **263**, 118367.
- 245.) E. Iglesia, *J. Phys. Chem.*, 1986, **90**, 5272–5274.

- 246.) G. J. Millar, C. H. Rochester and K. C. Waugh, *J. Chem. Soc., Faraday Trans.*, 1991, **87**, 1491–1496.
- 247.) Y. Yang, C. A. Mims, R. S. Disselkamp, J. H. Kwak, C. H. Peden and C. T. Campbell, *Journal of Physical Chemistry C*, 2010, **114**, 40, 17205–17211.
- 248.) J. Quan, T. Kondo, G. Wang and J. Nakamura, *Angewandte Chemie International Edition*, 2017, **56**, 3496–3500.
- 249.) G. Wang, Y. Morikawa, T. Matsumoto and J. Nakamura, *J. Phys. Chem. B*, 2006, **110**, 9–11.
- 250.) S. Li, S. Rangarajan, J. Scaranto and M. Mavrikakis, *Surface Science*, 2021, **709**, 121846.
- 251.) H. A. Hansen, J. B. Varley, A. A. Peterson and J. K. Nørskov, *J. Phys. Chem. Lett.*, 2013, **4**, 388–392.
- 252.) L. M. Ghiringhelli, J. Vybiral, S. V. Levchenko, C. Draxl and M. Scheffler, *Phys. Rev. Lett.*, 2015, **114**, 105503.
- 253.) F. Wang, H. Zhang, Z. Zhang, Q. Ma, C. Kong and S. Min, *Journal of Colloid and Interface Science*, 2022, **607**, 312–322.
- 254.) S. R. Docherty, N. Phongprueksathat, E. Lam, G. Noh, O. V. Safonova, A. Urakawa and C. Copéret, *JACS Au*, 2021, **1**, 450–458.
- 255.) Z. Karpiński, I. Ratajczykowa and W. Palczewska, *Annu. Rep. Prog. Chem., Sect. C: Phys. Chem.*, 1984, **81**, 137–184.
- 256.) D. Pavesi, F. Dattila, R. C. J. Van de Poll, D. Anastasiadou, R. García-Muelas, M. Figueiredo, G.-J. M. Gruter, N. López, M. T. M. Koper and K. J. P. Schouten, *Journal of Catalysis*, 2021, **402**, 229–237.
- 257.) L. Foppa, T. A. R. Purcell, S. V. Levchenko, M. Scheffler and L. M. Ghiringhelli, *Phys. Rev. Lett.*, 2022, **129**, 055301.

Appendix

Detailed energetics for all modelled steps in the reaction profiles of CO₂ hydrogenation to methanol on Pd (111), (100) and (110) surfaces are presented below. All structures associated with the work presented in the Chapter 3 are available from the NOMAD repository at DOI: [10.17172/NOMAD/2021.05.24-1](https://doi.org/10.17172/NOMAD/2021.05.24-1) (all data) and [10.17172/NOMAD/2021.05.25-1](https://doi.org/10.17172/NOMAD/2021.05.25-1) (optimised structures).

Tabulated adsorption enthalpy and energy

Table 22. The adsorption energy, E_{ads} , and the adsorption enthalpy, H_{ads} , across all intermediates in the CO₂ hydrogenation reaction over the FCC Pd (111), (110) and (100) surfaces. All numerical values are in eV.

| Adsorbate | $H_{\text{ads}} / \text{eV}$ | | | $E_{\text{ads}} / \text{eV}$ | | |
|-------------------------------|------------------------------|----------|----------|------------------------------|----------|----------|
| | Pd (111) | Pd (100) | Pd (110) | Pd (111) | Pd (100) | Pd (110) |
| CO ₂ | -0.21 | -0.18 | -0.16 | -0.21 | -0.18 | -0.16 |
| CO ₂ ^{δ-} | 0.09 | -0.09 | -0.19 | 0.06 | -0.13 | -0.23 |
| HCOO | -2.46 | -2.55 | -2.72 | -2.65 | -2.73 | -2.90 |
| HCOOH | -0.63 | -0.64 | -0.50 | -0.67 | -0.67 | -0.54 |
| H ₂ COOH | -1.93 | -2.12 | -2.25 | -2.11 | -2.35 | -2.40 |
| CH ₂ O | -0.58 | -0.83 | -0.94 | -0.75 | -0.93 | -1.05 |
| CH ₃ O | -2.33 | -2.51 | -2.39 | -2.13 | -2.35 | -2.17 |
| CH ₃ OH | -0.52 | -0.52 | -0.66 | -0.58 | -0.57 | -0.71 |

Tabulated energy of individual reaction steps

Table 23. The reaction energy (eV) of intermediate steps in CO₂ hydrogenation on the Pd (111), (110), and (100) surfaces. Each calculation is balanced stoichiometrically with energies of gas-phase molecules. * represents the catalyst surface.

| Reaction step | Pd (111) | Pd (110) | Pd (100) | Pd (111) + ZPE | Pd (110) + ZPE | Pd (100) + ZPE |
|--|----------|----------|----------|-------------------|-------------------|-------------------|
| * + CO ₂ + 3 H ₂ | 0.00 | 0.00 | 0.00 | 0.00 | 0.00 | 0.00 |
| *CO ₂ ^{δ-} + 3 H ₂ | 0.06 | -0.23 | -0.13 | 0.09 | -0.19 | -0.09 |
| *CO ₂ ^{δ-} + H* + 2.5 H ₂ | -0.59 | -0.67 | -0.67 | -0.53 | -0.49 | -0.61 |
| TS1 + 2.5 H ₂ | 0.49 | 0.17 | 0.40 | 0.60 | 0.33 | 0.49 |
| HCOO* + 2.5 H ₂ | -0.37 | -0.62 | -0.45 | -0.15 | -0.37 | -0.24 |
| HCOO* + H* + 2 H ₂ | -0.81 | -1.02 | -0.99 | -0.57 | -0.74 | -0.77 |
| TS2 + 2 H ₂ | -0.24 | -0.37 | -0.25 | -0.06 | -0.19 | -0.10 |
| HCOOH* + 2 H ₂ | -0.75 | -0.61 | -0.74 | -0.40 | -0.20 | -0.41 |
| HCOOH* + H* + 1.5 H ₂ | -1.37 | -1.14 | -1.32 | -0.99 | -0.59 | -1.06 |

| | | | | | | |
|---|-------|-------|-------|-------|-------|-------|
| TS3 + 1.5 H ₂ | -0.02 | -0.23 | -0.07 | 0.42 | 0.25 | 0.45 |
| H ₂ COOH* + 1.5 H ₂ | -0.11 | -0.49 | -0.32 | 0.38 | 0.15 | 0.09 |
| TS4 + 1.5 H ₂ | 0.36 | 0.03 | 0.37 | 0.78 | 0.59 | 0.77 |
| H ₂ CO* + OH* + 1.5 H ₂ | 0.29 | -0.42 | -0.38 | 0.71 | 0.13 | 0.06 |
| H ₂ CO* + H ₂ O* + H ₂ | -0.93 | -1.28 | -1.10 | -0.37 | -0.58 | -0.55 |
| H ₂ CO* + H ₂ O + H ₂ | -0.52 | -0.82 | -0.70 | -0.02 | -0.19 | -0.21 |
| H ₂ CO* + H* + H ₂ O + 0.5 H ₂ | -1.00 | -1.17 | -1.23 | -0.47 | -0.52 | -0.77 |
| TS5 + H ₂ O + 0.5 H ₂ | -0.23 | -0.52 | -0.60 | 0.27 | 0.14 | -0.08 |
| H ₃ CO* + H ₂ O + 0.5 H ₂ | -0.51 | -0.81 | -0.99 | 0.14 | -0.03 | -0.29 |
| H ₃ CO* + H* + H ₂ O | -1.15 | -1.25 | -1.57 | -0.47 | -0.50 | -0.94 |
| TS6 + H ₂ O | -0.66 | -0.86 | -0.87 | -0.02 | -0.08 | -0.21 |
| H ₃ COH* + H ₂ O | -1.62 | -1.76 | -1.54 | -0.75 | -0.75 | -0.68 |
| * + CH ₃ OH + H ₂ O | -1.05 | -1.05 | -1.05 | -0.26 | -0.26 | -0.26 |

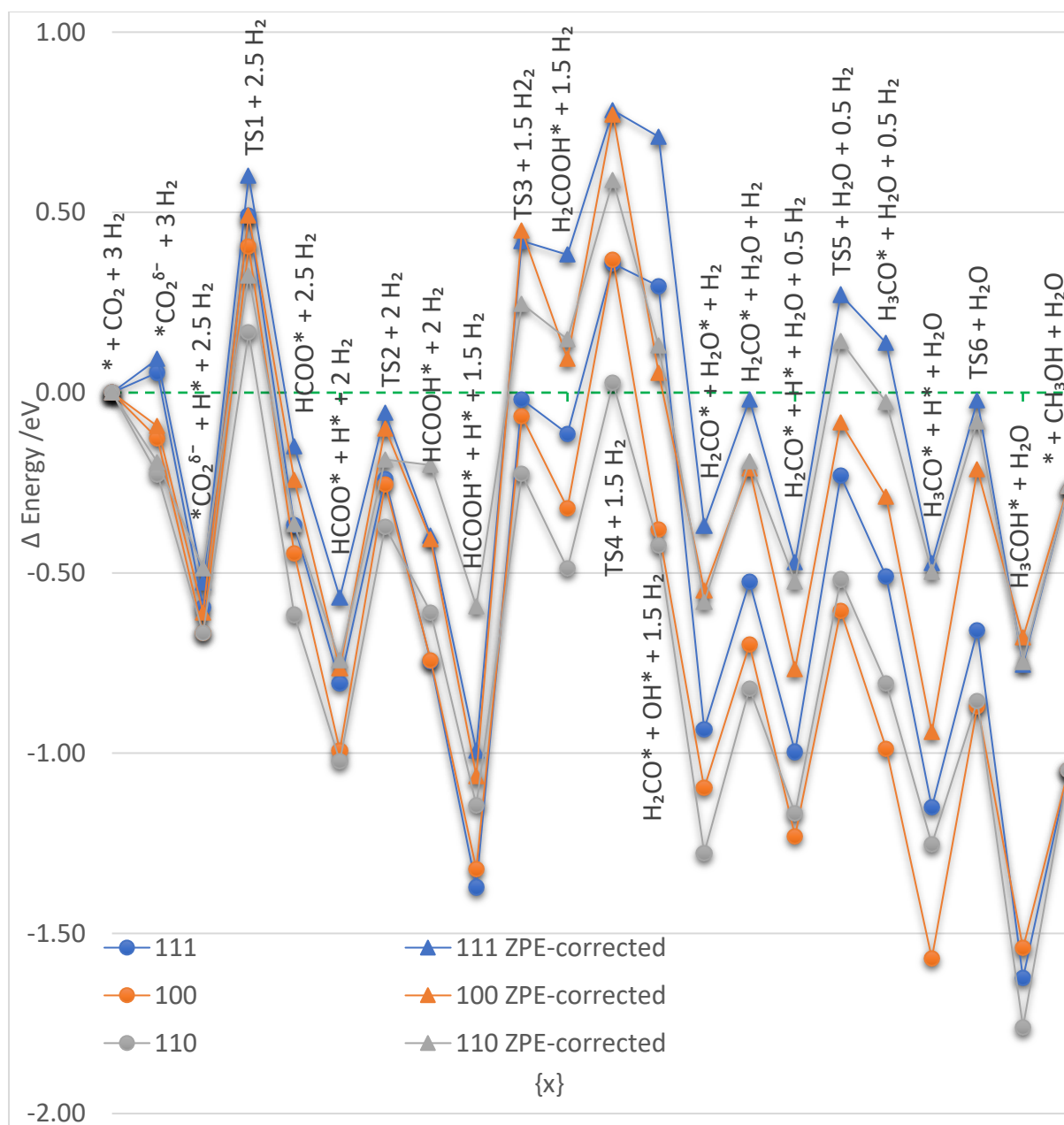
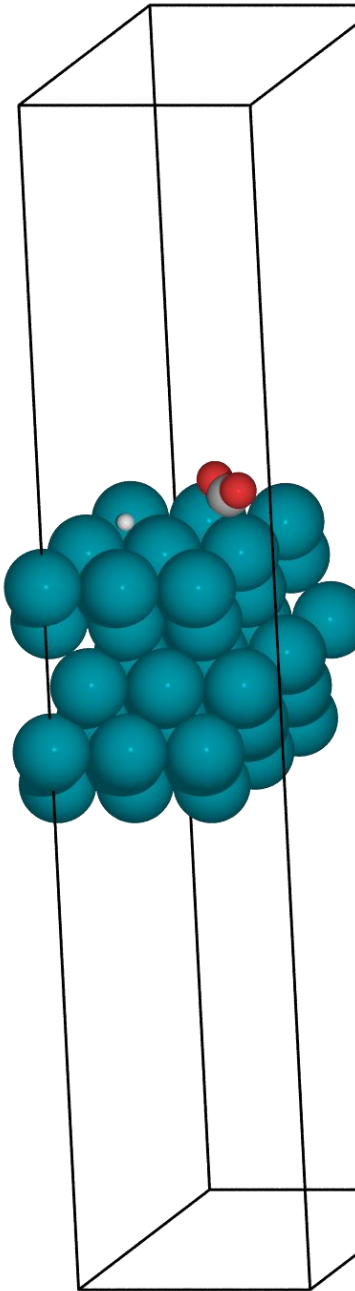
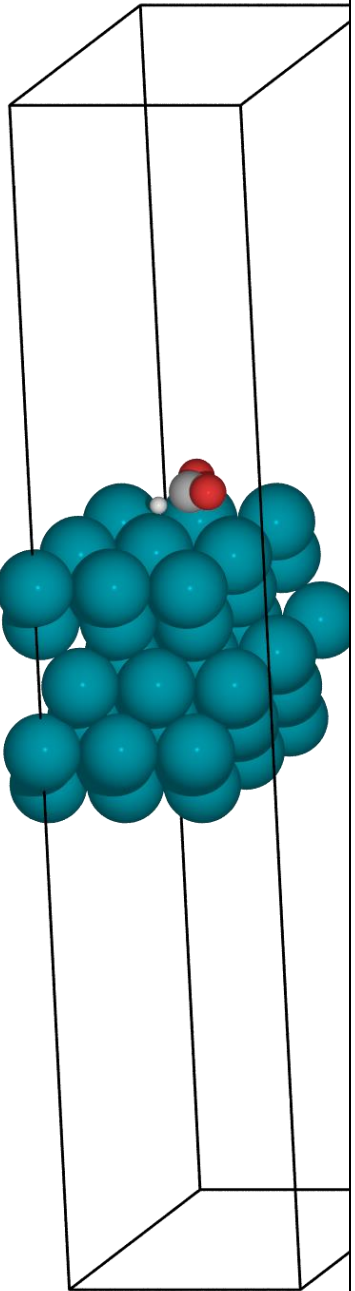
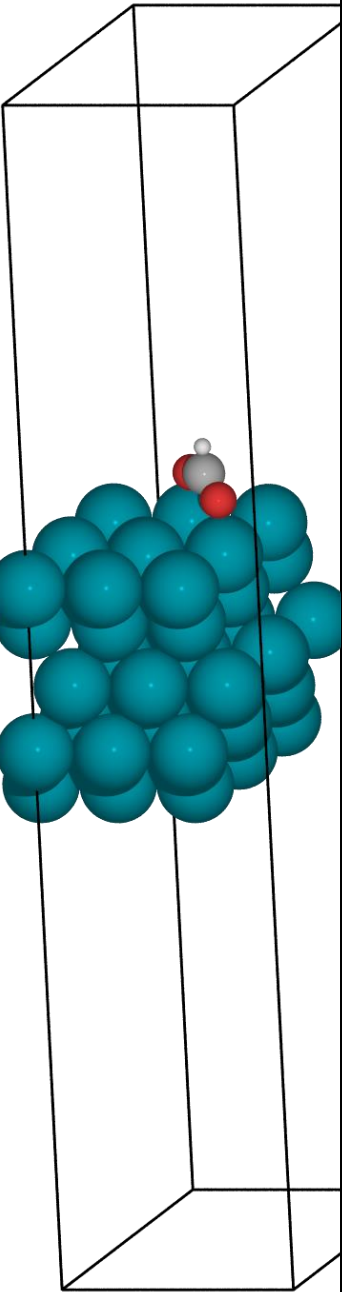
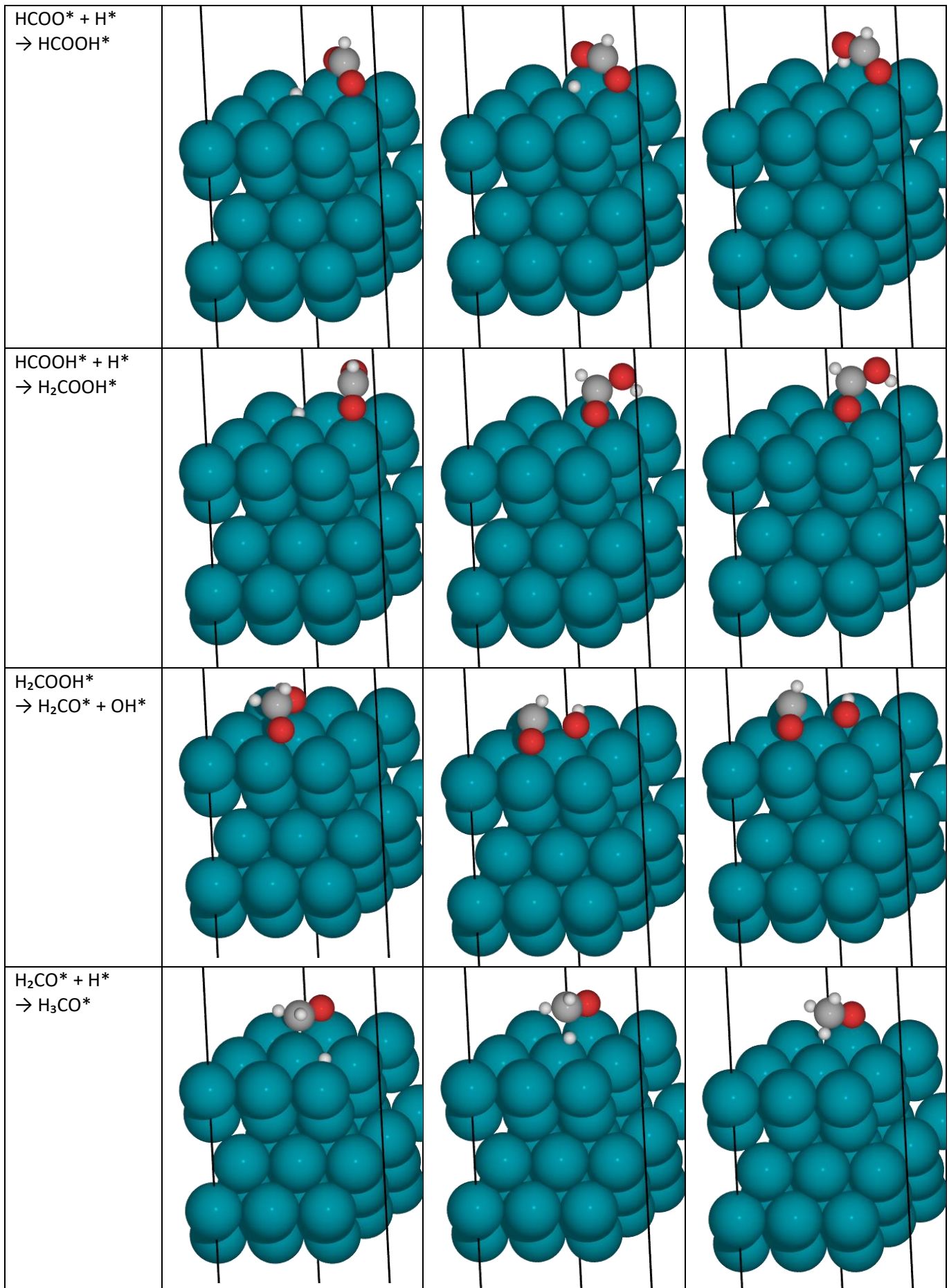


Figure 44. The energy profile of CO₂ hydrogenation to methanol, via the formate pathway, on Pd (111), (100), and (110) surfaces with and without ZPE-correction included, plotted in blue, orange, and grey, respectively, relative to the energy of pristine surface and gas phase reactants.⁹¹ Energies of intermediate structures and transition state geometries have been stoichiometrically balanced with energies of gas phase reactants; * indicates surface bound species.

Visualised adsorbates and transition states

Table 24. Graphical representation of initial, transition state and final geometries in E_{act} calculations on Pd (111) surface. The blue, red, grey and white spheres represent Pd, O, C and H atoms; the black lines indicate the edges of the simulation cell. The full size of the simulation cell, including all unit cell borders, is depicted for the initial reaction step to illustrate the vacuum region size.

| Reaction | Initial geometry | Transition state geometry | Final geometry |
|---|--|---|--|
| $\text{*CO}_2^{\delta-} + \text{H}^* \rightarrow \text{HCOO}^*$ |  |  |  |



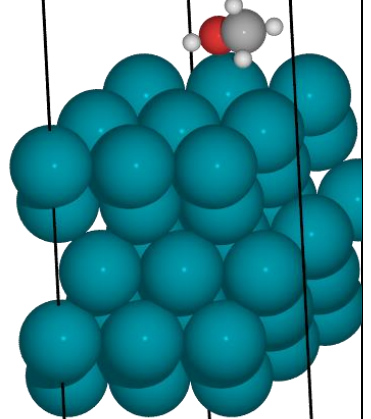
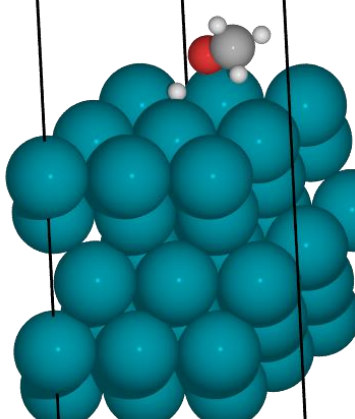
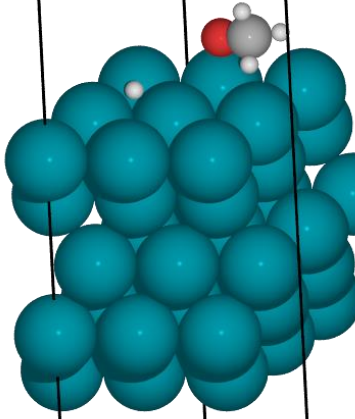
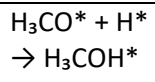
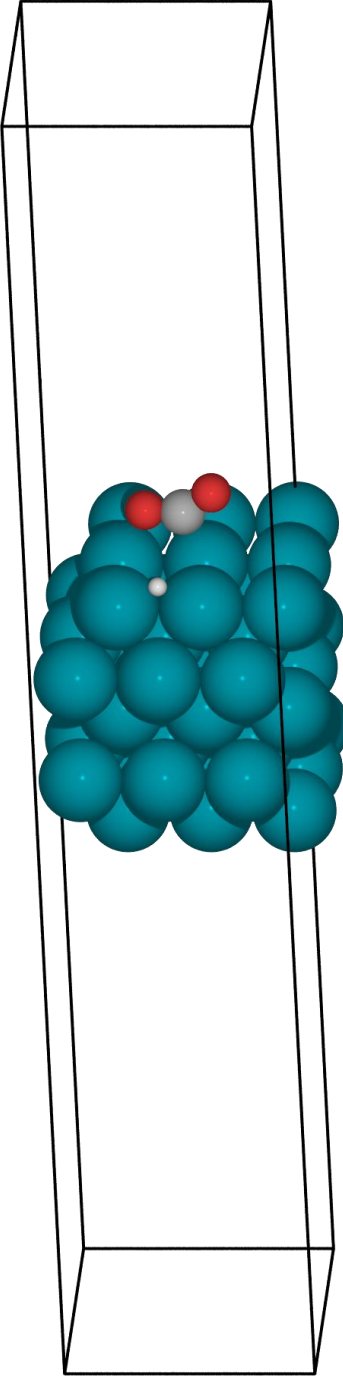
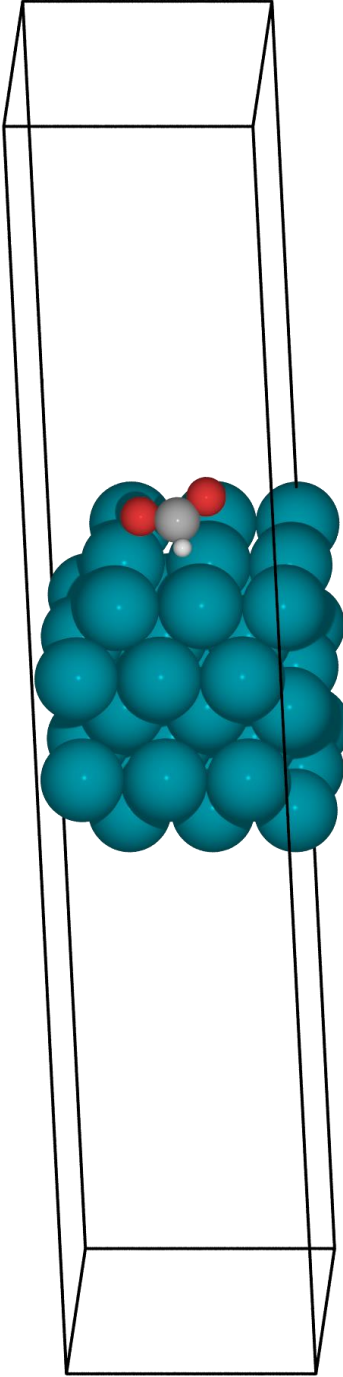
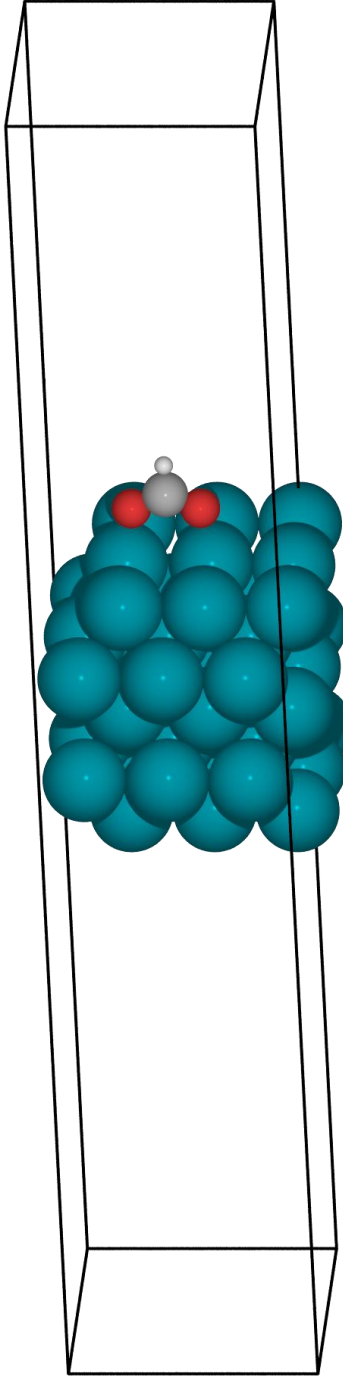
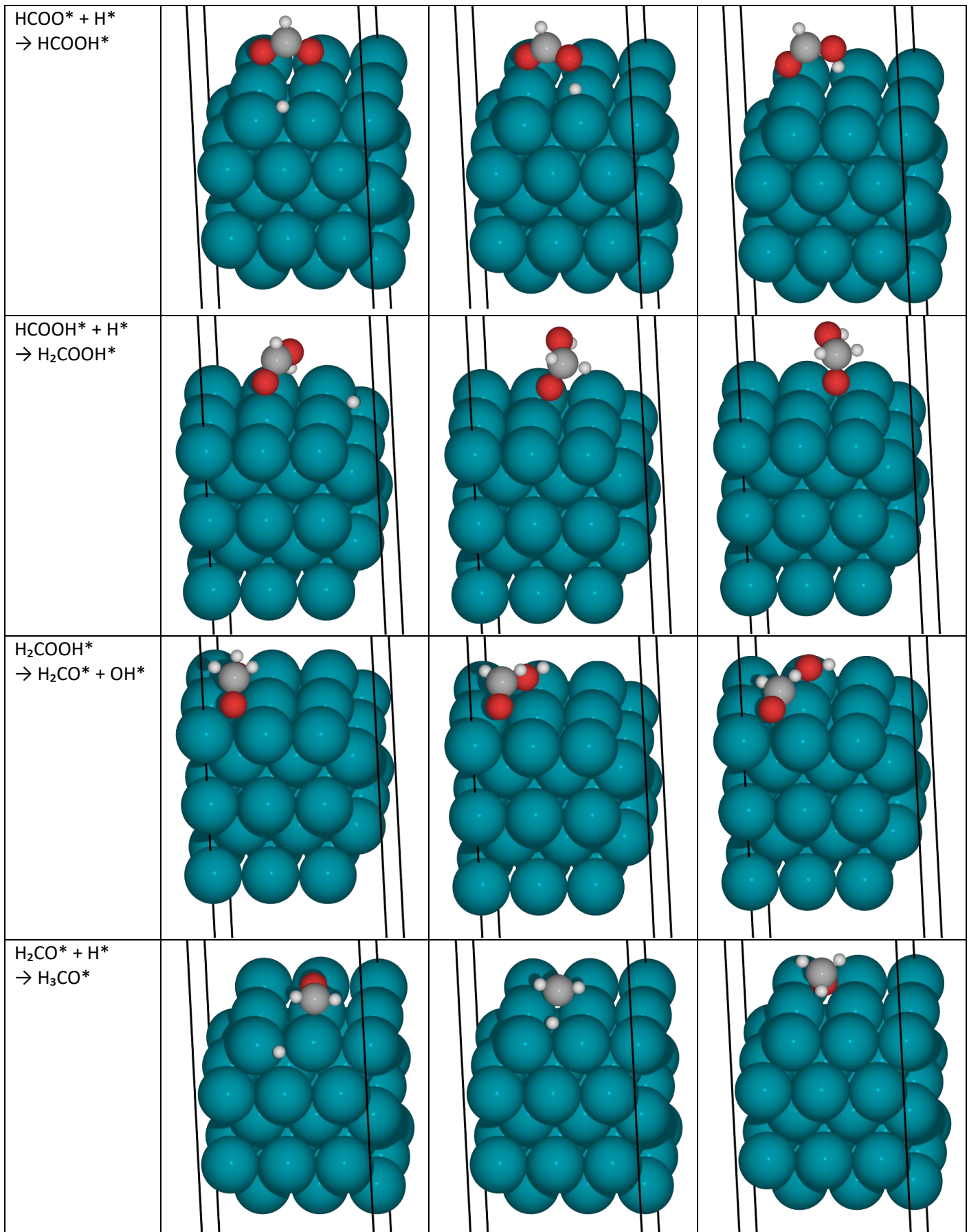


Table 25. Graphical representation of initial, transition state and final geometries in E_{act} calculations on Pd (100) surface. The blue, red, grey and white spheres represent Pd, O, C and H atoms; the black lines indicate the edges of the simulation cell. The full size of the simulation cell, including all unit cell borders, is depicted for the initial reaction step to illustrate the vacuum region size.

| Reaction | Initial geometry | Transition state geometry | Final geometry |
|--|--|---|--|
| $\text{*CO}_2^{\delta-} + \text{H}^*$ $\rightarrow \text{HCOO}^*$ |  |  |  |



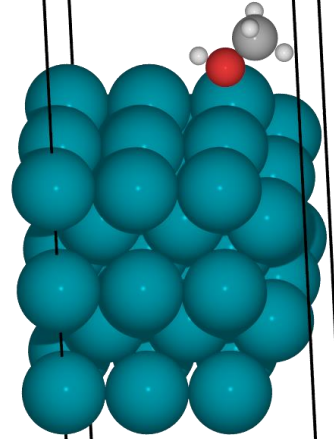
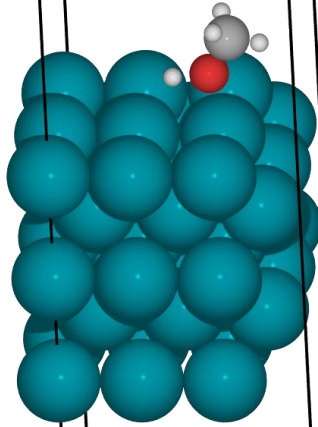
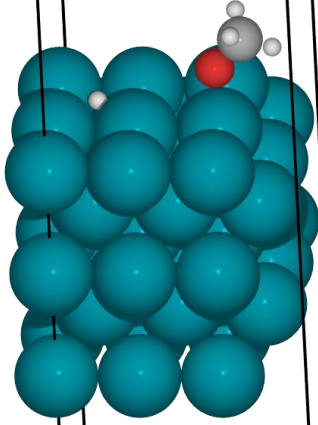
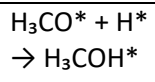
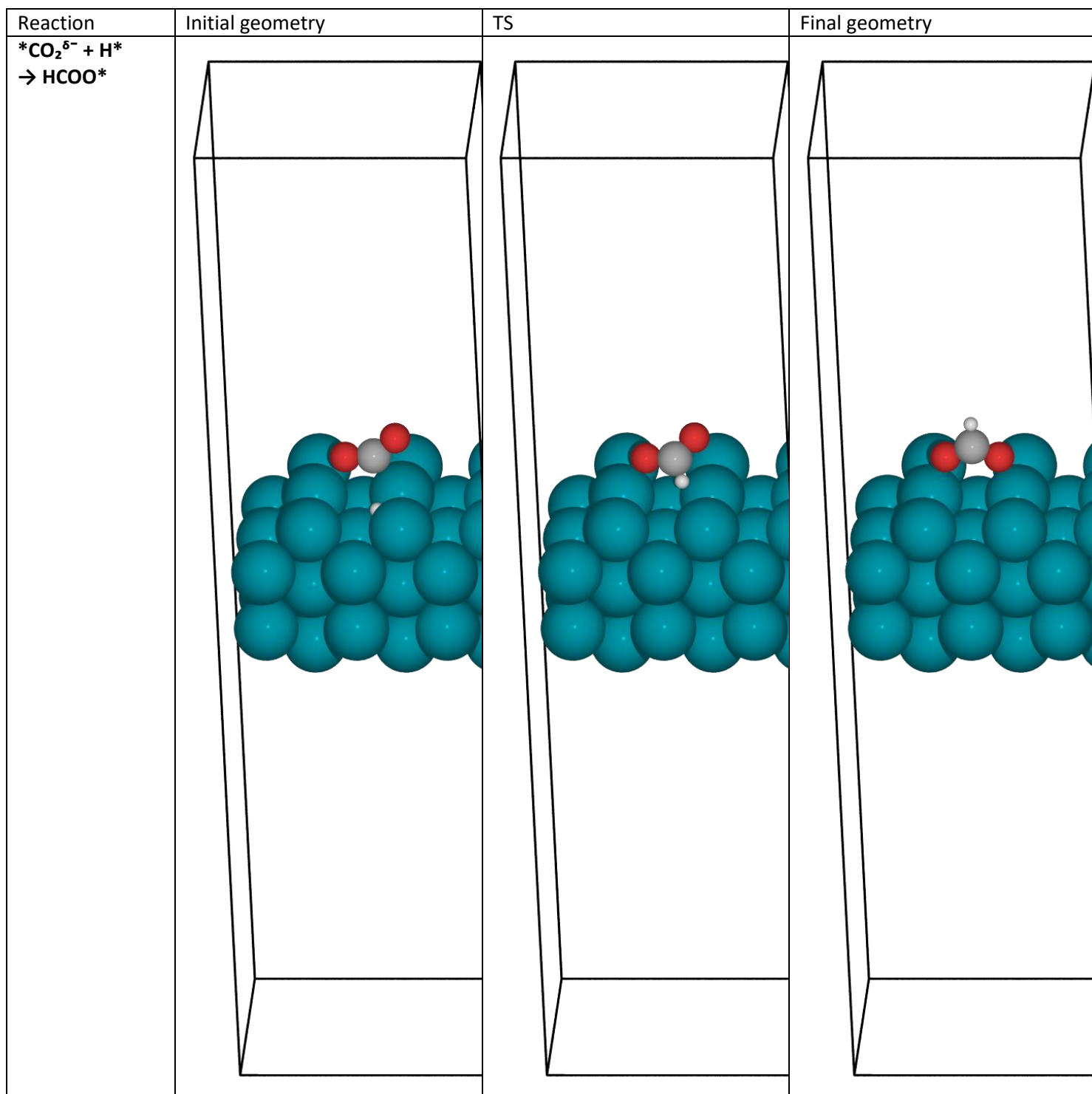
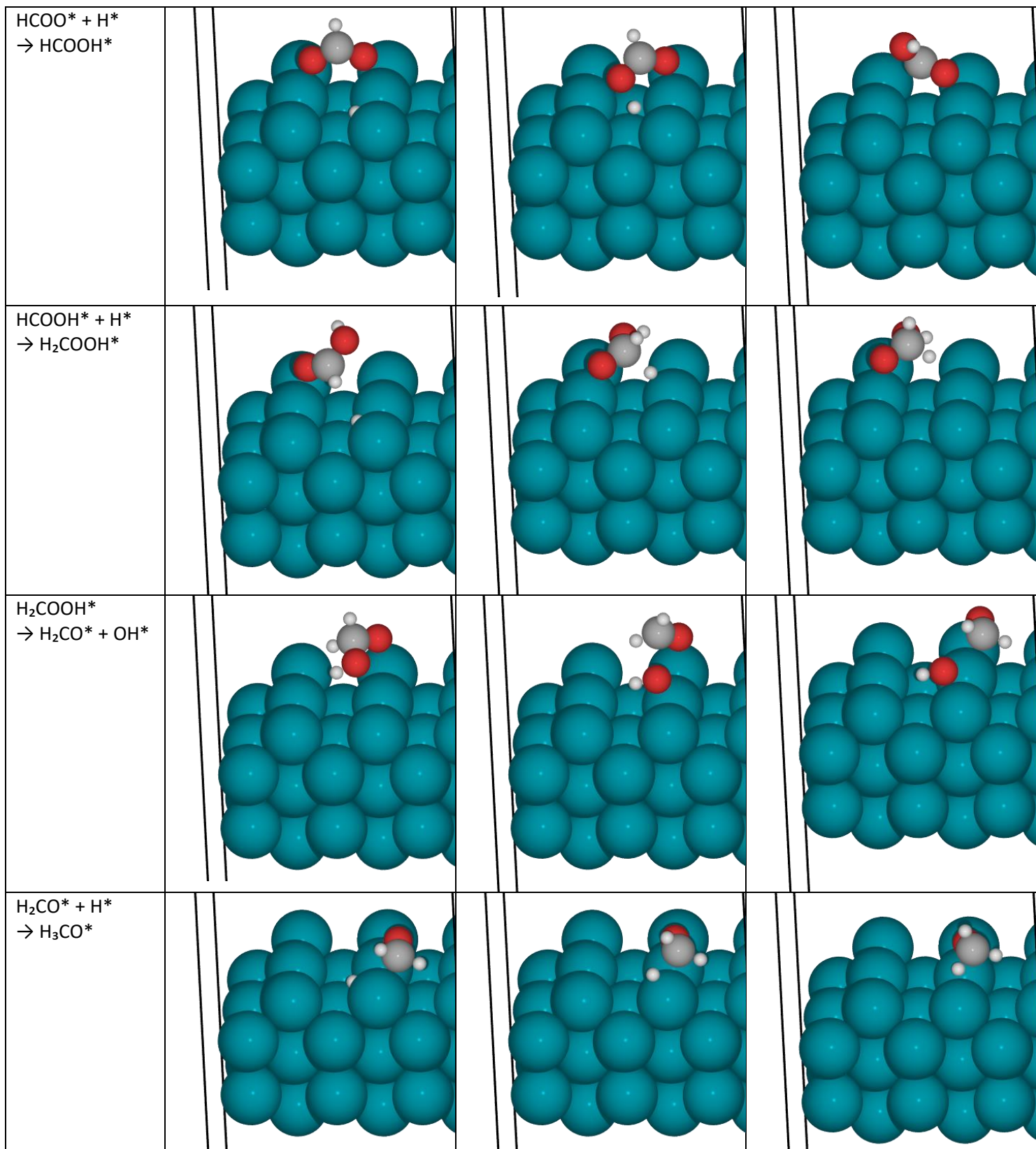
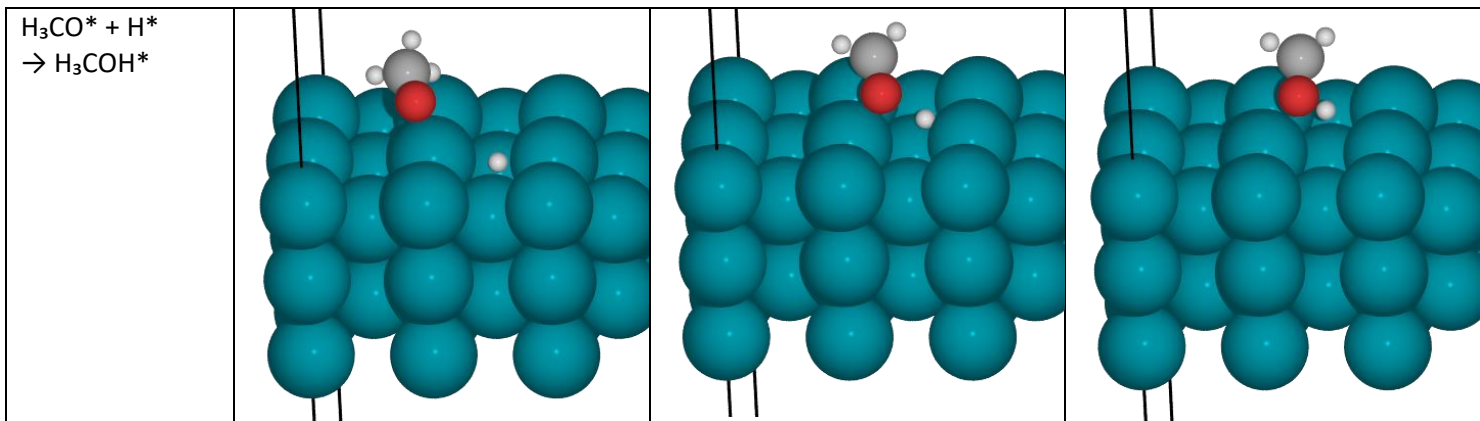


Table 26. Graphical representation of initial, transition state and final geometries in E_{act} calculations on Pd (110) surface. The blue, red, grey and white spheres represent Pd, O, C and H atoms; the black lines indicate the edges of the simulation cell. The full size of the simulation cell, including all unit cell borders, is depicted for the initial reaction step to illustrate the vacuum region size.







CO₂ dissociation and hydrogenation to formate

Table 27. Numerical data for CO₂ dissociation and CO₂ hydrogenation to formate on FCC Pd (111), (100), (110), FCC Cu (111), (100), (110), HCP Zn (0001), CuPd (110) and PdZn (101) and (110) surfaces; physisorbed and chemisorbed carbon dioxide species are denoted as CO₂ and CO₂^δ, respectively; monodentate and bidentate forms of formate intermediate are represented as HCOO^m and HCOO^b, respectively; + denotes co-adsorption of species; E_{ads} is measured with respect to gas phase substrates (CO₂ and/or ½H₂) and pristine surfaces in units of eV; atomic bond lengths, d(atom–atom) are measured in Å, where M represents the metal atom closest to the second atom; ∠species(O–C–O) is the oxygen-carbon-oxygen bond angle in units of °; E_{ads} of H is reported from structures with co-adsorbed physisorbed CO₂ and chemisorbed H atom; E_a (species) is the activation energy required for the formation of a transition state in reactions described in Chapter 5.3.4 and 5.3.8, starting from the species in brackets.; E_f/E_r is the ratio of the activation energy of the forward and reverse reaction of CO₂ hydrogenation to formate (E_a (CO₂ + H) divided by E_a (HCOO^b)).

| Species or process | surface facet | Pd (111) | Pd (100) | Pd (110) | Zn (0001) | PdZn (101) | PdZn (110) | CuPd (110) | Cu (110) | Cu (100) | Cu (111) |
|--|--|----------|----------|----------|-----------|------------|------------|------------|----------|----------|----------|
| HCOO ^m | $E_{ads}(\text{HCOO}^m) / \text{eV}$ | 0.57 | 0.43 | 0.17 | | 0.12 | -0.03 | 0.50 | 0.09 | 0.28 | |
| | dHCOO(H–M) / Å | 1.784 | 1.771 | 1.788 | | 2.310 | 1.987 | 1.882 | 1.846 | 1.878 | |
| | dHCOO(H–C) / Å | 1.216 | 1.213 | 1.206 | | 1.158 | 1.156 | 1.180 | 1.169 | 1.167 | |
| | dHCOO(M–C) / Å | 2.853 | 2.835 | 2.836 | | 3.103 | 2.970 | 2.795 | 2.702 | 2.778 | |
| | d ₁ HCOO ^m (C–O) / Å | 1.191 | 1.192 | 1.194 | | 1.197 | 1.197 | 1.194 | 1.196 | 1.194 | |
| | d ₂ HCOO ^m (C–O) / Å | 1.263 | 1.261 | 1.263 | | 1.284 | 1.285 | 1.277 | 1.276 | 1.279 | |
| | ∠HCOO(O–C–O) / ° | 132.9 | 132.6 | 132.3 | | 128.9 | 128.7 | 132.2 | 129.8 | 129.7 | |
| TS in CO ₂ hydrogenation to formate | $E_{ads}(\text{TS}) / \text{eV}$ | 0.65 | 0.53 | 0.33 | 1.11 | 0.34 | 0.49 | 0.5 | 0.52 | 0.64 | 0.64 |
| | dTS(H–M) / Å | 2.00 | 1.78 | 2.06 | 1.68 | 1.68 | 1.68 | 1.67 | 1.57 | 1.58 | 1.501 |
| | dTS(H–C) / Å | 1.16 | 1.23 | 1.15 | 1.63 | 1.60 | 1.68 | 1.43 | 1.70 | 1.63 | 1.71 |
| | dTS(M–C) / Å | 2.65 | 2.39 | 2.49 | 3.05 | 2.99 | 3.31 | 2.97 | 2.67 | 2.86 | 2.77 |
| | d ₁ TS(C–O) / Å | 1.21 | 1.21 | 1.21 | 1.17 | 1.17 | 1.17 | 1.18 | 1.17 | 1.17 | 1.176 |
| | d ₂ TS(C–O) / Å | 1.28 | 1.27 | 1.28 | 1.2 | 1.2 | 1.2 | 1.22 | 1.18 | 1.2 | 1.216 |
| | ∠TS(O–C–O) / ° | 128.5 | 133.1 | 127.2 | 152.3 | 149.7 | 153.1 | 145.5 | 150.9 | 151.2 | 146.4 |

| Species or process | surface facet | Pd (111) | Pd (100) | Pd (110) | Zn (0001) | PdZn (101) | PdZn (110) | CuPd (110) | Cu (110) | Cu (100) | Cu (111) |
|---|---|----------|----------|----------|-----------|------------|------------|------------|----------|----------|----------|
| H (from co-adsorption of CO ₂ and H) | $E_{\text{ads}}(\text{H}) / \text{eV}$ | -0.53 | -0.46 | -0.50 | 0.67 | -0.23 | 0.03 | -0.47 | -0.01 | -0.06 | -0.21 |
| CO ₂ + H | $E_{\text{ads}}(\text{CO}_2^{\delta-} + \text{H}) / \text{eV}$ | -0.32 | -0.50 | -0.49 | | 0.04 | 0.49 | -0.23 | 0.34 | 0.43 | |
| | $E_{\text{ads}}(\text{CO}_2 + \text{H}) / \text{eV}$ | -0.67 | -0.60 | -0.67 | 0.57 | -0.39 | -0.12 | -0.63 | -0.18 | -0.2 | -0.34 |
| CO ₂ | $E_{\text{ads}}(\text{CO}_2) / \text{eV}$ | -0.14 | -0.14 | -0.17 | -0.10 | -0.16 | -0.15 | -0.16 | -0.17 | -0.14 | -0.14 |
| | $E_{\text{ads}}(\text{CO}_2^{\delta-}) / \text{eV}$ | 0.15 | -0.08 | -0.25 | | 0.22 | 0.18 | 0.09 | 0.30 | 0.39 | |
| | $d\text{CO}_2^{\delta-}(\text{M}-\text{C}) / \text{\AA}$ | 2.04 | 2.01 | 2.00 | | 2.13 | 2.06 | 2.14 | 2.00 | 2.06 | |
| | $d_1\text{CO}_2^{\delta-}(\text{C}-\text{O}) / \text{\AA}$ | 1.19 | 1.2 | 1.21 | | 1.19 | 1.2 | 1.19 | 1.24 | 1.2 | |
| | $d_2\text{CO}_2^{\delta-}(\text{C}-\text{O}) / \text{\AA}$ | 1.24 | 1.24 | 1.23 | | 1.25 | 1.24 | 1.22 | 1.25 | 1.31 | |
| | $\angle\text{CO}_2^{\delta-}(\text{O}-\text{C}-\text{O}) / ^\circ$ | 139.1 | 139.1 | 137.3 | | 137.3 | 137.5 | 144.8 | 128.3 | 127.4 | |
| CO and O | $E_{\text{ads}}(\text{CO} + \text{O}) / \text{eV}$ | 0.79 | -0.02 | 0.06 | | 0.18 | 0.41 | 0.65 | 0.75 | 0.66 | |
| CO ₂ dissociation | $E_{\text{a}}(\text{CO}_2) / \text{eV}$ | 1.55 | 0.78 | 1.97 | | 1.39 | 1.61 | 1.39 | 2.53 | 1.35 | |
| | $E_{\text{a}}(\text{CO}_2^{\delta-}) / \text{eV}$ | 1.26 | 0.72 | 2.05 | | 1.01 | 1.28 | 1.14 | 2.06 | 0.82 | |
| | $E_{\text{a}}(\text{CO} + \text{O}) / \text{eV}$ | 0.62 | 0.66 | 1.74 | | 1.05 | 1.02 | 0.58 | 1.61 | 0.55 | |
| CO ₂ hydrogenation | $E_{\text{a}}(\text{CO}_2 + \text{H}) / \text{eV}$ | 1.32 | 1.13 | 1.00 | 0.54 | 0.73 | 0.61 | 1.13 | 0.68 | 0.84 | 0.98 |
| | $E_{\text{a}}(\text{CO}_2^{\delta-} + \text{H}) / \text{eV}$ | 0.97 | 1.03 | 0.99 | | 0.30 | 0.00 | 0.73 | 0.17 | 0.21 | |
| | $E_{\text{a}}(\text{HCOO}^{\text{b}} \text{ dissociation}) / \text{eV}$ | 0.99 | 1.02 | 0.96 | 1.74 | 1.15 | 1.36 | 1.00 | 1.59 | 1.51 | 1.22 |
| | E_i/E_r | 1.33 | 1.12 | 1.04 | 0.31 | 0.63 | 0.45 | 1.13 | 0.43 | 0.56 | |